Faculté des Sciences Appliquées
Département d'Architecture, Géologie, Environnement et Constructions

Finite element mesoscopic analysis of damage in microalloyed continuous casting steels at high temperature

–

Analyse mésoscopique par éléments finis de l'endommagement à haute température des aciers microalliés de coulée continue

Sylvie Castagne

Année académique 2006-2007

Secteur Mécanique des Solides, des Fluides et des Structures
Chemin des chevreuils, 1 B-4000 Liège 1 (Belgique)
anne.habraken@ulg.ac.be www.argenco.ulg.ac.be

Finite element mesoscopic analysis of damage in microalloyed continuous casting steels at high temperature

–

Analyse mésoscopique par éléments finis de l'endommagement à haute température des aciers microalliés de coulée continue

Thèse présentée en vue de l'obtention du grade de
Docteur en Sciences Appliquées
par Sylvie Castagne

Année académique 2006-2007

Thèse défendue avec succès le 12 février 2007

Membres du jury :

S. Cescotto, Professeur, Université de Liège (Président du jury)
A. Magnée, Professeur, Université de Liège
J. Lecomte-Beckers, Chargée de cours, Université de Liège
A.M. Habraken, Directeur de recherches FNRS, Univesrité de Liège (Promoteur)
M. Bobadilla, Arcelor Research, Maizières-les-Metz, France
P. Onck, Associate Professeur, University of Gnoningen, Pays-Bas
A. Pineau, Professeur Emérite, Ecole des Mines de Paris, France

Coordonnées de l'auteur :

Dr Ir Sylvie Castagne
UNSW Asia
Division Engineering, Science and Technology
1 Kay Siang Road
Singapore 248922

Phone: +65 6304 1414
Fax: +65 6472 2849
Email: sylvie.castagne@unswasia.edu.sg
URL: www.unswasia.edu.sg

Acknowledgements

I would like to express my sincere gratitude to Anne Marie Habraken for her guidance, enthusiasm and encouragements, which made the completion of this thesis possible. Her initial impact on my academic career, day-to-day support throughout this study and critical comments during the preparation of the manuscript are fully appreciated. I would also like to thank Jacqueline Lecomte-Beckers, who initiated my interest for the field of materials science and whose contributions to this research are innumerable. Furthermore, I owe many thanks to the numerous experts, both from academia and industry, who participated directly to this work through discussions, meetings, experimentation and data collection; in this respect, special thanks go to Serge Cescotto, Adrien Magnée and Manuel Bobadilla, who have contributed all along. The financial support from the University of Liège (Crédit d'Impulsion), F.N.R.S. and Arcelor to this research work is also gratefully acknowledged.

Many thanks go to all my colleagues at the University of Liège who contributed directly or indirectly to this work and to the engineers and technicians at the IBF, CRM and ULg who participated in the experimental study. I would also like to thanks all my colleagues and friends in Belfast for the excellent working and social atmosphere I have been plunged into during my stay in Northern Ireland.

J'ai également une pensée pour tous mes proches, famille et amis, qui ont fait preuve de beaucoup de patience et m'ont toujours encouragée. J'espère maintenant être plus disponible et leur rendre ce que je leur dois. Enfin, je souhaite remercier en particulier mes parents pour leur influence initiale sur mon parcours, ainsi que ma sœur Delphine pour son hospitalité et la relecture pointilleuse de ce manuscrit.

Sylvie Castagne,
Liège, December 2006

Contents

Summary

This thesis addresses the problem of damage at elevated temperature with a view to analysing transverse cracking during the continuous casting of microalloyed steels. Based on the results of a previous project undertaken at the University of Liège to simulate the continuous casting process at the macroscopic level, the present research aims at studying the damage growth using a finite element mesoscopic approach that models the grains structure of the material. The developments are done at the mesoscopic scale using information from both the microscopic and macroscopic levels.

In order to determine the constitutive laws governing the damage process at the mesoscopic scale, the physical mechanisms leading to the apparition of cracks during steel continuous casting are first investigated. It is acknowledged that in the studied temperature range (800 to 1200 °C), the austenitic grain boundary is a favourable place for cracks to initiate and propagate. The mechanisms of voids nucleation, growth and coalescence are established, the cavities evolving under diffusion and creep deformations.

Having identified the damage mechanisms occurring under continuous casting conditions, a numerical approach for the modelling of these phenomena at the grain scale is proposed. The mesoscopic model, which is implemented in the Lagrangian finite element code LAGAMINE developed at the University of Liège, is built on the basis of a 2D mesoscopic cell representative of the material. The finite element discretization comprises solid elements inside the grains and interface elements on the grains boundaries. An elastic-viscous-plastic law of Norton-Hoff type, which represents the thermo-mechanical behaviour of the material, is associated to the solid elements for the modelling of the grains; and a damage law accounting for cavitation and sliding is linked to the interface elements for the modelling of the damage growth at the grains boundaries. The transfer between the macroscopic and mesoscopic scales is realised by

imposing the stress, strain and temperature fields, collected during the parent macroscopic simulation, as boundary conditions on the mesosopic cell.

Macroscopic experiments, analytical computations and finite element simulations, as well as literature review and microscopic analyses, are used to define the parameters of the material laws. The experimental results and the identification methodology leading to the definition of the set of parameters specific to the studied steel are described.

Finally, the influence of oscillation marks and process defects on cracks formation during the industrial process of continuous casting is analysed. The results are compared with in-situ observations and cracking risk indicators computed by the macroscopic model.

Principal symbols

NOTATIONS

$\underline{\times}$	vector (row)
$\{\times\}$	vector (column)
$[\times]$	matrix
$\lvert\times\rvert$	determinant
$\times^T$	transposition
$\dot{\times} = \frac{d\times}{dt}$	temporal derivative
$d\times$	differentiation
$\delta\times$	variation
$\times_0$	initial or reference value
$\times_c$	variable relative to the contact problem
$\times_{crack}$	variable at crack initiation
$\times_i$	variable at step *i*
$\times_R$	variable at rupture
$\times_t$	variable at time *t*
$\times_{thr}$	threshold value

LATIN LETTERS

a	void size (radius)
B	creep coefficient
b	void spacing (half length between centre of voids)

$[C]$	compliance matrix
d	grain size (diameter)
	contact distance in global axes
$ddam$	damage variable
d_{lim}	damage threshold for crack initiation
D	diffusion parameter
	damage variable (continuum damage mechanics
E	Young's modulus
e	thickness of a slice in generalized plane state
$(\underline{e}_n, \underline{e}_s)$	local coordinates base vectors relative to the contact surface
$(\underline{e}_r, \underline{e}_\theta, \underline{e}_z)$	cylindrical coordinates base vectors
$(\underline{e}_x, \underline{e}_y, \underline{e}_z)$	global coordinates base vectors
$\underline{F}$	contact force, equivalent nodal forces
F_n	nucleation parameter
f	area fraction of grain boundary cavitated
h	height of the compression specimen
I_1, I_2	macroscopic crack risk indicators
$[J]$	Jacobian matrix
$[K]$	stiffness matrix
k_s, k_n	shear, normal penalty coefficient
L	length scale for diffusive and creep void growth
l	abscissa along the contact element
N	nucleation coefficient
N_I	cavity density for nucleation
	interpolation functions
N_{max}	maximum cavity density
n	creep exponent
p	contact pressure
p_1, p_2, p_3, p_4	parameters of the modified Norton-Hoff law
Q_b	activation energy
$[R]$	rotation matrix

RA	reduction of area
S	parameters characterizing the state of the material before nucleation
S_0, S_f	Initial, final cross section of a cylindrical specimen
T	temperature
t	time
$\underline{U}$	vector of the nodal displacements
$\underline{u}$	vector of the global displacements
V	void volume
$\underline{v}$	vector of the global velocities
$\dot{u}$	sliding velocity computed from nodal displacements
$\dot{u}_s$	sliding velocity computed from grain boundary sliding law
w	grain boundary thickness Gauss integration weight
$\underline{X}$	vector of the nodal coordinates
$\underline{x}$	vector of the global coordinates

GREEK LETTERS

$(\alpha_1, \alpha_2, \alpha_3)$	coordinates relative to the generalized plane state
Δ	contact distance in local axes
δ	contact penetration distance
$\dot{\delta}$	average separation rate computed from nodal displacements
$\dot{\delta}_c$	average separation rate computed from voids evolution law
$\dot{\varepsilon}$	uniaxial strain rate
ε_e	equivalent strain
$\dot{\varepsilon}_e$	equivalent strain rate
$\dot{\varepsilon}_B$	grain boundary strain rate parameter
η	second intrinsic coordinate
η_B	grain boundary viscosity
ν	Poisson's ratio
ξ	first intrinsic coordinate

Σ_0	normalization stress
σ_1	maximal principal stress
σ_e	von Mises equivalent stress
σ_n	normal stress
σ_{yield}	yield stress
$\tilde{\sigma}$	effective stress
τ	contact shear stress
ψ	cavity angle
Ω	atomic volume

Chapter 1

Introduction

1.1 SCOPE AND OBJECTIVES OF THE STUDY

Continuous casting of steel has been introduced industrially around 1960. It has become more and more important for steel producers because of its advantages compared to the older technology of ingots casting: continuous production, energy and manpower savings, improvement of steel quality through a finer control of the process and better yield due to scrap reduction. Steel, aluminium and copper are continuously cast, but steel constitutes the highest tonnage proportion.

Although the conditions to optimise the process have been widely studied during the past 30 years, one of the major problems that remains in steel continuous casting is transverse cracking. To minimize surface and internal cracks formation, the control of the steel chemistry and of the cooling rate is absolutely essential and a lot of research work is done in this domain by the metallurgical community. Nevertheless, the measures to prevent transverse cracks are divided into two parts: certainly the control of the steel chemistry but also the prevention of cracks initiation and propagation due to the thermo-mechanical loadings during the process. This second point is the principal objective of this study.

Based on the results of a previous project undertaken at the University of Liège to analyse the continuous casting process from a macroscopic point of view, the present research aims at modelling the damage process at elevated temperature using a mesoscopic approach. The damage model is built on the basis of a 2D mesoscopic cellular model representative of the material. It allows the analysis of the effect of

factors such as grain size, oscillation marks, spatial gradient of composition or microstructure on the crack initiation and its propagation. Macroscopic experiments and simulations, as well as literature review and microscopic analyses, are used to define the parameters of the constitutive damage law.

The present research lies at the intersection of various disciplines and in particular metallurgy, materials engineering and continuum mechanics. The length scales commonly dealt with in these fields are different and therefore the meaning given to the terms *macro* and *micro* differs among experts depending on their specific background. In this thesis, the terminology *macro* refers to the analysis at the process level, when continuum mechanics can be applied; *meso* refers to the modelling at the grain scale, the mesoscopic cell being a group of grains; and *micro* concerns the mechanisms that are linked to the smaller scales such as voids or inclusions. In this project, the developments are done at the mesoscopic scale using information from both the microscopic and macroscopic scales.

The mesoscopic damage model is implemented in the non-linear Lagrangian finite element code LAGAMINE and applied to model the material behaviour during the industrial process of steel continuous casting. The development of LAGAMINE started in the MSM Department of the University of Liège in 1982 with the modelling of the rolling process of steel beams and pile sheets (Cescotto and Grober 1985). The library of solid elements (Jetteur and Cescotto 1991, Zhu and Cescotto 1995, Li and Cescotto 1997a, Li and Cescotto 1997b) and contact elements (Cescotto and Charlier 1993, Habraken and Cescotto 1998a) has been progressively increased thanks to various research projects. The code is clearly focused on the modelling of material behaviour. In particular, studies have concentrated on solid phase transformation (Habraken and Bourdouxhe 1992a, Pascon *et al.* 2005) or recristallization (Habraken *et al.* 1998b), damage models to predict crack appearance (Zhu and Cescotto 1992b, Castagne *et al.* 2002, Remy *et al.* 2002b, Castagne *et al.* 2003), phenomenological laws with gradient plasticity (Li and Cescotto 1996) or micro-macro laws (Duchêne *et al.* 2002, Habraken and Duchêne 2004). Specific processes such as deep drawing (Li *et al.* 1995, Duchêne and Habraken 2005), forging (Dyduch et al. 1992) or continuous casting (Pascon *et al.* 2000, Castagne *et al.* 2004, Pascon *et al.* 2006) have also been simulated.

Although the practical application of the model developed in this thesis is the simulation of the continuous casting process, the ultimate goal of the research is the exploration and development of techniques facilitating damage modelling at elevated temperature. The implementation of the model in a finite element code and its

application to an industrial forming process is essential to prove the viability and practicability of the method.

1.2 CONTEXT OF THE RESEARCH

This research project has been initiated at the University of Liège on the basis of previous work carried out in the field of metal forming and continuous casting modelling. Initial funding from the Belgian National Fund for Scientific Research (F.N.R.S.) and from the University of Liège (Crédit d'impulsion), has permit to set the foundations of the numerical model, to perform the experimental analyses and to present a proof of concept to the industrial partner Arcelor who had already shown a great interest in this research. The technical and financial support provided by Arcelor has been essential for the completion of the practical phase of the project. The involvement of Arcelor is also of great significance for the ultimate relevance of the work.

1.3 OUTLINE OF THE THESIS

After this introduction, the second chapter presents a literature review of damage at elevated temperature focusing on the models susceptible to be applied in continuous casting conditions. It starts with a description of the continuous casting process, followed by a review of cracks formation in continuous casting looking at the factors that are responsible for transverse cracking and at the involved physical mechanisms. Then, models developed for the analysis of cracks are presented, starting with traditional fracture and continuum damage mechanics models before focusing on multi-scale approaches and numerical modelling of the crack propagation phase. This step is essential in determining the way forward for the development of the continuous casting damage model.

Chapter 3 describes the finite element mesoscopic model. The main features of the model are the interface finite element which is used for the representation of the grain boundaries and the associated constitutive damage law that accounts for the damage processes at the mesoscopic scale. Solid elements that represents the grains are also included in the model, they are linked to an elastic-viscous-plastic constitutive law that defines the thermo-mechanical behaviour of the material. Initial simulations carried

out to verify the model and technical developments linked to its implementation within the finite element code LAGAMINE are also presented.

The experimental analyses that have been carried out to define the parameters of the model are presented in Chapter 4 together with the numerical simulations which have been performed to identify these parameters. In particular, a metallographic analysis combining optical microscopy and picric acid etching has been preformed to establish the crystalline structure of the material. Mechanical compression tests have been carried out to determine the material properties of the steel and damage tests have been performed to calibrate the parameters that have to be introduced in the damage model.

The object of Chapter 5 is the application of the damage model to the continuous casting process, starting with the definition of the appropriate cell size before transferring data from the macroscopic simulation to the mesoscopic cell. The final application is the comparison of the damage effects on a cell with or without oscillation marks when continuous casting conditions are applied. A reference case without defect and a case with misalignment of one pair of rolls, which is a problem that can arise during the industrial continuous casting process, are compared with in-situ observations and risk indices computed by the macroscopic continuous casting model.

The last chapter summarizes the content of the thesis, presents generic conclusions and proposes recommendations for the future developments and applications of the mesoscopic damage model.

1.4 METHODOLOGY

The methodology followed comprises four main aspects corresponding to the four essential stages required to derive a viable model for the analysis of intergranular crack initiation and propagation at elevated temperature. These four steps also correspond to the four core chapters of the thesis:

- identification of the involved physical phenomena and analysis of the existing theories and models that could be used as a starting point for the development of the mesoscopic damage and fracture model at elevated temperature (Chapter 2),
- development, numerical implementation and verification of the model (Chapter 3),

- experimental analyses and calibration of the model for the particular material tested (Chapter 4),
- application to the continuous casting process and validation of the model (Chapter 5).

1.5 ORIGINAL CONTRIBUTIONS

The work presented in this thesis follows an exploratory path that addresses the problem of crack initiation and propagation at elevated temperature with a particular application in the field of continuous casting. The following aspects can be emphasized as original contributions to this research project:

- selection of a mathematical model that represents the physical phenomena linked to crack initiation and propagation at elevated temperature in the context of the modelling of transverse cracking during steel continuous casting,
- implementation, verification and validation of an interface finite element associated with a damage law and adaptation of the finite element code LAGAMINE for the treatment of the mesoscopic model which comprises interface and grain elements,
- proposition to use acoustic tests for the calibration of the damage law parameters and realisation of the parameters identification based on this technique,
- definition of a methodology for the data transfer between the macroscopic and mesoscopic levels,
- application of the developed mesoscopic model to the analysis of transverse cracking at the grain scale during the straightening phase of the continuous casting process.

Chapter 2

An overview of damage in the context of continuous casting

2.1 DESCRIPTION OF THE CONTINUOUS CASTING PROCESS

The main objective of this thesis is to develop a local damage model to be applied to steel subjected to continuous casting loading conditions. Therefore, the present section aims at introducing the basic concepts of continuous casting to give an understanding of the process before studying the local damage effects. A detailed description of the continuous casting process, as part of the whole steel production cycle, has been presented by Pascon (2003).

The continuous casting process transforms molten steel coming from blast or electric arc furnaces into cast products, which are then processed by hot rolling before being commercialised as final products. The cross section of the cast products extracted from continuous casting mills depends on the shape of the final product. Two major families of final products can be distinguished: flat products (steel plates or sheets) produced by hot rolling of cast products of relatively wide rectangular cross-section called slabs (50 to 250 mm thick and 0.5 to 2.2 m wide), and long products (beams, rails, wires) produced by hot rolling of cast products of roughly square cross-sections called blooms (up to 400 mm thick and 600 mm wide) or billets (100 to 200 mm thick). More specific cast products cross-sections can be produced with a view to reducing the number of rolling passes, e.g. beam blanks for the production of I-beams.

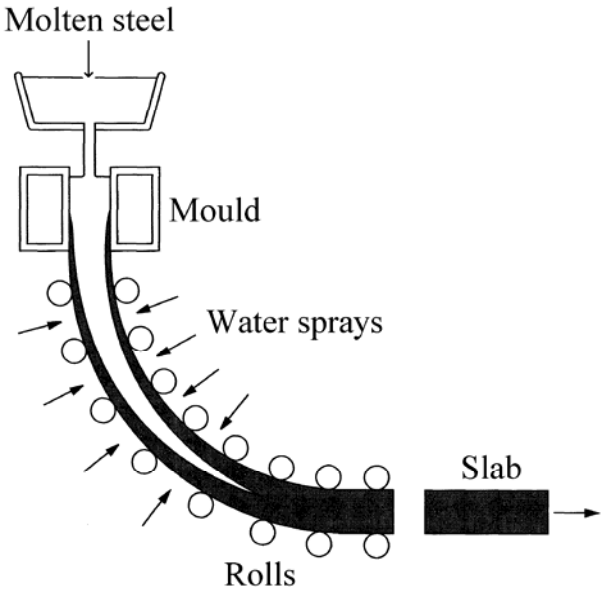

Figure 2.1. Continuous casting process.

Continuous casting mills can be straight or curved, depending on the application. Figure 2.1 shows a schematic representation of a curved continuous casting mill corresponding to the type of machine used to produce the cast products analysed in this thesis.

Throughout the continuous casting process, molten steel is poured into a bottomless copper mould where it starts to solidify. A water cooling system helps to keep the surfaces of the mould at a relatively low and constant temperature (between 100 and 200 °C) allowing the primary cooling phase to occur within the mould. During this phase, the liquid steel freezes in contact with the mould and a solidified skin starts to grow while the steel is moving down. To protect steel from oxidation, a specific powder is continuously put onto the free liquid steel surface in the mould. Lubricant agents are also contained in this anti-oxidation powder which develops its lubricant properties while melting in contact with the steel. In addition to the lubricant agents, a vertical oscillating movement is imposed to the mould to prevent sticking between the mould and the strand. The mould oscillations lead to the formation of marks on the slab surface which remain visible on the surface of the cast product and can be damaging for the final product if not properly controlled. These aspects are explained in more details in section 2.2.

The secondary cooling phase takes place outside the mould where the steel continues to solidify. At the exit of the mould, the steel is still partially liquid and three material phases can be distinguished: the external solidified shell, the mushy zone made

of liquid and solid fractions, and the liquid core. The external shell must be thick enough to avoid cracking and contain the liquid steel. The control of the thickness of this shell is a very important factor for the quality of the process. Under the mould, extracting rolls pull the strand out and make it move forward in the machine at a controlled velocity called the casting speed. The position of the rolls imposes the path of the strand in the machine and controls its bending and straightening. Water sprays are placed between the rolls to continue the cooling of the strand and to regulate the solidification progression. The contact between the rolls and the strand also contributes to cooling as the rolls are equipped with an internal water cooling system, although the main purpose of the internal cooling system is to avoid rolls deformation. As the strand moves down, the thickness of the solidified shell grows until the entire section is solidified. The strand can then be cut and sent to storage before rolling.

The loads that have to be sustained by the steel shell during solidification in the continuous casting mill are of various types: a ferrostatic pressure is imposed by the liquid core on the solidified shell which acts as a pressurized tube; compression and tensile loads are present in the shell due to the bending and straightening of the strand; frictional and compression loads, as well as indirect tensile loads due to the extraction forces, are imposed by the rolls; and finally thermal and phase transformation loads are initiated due to the thermal history.

Computational modelling of continuous casting is an area of research in constant development (Thomas 2002, Costes 2004, Pascon *et al.* 2006). Mathematical models and simulations are used to analyse the effect of the parameters that have to be controlled to ensure high quality products, i.e. the mould cross-section and taper, casting speed, cooling rate or rolls position (Barber *et al.* 1991, Thomas and Ho 1991, Louhenkilpi *et al.* 1993, Ridoffi *et al.* 1994, Miyake *et al.* 1998, Ren and Wang 1998, Huespe *et al.* 2000, Pascon *et al.* 2000, Park *et al.* 2002, Li and Thomas 2004).

2.2 CRACK FORMATION IN STEEL CONTINUOUS CASTING

Different types of internal and surface cracks may occur during the continuous casting process as illustrated in Figure 2.2. Two zones of low ductility are usually emphasized in steels: the first zone exists above 1340°C and accounts for the formation of all internal (midway, triple-point, centreline, diagonal) and surface longitudinal cracks while the second low ductility zone lies between 700 and 900°C and is related to the appearance of transverse cracks (Brimacombe and Sorimachi 1977).

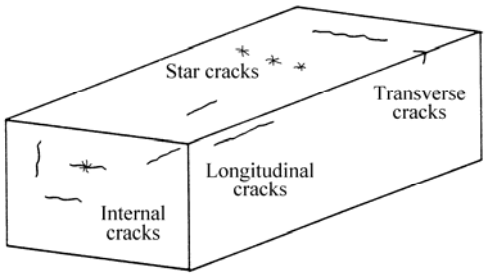

Figure 2.2. Types of cracks in continuous casting.

Steel ductility at high temperature and its relationship to the problem of crack formation after steel solidification in continuous casting conditions has been widely studied (Lankford 1972, Myllykoski and Suutala 1983, Revaux *et al.* 1994, Patrick *et al.* 1997, Hiebler and Bernhard 1999). In particular, detailed reviews focusing hot ductility of steels and its link to transverse cracking have been published by Mintz (Mintz *et al.* 1991, Mintz 1999).

2.2.1 FACTORS INFLUENCING TRANSVERSE CRACKING

Although the factors responsible for the formation of the majority of internal and surface cracks are known, transverse cracking in particular is extremely damaging for final products and constitute an important area of research. Cast products are inspected before rolling but the inspection phase does not always permit to detect and remove all transverse cracks. A transverse crack of a few millimetres depth on a slab can then be at the origin of defects that extend several meters on rolled plates or sheets as illustrated in Figure 2.3.

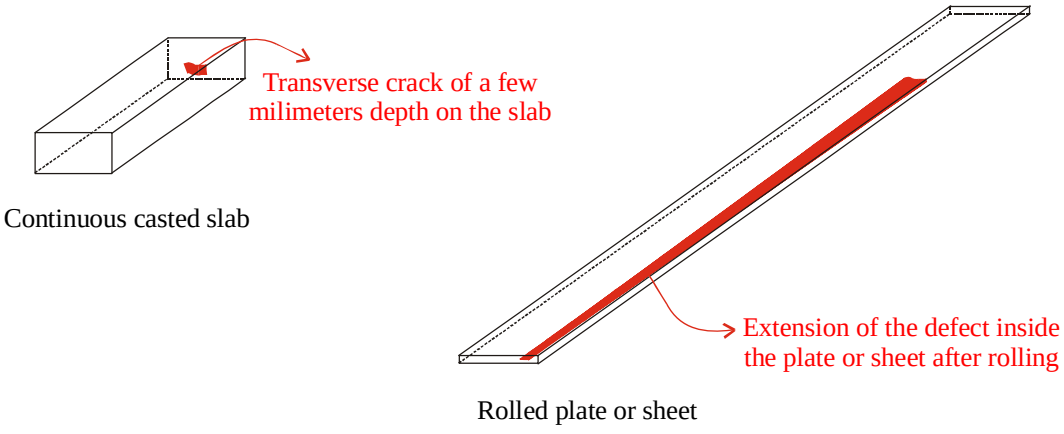

Figure 2.3. Schematic illustration of the extension of a transverse crack after rolling.

Transverse cracks initiation takes place during the unbending phase of the continuous process when the slab is straightened at temperatures which coincide with the second low ductility zone of the material. Strain rate, grain size, precipitation state and inclusions content are the major parameters that influence hot ductility and transverse cracking in this temperature range.

Increasing the strain rate and refining the grain size improve ductility by reducing the amount of grain boundary sliding and making it more difficult for cracks to propagate along the grain boundaries (Fu *et al.* 1988, Mintz *et al.* 1991). Fine precipitates generally weaken the grain boundaries and facilitate cracks interlinking. Although addition of titanium seems to be the most efficient to maintain a high ductility, typical micro-alloying elements such as aluminium, niobium and vanadium are usually responsible for a reduction in ductility and should be kept at the lowest level to meet the property requirements of the final product (Bernard *et al.* 1978, Cepeda *et al.* 1989, Harada *et al.* 1990, Mintz and Abushosha 1993, Cardoso *et al.* 1995). In particular, the combination of nitrogen with aluminium, which is used to prevent oxidation, niobium or vanadium is very detrimental due to the precipitation of nitrides and carbonitrides along grain boundaries (Vodovipec 1978, Mintz *et al.* 1991, Weisgerber et al. 1999). Niobium and vanadium can improve steel strength and weldability but undergo dynamic precipitation during straightening. Residual elements such as copper, sulphur and phosphorus influence precipitation and their presence should be limited (Mintz 1999). The carbon content is also a very important factor in mild steels, with a maximum susceptibility to transverse cracking between 0.10 and 0.15 wt% (weight percentage) of carbon (Maehara *et al.* 1985).

In addition to the factors presented here before, oscillations marks, which are caused by the vertical oscillations of the mould during the continuous casting process, are recognized as a factor at the origin of cracks initiation (Maehara *et al.* 1987, Suzuki *et al.* 1999). Transverse cracks may be formed at the subsurface below an oscillation mark where the local segregation is important and the material more fragile. The formation mechanism of the surface segregation, particularly of phosphorus which is present in the slag, has a close relation with the formation of oscillation marks (Harada *et al.* 1990). When an oscillation mark is formed, the partially solidified shell is deformed and the dirty segregated liquid steel present between the dendrite arms is squeezed out to the surface. The degree of segregation depends on the depth of the oscillation marks.

2.2.2 MECHANISMS OF TRANSVERSE CRACKS INITIATION AND PROPAGATION

Ashby deformation-mechanisms maps indicate the field of dominance of a given deformation mechanism as a function of the normalized shear stress and temperature. Such maps have been defined for various materials (Ashby *et al.* 1979, Gandhi and Ashby 1979, Frost and Ashby 1982). Figure 2.4 gives two examples of deformation-mechanisms maps, one for pure iron and one for a low-alloy steel.

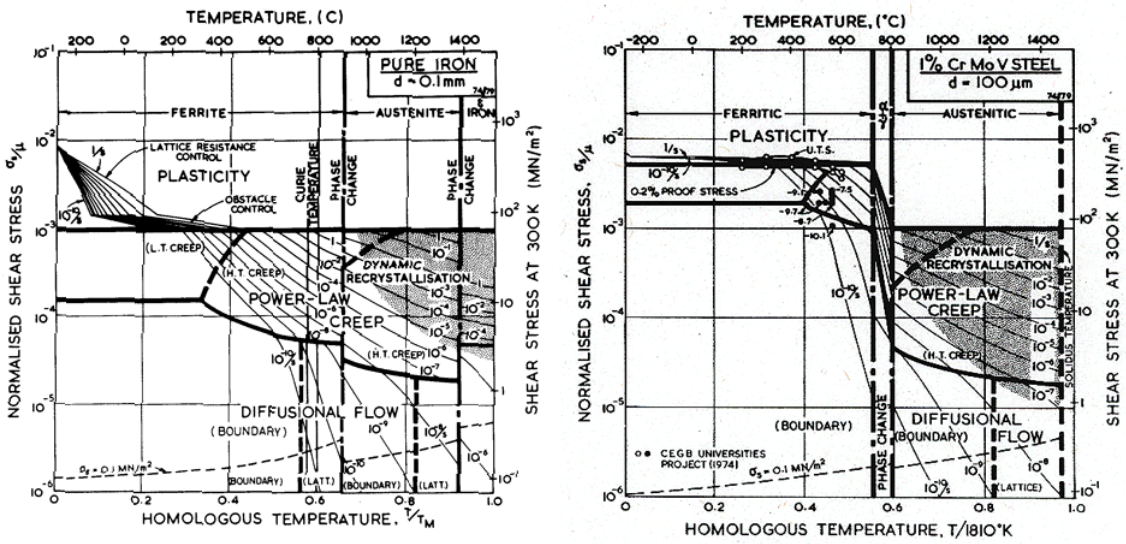

Figure 2.4. Deformation-mechanism maps for pure iron and low-alloy steel (Frost and Ashby 1982).

General characteristics can be drawn by comparison of the Ashby maps. In particular, it is shown that for high temperature and low stress, the prevalent deformation mechanism is diffusional flow. Experimentally, transverse cracks in continuous casting have been shown to be intergranular, meandering along prior austenite grain boundaries. Moreover, during the continuous casting process, the stress and temperature levels are in accordance with the zone corresponding to boundary diffusional flow of the Abshy maps. Therefore, it is recognized that cracks in continuous casting are formed by integranular creep damage.

The effect of creep on transverse cracking is associated with grain boundary sliding and diffusion (Ashby *et al.* 1979, Guttman 1982, Suzuki *et al.* 1984, Mintz *et al.* 1991, François et *al.* 1993). In the lower temperature of the austenitic phase, dynamic recrystallisation becomes difficult and grain boundary sliding occurs to accommodate the creep deformation in the austenitic grains. This process stimulates the nucleation of voids at the grain boundaries. The local diffusion of voids, associated with the inverse

flow of material, contributes to their growth and to the creation of micro-cracks along the grain boundaries.

A second mechanism linked to transverse cracking, and that explains the presence of a ductility trough for temperatures between 700 and 900°C, is the embrittlement by strain concentration and micro-voids coalescence at the grain boundaries. This phenomenon is induced by austenite-ferrite transformation that initiates along the grain boundaries and creates a thin film of softer ferrite around the grain boundaries, particularly in low and medium plain-carbon steel (0.05 to 0.4 wt% of carbon) (Suzuki *et al.* 1984). In niobium containing steels, the embrittlement is also linked to the formation of a weak free precipitate zone around the grain boundaries, which accompanies the grain boundaries precipitation (Mintz *et al.* 1991).

During the strengthening of the slab, when the surface temperature coincides with the ductility trough, a combination of these mechanisms triggers crack initiation and propagation.

2.3 MODELLING OF CRACKS AT HIGH TEMPERATURE

Computational modelling of crack initiation and propagation in continuous casting conditions is not abundant in literature and particular applications to transverse cracking are almost inexistent. Li and Thomas (2004) propose a finite element model to analyse crack formation during the primary cooling phase. Pascon (2003) models the whole continuous casting process and uses macroscopic damage criteria to rank damaging events such as blocked nozzles or misaligned rolls that could affect the process. Gamsjäger *et al.* (2001) look at the austenite-ferrite transformation and its effect on strains at the grain boundary. Although these models help to understand the damaging effects of various parameters, none of them looks at local aspects of transverse cracking as part of the macroscopic continuous casting process.

In order to determine the approach that should be followed to model transverse cracking in the scope of this thesis, it is necessary to analyse the problem of crack initiation and propagation in a more global context. Two separate currents of research have to be explored regarding cracks problems: fracture mechanics and damage mechanics. Multi-scale techniques constitute another area of interest since one the objective of the thesis is to link macroscopic data to local cracking behaviour. These approaches have overlaps with the two previous fields but are described in a separate section. Finally, the last section presents some of the techniques that have been used in

computational models to represent crack propagation. Most of the models presented hereafter have been developed for ambient temperature conditions; nevertheless, when information is available, specific high temperature applications are highlighted.

2.3.1 FRACTURE MECHANICS

Fracture mechanics is a relatively new science that has emerged in the 1920s with Griffith work (Griffith 1920) and has been more widely developed since the 1950s (Broek 1986, Leblond 2003, Anderson 2005). It initially focused on purely brittle materials and was further extended independently by Irwin (1948) and Orowan (1949) to account for plasticity at the crack tip.

Brittle materials usually fail by cleavage, i.e. separation of atomic plans. Based on this assumption, different concepts have been developed to determine fracture criteria. Griffith first proposed that energy had to be released from the system to create new crack surfaces, the development of this idea led to the introduction of a new parameter to characterize the material: the critical energy released rate, which can be used as a fracture criterion (Irwin 1956). The concept of stress intensity factors, linking classical solid mechanics (strength of material) and fracture mechanics, has been developed later and fracture toughness proposed as another fracture criterion. The *J*-integral developed by Rice (1968), which is an extension of Griffith energy method, and the crack tip opening displacement as proposed by Wells (1963), are two other fracture mechanics approaches that lead to the definition of fracture criteria.

Fracture mechanics is used in industry to assess the danger of propagation of existing cracks and to design parts and structures that will sustain the load until detectable cracks are formed. This approach is often applied in conjunction with fatigue theories to predict the safe life of mechanical components.

Nevertheless, fracture mechanics is not appropriate for applications at high temperature where large amount of plastic deformations are involved. Moreover, it does not account for any of the damage processes that occur before crack initiation and in particular for the diffusion phenomena that are important at high temperature.

2.3.2 DAMAGE MECHANICS

Damage mechanics, often referred to as ‘continuum damage mechanics’, generally concerns more ductile materials although it can be applied to creep, fatigue or

brittle failures (Lemaitre and Desmorat 2005, Voyiadjis 2005). This subject emerged in the 1960s and has been extensively studied in the past thirty years.

There are two common ways to predict rupture in the field of continuum mechanics. The first method consists in using classical constitutive laws coupled with macroscopic rupture criteria. This approach is easily implemented in any numerical code. Nevertheless, this method is not general as it is difficult to find a single rupture criterion that can represent various modes of rupture. The second approach is a coupled damage analysis which is based on damage constitutive laws. Damage is treated through internal state variables that describe the irreversible process of internal structure degradation due to micro-defects. Damage in the material is represented by damage variables which measure the porosity of the material. The mechanical properties of the material are reduced according to these damage variables. Damage increases in the material due to plastic deformations and these phenomena lead to void growth and final failure by void coalescence. The coupled method, which integrates the stiffness decrease due to damage in the stress and strain computation, allows the prediction of different rupture types, the localisation of the rupture zone and the tracking of the crack growth path.

2.3.2.1 Creep damage models

As creep is recognised as one of the major phenomena that lead to crack formation during continuous casting, this first section focuses on creep damage models.

The concept of damage variable and effective stress in damaged material was first introduced by Kachanov (1958) and Rabotnov (1968) for the modelling of creep. The initial creep damage law assumed that the damage evolution was a function of the effective stress in the material. In the uniaxial case of isotropic damage, the effective stress $\tilde{\sigma}$ is formulated as follow:

$$\tilde{\sigma} = \frac{\sigma}{(1-D)} \tag{2.1}$$

in which D is a scalar internal damage variable corresponding to the surface density of micro-cracks ($D = 0$ in the undamaged state) and σ the Cauchy stress. The time to rupture is calculated by integration of the damage evolution law up to a critical damage value.

Since the pioneering works of Kachanov and Rabotnov, a large number of papers on the modelling of creep damage for polycrystalline material have been published; Betten *et al.* (1999) present a review on the subject. Most analyses at

elevated temperature focus on the computation of the life time of structures in service. Usually creep damage parameters are incorporated into the models but time to rupture, t_R, remains one of the most critical variable of the problem (McLean and Dyson 2000, Murakami *et al.* 2000, Ragab 2002).

Betten *et al.* (1999) propose a three-dimensional creep model coupled with a damage vector. The model describes simultaneously damage induced anistotropy, different damage in tension and compression and different creep behaviour in tension and compression. Using the same initial formulation, they propose variations of the model able to reproduce the three stages of creep evolution for constant load (see Figure 2.5): primary creep (decelerating strain growth), secondary creep (linear portion) and tertiary creep (accelerated strain growth) which finally leads to failure (Nabarro and de Villiers 1995). t_R is the time at which the rupture occurs and ε_R the corresponding strain.

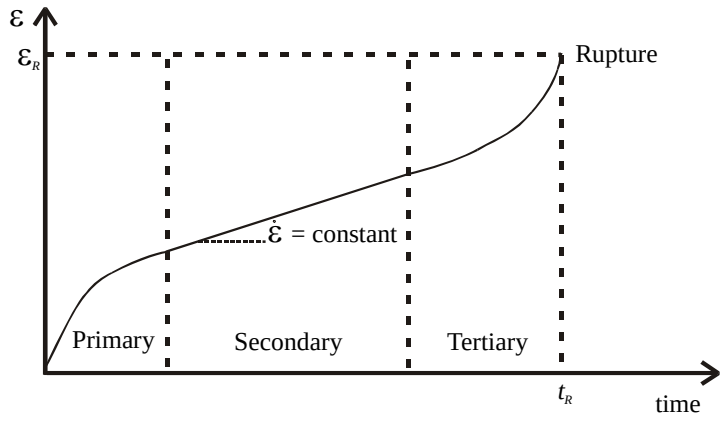

Figure 2.5. Typical creep deformation evolution at constant stress and temperature.

Due to the high temperatures involved, the diffusion phenomena that induce creep facture occur at relatively high speed during the continuous casting process. Therefore, the classical models dedicated to creep are not appropriate to reproduce the damage phenomenon in continuous casting, whose time scale is smaller than traditional applications. Moreover, these models perform macroscopic analysis which focus on time and do not integrate the microscopic behaviour of the grain boundary.

2.3.2.2 Damage models developed in the context of ductile fracture

With a view to defining suitable models to be developed and applied for high temperature conditions, this section presents some continuum damage models initially dedicated to ductile fracture. Nowadays, the continuum damage theory is a field where a

tremendous amount of research work is available; Habraken (2001) proposes a detailed review of these models. Initially, Gurson (1977), Tvergaard (1982), Lemaitre and Chaboche (1985) and Perzyna (1986) proposed elastic-plastic and elastic-viscous-plastic continuum theories for isotropic damage sensitive materials. New extensions which cover anisotropic cases have then been developed (Charles *et al.* 1997, Voyiadjis, and Deliktas 2000, Benzerga *et al.* 2004).

Two types of constitutive relations are found in literature to model the coupled phenomena of elastic-plasticity and material damage, either at the macroscopic or microscopic scale.

Macroscopic damage models

The macroscopic approach is based on phenomenological observations and thermodynamics considerations (Lemaitre 1985, Rousselier 1987, Ju 1989, Murakami *et al.* 1998, Voyiadjis and Park 1999). It is motivated by microscopic considerations but not deduced from them. The method only requires simple macroscopic experiments but is often confronted with localisation problems.

The ductile fracture model proposed by Lemaitre is based on the concept of effective stress $\tilde{\sigma}$ introduced by Kachanov and Rabotnov for the purpose of modelling fracture due to creep (see equation (2.1)). Using the hypothesis of energy equivalence, the constitutive relations of the damaged material are derived from those of the undamaged material by replacing the nominal stress σ by the effective stress $\tilde{\sigma}$. In case of non-isotropic damage, the scalar damage variable is replaced by a damage tensor and the effective stress by the stress tensor. The thermodynamics of irreversible processes is used to define the laws governing the evolution of the internal variables (Lemaitre 2005).

Using a similar approach, Rousselier (1987) proposed a model where the damage parameter is a function of the density of the material. For some particular values of the parameters, if the void volume fraction is low and the triaxiality is high, the yield surface becomes identical to the Gurson potential presented in the next section, which was obtained following a totally different approach. He also treated the viscous-plastic case by modelling it numerically like a plastic material but with a hardening curve depending on the strain rate (Rousselier *et al.* 1989). The resulting viscous-plastic model allowed the analysis of temperature effects on ductile fracture. Temperature dependence was introduced into a critical cavity growth criterion on the basis of experimental data. The model was applied to the damage analysis of stainless steel up to a temperature of 300°C. An extension of the Rousselier model has been

presented by Tanguy and Besson (2002) for the finite element analysis of ductile rupture under various strain rate and temperature conditions.

Microscopic damage models

Macroscopic continuum damage mechanics enables to compute damage evolution in complex structure. Nevertheless, for some applications, a more detailed physical description of microscopic processes involving damage are necessary to improve existing models. Indeed, it is difficult to account for all the physics of the phenomena with only macroscopic descriptions. Moreover, macroscopic damage models suffer from a lack of mesh independence and from localization phenomenon. The introduction of a material length scale is necessary to overcome this problem.

The microscopic approach, also called local approach, is based on a detailed analysis of voids nucleation, growth and coalescence (Gurson 1977, Tvergaard and Needleman 1984, Leblond 2003). It requires microscopic experimental studies to define the model parameters and a transition or homogenisation method, such as those presented in section 2.3.3.1, to transfer results from the non-homogeneous microscopic state to the macroscopic level.

Gurson model was initially developed on the basis of analytical studies of a microscopic cell containing a hollow sphere subjected to axisymmetric loadings. The cell was defined to represent an elementary volume in a porous medium and was made of rigid-ideally plastic material. In this model, the damage variable is the volume fraction of cavities, i.e. the porosity, whose evolution law contains contributions from voids nucleation and growth. Phenomenological evolution laws, which can be linked with statistically-based expressions (Chu and Needleman 1980), are defined for voids nucleation, either controlled by stress or plastic strain. Gurson model also comprises a yield function or plastic potential which links the macroscopic stress to the damage parameter and an associated flow rule which defines the macroscopic plastic strain; based on these characteristics, it is often categorized as a macroscopic model.

The original Gurson model was initially dedicated to low porosity, spherical voids and random voids distribution, and presented the highest accuracy for high triaxialities. It was then extended and adjustable parameters were introduced to account for the void shape, the interaction between cavities and to avoid overestimation of the rupture strain (Tvergaard and Needleman 1984).

Gurson model has been further developed by various authors in order to account for non spherical voids (Gologanu *et al.* 1993), to introduce hardening (Leblond *et al.* 1995) or to avoid the localisation problem (Berger 1998). The study of a microscopic

representative unit cell was used to determine the macroscopic parameters to be introduced in these models. This approach, used for porous material, could also be used for damage in creeping material although the length scale in the case of creep rupture is smaller than for ductile fracture in porous material.

Usually, Gurson model is not used at elevated temperature as the mechanism of creep is not directly included in the existing evolution laws. Nevertheless, Berger (1998) developed a model using the same principle of void growth in a unit cell and applied it to the determination of damage in stainless steels at temperatures up to 1100°C.

Horstemeyer and Mosher (1999) developed a law comprising nucleation, growth and coalescence of voids, whose plastic potential is similar to Gurson potential but whose damage evolution equations are different. The model is characterised by a multiplicative decomposition of the damage into nucleation and growth terms instead of an additive decomposition. The temperature appears explicitly in the damage constitutive law as a variable. The law is used from cold to hot temperature but the particular mechanisms appearing at different temperatures are not differentiated. Particularly, the high temperature sensitivity has been studied on notched tests for stainless steel. The parameters were determined over a range of temperatures varyig from 25 to 1000°C.

Recently, Lassance *et al.* (2007) published a study focusing on the micromechanics of fracture in 6xxx series aluminium alloys for temperatures ranging between 20 and 600 °C. Damage micro-mechanisms specific to room and elevated temperature for this family of alloys were highlighted. Based on these experimental considerations, they proposed an extension to the Gurson model to capture the complexity of these various mechanisms.

2.3.3 MULTI-SCALE APPROACHES FOR CRACK ANALYSIS

In this section, multi-scale approaches are envisaged as a modelling technique for crack analysis in continuous casting: on the one hand, the physical description of cracks initiation and propagation in continuous casting involves steel microstructure and especially grain boundaries, which naturally leads to developing a model at the grain level also referred to as the mesoscopic level; on the other hand, a macroscopic modelling is required in order to capture the influence of the parameters of the industrial process.

Homogenisation techniques, which are necessary to transfer data and simulation results from one modelling scale to another, are first presented. Then, models to represent the microscopic phenomena of nucleation, growth and voids coalescence that lead to creep and ductile fractures are discussed. Finally, existing methods for the modelling of intergranular damage are described.

2.3.3.1 Homogenisation techniques

Most of the engineering materials are heterogeneous by nature. For example, porous materials, composites or polycrystalline materials are made of different phases. In particular, damaged materials are constituted of an intact matrix in which voids are included and can be treated either as porous materials or as a particular type of composites. Theories developed to define the macroscopic behaviour of heterogeneous materials are similar, whether they are specific to porous, polycrystalline, composites or damaged materials.

A first approach to determine the mechanical behaviour of heterogeneous materials is to confine rigorously the macroscopic behaviour between an upper and lower bound. This method was developed on the basis of the mixing rules initially developed by Voigt and Reuss. In elasticity, the upper bound of Voigt is defined supposing that the deformations are uniform in the material while the lower bound of Reuss is defined considering that the stresses are homogenous in the material (Hill 1952, Swan and Kosaka 1997). The bounds method has been extended to plasticity using the theory developed by Sachs, Taylor, Bishop and Hill (Goldsztein 2001). When the phases are very different, the bounds method results in a very large interval and it is necessary to have an estimation of the macroscopic behaviour using more sophisticated homogenisation methods.

Other approaches estimate the macroscopic behaviour by averaging information from the microscopic state. Homogenisation methods have been first developed for elastic behaviour: knowing the macroscopic stress-strain state, the microstructure and the constitutive laws for the microscopic state, a localization tensor can be define which is used to compute the global stiffness tensor. In particular, multi-scale approaches are very common for the study of composite materials, which constitute an important source of information in the field of homogenisation. The most direct approach determines the properties of the composite by average on the constituents. This can also be applied to metal matrix with voids or inclusions or to other heterogeneous material such as concrete. Effective medium approximations, as proposed by Eshelby (1957), constitute a more refined approach to the problem of homogenisation. Eshelby is the

precursor in the development of self-consistent methods (Hill 1965), which were initially developed for the homogenisation of elastic polycrystalline materials to reduce the analysis of the whole material to the problem of one inclusion in a matrix: each grain sees the surrounding material as a homogenized material. He also proposed the idea of the equivalent inclusion method where the inclusion is replaced by a localized strain. In particular, the dilute limit method has been proposed to study materials where the density of inclusions is very weak, i.e. when there is no interaction between inclusions. The inclusion is analysed as if it was in an infinite medium with the properties of the matrix submitted to a macroscopic deformation. If the interactions between the inclusions have to be taken into account, the matrix behaviour can be replaced by the homogenized behaviour of the material, this technique is then equivalent to using the self-consistent method. To account for the matrix deformation, the method consists in considering that the mean deformation of the representative volume element is equal to the average of the deformations of the virgin matrix (Mori and Tanaka 1973).

For non linear cases, the homogenisation methods presented here before are not accurate. In this case, the problem of deformation localization can no longer be resolved exactly and estimations of the local strain have to be computed by finite element analysis, by linearising the behaviour on an infinitesimal time interval or by comparison with a linear medium (Ponte Castañeda 1991, Suquet 1993). In particular, localization in a non linear matrix has been resolved using the Gurson model or methods introducing a perturbation in existing potentials (Duva and Hutchison 1984, Lee and Mear 1992). Homogenisation methods, specific to damage analysis in polycrystalline and composite materials (Chaboche *et al.* 1998, Pottier 1998, Gonzales and Llorca 2000) or to creep fracture analysis (Nguyen *et al.* 2000), have also been developed.

Recently, computational homogenisation methods have been developed to overcome problems such as large deformations, complex loading paths or evolving microstructures (Ghosh *et al.* 1996, Kouznestova *et al.* 2002, Feyel 2003). These methods, also referred to as FE^2 methods in the literature, are characterized by the definition of a representative volume element (RVE) and are based on the solution of two boundary problems, one for the macroscopic and one for microscopic scale. This technique does not aim at defining a macroscopic constitutive law for the material but to compute the macroscopic behaviour by performing a detailed microstructural calculation at each particular point of interest (see Figure 2.6). Computational homogenisation methods require high computer resources and they should only be used when the classical models fail to give the correct solution.

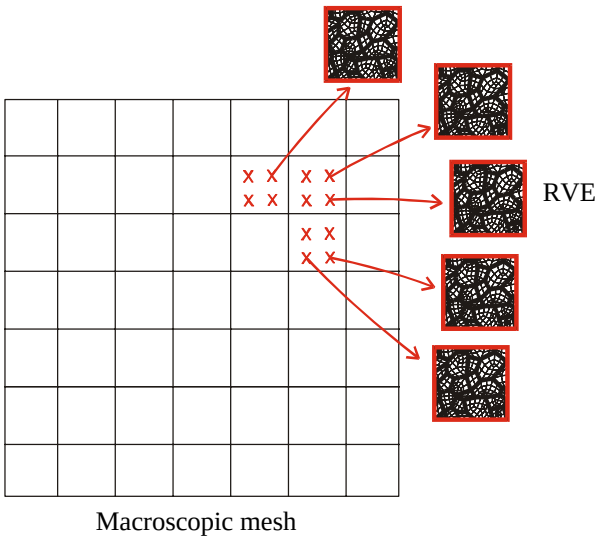

Figure 2.6. Illustration of the FE^2 method: macroscopic mesh and RVE associated to each integration point.

Another alternative to the problem of multi-scale modelling consists in using a finer finite elements discretization in specific areas when the position of the zones to be modelled with more details is known, e.g. a zone known to be more susceptible to crack initiation or a zone around an existing crack. Two-level models are represented in Figure 2.7, they comprise a first level model for the macroscopic scale and a second level model for the mesoscopic scale. Transfer of data is performed either by imposing forces or displacements extracted from a primary model at the macroscopic scale to a sub-model at the mesoscopic scale (Kiss and Dunai 2002) or through a progressive variation in the mesh refinement, going from coarse elements for the macroscopic state to finer specific elements for the mesoscopic state (Héraud 1998, Onck *et al.* 2000). Using this type of two-level models ensures that the boundary conditions are correctly applied to the mesoscopic zone.

The combination of FE^2 methods with multi-level discretization in a single model is often useful to take advantage of the particular capabilities of each of the techniques (van der Giessen *et al.* 2000, Ghosh *et al.* 2001, Raghavan et *al.* 2004). In these models, several computational sub-domains are defined, allowing the definition of different levels of homogenisation. The interest of the method is to define progressively more detailed models when approaching heterogeneous zones in the studied piece of material.

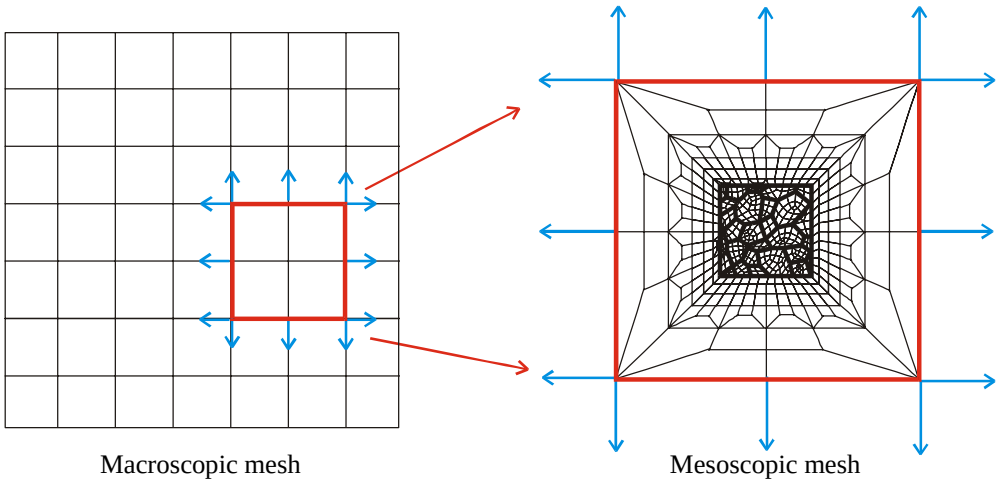

(a)

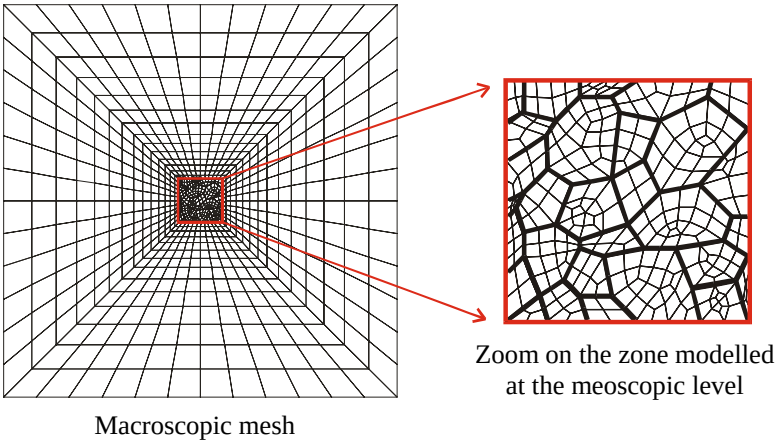

(b)

Figure 2.7. Illustration of the two-level method. a) Extraction of the data from the macrosopic level and transfer to the mesoscopic level (two calculations), b) progressive mesh refinement (one calculation).

2.3.3.2 Nucleation, growth and coalescence of voids

The important aspects of crack initiation and propagation at the microscopic scale are the mechanisms of voids nucleation, growth and coalescence. Various models that represent these phenomena have been developed for creep and ductile fractures. A review of these models is necessary before integrating these mechanisms into a meso-macro approach.

In most engineering alloys, cavities have been observed to nucleate continuously. An experimental relation proposed by van der Giessen and Tvergaard (1994) suggests that the nucleation rate is a function of the normal stress, introduced to allow a faster nucleation on those grain boundaries which are perpendicular to the

loading direction, and the strain rate. It has also been established that in steady state creep, the number of cavities increases linearly with the creep strain (Aria and Ogata 1998). The study of Hatanaka *et al.* (1999) who examined the correlation between the creep void parameters and the stress components by SEM observations of notched specimen associated with finite element calculations, confirmed that creep voids have a tendency to initiate and grow much easily at the grain boundaries that are perpendicular to the loading axis. In particular, detailed models have been developed to represent non uniform nucleation and hydrogen induced nucleation (Shewmon and Anderson 1998, Liang and Sofronis 2004) or void initiation by matrix/particle decohesion in ductile or composite materials (Lim and Dunne 1996, Sabirov and Kolednik 2005).

The growth of grain boundary cavities has been widely studied since the 1950s, starting with the work of Hull and Rimmer (1959) for growth by grain boundary diffusion assisted by surface diffusion: the cavity grows by a diffusion of voids through the grain boundary coupled to an inverse flux of material from the internal surface of the cavity to the grain boundary. More elaborated mathematical formulation in which the defect geometry is introduced as a unknown parameter have been proposed later by Chuang *et al.* (1979). Models for pure creep growth have been proposed by Budiansky *et al.* (1982) who analysed the growth of spherical voids diluted in a power-law creeping solid without diffusion. The coupling between diffusional and creep cavity growth has been studied by Needleman and Rice (1980) who pointed out that there is an interaction between these two mechanisms. They proposed a unified variational principle which constitutes the basis of most of the numerical techniques developed up until now for the simulation of cavity growth under creep conditions (Tvergaard 1984, van der Giessen *et al.* 1995, Liu *et al.* 1998, Mohan and Brust 2000).

Various cavity growth models are developped for specific practical applications. Westwood *et al.* (2000) propose a simplified numerical model for cavity growth by couple surface and grain boundary diffusion whose objective is to simulate creep damage localisation and diffusional crack propagation in polycrystalline materials and to analyse multi-cavity growth. Fracture modelling of ductile materials also requires particular void growth models (Biwa 1997, Thomson *et al.* 1999).

The coalescence phenomenon is very important as it defines the rupture criterion and corresponds to the creation of micro-cracks. Nevertheless, as for nucleation, coalescence has not been studied as extensively as void growth in the literature. A typical way to account for coalescence is to define a rupture criterion linked to the maximum value of the voids volume fraction or to the voids spacing for which the material is still able to sustain the load (Tvergaard 1982, Onck and van der Giessen

1998, Ragab 2002). Generally, the value of the criterion is arbitrarily specified to be used in parametric studies or is fitted to match experimental results. Specific coalescence studies have been realised in the context of ductile fracture. In this case, the interactions that take place between neighbouring voids lead to the localization of the plastic flow within the ligament between voids. This phenomenon, coupled with the directional growth of the voids, dictates the onset of the void coalescence process. Recent work in this area has been published by Pardoen and Hutchinson (2000), Benzerga (2002), Thomson *et al.* (2003), Bandstra *et al.* (2004), Seppälä *et al.* (2004) and Lassance *et al.* (2006).

2.3.3.3 Intergranular damage modelling

Different approaches to model integranular creep damage are presented in literature using either a continuum damage formulation (Liu *et al.* 1998, Michel 2004) or a discrete approach (Onck and van der Giessen 1997).

Liu *et al.* (1998) introduce a continuum damage variable, whose evolution is calculated on the basis of finite element simulations of a mesoscopic cell built to represent the polycrystalline microstructure of the material using the Voronoi tessellation method. Mechanism-based analyses of cavity nucleation and growth such as those presented in section 2.3.3.2 are implemented in the model. Within the mesoscopic cell, the damage variable, which is a tensor in the anisotropic case, accounts for the cracks and defects that are randomly distributed on the grain boundaries. This damage tensor, which is a purely geometrical representation of the internal microstructure degradation of material, is then coupled with the constitutive equations of continuum mechanics to analyse creep damage at the macroscopic level. Contrarily to the damage model, the material constitutive equation is formulated for a smeared continuum medium without considering its internal microstructure. The model was tested on copper up to 250°C subjected to uniform stress loading of uniaxial tension and reversed pure shear.

Voronoi tessellation is used by various authors to model the polycrystalline microstructure of the material in order to have a certain randomness in the grain shapes while keeping the specific characteristics of the studied material (Cannmo *et al.* 1995, Liu *et al.* 1998, Wu and Guo 2000). The method consists in finding all the nearest points to a given nucleus and linking them to this nucleus to form a grain, all the nuclei having been randomly defined before. Considering that the growth rate of each grain is the same in all directions and that all the grain nuclei appear at the same time but are

located randomly in space, the microstructures derived by Voronoi tessellation are topologically equivalent to real metals or ceramics microstructures.

Onck and van der Giessen (1997, 1998, 1999) propose a mesoscopic approach to creep damage in which the grains surrounding a propagating crack are represented individually in the near-tip region inside the damage zone while the surrounding undamaged material is described as a continuum. Cavitation and sliding along all grain boundaries in the damaged zone are described by a set of constitutive equations based on micromechanical studies at the smaller scales (van der Giessen *et al.* 1995). The numerical model proposed is based on the grain element representation (Onck and van der Giessen 1997). Each grain is represented by a special hexagonal finite element, the grain element, that accounts for creep deformation inside the grain in an average manner. The grain elements are connected by grain boundary elements that account for cavitation and sliding (van der Giessen and Tvergaard 1991). The grains and their grain boundaries are represented discretely. Propagation of the main crack occurs by linking up of neighbouring facet microcracks (Onck and van der Giessen 1999). Regular hexagonal grains are used in most of the applications but randomness can also be introduced in the model (Onck and van der Giessen 1997).

Contrarily to the two previous models, Michel (2004) does not physically represent the microstructure of the material in terms of grains and grain boundaries but accounts for nucleation, growth and coalescence of intergranular voids through the evaluation of a continuum creep damage state variable which is based on physical foundations. The model offers the advantage of requiring only the identification of two parameters to fit nucleation and diffusion rates. It has been applied to austenitic steel at 600°C.

2.3.4 NUMERICAL MODELLING OF CRACK PROPAGATION

Traditional fracture models focus on the prediction of damaged zones, where the material has lost part of its mechanical properties, and estimate crack initiation using fracture criteria. In many applications, it is not required to model the physical propagation of the crack within the material and the detection of the damaged zones is sufficient to optimise the design or the involved forming processes.

When the definition of the crack propagation path is important, e.g. to analyse the fragmentation pattern, it is necessary to develop specific models which allow the visualisation of the evolution of the crack within the material. Such approaches are presented hereafter.

2.3.4.1 De-bonding and cohesive zone models

In order to represent the propagation of a crack, i.e. the creation of new free surfaces, the numerical model has to include specific features that allow the mesh to de-bond along certain surfaces. To apply this type of model, it is necessary to define a cohesive zone, i.e. an interface where the crack is allowed to propagate, an associated constitutive relation that relates forces and displacement jumps across the bond line, and a criterion for de-bonding (Needleman and Rosakis 1999). The technique requires that the crack propagates along elements boundaries and is therefore mesh dependant by definition. Cohesive zone surface elements can be used in the entire volume to be modelled (Tijssens *et al.* 2000), in specific zones where the crack is susceptible to propagate or at interfaces between different phases in composite materials (Foulk *et al.* 2000, Tvergaard 2003), or inserted dynamically within the mesh when required to simulate any crack propagation path (Zhou and Molinari 2004). Cohesive zone models can be coupled with multi-scale approaches. This is done by describing the micromechanical phenomena occurring during crack growth and capturing these in a constitutive description of the cohesive surface (Xu and Needleman 1994).

Creep cracks, which are known to be intergranular, constitute a typical application where cohesive models can be efficiently applied as the probable crack propagation paths are well defined in advance. The model is developed considering that the grain boundaries and the cohesive or de-bonding surfaces coincide (Onck and van der Giessen 1998, Xu and Bassani 1999). The cohesive zone technique is also advantageously applied to the analysis of delamination in composite materials (Espinosa *et al.* 2000, de Borst and Remmers 2006).

2.3.4.2 Extended FEM and meshless methods

A recent approach to crack analysis is the extended finite element method (X-FEM) which predicts crack propagation without remeshing or predefining possible crack growth paths (Daux *et al.* 2000, Moës and Belytschko 2002, Bordas and Moran 2006). Discontinuities such as cracks or voids are represented through enriched discontinuous functions that are associated with the regular finite element shape functions. The X-FEM allows a mesh independent crack propagation modelling which does not require the meshing of the cracks. Cracks are treated as separate geometric entities and the only interaction between the mesh and the crack occurs through the selection of the enriched nodes.

The element-free Galerkin method constitutes another approach to crack propagation without the need for remeshing as no mesh is present (Carpinteri *et al.* 2003, Duflot and Nguyen-Dang 2004, Brighenti 2005). The models are built using a cloud of nodes for the resolution of the partial differential equations that govern the problem and do not require any connectivity concept such as in the finite element method. This approach is often used in the context of fracture mechanics to study the propagation of existing cracks. In this case enriched shape functions are developed to account for the singularity at the crack tip.

The natural element method (Sukumar *et al.* 1998) can also be advantageously applied to fracture mechanics problems. This method uses a multivariate data interpolation scheme referred to as natural-neighbour interpolation, which relies on concept such as Voronoi tessellation, and does not require a mesh.

X-FEM and meshless methods are certainly of great interest to solve the problem of mesh dependency linked to the modelling of cracks propagation. Nervertheless, the model developed in this thesis aims at studying intergranular cracks whose possible propagation paths are known. Therefore, a classical finite element approach with specific interface elements to model the grain boundaries is an adequate choice for the resolution of this problem.

2.4 OUTCOMES OF THE LITERATURE REVIEW

The literature review presented in this chapter comprises two main aspects. The first part focuses on a global description of the industrial continuous casting process and on the physical mechanisms linked to the problem of transverse cracking for steel. The second part addresses the modelling of damage and crack propagation with a particular emphasis on approaches applicable at elevated temperature.

It has been shown that in the studied temperature range (700 to 1200 °C), the austenitic grain boundary is a favourable place for cracks to initiate and propagate. The mechanisms of voids nucleation, growth and coalescence have been established, the cavities evolving under creep deformations and diffusion. The embrittlement by strain concentration and micro-voids coalescence at the grain boundaries has also been highlighted, this phenomenon being induced by austenite-ferrite transformation. The straightening phase of the continuous casting process appears to be the most critical for transverse cracks formation. In this zone of the caster, the temperature of the external part of the slab coincides with the low ductility trough for the material. Low carbon

steels with micro-alloying elements such as aluminium, niobium or vanadium are known to be susceptible to transverse cracking.

Different theories developed in the field of fracture and damage mechanics have been presented. Fracture mechanics approaches that use energy criteria or stress intensity factors, will not be considered for the study of crack initiation at elevated temperature, mainly because they do not incorporate the various mechanisms occurring before crack initiation. Damage mechanics approaches integrating creep and diffusion processes are more appropriate for the present application. As the grain scale is the level at which the most relevant physical phenomena linked to transverse cracking appear, a multi-scale approach focusing on the development of a damage model at the mesoscopic scale using information from both the microscopic and macroscopic levels should be envisaged. The studied cracks meandering along the grain boundaries, the model will be developed using a standard finite element approach which incorporates specific elements to be localized at the grain boundaries for the modelling of the damage processes. These elements will be specifically designed to allow the de-bonding of the interface and the opening and propagation of the cracks. The developments of the numerical model are presented in details in the next chapter.

Chapter 3

Numerical model: the mesoscopic cell

3.1 CHOICE OF THE MODEL

The literature survey presented in Chapter 2 in combination with discussions with experts in the field of metallurgy has identified creep as a major driver for transverse cracks propagation in continuous casting. The principal damage mechanisms that have to be modelled are grain boundary sliding and voids growth controlled by diffusion and creep deformation. By nature, creep damage is located at the grain boundaries, which implies that possible paths for the crack propagation are defined in advance when the microstructure is known. Therefore, the development of a grain type finite element model associated with a grain boundary damage model, such as the one presented by Onck and van der Giessen (1999), is adequate for the resolution of the problem. A major difference in continuous casting, compared to traditional applications in which creep is dominant, is that the temperatures are much higher. This means that the diffusion process progresses more quickly and that smaller time scales are involved.

A grain type model can be implemented in the LAGAMINE finite element code using existing elements and constitutive laws, and introducing new developments specific to the microstructure modelling when required. The model at the grain scale is presented in the following sections and contains two-dimensional (2D) solid finite elements for the grains (section 3.3.1) and one-dimensional (1D) interface elements for their boundaries (section 3.4.2). An elastic-viscous-plastic law is used inside the grains (section 3.3.2) and a law with damage at its boundaries (section 3.4.3).

3.2 MULTI-SCALE CONTINUOUS CASTING MODELLING

The main objective of the research is to model the continuous casting process and the evolution of the damage at the grain scale, referred to as the mesoscopic scale. Due to the huge amount of computational resources that would be required, it is not realistic to model the whole steel slab at the mesoscopic scale. Nevertheless, as the critical areas for crack initiation are well known, it is possible to determine specific zones on which the analyses have to be performed. Each specific studied zone can then be modelled using a mesoscopic representative cell which contains grains and grain boundaries. The mesoscopic model requires information from the macroscopic scale, which are available through a macroscopic finite element analysis of the continuous process previously carried out (Pascon 2003).

Figure 3.1 illustrates the continuous casting problem at different scales: first at the slab scale (upper left corner) where the possible sections for a two-dimensional representation are shown in relation with the oscillation marks orientation; then at the section level (upper right corner) where the thermomechanical state, computed from the macroscopic model, can be applied to be transferred to the mesoscopic cell via the transition zone; then at the grain level (lower right corner) where the finite elements are defined; and finally at the grain boundary level where the damage mechanisms come into play through grain boundary sliding and voids growth (lower left corner).

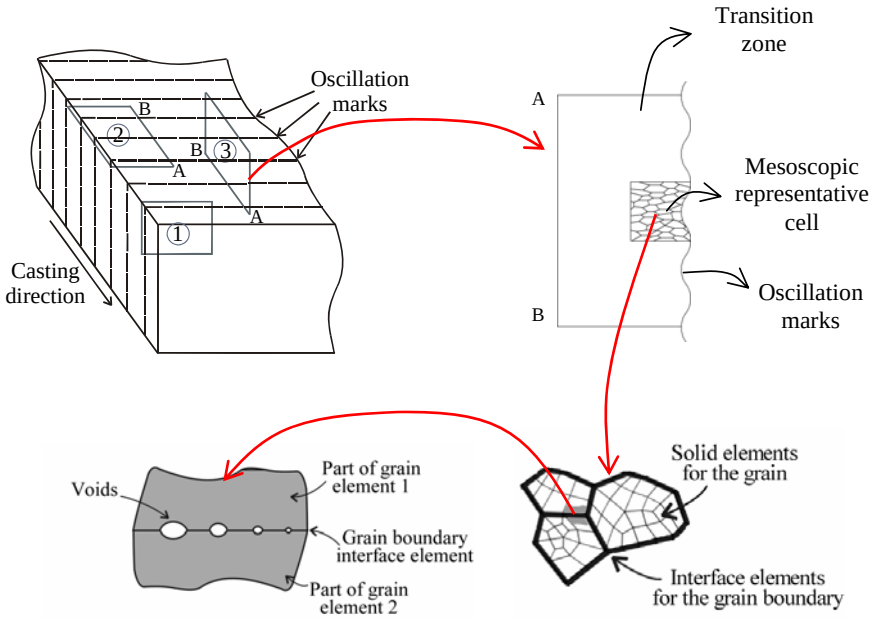

Figure 3.1. Multiscale continuous casting modelling.

The work presented in this thesis focuses on the mesoscopic scale but it is evident from the analysis of Figure 3.1 that it encompasses both the *micro-meso* (from the voids to the grains) and the *macro-meso* (from the slab to the grains) transitions.

3.3 MODELLING OF THE GRAIN

To describe the grains, it is essential to define the elements and the material law by which they are represented. At the mesoscopic scale, each grain is considered as a continuum and is modelled using 2D solid elements. This section starts by a description of the solid elements used in the simulations before introducing the material law representative of the behaviour of metals at high temperatures.

3.3.1 DESCRIPTION OF THE SOLID ELEMENTS

The solid elements are used to model the inside of the grains at the mesoscopic level but also the steel as a continuum at the macroscopic level. Two solid elements are presented hereafter as well as the notion of generalized plane state.

3.3.1.1 Mixed 4-node quadrilateral elements

The grain model is developed using thermomechanical, 4-node, first-degree, quadrilateral elements of mixed type with one integration point as represented in Figure 3.2 (left) (Zhu *et al.* 1995).

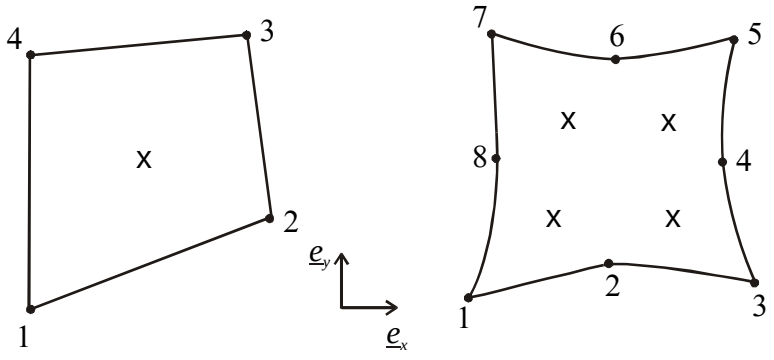

Figure 3.2. 4-node and 8-node solid elements.
Dots symbolize nodes and crosses represent integration points.

This element was derived using the Hu-Washizu variational principle (Washizu 1982) for the calculation of the internal forces and stiffness matrix. The reduced-integration scheme used in this element (i.e. integration limited to one single integration

point) can induce zero-energy displacements fields, whose corresponding deformations look like an hourglass and are called hourglass deformation modes (see Figure 3.3). Therefore, this element contains anti-hourglass stresses that prevent such zero-energy hourglass deformation modes to appear.

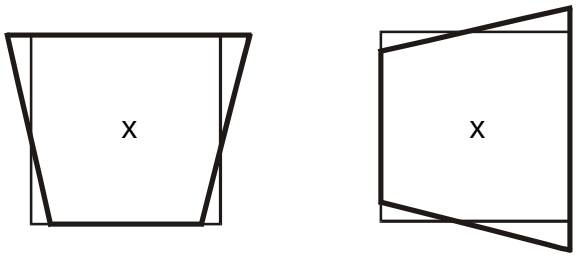

Figure 3.3. Example of a zero-energy hourglass deformation mode in 2D.

An assumed strain method, in which the gradient matrix of the standard displacements is replaced by an assumed non-homogeneous gradient matrix, has also been used in the derivations to prevent shear and volume locking (Zhu 1992a).

Throughout the thesis, this element is referred to as the mixed 4-node quadrilateral element. It was initially available for axisymmetric and plane strain states.

3.3.1.2 Standard 8-node quadrilateral elements

A second type of solid element has been used in specific sections of the work and in particular for the macroscopic simulations. It is referred to as the standard 8-node quadrilateral element and consists in a thermomechanical, 8-node, second-degree, element with four integration points (see Figure 3.2 (right)). This element, which is based on a standard isoparametric displacement formulation, has been specially developed for simulations in large deformations. Second-degree quadrilateral elements are recognised to provide the most accurate results when used with 4 integration points. Therefore, it does not require any anti-hour glass stresses as the under-integration is not used in this case. This element has been developed for axisymmetric, plane stress, plane strain and generalized plane states.

3.3.1.3 Generalized plane state

Definition and use of the generalized plane state

The generalized plane state is a modelling technique which lies between the 2D and 3D state. It consists in using standard 2D finite elements whose thickness varies

linearly as a function of the global coordinates x and y. This approach is realised by adding three additional degrees of freedom to the model $(\alpha_1, \alpha_2, \alpha_3)$, which account for the thickness variation of the slice of material (see Figure 3.4).

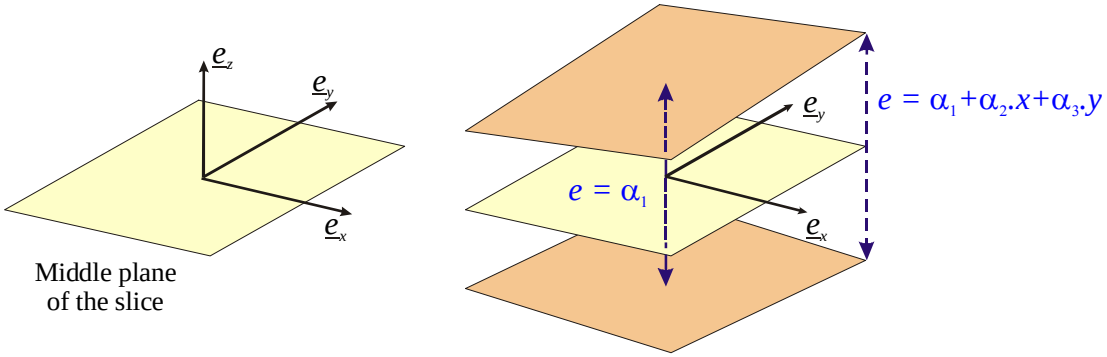

Figure 3.4. Illustration of the generalized plane state (Pascon 2003).

The technique is particularly useful for the modelling of continuous casting problems as it can easily reproduce the dilatation of a slice of slab as well as its deformations in the bending and unbending zones of the continuous casting machine (Pascon 2003). It is also adequate to model a slice of material whose thickness is constant spatially but varies with time as it is the case for the mesoscopic cell. The advantage compared to full 3D elements is obvious for the applications presented here as the required 3D effects can be modelled without increasing dramatically the number of nodes and degrees of freedom.

Implementation of the generalized plane state for the mixed 4-node element

As the generalized plane state was not initially available with the mixed 4-node quadrilateral element, it has been decided to implement it in order to keep the advantage of using 4-node elements for the modelling of the microstructure. The mathematical derivations that have been performed to update the element are presented in details in the Appendix A.

This section focuses on the initial tests that have been realised with the mixed 4-node quadrilateral element in generalized plane state. In particular, several finite element simulations have been performed to verify that the modification brought to the mixed 4-node quadrilateral element for the introduction of the generalized plane state are correct and that this element is still efficient in terms of CPU time.

Calculation for one single finite element

First, a calculation has been performed on one single finite element on which a uniaxial tension was applied. The results in terms of stresses and strains have been compared between the mixed 4-node quadrilateral element (four nodes, one integration point) and the standard 8-node quadrilateral element (eight nodes, four integration points) for a simulation in generalized plane state. The results obtained by the two simulations are very close with respect to the numerical errors and approximations relative to the finite element method. As the standard 8-node quadrilateral element in generalized plane state has been validated earlier, it can be concluded, as the same results are obtained, that the calculation with the mixed 4-node quadrilateral in generalized plane state are also correct.

Then, for each of the elements (mixed 4-node and standard 8-node) the plane strain and axisymmetrical states have been simulated using either directly the plane strain or axisymmetrical state or the generalized plane state with particular value for the degrees of freedom of the additional node. Indeed, it is possible to reproduce the plane strain or axisymmetrical state by imposing:

- for the plane strain state: $\alpha_1 = 1$, $\alpha_2 = \alpha_3 = 0$ (with all the degrees of freedom α_I fixed),
- for the axisymmetrical state: $\alpha_1 = 0$, $\alpha_2 = 1$, $\alpha_3 = 0$ (with all the degrees of freedom α_I fixed).

For these cases, the results obtained with the different methods are also similar. This confirms that the generalized plane state is correctly implemented in the mixed 4-node element and that the calculations in plane strain and axisymmetrical states continue to give accurate results after the modification of the mixed 4-node element.

Full thermomechanical calculation

A thermomechanical simulation has been performed with a mesh comprising approximately 400 mixed 4-node finite elements in axisymmetrical state. The objective was to verify that the global CPU time did not increase excessively after the introduction of a new loop in the mixed 4-node element. The comparison between the initial and the updated versions of the element shows that for the axisymmetrical state, the results are identical in terms of stresses and strains, which is an additional verification with regard to programming errors, and in terms of CPU time. In conclusion, it can be stated that the modifications proposed to account for the generalized plane state do not increase the global CPU time of the element.

3.3.2 GRAIN MATERIAL LAW: ELASTIC-VISCOUS-PLASTIC MATERIAL

Inside the grains, the material is considered as a continuum and the hypothesis has been made that it follows a constitutive law identical to the law used for the macroscopic simulations. At elevated temperatures, viscosity plays an important role on the behaviour of metals, which implies that the strain rate influences the stress level. In particular, steel is known to follow an elastic-viscous-plastic law for the range of temperatures studied here (between 800°C and 1200°C).

The law implemented in the code for the analysis of metals at elevated temperatures is a Norton-Hoff power law, which has been modified to account for softening and hardening effects (Habraken *et al.* 1998b, Pascon 2003). Its expression in terms of Von Mises equivalent stress σ_e, strain ε_e and strain rate $\dot{\varepsilon}_e$ is given by equation (3.1):

$$\sigma_e = \varepsilon_e^{p_4} . exp\left(-p_1 \varepsilon_e\right) . p_2 . \sqrt{3} . \left(\sqrt{3} . \dot{\varepsilon}_e\right)^{p_3} \tag{3.1}$$

where the parameters p_1 to p_4 are temperature dependent. p_1 represents the effect of softening, p_2 is linked to the general level of the curve, p_3 models the viscosity and p_4 the hardening. Figure 3.5, which represents the equivalent stress versus the equivalent strain rate, illustrates the effect of the variation of each of these parameters at constant temperature and strain rate, except for Figure 3.5(c) where three strain rates are compared.

By increasing p_1, it is possible to enhance the effect of softening for large strains as shown in Figure 3.5(a), where the end of the $\left(\sigma_e, \varepsilon_e\right)$ curve decreases more quickly with ε_e for higher values of p_1. Figure 3.5(b) shows that when p_2 increases, the maximum stress level reached is also increased. In this case, as all the other parameters are fixed, the general shape of the curve is not altered. The viscosity effect is highlighted in Figure 3.5(c) where three strain rates and two values of p_3 have been tested. The first comment to be made is that the maximum stress level reached is a function of the strain rate: the higher the strain rate, the higher the stress for the same strain. The parameter p_3, which also influences the general level of the curves, is mainly used to calibrate the significance of the viscosity effect. For $0 < \dot{\varepsilon}_e < 1$, which is the case for all the simulations in this thesis, an increase of p_3 reduces the viscosity effect, i.e. the variation between the curves $\left(\sigma_e, \varepsilon_e\right)$ with the strain rate is smaller for higher values p_3. Figure 3.5(d), illustrates the hardening effect at small strains. The parameter p_4 is important to model properly the beginning of the $\left(\sigma_e, \varepsilon_e\right)$ curve. It can be seen in Figure 3.5(d) that the hardening effect increases when p_4 decreases, i.e. when all the

other parameters are fixed, the stress level reached at the beginning of the curve is higher for smaller values of p_4. The modified Norton-Hoff law as defined by equation (3.1) allows the modelling of very detailed material behaviour, especially taking into account the fact that each of the parameters p_1 to p_4 can be given different values in function of the temperature. In practical examples, the parameters are fit using experimental tests results relating to several distinct temperatures and the program interpolates the coefficients linearly for the intermediate temperatures.

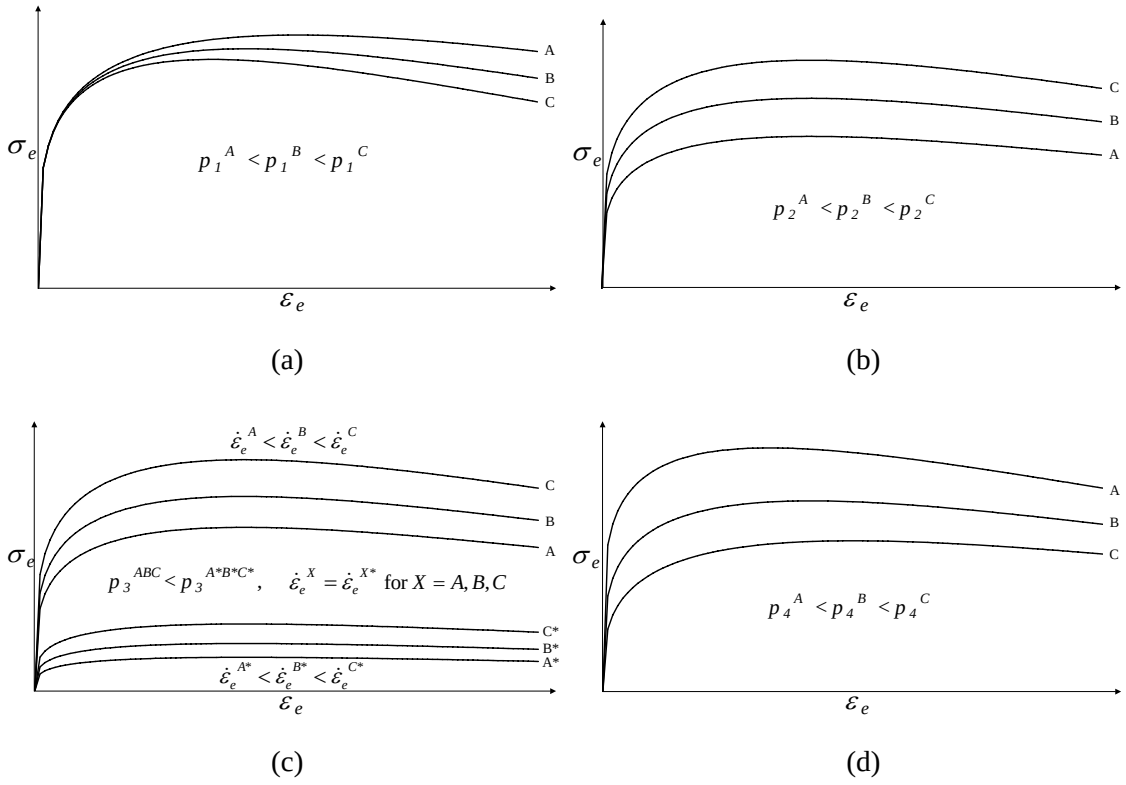

Figure 3.5. Examples of variation of the parameters of the modified Norton-Hoff law at constant temperature: a) variation of p_1 at constant strain rate, b) variation of p_2 at constant strain rate, c) variation of p_3 for three strain rates, d) variation of p_1 at constant strain rate.

The modified Norton-Hoff law comprises an elastic part to account for the reversible deformations. The elastic behaviour follows the isotropic linear elastic Hooke's law, defined through the Young's modulus E and the Poisson's ratio ν, these two parameters being temperature dependent. The Hooke's law is also used in case of unloading, where the stress decreases linearly along a straight line determined by the Young's modulus.

Due to the dependence of the modified Norton-Hoff law to the temperature and strain rate, the definition of the yield limit σ_{yield} is not straightforward and various

options have been proposed to define the yield limit and to account for the passage between the elastic and viscous-plastic behaviour (Pascon 2003). For the applications presented in this thesis, the yield limit is automatically calculated by the program and corresponds to the intersection between the Hooke's straight line and the modified Norton-Hoff curve. Figure 3.6 illustrates the application of the method at constant temperature, considering that the loads on the element result in an equivalent strain rate $\dot{\varepsilon}_e^{\,B}$. In this particular case, the model first follows the linear elastic law up to the point $\left(\sigma_{yield}, \varepsilon_{yield}\right)$ as defined in Figure 3.6 and then continues on the curve *B*, which corresponds to the modified Norton-Hoff law for $\dot{\varepsilon}_e = \dot{\varepsilon}_e^{\,B}$.

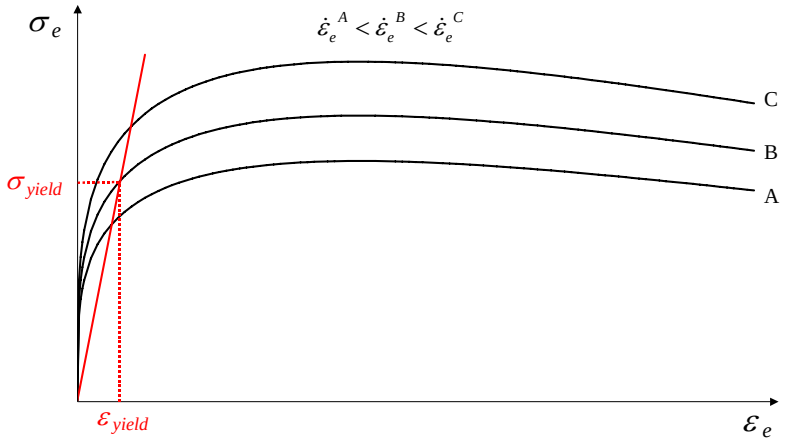

Figure 3.6. Passage from the elastic to the viscous-plastic behaviour.

Figure 3.6 also shows that for a higher strain rate, the yield limit would be higher and vice-versa. When the strain rate varies, using the intersection of the curves to define the yield limit by opposition to defining a unique yield limit per temperature, improves the convergence properties of the model as it avoids jumps between the curves that would occur during the simulation if the second solution was to be used.

Thermal dilatations due to temperature variations are computed using a thermal expansion coefficient (Pascon *et al.* 2006) that defines the thermal contributions to be added to the mechanical strain rate tensor associated to the modified Norton-Hoff law.

3.4 MODELLING OF THE GRAIN BOUNDARY

The grain boundary model has to account for grain boundary sliding and voids growth. It is represented by 1D interface elements associated with a damage law. Before describing the specific features of the interface damage model, i.e. the interface element and the damage law, it is useful to summarize the characteristics of the traditional contact finite element which serves as a basis for the new developments.

3.4.1 GENERAL DESCRIPTION OF THE CONTACT FINITE ELEMENT

The interface element developed for intergranular crack modelling is based on a thermo-mechanical contact finite element initially developed to account for contact with friction between two strained bodies in large deformation (Habraken *et al*. 1992b, Habraken and Cescotto 1998a). The behaviour at the contact surface is calculated using a penalty method. Although the contact element presented in this section relates to the 2D case, assuming a constant unit thickness for the element, there is no restriction to extend the developments to the 3D case.

3.4.1.1 Mathematical formulation of contact and notations

The physical quantities that are used to define the contact element are similar to those used for typical solid elements: a stress tensor and a strain tensor conjugated within a constitutive law. For the particular case of contact elements, these quantities are represented by vectors which have specific physical meanings. Their definitions are introduced in this section.

Definition of the contact stress vector

The forces that result from the contact between two solids are represented in Figure 3.7. $\underline{F}^{AB}$ is the force applied by solid A on solid B, while $\underline{F}^{BA} = -\underline{F}^{AB}$ is the reaction force applied by solid B on solid A.

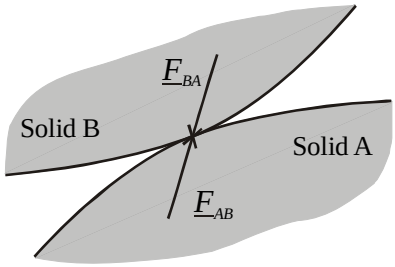

Figure 3.7. Contact between two solids.

The contact force can be decomposed into its normal and tangential projections onto the contact surface as represented in Figure 3.8 for the force $\underline{F}^{BA}$ applied by solid B on solid A, where $\underline{F}_n^{BA}$ is the normal component of the contact force and $\underline{F}_s^{BA}$ is its tangential component.

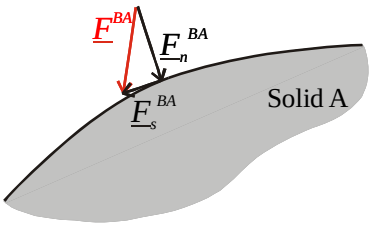

Figure 3.8. Decomposition of the contact force.

The zone of contact is generally not limited to a single point, therefore a contact surface has to be introduced, together with the concept of force by surface area. The components of the contact forces by contact surface area along the normal and tangential axes to the contact surface are used to define the contact stress vector $\underline{\sigma}_c$ in the local system of coordinates $\left(\underline{e}_n, \underline{e}_s\right)$:

$$\underline{\sigma}_c = \begin{Bmatrix} p \\ \\ \tau \end{Bmatrix} \tag{3.2}$$

where p is the contact pressure (positive in compression for the general contact case) and τ the contact shear stress (see Figure 3.9).

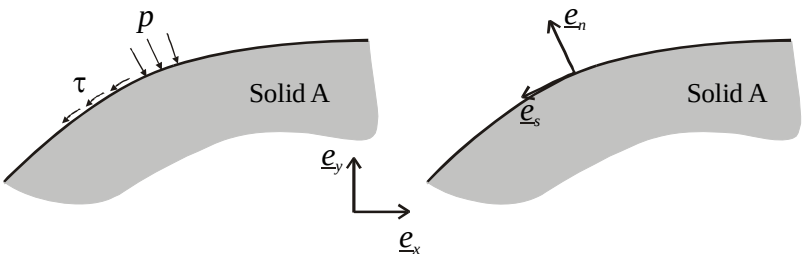

Figure 3.9. Contact pressure, shear stress and local axes at point of contact in solid A.

As p and τ are forces by surface area, the integral of the contact stresses on the contact surface is equal to the total contact force:

$$\int_{\text{contact surface}} \left(-p \cdot \underline{e}_n + \tau \cdot \underline{e}_s\right) ds = \underline{F}_n^{BA} + \underline{F}_s^{BA} = \underline{F}^{BA} \tag{3.3}$$

where *ds* is the elementary surface area.

The contact stress vector is objective, i.e. that it is not affected by rigid body motion. Therefore, its variation rate is equal to its temporal derivation:

$$\dot{\underline{\sigma}}_c = \frac{d\underline{\sigma}_c}{dt} \tag{3.4}$$

Definition of the contact strain rate

The contact strain rate vector $\dot{\underline{\varepsilon}}_c$ has a particular definition in the context of the contact element. It is associated to the relative velocity between the two surfaces in contact and can be represented in the local axes by:

$$\dot{\underline{\varepsilon}}_c = \begin{Bmatrix} \dot{\delta} \\ \\ \dot{u} \end{Bmatrix} \tag{3.5}$$

where $\dot{\delta}$ is the normal component of the relative velocity between the two surfaces in contact and $\dot{u}$ its tangential component.

In case of large deformations, the relative displacement between the two surfaces in contact can not be uniquely defined and therefore the integration of equation (3.5) has no physical meaning. Indeed, each point of one of the two solids will be in contact with a succession of different points of the second solid during the contact phase. The only quantity that can be uniquely defined is the distance between the two surfaces Δ (see Figure 3.10). Its value can be calculated at each instant but is not equal to the integration of $\dot{\delta}$.

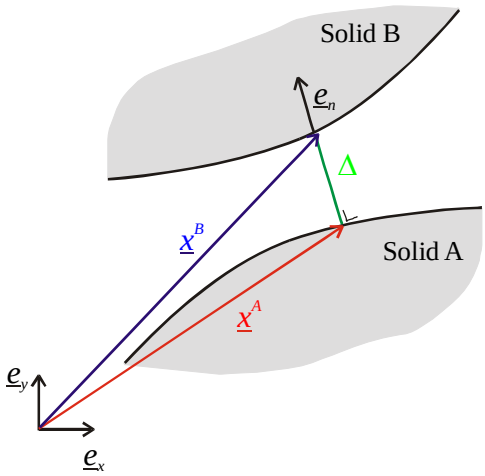

Figure 3.10. Distance between the two faces of the interface element.

If $[R]$ is the rotation matrix connecting the global axes $(\underline{e}_x, \underline{e}_y)$ to the local axes $(\underline{e}_n, \underline{e}_s)$, the distance relation between the distance vector in global axes $\underline{d}$ and in local axes $\underline{\Delta}$ is given by:

$$\underline{\Delta} = [R]\,\underline{d} = [R]\left(\underline{x}^A - \underline{x}^B\right) \tag{3.6}$$

As $\underline{\Delta}$ is an objective vector of the distance, the relative velocity between the two solids can then be computed by its temporal derivation:

$$\begin{aligned} \underline{\dot{\varepsilon}}_c &= \frac{d\underline{\Delta}}{dt} = [R]\left(\frac{d\underline{x}^A}{dt} - \frac{d\underline{x}^B}{dt}\right) + \frac{d[R]}{dt}\left(\underline{x}^A - \underline{x}^B\right) \\ &= [R]\left(\underline{v}^A - \underline{v}^B\right) + \left[\dot{R}\right]\left(\underline{x}^A - \underline{x}^B\right) \end{aligned} \tag{3.7}$$

Equation (3.7) shows that the relative velocity between the two surfaces comprises, in addition to the projection in the local axes of the difference between the velocities of each surface in global axes, a second term that accounts for the rotation velocity of the local axes. In most practical cases, the rotations are small so that the second term of equation (3.7) can be neglected. This is particularly the case when a penalisation method is used as a small interpenetration is required.

Mathematical conditions of contact

The mechanical contact between two solids is driven by a series of mathematical conditions. The first condition is that the contact pressure is always equal to zero (no contact) or positive (contact pressure):

$$p \geq 0 \tag{3.8}$$

The second condition is the non penetration condition given by equation (3.9) where $\Delta\underline{v} = \underline{v}^A - \underline{v}^B$ is the relative velocity between the two solids:

$$\Delta\underline{v} \cdot \underline{e}_n \leq 0 \tag{3.9}$$

where $\underline{e}_n$ is the external normal at the contact point on solid A.

$\Delta\underline{v} \cdot \underline{e}_n = 0$ corresponds to a contact case where the relative velocity can only be tangential (sliding contact) or equal to zero (sticking contact), while $\Delta\underline{v} \cdot \underline{e}_n < 0$ implies a loss of contact (the bodies start moving apart from each other).

The mechanical (equation (3.8)) and kinetic (equation (3.9)) relations are linked together in such a way that they can describe every contact situation. A third equation

makes this link and the complete set of three equations is known as the Signorini's conditions of unilateral contact:

$$\begin{cases} p \geq 0 \\ \Delta \underline{v} \cdot \underline{e}_n \leq 0 \\ \left(\Delta \underline{v} \cdot \underline{e}_n \right) \cdot p = 0 \end{cases} \tag{3.10}$$

The third equation forces the stress to be equal to zero when the contact is lost (i.e. when $\Delta \underline{v} \cdot \underline{e}_n < 0$), and the contact to remain (i.e. $\Delta \underline{v} \cdot \underline{e}_n = 0$) when a contact pressure exists (i.e. when $p > 0$).

To respect the non penetration condition as defined by equation (3.9) it is necessary to introduce specific constraint conditions linked to the contact element. Different approaches can be used to impose these constraints, e.g. the use of Lagrange multipliers, a penalty approach or an augmented Lagrangian method (Zienkiewicz and Taylor 2005).

The method using Lagrange multipliers consists in imposing an additional force on each node of the contact element to prevent penetration, the exact geometry of the contact surfaces is respected and the stresses are calculated knowing the strain rate. The method introduces new unknowns, the Lagrange multipliers, which are added to the global vector of degrees of freedom during the finite element assembly process. The resolution of the equations system requires special attention as the global matrix is not positive definite when using the Lagrange multipliers technique because a zero diagonal local stiffness matrix corresponds to each multiplier term.

The penalty technique relaxes the condition of non penetration by allowing a small penetration between the two solids in contact. This method avoids the computational difficulties of the Lagrange multipliers method but introduces small errors on the displacements. This technique has been implemented in the finite element code LAGAMINE and is further developed here below.

The augmented Lagrangian approach is a compromise between the two previous methods where a penalty-method is used in conjunction with Lagrange multipliers which are updated during the simulation process (Simo and Laursen 1992, Bille *et al.* 1994).

Penalty method and contact constitutive law

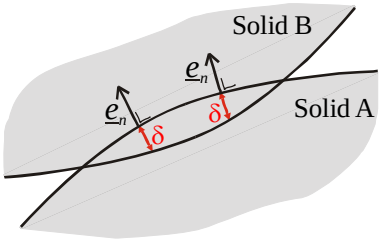

Figure 3.11. Penetration of two solids for penalty technique.

The penalty method aims to penalize the penetration of the solids into each others. To respect the non penetration condition, the penetration distance between the two solids in contact, δ, should be equal to zero in case of contact. However, the penalty technique consists in resolving the contact problem by allowing a small penetration. The value of δ is considered as positive in case of penetration, it should be as small as possible and is dependant on the penalty coefficients chosen. The penetration of the two solids generates a repulsive stress that rejects the solids from each others. This stress corresponds to the contact pressure and is related to the penetration distance δ, which is the relative displacement in the penetration direction $\underline{e}_n$. In terms of increments, this relation can be written:

$$\dot{p} = k_n \cdot \dot{\delta} \tag{3.11}$$

where $\dot{\delta}$ is the normal relative velocity between the two solids and k_n a penalty coefficient.

In the same way, a reversible, i.e. elastic, slide is authorized, but a tangential force withstands this move:

$$\dot{\tau} = k_s \cdot \dot{u} \tag{3.12}$$

where $\dot{u}$ is the relative velocity along $\underline{e}_s$ and k_s another penalty coefficient.

Equations (3.11) and (3.12) form the constitutive law that links the stresses and strains in case of elastic contact. The contact constitutive tensor [C] is given by the diagonal matrix of the penalty coefficients:

$$[C] = \begin{bmatrix} k_n & 0 \\ 0 & k_s \end{bmatrix} \quad \text{with} \quad \underline{\dot{\sigma}}_c = [C]\,\underline{\dot{\varepsilon}}_c \tag{3.13}$$

To model the contact, the penetration must be as small as possible, i.e. the penalty coefficients have to be as high as possible. Nevertheless, they can not increase up to a certain limit, which depends on the problem, to avoid convergence difficulties due to a poor conditioning of the global stiffness matrix.

For the traditional contact element, when the contact shear stress reaches a threshold value, irreversible, i.e. plastic, sliding appears. One possibility to model these dissipation phenomena is to use the Coulomb's friction law which introduces a friction parameter in the model and additional terms in the compliance matrix (Habraken *et al.* 1992b).

3.4.1.2 Contact element description and derivation of the stiffness matrix

The contact element is defined by 2 or 3 nodes, for first or second degree discretization, respectively. These nodes are conventionally numbered in chronological order along the boundary of the solid, considering that the solid is on the left and its foundation (tool or other solid) is on the right (Figure 3.12).

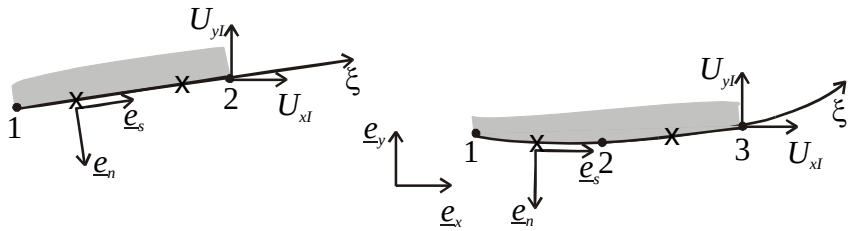

Figure 3.12. Isoparametric 2-node (first degree) and 3-node (second degree) contact element.

Local axes are defined as follows: $\underline{e}_n$ is the external normal to the solid and $\underline{e}_s$ is tangential to the surface, oriented from the first to the second or third node. For the foundation elements, the convention is to number the nodes in chronological order considering that the second solid or tool is located on the right. The external normal to the foundation $\underline{e}_f$ can then be uniquely defined. This convention, which is consistent with the definitions of Figure 3.9, is important to determine when the contact between an element and the foundation is possible. Figure 3.13 shows that one of the conditions that suggest a possibility of contact is that the normal vectors are oriented in such a way that $\underline{e}_n \cdot \underline{e}_f < 0$, i.e. that the two solids face each other.

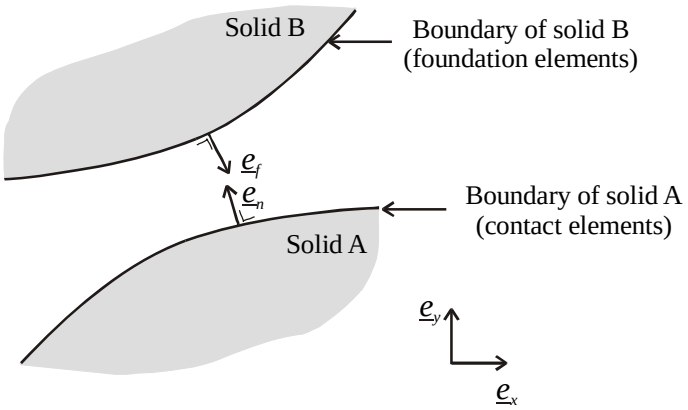

Figure 3.13. Orientation of the vectors normal to the foundation and to the contact elements.

The elements shown in Figure 3.12 have two integration points represented by crosses. The code allows to choose up to ten integration points for the modelling but for most of the applications two integration points are sufficient.

When contact occurs, each integration point of each contact element is associated to a segment of foundation with which it is in contact. The foundation can be a tool or another solid, it can be rigid or deformable. In the derivation presented in this chapter, the contact element is always located on solid A and the foundation on solid B, except otherwise stated. Contact and foundation elements have to be compatible with the solid elements to which they are attached as they will share the same nodes, therefore the number of nodes chosen for the contact and foundation elements will depend on the degree of the solid elements used.

The isoparametric contact element uses the same interpolation functions for the coordinates $\underline{x} = [x, y]$ and the displacements $\underline{u} = [u_x, u_y]$:

$$\underline{x} = \sum_I N_I(\xi)\,\underline{X}_I \quad \text{and} \quad \underline{u} = \sum_I N_I(\xi)\,\underline{U}_I \tag{3.14}$$

where $\underline{X}_I = [X_I, Y_I]$ are the nodal coordinates, $\underline{U}_I = [U_{x_I}, U_{y_I}]$ the nodal displacements, $N_I(\xi)$ the interpolation functions and ξ the intrinsic coordinate of the element, which is in the range $-1 \le \xi \le 1$. The index I takes the values 1 and 2 for the first degree element and 1, 2 and 3 for the second degree element. The vector $\underline{X}$ comprises all the nodal coordinates of one element, i.e. for $I = 1$ to 2 or 3, likewise $\underline{U}$ comprises all the nodal displacements of one element. The same technique is used to discretize the foundation.

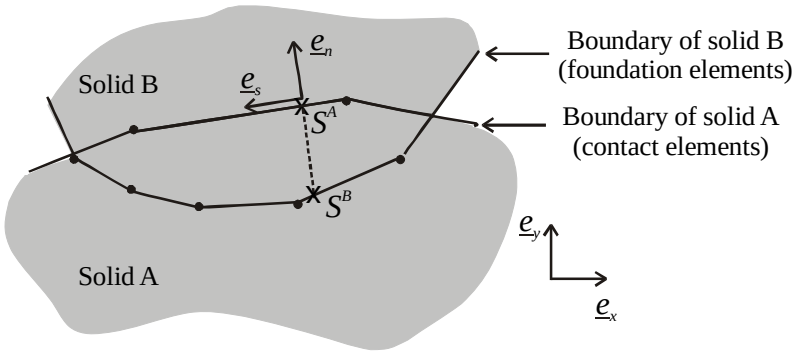

Figure 3.14. Discretization of the two solids.

In the finite element model, the interpenetration distance is determined by calculating the distance between the points S^A and S^B, where S^B is defined by the intersection between the normal to the contact element at the integration point S^A on solid A and the foundation element on solid B, as shown in Figure 3.14. In the global system of coordinates $\left(\underline{e}_x, \underline{e}_y\right)$, the coordinates and displacements of S^A can be defined as a function of the nodal variables using equation (3.14). As the position of S^B depends on the local system of coordinates $\left(\underline{e}_n, \underline{e}_s\right)$ at point S^A, the expression of its coordinates and displacements in the global system of coordinates will not only depend on the nodal coordinates and displacements of solid A $\left(\underline{X}^A, \underline{U}^A\right)$ but also on those of solid B $\left(\underline{X}^B, \underline{U}^B\right)$. Therefore, the strain rate vector at the integration point of the contact element on solid A can be expressed as:

$$\underline{\dot{\varepsilon}}_c = \underline{\dot{\varepsilon}}_c\left(\underline{X}^A, \underline{X}^B, \underline{\dot{U}}^A, \underline{\dot{U}}^B\right) \tag{3.15}$$

It can be shown that this expression takes the following form:

$$\underline{\dot{\varepsilon}}_c = \begin{Bmatrix} \dot{\delta} \\ \dot{u} \end{Bmatrix} = \left[Q^A; Q^B\right] \begin{Bmatrix} \underline{\dot{U}}^A \\ \underline{\dot{U}}^B \end{Bmatrix} = \left[Q\right]\underline{\dot{U}} \tag{3.16}$$

where the component of the matrix $\left[Q\right]$ depend on $\underline{X}^A$ and $\underline{X}^B$ (Habraken and Cescotto 1998a). Similarly, if virtual displacements $\delta\underline{U}$ are given to the nodes of the contact elements, the corresponding virtual contact strains are:

$$\delta\underline{\varepsilon}_c = \left[Q^A; Q^B\right] \begin{Bmatrix} \delta\underline{U}^A \\ \delta\underline{U}^B \end{Bmatrix} = \left[Q\right]\delta\underline{U} \tag{3.17}$$

The virtual work performed by the contact stresses on the element is:

$$\delta W_{el} = \int_{el} \underline{\sigma_c}^T \, \delta\underline{\varepsilon_c} \, dl = \int_{-1}^{1} \underline{\sigma_c}^T \, \delta\underline{\varepsilon_c} \, |J| \, d\xi \tag{3.18}$$

where l is the abscissa along the element and $|J|$ the determinant of the Jacobian of the $l \to \xi$ transformation given by $J = \frac{dl}{d\xi}$.

The virtual work can also be written:

$$\delta W_{el} = \underline{F}^T \delta\underline{U} \tag{3.19}$$

Using equations (3.17), (3.18) and (3.19), the nodal forces energetically equivalent to the stresses in the element are computed as follows:

$$\begin{aligned} \underline{F}^{AT} &= \int_{-1}^{1} \underline{\sigma_c}^T \left[Q^A\right] |J| \, d\xi = \sum_{IP} \underline{\sigma_c}^T \left[Q^A\right] |J| w \\ \underline{F}^{BT} &= \int_{-1}^{1} \underline{\sigma_c}^T \left[Q^B\right] |J| \, d\xi = \sum_{IP} \underline{\sigma_c}^T \left[Q^B\right] |J| w \end{aligned} \tag{3.20}$$

where $\underline{F}^{AT}$ and $\underline{F}^{BT}$ are the energetically equivalent forces computed from the contact stresses on the contact element and acting on the nodes of the contact element and its foundation respectively, $\sum_{IP}$ indicates the sum on the integration points and w are the Gauss integration weight.

The example presented here privileged the solid A by considering that contact elements were present on one side of the contact surface only. It is possible to do the same analysis using solid B as a reference in which case the energetically equivalent forces will be computed from the contact stresses on solid B. In theory, theses forces should be equal to those obtained by equation (3.20) but in practice, there will be some differences due to the numerical integration and discretization. Therefore, in case of coupled analysis with no privileged solid, the best practice rule is to put contact elements on each solid and to average the forces resulting from the calculations on each side. In this case, the nodal forces are divided by two in order to avoid a double stress evaluation, as each element already takes into account the action and reaction forces.

The component of the stiffness matrix of the contact element are calculated by derivation of the contact forces with regard to the degrees of freedom, i.e. with regard to the nodal displacements. A classical assembly operation is then performed to obtain the global stiffness matrix of the finite element model (Habraken and Cescotto 1998a).

3.4.2 DESCRIPTION OF THE INTERFACE FINITE ELEMENT

In the mesoscopic model, the 2D solid elements modelling the grains are connected by interface elements to account for cavitation and sliding at the grain boundary. As the thickness of the grain boundary is small in comparison with the grain size, the grain boundary can be represented by 1D interface elements. These elements have two nodes and two integration points and are associated with a constitutive law which includes parameters linked to the presence of precipitates, voids, etc. The damage variable explicitly appears in this law.

3.4.2.1 Features of the interface element

The interface element is composed of a modified contact element and a foundation element as represented in Figure 3.15. The nodes $(\bullet)$ of the linear elements coincide with the nodes of the quadrangular elements to which they are attached and possess the same degrees of freedom. The additional nodes $(\circ)$ drawn on the exploded view in Figure 3.15 do not exist independently and are only represented for illustration purpose.

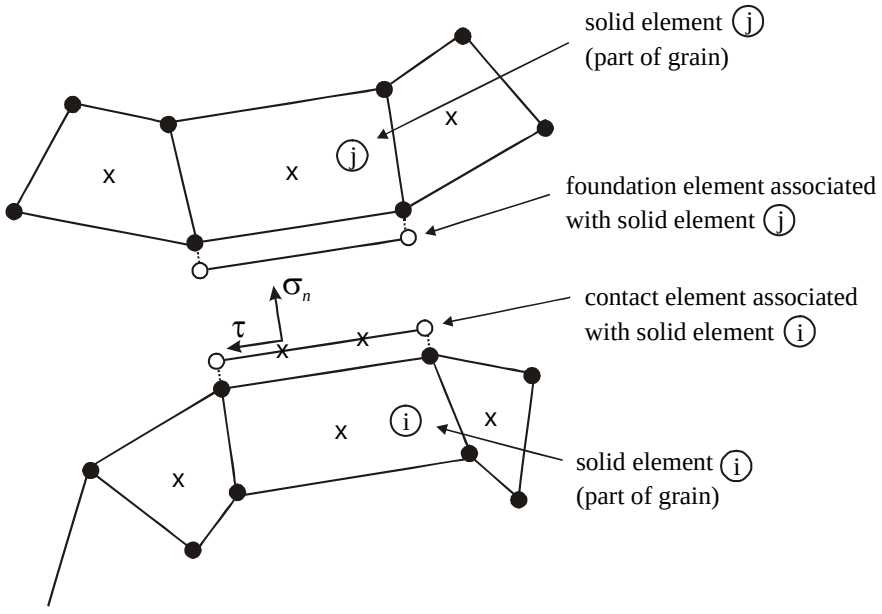

Figure 3.15. Interface element: contact element, associated foundation, linked solid elements. Dots symbolize nodes and crosses represent integration points.

At each iteration, the program determines the foundation element associated to each integration point of each contact element by searching the intersection between the normal of the contact element at this integration point and the foundation elements

surrounding the area. The state variables for each integration point of each interface element are computed at each iteration using information from the two solids elements in contact (elements i and j in Figure 3.15), i.e. the solid elements attached to the contact element and foundation element determined for this particular integration point at this iteration. The state variables in the interface element are the corresponding mean values at the integration points of elements i and j. As the two surfaces of the interface can slide against each other, the foundation element facing a contact element may change during the simulation. Likewise, two integration points of a contact element may be linked to two different foundation elements, i.e. to two different solid elements.

The original contact element was described in section 3.4.1 and is usually combined with a Coulomb's friction law. This element has been modified in order to introduce a new interface law and a cohesion criterion. The stress components of the contact element are represented in Figure 3.15, their evolution is described by the following viscous-elastic-type relationships:

$$\dot{\tau} = k_s \left(\dot{u} - \dot{u}_s \right) \text{ and } \dot{\sigma}_n = k_n \left(\dot{\delta} - \dot{\delta}_c \right) \tag{3.21}$$

In this penalty method, the penalty coefficients k_s and k_n are large to keep the deviations $\left(\dot{u} - \dot{u}_s \right)$ and $\left(\dot{\delta} - \dot{\delta}_c \right)$ small. $\dot{u}$ and $\dot{\delta}$ are respectively the relative sliding velocity of adjacent grains due to shear stress τ and the average separation rate, normal to the interface, due to damage growth. These variables are directly computed from nodal displacements. $\dot{u}_s$ and $\dot{\delta}_c$ are the corresponding variables to $\dot{u}$ and $\dot{\delta}$ but related to the damage law. Their evolutions are described in the section 3.4.3 (equations (3.23) and (3.39)). Equation (3.21) enforces $\dot{u}$ and $\dot{\delta}$ to be equal to $\dot{u}_s$ and $\dot{\delta}_c$, respectively.

3.4.2.2 Behaviour of the interface compared to the classical contact element

In order to implement properly the interface element in the finite element code LAGAMINE, a comparison with the classical contact element described in section 3.4.1 is required.

First, the interface element is linked to the same degrees of freedom than the classical contact element, which are the displacements of the nodes of the element itself and its foundation. The same stress vector can be used for both elements, although the normal stress defined by equation (3.21) must be related to the pressure component of equation (3.2) by the following relation:

$$\dot{p} = -\dot{\sigma}_n \tag{3.22}$$

The strain vector is equal for both elements and is given by equation (3.5). The penalty method is used in both cases: for the classical contact element, the objective is to impose the non-penetration condition whereas for the interface element, the objective is to impose a given displacement as shown by equation (3.21).

The quantities $\dot{u}_s$ and $\dot{\delta}_c$ are calculated at each step of the simulation. They are indirectly function of the displacements of the nodes of the finite element mesh through the stresses and strains that are used in their calculation (see section 3.4.3). Nevertheless, this link is a second order effect which occurs through the sharing of state variables and it is acceptable to consider that $\dot{u}_s$ and $\dot{\delta}_c$ are constant for the derivation of the stiffness matrix of the interface element. Therefore, the same stiffness matrix as for the classical contact element can be used for the interface element within the Newton-Raphson solution process. The calculation of the nodal forces as given by equations (3.20) is done using the expressions (3.21) for the stress components and it is at this point that $\dot{u}_s$ and $\dot{\delta}_c$ are taken into account for the equilibrium. Indeed, the global solution equilibrates the external forces and the internal forces, which directly account for $\dot{u}_s$ and $\dot{\delta}_c$.

The Signorini's conditions defined in section 3.4.1.1 do not have to be respected for the interface element as the interface can be in tension. Likewise, the interface can be open without loss of contact and a negative penetration is allowed. The conditions for loss of contact, also called de-bonding, are not linked to the sign of the interpenetration or to the occurrence of a contact pressure but to the value of a damage criterion to be defined in section 3.4.3.2.

At the beginning of the simulation, the contact and foundation elements constituting the interface are attached to each other and the damage inside the interface progressively increases due to the stresses and strains in the immediate environment of the element. When the fracture criterion is reached, the nodes of the interface de-bond, i.e. the contact element is no longer attached to the foundation, and the contact stresses are put to zero. From this stage, the two parts of the interface are considered as two independent solids. In case of recovering of contact, an element which has previously de-bonded, follows the classical contact behaviour associated with the Coulomb's friction law.

3.4.3 INTERFACE MATERIAL LAW: EVOLUTION OF THE DAMAGE

The major damage mechanisms at the mesoscale are viscous grain boundary sliding, nucleation, growth and coalescence of cavities leading to microcracks. The linking-up process subsequently leads to the formation of a macroscopic crack.

3.4.3.1 Grain boundary sliding

Grain boundary sliding is governed by:

$$\dot{u}_s = w\frac{\tau}{\eta_B} \tag{3.23}$$

where $\dot{u}_s$ is the relative velocity between two adjacent grains, *w* is the thickness of the grain boundary, η_B is the grain boundary viscosity and τ the shear stress component (Ashby 1972). However w/η_B can be expressed in terms of the strain rate parameter $\dot{\varepsilon}_B$ defined as follows:

$$\dot{\varepsilon}_B = \dot{\varepsilon}_0\left(\frac{w\sigma_0}{\eta_B d\dot{\varepsilon}_0}\right)^{\frac{n}{n-1}} \tag{3.24}$$

where *d* is a length parameter related to the grain size and *n* is the creep exponent (Onck and van der Giessen 1999). σ_0, $\dot{\varepsilon}_0$ are reference stress and strain rate that depend on the steel grade. The intergranular sliding can be characterized by the ratio $\dot{\varepsilon}_e/\dot{\varepsilon}_B$ between the grain equivalent deformation rate $\dot{\varepsilon}_e$ and the boundary deformation rate $\dot{\varepsilon}_B$. This ratio $\dot{\varepsilon}_e/\dot{\varepsilon}_B$ measures the relative resistance between the grain and the grain boundary. In case of free sliding (η_B = 0), $\dot{\varepsilon}_e/\dot{\varepsilon}_B$ = 0. When there is no sliding ($\eta_B \to \infty$), $\dot{\varepsilon}_e/\dot{\varepsilon}_B \to \infty$.

The Norton classical creep law is defined as:

$$\dot{\varepsilon}_e = \dot{\varepsilon}_0\left(\frac{\sigma_e}{\sigma_0}\right)^n = B\left(\sigma_e\right)^n \tag{3.25}$$

Using equations (3.24) and (3.25), the ratio w/η_B becomes:

$$\frac{w}{\eta_B} = d\left(\dot{\varepsilon}_B\right)^{\frac{n-1}{n}}\left(B\right)^{\frac{1}{n}} \tag{3.26}$$

where B is the creep coefficient. Finally, equation (3.26) is used in combination with equation (3.23) to calculate the grain boundary sliding $\dot{u}_s$ as a function the shear stress component τ. The ratio w/η_B is known when the viscosity parameter $\dot{\varepsilon}_e/\dot{\varepsilon}_B$, the grain

size *d* and the creep parameters *n* and *B* are known; therefore, the ratio $\dot{\varepsilon}_e / \dot{\varepsilon}_B$ can be used as an input data instead of *w* and η_B.

Four parameters are then necessary to define grain boundary sliding: the creep exponent *n*, the creep coefficient *B*, the grain size *d* and the parameter characterizing the grain boundary viscosity $\dot{\varepsilon}_e / \dot{\varepsilon}_B$. The three first parameters are determined in Chapter 4 using the experimental results, $\dot{\varepsilon}_e / \dot{\varepsilon}_B$ is chosen equal to an intermediate value of 10 (Onck and van der Giessen 1999).

3.4.3.2 Voids evolution

In the context of damage at high temperature, the mechanism of voids nucleation, growth and coalescence is established.

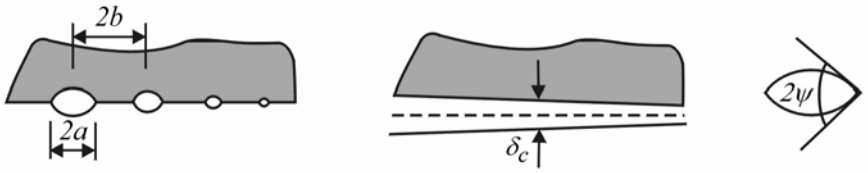

Figure 3.16. Discrete and continuous representations of the grain boundary (Onck and van der Giessen 1999) and definition of the cavity angle ψ.

The model uses an idealized formulation of the grain boundary geometry where the cavities are supposed to be uniformly distributed on each grain boundary segment (i.e. at each integration point) with an average spacing of 2*b* and a diameter of 2*a*. Figure 3.16 illustrates this idealized representation: on the left, each individual void is represented; and on the right, the voids are replaced by a continuous variable δ_c. Its evolution rate $\dot{\delta}_c$ is computed at the integration points of the interface elements to account for the interface thickness updating due to the presence of voids at the grain boundaries (see equation (3.21)). Detailed equations for the variables used for the computation of $\dot{\delta}_c$ are presented in the next sections. A fracture criterion is also proposed.

Voids nucleation – computation of the cavity spacing growth rate $\dot{b}$

In most engineering alloys, cavities have been observed to continuously nucleate. The following experimental relation has been suggested:

$$\dot{N} = \beta \sigma_n^2 \dot{\varepsilon}_e = F_n \left(\frac{\sigma_n}{\Sigma_0} \right)^2 \dot{\varepsilon}_e \text{ with } \sigma_n \geq 0 \qquad (3.27)$$

N is the average number of cavities per unit length of grain boundary. $\dot{\varepsilon}_e$ is the equivalent creep strain rate from the modified Norton-Hoff law (equation (3.1)). σ_n is the normal stress, introduced to allow a faster nucleation on those grain boundaries which are perpendicular to the loading direction. β is a material constant (van der Giessen *et al.* 1994) which is related to Σ_0 and to F_n. Σ_0 is a normalization constant representative of the average stress level in the material surrounding the crack. F_n is the microstructural parameter which influences the nucleation rate at the grain boundary; zones where nucleation is more important can be modelled by increasing the value of this parameter. F_n can represent, among others, the precipitation state or the influence of the thin ferrite film that can form close to the grain boundary leading to strain concentration (Mintz *et al.* 1991). According to equation (3.27), the nucleation will begin with the plastification. However, experiment shows that nucleation appears later, that is why a threshold is used to indicate the beginning of the nucleation. For this purpose, the parameter S which combines the stress and the cumulated strain is defined as:

$$S = \left(\sigma_n / \Sigma_0\right)^2 \varepsilon_e \tag{3.28}$$

The parameter S characterizes the state of the material before nucleation. It will grow with the strain until the threshold value S_{thr} is reached. S_{thr} is assumed to be related to the minimum cavity density N_I from which nucleation can be observed and to the factor F_n that indicates the importance of the nucleation activity of the material:

$$S_{thr} = N_I / F_n \tag{3.29}$$

Once nucleation begins the parameter S is not used any longer in the model.

Finally, experience shows that the cavity density tends to saturate for large creep strains, then the nucleation of new cavities stops when N reaches the value $N_{max.}$ If $2b$ is the cavity spacing (see Figure 3.16), N is related to it by:

$$N = 1/\pi b^2 \tag{3.30}$$

The evolution of the cavity spacing is found by derivation of equation (3.30):

$$\dot{b} = -\frac{1}{2}\frac{\dot{N}}{N} b \tag{3.31}$$

Substituting equations (3.27) and (3.30) in equation (3.31) leads to:

$$\dot{b} = -\frac{\pi}{2} b^3 \beta \sigma_n^2 \dot{\varepsilon}_e \tag{3.32}$$

The nucleation rate $\dot{N}$ is related to the internal state variable of the material *N* as well as to the stress σ_n and strain rate $\dot{\varepsilon}_e$ applied on the grain boundary. With a one-dimensional element, this nucleation rate $\dot{N}$ can be interpreted as a measure of the rate of evolution of the cavity spacing $\dot{b}$. In practice, the finite element model uses equations (3.27) and (3.31) to compute the decrease rate of *b* due to continuous nucleation of cavities.

Voids growth – computation of the cavity size growth rate $\dot{a}$

A detailed formulation of the cavity growth under diffusion and creep deformations was proposed by Tvergaard (1984). Assuming that a cavity is defined by two parameters: ψ the cavity tip angle and *2a* its size, the cavity growth rate is:

$$\dot{a} = \dot{V} / \left[4\pi a^2 h(\psi) \right] = \left(\dot{V}_1 + \dot{V}_2 \right) / \left[4\pi a^2 h(\psi) \right] \tag{3.33}$$

where $h(\psi) = \dfrac{(1+\cos\psi)^{-1} - 0.5\cos\psi}{\sin\psi}$ (shape function of the cavity) and $\dot{V}$ is the total cavity volume growth rate, which is divided into diffusion growth $\dot{V}_1$ (equation (3.34)) and creep deformation $\dot{V}_2$ (equation (3.35)):

$$\dot{V}_1 = 4\pi D \frac{\sigma_n}{\ln(1/f) - (3-f)(1-f)/2} \tag{3.34}$$

$$\dot{V}_2 = \begin{cases} -A\left(\dfrac{3}{2n}\left|\dfrac{\sigma_m}{\sigma_e}\right| + C \right)^n & \text{for } \dfrac{\sigma_m}{\sigma_e} < -1 \\ A\left(\dfrac{3}{2n} + C \right)^n & \text{for } \left|\dfrac{\sigma_m}{\sigma_e}\right| \le 1 \\ A\left(\dfrac{3}{2n}\dfrac{\sigma_m}{\sigma_e} + C \right)^n & \text{for } \dfrac{\sigma_m}{\sigma_e} > 1 \end{cases} \tag{3.35}$$

where $C = \left[(n-1)(n+0.4319) \right] / n^2$ and $A = 2\pi\dot{\varepsilon}_e a^3 h(\psi)$. *D* is a constant related to the material diffusion, *n* is the creep exponent, σ_e and σ_m are the equivalent and mean stresses sustained by the material surrounding the grain boundary and σ_n is the normal stress applied on the grain boundary. The variable *f* used in equation (3.34) is the area fraction of grain boundary cavitated. It is defined as follows:

$$f = max\left\{ (a/b)^2, \left[a/(a+1.5L) \right]^2 \right\} \tag{3.36}$$

where $L = \left(D\,\sigma_e / \dot{\varepsilon}_e \right)^{1/3}$ is a characteristic length which accounts for the coupling between diffusive and creep contributions to void growth. This coupling has the effect to shorten the diffusion path to a distance of order *L*, hence the definition of *f* by equation (3.36). Cavity growth is dominated by diffusion for small values of *a/L* (i.e. $a/L \le 0.1$). For larger values of *a/L*, creep growth starts to dominate. Equations (3.34) and (3.35) have been established with $a/L \le 10$.

The diffusion parameter can be expressed as a function of the temperature by:

$$D = \frac{D_{b0}\delta_b \Omega}{kT} \cdot exp\left(-\frac{Q_b}{RT} \right) \tag{3.37}$$

with $D_{b0}\delta_b$ the grain boundary diffusion coefficient, Ω the atomic volume, Q_b the activation energy, *T* the temperature in Kelvin, *k* the Boltzmann's constant and *R* the universal gas constant.

Finally the discrete cavity distribution is replaced by a continuous distribution on each facet of the grain boundary so that the average separation between two grains δ_c, which is equivalent to a grain boundary thickness, evolves in a continuous way on the facet (see Figure 3.16). δ_c is determined using the volume of grain boundary cavities *V* and their average spacing *b*:

$$\delta_c = \frac{V}{\pi b^2} \tag{3.38}$$

Then, the separation rate $\dot{\delta}_c$ used in equation (3.21) is given by:

$$\dot{\delta}_c = \frac{\dot{V}}{\pi b^2} - \frac{2V}{\pi b^2}\frac{\dot{b}}{b} \tag{3.39}$$

Finally, to resolve the equations of this section, the following independent parameters have to be defined: the initial voids size a_0 and spacing b_0, the nucleation parameter F_n, the normalization constant Σ_0, the cavity tip angle ψ, the initial cavity density for nucleation N_I and the maximum cavity density N_{max} where nucleation stops. They are determined in Chapter 4 using the damage experiments except for ψ, which is assumed to remain constant during voids growth and taken equal to 75° (Onck and van der Giessen 1998).

Voids coalescence and fracture criterion

Coalescence takes place when cavities are sufficiently close to each other to collapse. The parameter used to define the coalescence activation is the ratio *a/b*. It is called a damage variable in the current model. When this ratio reaches a critical threshold value d_{lim}, coalescence is triggered and a crack appears. At this moment the contact is lost between the foundation and the contact element of the interface element where the criterion has been reached and a crack physically appears in the finite element model.

3.5 NUMERICAL IMPLEMENTATION OF THE MODEL

The numerical implementation of the material constitutive laws and interface element has been updated all along the development and validation of the model in order to improve the convergence of the simulations and the accuracy of the results. The following description summarizes the final choices and explains their historical reasons. The potential improvements that have not been implemented are also listed.

3.5.1 INTEGRATION OF THE CONSTITUTIVE DAMAGE LAW

Different solutions are possible for the implementation of the damage constitutive law. In particular, regarding the integration of the law, one solution consists in calculating the evolution of each variable independently based on the calculation of its increment for each time step. A second solution consists in choosing two driving parameters, e.g. *a* and *b*, for which the increments are calculated and to compute all the other variables based on the integrated values of these variables. Due to the interdependence of the equations and to the different degree of non-linearities in the problem, this second method is more appropriate. It has been applied in practice in this research as it gives more coherent results between the variables at the end of the converged step although the model is less coupled as with the first method. Another improvement to the first method would have been to use under-intervals for the integration but this technique would have increased considerably the computation time.

The state variables and their signification have been reported in Table 3.1. The equivalent strain, strain rate and stress as well as the mean stress are not directly associated to the interface but come from the surrounding solid elements. In practice, they are calculated by averaging the values found in the two solid elements directly attached to the interface.

Table 3.1. State variables.

Variable	Description
ddam	Damage variable $\left(\frac{a}{b}\right)$
$\dot{u}_s$	Sliding velocity
$\dot{\delta}_c$	Interface spacing velocity
V	Cavity volume
$\dot{\varepsilon}_e$	Equivalent strain rate
ε_e	Equivalent strain
N	Nucleation variable
a	Void size
b	Void spacing
σ_n	Normal stress on the edge of the interface
σ_m	Mean stress
σ_e	Equivalent von Mises stress

Threshold values have been introduced for the variables *a* and *b* to avoid inconsistencies in case of compression in the structure. These thresholds are defined in sections 3.5.1.1 and 3.5.1.2, respectively. Damage grows mostly due to tensile loads, nevertheless the model has to give realistic answers when certain elements are in compression. This situation can appear when the global structure is in compression or in tension. Indeed, even if the global structure is in tension, the heterogeneity introduced when an actual grain microstructure is modelled can lead to particular zones being in compression due to the movement and accommodation of the grains. Without a threshold value, negative values for *a* are allowed, which is unfeasible in practice as it corresponds to a negative void size. Likewise, the void spacing is limited by void saturation and there is a specific threshold underneath which *b* can not decrease when the maximum number of cavities has been reached.

3.5.1.1 Evolution of *a* and *V*

The volume increase at step *i* is calculated using all the information directly available at this step. In particular, the equivalent and mean stresses (σ_e and σ_m) and strain rate ($\dot{\varepsilon}_e$) are calculated using the data of the current step. These data are available because they are calculated as an average between the corresponding state variables of the solid elements attached to the interface element at which the damage is calculated, the solid elements being treated before the interface elements by the finite element code.

For the other variables appearing in the equations, and especially for the state variables directly calculated in the interface damage law (a, b, σ_n), the most recent converged data available are used, i.e. the data corresponding to the values at step i-1. The index i or i-1 identifies for each variable the instant at which the value is adopted.

Using equations (3.36) and (3.34), the computation of V_1 (part of the void volume due the growth by diffusion) is realised as follows:

$$f_i = \max\left\{\left(a_{i-1}/b_{i-1}\right)^2, \left[a_{i-1}/\left(a_{i-1}+1.5L_i\right)\right]^2\right\} \text{ where } L_i = \left(D\sigma_{ei}/\dot{\varepsilon}_{ei}\right)^{1/3} \quad (3.40)$$

$$\dot{V}_{1i} = 4\pi D \frac{\sigma_{ni-1}}{\ln\left(1/f_i\right) - \left(3-f_i\right)\left(1-f_i\right)/2} \quad (3.41)$$

The sign of $\dot{V}_{1i}$ is directly linked to the sign of σ_{ni-1} as the denominator of equation (3.41) is always positive because $f_i \in [0,1]$. The void size increases in tensile state and decreases in compression state.

Using equation (3.35), the computation of V_2 (part of the void volume due the creep deformation) is realised as follows:

$$\dot{V}_{2i} = \begin{cases} -2\pi\dot{\varepsilon}_{ei} a_{i-1}{}^3 h(\psi)\left(\frac{3}{2n}\left|\frac{\sigma_{mi}}{\sigma_{ei}}\right| + \frac{(n-1)(n+0.4319)}{n^2}\right)^n & \text{for } \frac{\sigma_{mi}}{\sigma_{ei}} < -1 \\ 2\pi\dot{\varepsilon}_{ei} a_{i-1}{}^3 h(\psi)\left(\frac{3}{2n} + \frac{(n-1)(n+0.4319)}{n^2}\right)^n & \text{for } \left|\frac{\sigma_{mi}}{\sigma_{ei}}\right| \le 1 \\ 2\pi\dot{\varepsilon}_{ei} a_{i-1}{}^3 h(\psi)\left(\frac{3}{2n}\frac{\sigma_{mi}}{\sigma_{ei}} + \frac{(n-1)(n+0.4319)}{n^2}\right)^n & \text{for } \frac{\sigma_{mi}}{\sigma_{ei}} > 1 \end{cases} \quad (3.42)$$

The sign of $\dot{V}_{2i}$ also implies a growth of the cavity size in tension and a reduction in compression except for low triaxialities $\left|\frac{\sigma_{mi}}{\sigma_{ei}}\right| \le 1$ for which equation (3.42) implies void growth.

It is then possible to compute the evolution of a using equation (3.33) and taking into account the minimum threshold a_{min}:

$$\dot{a}_i = \dot{V}_i / \left[4\pi a_{i-1}{}^2 h(\psi)\right] = \left(\dot{V}_{1i} + \dot{V}_{2i}\right) / \left[4\pi a_{i-1}{}^2 h(\psi)\right] \quad (3.43)$$

$$a_i = a_{i-1} + \dot{a}_i \Delta t$$
$$\text{If} \quad a_i \le a_{\min} \quad \text{then} \quad a_i = a_{\min} \tag{3.44}$$

The sign of $\dot{a}_i$ is identical to the sign of $\dot{V}_i$. Therefore, the minimum value $a_{\min}$ can only be reached if $\dot{V}_i$ is negative, i.e. in case of compression state. The value of $a_{\min}$ is chosen equal to the initial void size given to the program. Another value could be chosen but it has to be greater than zero otherwise the voids will never grow again once the minimum value is reached as shown by equations (3.40) to (3.44).

Finally the computation of the total volume of voids is realised at the end of the step using:

$$V_i = \frac{4}{3}\pi a_i^{\,3} h(\psi) \tag{3.45}$$

The total volume of voids could also be calculated by adding the increment $\Delta V_i = \dot{V}_i \Delta t$ to the previous step value V_{i-1}, but in this case there is a risk that equation (3.45) is no longer satisfied if the time steps are not small enough.

3.5.1.2 Evolution of *b* and δ

For the computation of *b*, δ and their associated variables, the same technique as presented in the preceding section is used.

The nucleation threshold $S_{thr} = N_I / F_n$, which is a constant for the simulation, is calculated using the initial parameters of the model. The first step is then to verify if this threshold has been reached by calculating S_i as given by equation (3.28):

$$S_i = \left(\sigma_{ni-1} / \Sigma_0\right)^2 \varepsilon_{e\,i} \tag{3.46}$$

If the threshold is exceeded ($S_i \ge S_{thr}$) and if the integration point is in tensile state ($\sigma_{ni-1} \ge 0$), there is nucleation and *b* evolves according to equations (3.27) and (3.31) until saturation is reached:

$$\dot{N}_i = F_n \left(\sigma_{ni-1} / \Sigma_0\right)^2 \dot{\varepsilon}_{e\,i} \quad \text{and} \quad \dot{b}_i = -\frac{1}{2}\frac{\dot{N}_i}{N_{i-1}} b_{i-1} \quad \text{for} \quad \sigma_{ni-1} \ge 0 \tag{3.47}$$

$$\dot{N}_i = 0 \quad \text{and} \quad \dot{b}_i = 0 \quad \text{for} \quad \sigma_{ni-1} < 0 \tag{3.48}$$

$$b_i = b_{i-1} + \dot{b}_i \Delta t$$
$$\text{If} \quad b_i \le b_{\min} \quad \text{then} \quad b_i = b_{\min} \tag{3.49}$$

It can be noticed that the value of b can only decrease. In compression state, b does not evolve, i.e. when the voids have been created they can not be 'repaired'. The value of $b_{\min}$ corresponds to the value of b for which the nucleation threshold $N_{\max}$ is reached. Using equation (3.30) this gives:

$$b_{\min} = \sqrt{\frac{1}{\pi N_{\max}}} \tag{3.50}$$

The evolution of $\dot{\delta}_c$ is then computed using increments calculated by equations (3.41), (3.42) and (3.47) for $\dot{V}$ and $\dot{b}$ and the values at the beginning of the step, which are equivalent to the values at the end of the previous step, for V and b:

$$\dot{\delta}_{ci} = \frac{\dot{V}_i}{\pi b_{i-1}^{\ 2}} - \frac{2V_{i-1}}{\pi b_{i-1}^{\ 2}} \frac{\dot{b}_i}{b_{i-1}} = \frac{\dot{V}_{1i} + \dot{V}_{2i}}{\pi b_{i-1}^{\ 2}} - \frac{2V_{i-1}}{\pi b_{i-1}^{\ 2}} \frac{\dot{b}_i}{b_{i-1}} \tag{3.51}$$

Finally, the remaining state variables are calculated at the end of the step:

$$N_i = \frac{1}{\pi b_i^{\ 2}} \quad \text{and} \quad \delta_{ci} = \frac{V_i}{\pi b_i^{\ 2}} \tag{3.52}$$

3.5.1.3 Other improvements to be considered in the future

The different variables that appear in the damage law offer the possibility to add additional features to the model in order to represent more detailed material behaviours. Although some modifications are pretty straightforward, these ideas have not been implemented in the code during the development phase of the model. Indeed, the focus was initially on the resolution of particular problems linked to damage in continuous casting and to the numerical performance of the simulations. Introducing new code developments implies phases of verification and validation which are time consuming and deviate from the global goal of the project. Nevertheless, it is worth to highlight at this point some of the possibilities and to keep them in mind for future developments.

The damage history in the material could be recorded through the minimum void size parameter $a_{\min}$. In the standard model $a_{\min}$ is taken equal to the initial void size a_0 but in reality, it is not excluded to have $a_{\min} \leq a_0$. This choice could be useful to model cases where the void size actually decreases under its initial value in compression state, e.g. if the voids close up when grain boundaries get closer to each other.

Another possibility is to consider that the minimum voids size threshold increases during the simulation to account for an irreversible damage progression. In this case, the void size can still decrease in compression, allowing for the voids to close

up slightly, but the maximum closure acceptable is reduced in proportion with the damage previously incurred. In this case, the impact on $a_{\min}$ is opposite to what has been described in the previous paragraph but for practical applications a combination of both effects can be taken into account. Characteristic curves for $a_{\min}$ can be introduced in the model as functions of other variables rather than single points if necessary.

Concerning the minimum void spacing value $b_{\min}$, the model intrinsically considers that the value of b can only decrease until saturation. Voids are created but they never disappear, so an increase of b or $b_{\min}$ is not allowed. If the elements are in compression, the voids size can decrease but the voids will stay present (damaged grain boundaries never completely re-bond). Therefore, if it is required to allow re-bonding of the grain boundaries for particular applications, it has to be introduced via additional equations, independently from the nucleation process.

The standard model allows shear stress to evolve without limit following the elastic penalty law during the simulation. A simple solution to avoid this problem is to impose a maximum critical shear stress τ_c for the simulation. When τ_c is exceeded, the shear stress τ does not increase any longer, the evolution of τ following to an elastic-perfectly plastic model. Likewise, it is necessary to introduce a maximum shear displacement threshold for which fracture in shear appears if the shear deformations are too high. These improvements are not relevant for actual continuous casting simulations as the displacements in shear are very limited for this particular application.

3.5.2 MODELLING OF THE CONTACT

3.5.2.1 De-bonding of the interface element

One of the most important features of the damage model is its ability to account for loss of contact when the fracture criterion is reached at one integration point. In the first developed model, in case of loss of contact, when the corresponding elements of the compliance matrix [*C*] were put to zero together with the contact pressure σ_n and shear stress τ, the contact state index *CI* was simultaneously set to its 'non-contact case' value. Using this method, the system started the next iteration in a non-contact configuration, which could lead to large oscillations of the associated equilibrium forces and to poor convergence properties.

The solution adopted to improve convergence is based on the fact that if the contact state index is set to its 'non-contact case' value as soon as the fracture threshold is reached during one iteration within a time step of the simulation, the next iteration

will begin with a configuration corresponding to a non-contact case even if there is no certitude regarding the state of the contact at this point as the convergence criteria has not been reached yet. Therefore, it is preferable to update the contact case index only after convergence to avoid introducing unnecessary oscillations in the simulations when integration points detach during the iterations.

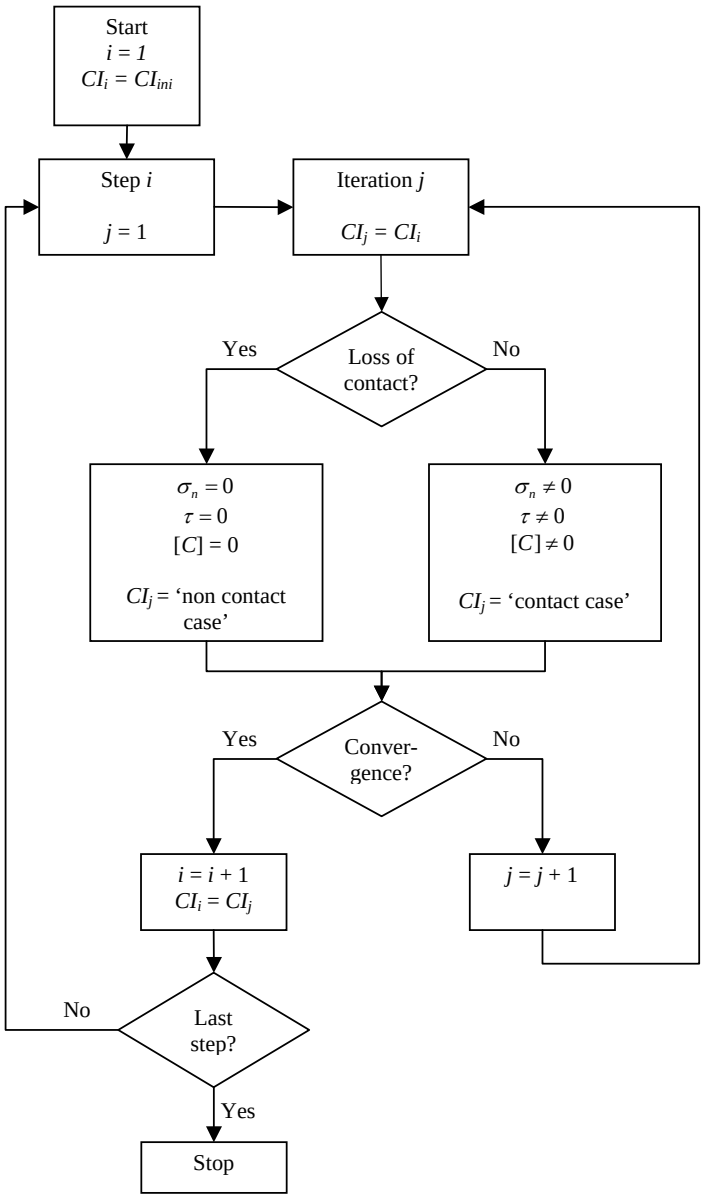

Figure 3.17. Calculation of the contact case index *CI* during the iterations process.

Using this method, in case of loss of contact, σ_n, τ and the elements of the compliance matrix [*C*] are set to zero for the corresponding iteration, but the new state

of the contact affects the contact configuration only at the beginning of the next time step, which globally increases the convergence performances while maintaining the accuracy of the results. This process is schematized on the flowchart of Figure 3.17.

3.5.2.2 Single versus double interface

For the modelling of contact using classical contact elements, it is sometimes required to use a contact element and a foundation on each side of the contact surface to represent accurately two deformable bodies (Habraken and Cescotto 1998a). In this case, the nodal forces are divided by two when computing the terms of the stiffness matrix. The use of contact elements on one side of the contact surface, with foundations on the other side only, is sometimes recommended when one of the bodies can be privileged with regard to the other. This approach has the advantage of reducing the number of contact elements and can be justified in some circumstances. If the two bodies are not discretized with the same accuracy, the privileged body, on which the contact elements are placed, must be the one with the more refined mesh.

The standard interface element consists in a contact element associated with a foundation element as described in section 3.4.2. As this element is based on the traditional contact element, the two options discussed here before have been implemented and investigated. The objective was to analyse how the crack propagates when single or coupled double interfaces are used to model the grain boundaries.

The first solution consists in using a single contact element with its associated foundation (single interface) as represented in Figure 3.15 and Figure 3.18(a). The second solution consists in putting a contact element and a foundation on each side of the interface, the global interface being composed of two single interface elements which are coupled as represented in Figure 3.18(b) (double interface). The contact element *A* attached to the solid element 1 is associated with the foundation element *A* attached to the solid element 2 to form the interface element *A*. Likewise, the contact element *B* attached to the solid element 2 is associated with the foundation element *B* attached to the solid element 1 to form the interface element *B*. In the double interface case, the nodal forces are divided by two during the computation of the terms of the stiffness matrix. The advantage of using the coupled double interface is that it facilitates the meshing of the grain structure. Indeed, as there is contact and foundation elements on every grain boundary segment, there is always a foundation facing a contact element to form an interface element, even if the grains slide against each others.

Two possibilities can be envisaged to represent the foundation: either defining a single global foundation made of all the foundation segments or defining for each contact element a foundation made of the segment facing the element in the initial state and of its direct neighbours. In the first case, the foundation segments list is pretty easy to realise but the search of the foundation segment in contact can be very time consuming during the simulation. The second solution reduces the contact search time during the simulation but complicates the meshing phase.

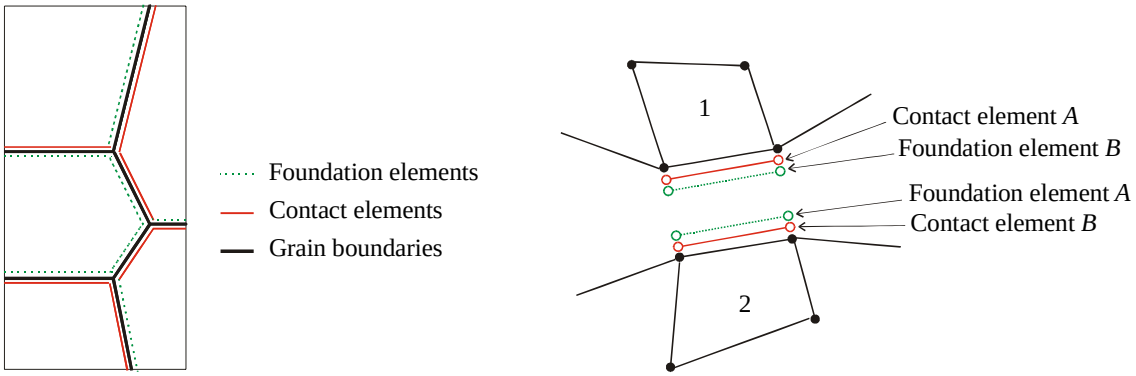

Figure 3.18. Position of the foundation and contact elements in case of a) single interfaces, b) double interface element.

The comparison between the two techniques (single versus double interface element) has been realised using the simple symmetric mesh of Figure 3.19. The mesh contains three interface elements (simple for the first simulation and double for the second one) represented by the bold line. The arrows correspond to enforced displacements while the lines ended by a stroke represent fixed nodes. The loads have been chosen to reproduce a tensile state around the zone with interface elements. The tensile stresses appear due to the bending of the specimen and are perpendicular to the possible crack propagation path, i.e. to the line of interface elements.

The simulations have shown that with the use of double interface elements it is not possible to follow the propagation of the crack in an accurate way without important modifications in the finite element code. Indeed, a soon as one integration point reaches the maximum damage threshold on one side of the interface and detaches itself, the nodal forces of the corresponding interface element decrease. Therefore, the integration point that faces directly the detached one on the other side of the interface does not have to sustain the same forces, which implies that the damage at this integration point does

not increase as much and does not reach the de-bonding condition level. This phenomenon, which can be explained by numerical imprecision, appears even in a perfectly symmetric case where the two integration points are initially localised exactly at the same point in space and the attached solid elements are submitted to the same loads. In the particular example described by Figure 3.19, the crack evolves by de-bonding of the integration points of the contact element on one side of the interface only, alternating from one side to the other when progressing from element to element. The second contact element composing each double interface does not detach itself, meaning that no true crack appears.

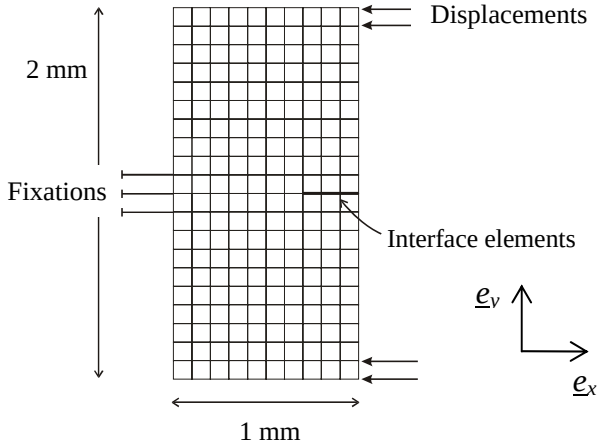

Figure 3.19. Mesh used to compare single and double interface.

To be able to use the double interface in a correct way, it would be necessary to implement the element in such a way that when one integration point detaches itself on one side of the interface, the corresponding integration point on the opposite side of the interface detaches simultaneously. This technique creates an artificial link between the contact elements and complicates the numerical developments.

The analysis with single interface elements shows that the propagation of the crack can be modelled by successive de-bonding of the integration points of the elements.

These tests have proved that it was better to develop the model using single interface elements to avoid errors and programming difficulties. Moreover, the use of double interfaces is not justified because on the one hand, for the particular problem of continuous casting, it is unlikely that large sliding movements between grains occur and on the other hand, due to the nature of the problem, both sides of the contact surface are discretized with the same precision, which means that no side of the interface will be

privileged while using single interfaces. Developments using double interfaces would require much more effort without bringing any added value. As a consequence of this choice, particular attention has to be given to the realisation of the mesh with regard to the respective position of the contact and foundation elements that constitute each interface element.

3.5.2.3 Best practices for mesh generation

To model a microstructure comprising grains and grain boundaries, it is essential to define one single interface element on every grain boundary segment and to avoid duplication. The orientation of the contact and foundation elements is also important as it determines the orientation of the external normal vectors which are used to check if the contact is possible.

The mesh can be easily realised using the mesh generator GMAILL. The input files require the definition of all the zones and contours to be meshed and of the type of elements to be used for each zone. Various density of elements can also be defined, e.g. to impose a finer mesh along the grain boundaries.

At the intersection of three grain boundaries (triple point), three different nodes have to be defined, each of them belonging to one of the grains that are in contact at the triple point. These nodes are localized at the same coordinates in the initial configuration but have independent degrees of freedom. This technique allows the grains to move against each others and to separate in case of crack propagation.

The grains are the zones to be meshed with solid elements. These zones have to be defined counter-clockwise following the grain contour. As independent nodes have been defined at the triple points, all the grains are independent and are only linked via the interface elements.

The grain boundaries are the contours to be meshed by interface elements. To constitute the interface elements, the grain boundaries segments have two sides, one with contact elements and one with foundation segments, each of which belonging to two independent grains. The technique used to mesh the grain boundaries is to follow each grain contour counter-clockwise and to define contact elements progressively if no contact element is already present on the other side of the grain boundary, i.e. on the part of the contour of the adjacent grain just facing it. This method is illustrated in Figure 3.20, for the meshing of the boundaries of ten successive grains, the arrows representing the numbering order for the contact elements.

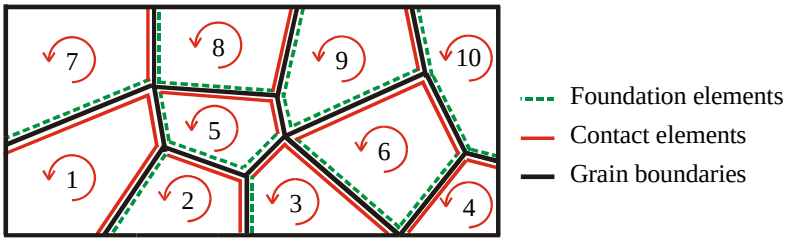

Figure 3.20. Illustration of the meshing process for the grain boundaries.

The parts of the contours that do not receive contact elements receive foundation elements. The nodes of the foundation segments are registered clockwise, i.e. in the opposite direction of the one defined by the arrows for the contact elements in Figure 3.20, so that the orientation of the normal vectors is consistent with the convention discussed in section 3.4.1.2. By following rigorously this technique, the mesh realised will be complete and the elements correctly oriented.

3.5.2.4 Contact search methodology

The search of contact is a time consuming operation which has to be performed at each step of the simulation in order to define which foundation element can be associated with the contact element to form the interface element and to check if there is contact. Therefore, it is necessary to define a methodology that simplifies this operation and accelerates the simulation.

For the modelling of a grain structure, the time required for the contact search is still increased due to the large amount of interface elements involved. In particular, if one single foundation that comprises all the foundation segments (i.e. corresponding to all the grain boundaries) is defined, the contact algorithm checks if there is an intersection between the normal to the contact element and every possible segment of foundation. As the displacements of the grains along one another are quite small, only several foundation elements can be in contact with a particular contact element. It is then possible to define a mesh where each grain boundary is associated with a particular reduced foundation but this choice complicates the generation of the mesh if it has to be done manually. To avoid these difficulties, the technique implemented in the code consists in defining a single foundation which comprises all the possible foundation segments and to use the traditional contact search algorithm to find a subset of foundation segments associated to each individual contact element. The subset of possible foundation segments of each contact element comprises the foundation segment which directly faces the contact element in the initial configuration and its closest neighbours. The number of neighbours to register has been fixed to five in the

present application. This operation is realised only once during the pre-processing phase. During the simulation, the contact search algorithm only takes into account the particular subset of foundation segments that has been initially defined for each individual contact element.

3.5.2.5 Loss and recovering of contact

When tensile and compression loads alternate, the interface element may lose contact and recover it successively. In the present model, all the interface elements are supposed to be in contact at the start of the process, unless there is already a crack in the model. During the loading of the material, the interface elements stay in contact until the maximum damage threshold is reached, i.e. until the interface breaks. Once an interface element is cracked at one integration point, the damage variable associated to this integration point is no longer taken into account and the interface behaves like a classical contact element with a Coulomb's friction law.

As the damage can not be repaired even if a compression load is applied on the cracked interface element, the two solid elements forming both sides of the interface are considered as two independent bodies in contact as soon as the contact is lost and for the remaining of the simulation.

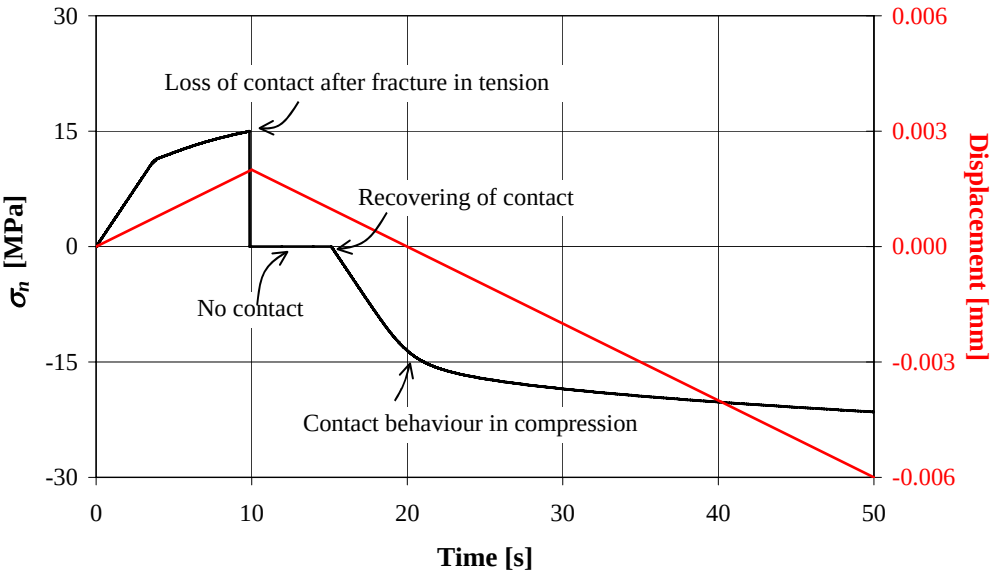

Figure 3.21. Verification of the behaviour of the interface element in case of loss and recovering of contact.

A simulation using two solid elements linked by one interface element has been carried out to verify the behaviour of the interface element when the contact is lost and recovered. The two solid elements have a size equal to 1 mm × 1 mm. A vertical displacement is imposed on the upper nodes of the top element and the vertical displacement of the lower nodes of the bottom element is restrained. The enforced displacement and the normal stress recorded in the interface during the simulation are shown in Figure 3.21. The model is first in tension: a positive displacement is imposed, which gives rise to a positive normal stress σ_n in the interface. During that phase, the interface is in contact but the damage and the thickness of the interface progressively increase. At $t \approx 10$ s, the damage threshold is reached and the interface breaks, the contact is lost and the normal stress in the interface is set back to zero. As the contact is lost, there is no load applied on the material and the two solid elements, which have been plastically deformed, are unloaded according to the elastic law. After that instant, the enforced displacement is reversed. At the beginning of this second phase, the two solid elements are still separated from each other by a distance linked to the thickness of the interface just before fracture and to the springback effect. Therefore, the contact is only recovered when the top element has been moved down to reach the bottom element. After that point, the model is in compression and the contact is regulated by the Coulomb's friction law; a negative normal stress is recorded in the interface, which corresponds to a positive contact pressure.

With this example, it has been proved that the code will manage properly situations of loss and recovering of contact, should they happen in the application simulations.

3.6 INITIAL SIMULATIONS AND VERIFICATION OF THE MODEL

To test the robustness of the new developments presented in this chapter, it is necessary to verify the numerical behaviour of the microstructural model, which comprises the elements and the constitutive laws presented in the preceding sections. The microstructural model is referred to as the mesoscopic cell and consists of grains, represented by 2D-solid elements with a modified Norton-Hoff constitutive law, and grain boundaries, represented by 1D-interface elements with a damage constitutive law, as described in section 3.4. Before studying actual grain microstructures, the model is tested using several simple structures.

As a first application of the model, the simple examples tested in this chapter allow the analysis of the stability of the LAGAMINE code during the propagation of a crack. They are also used to fix some parameters of the model such as the penalty coefficients k_s and k_n.

The first examples, which focus on the analysis of the damage law, are done using a purely elastic law in the zone representing the grains. Then the elastic-viscous-plastic law is substituted to the elastic law to model the actual behaviour of the grains. All these examples are useful to isolate and to solve the numerical problems relative to the intrinsic discontinuous behaviour of the model.

3.6.1 DESCRIPTION OF THE CELLS

The tested cells evolve from a simple case with only one grain boundary zone surrounded by a grain area through more complicated configurations to finally a structure which is relatively close to an actual grain microstructure. Every cell has the following dimensions: height $h = 2\,\text{mm}$ and width $w = 1\,\text{mm}$; these dimensions being chosen on the basis of the information known with regard to the grain size at the beginning of the project.

For each cell, the bold lines indicate the zone where interface elements have been introduced, i.e. the paths that the crack will have the possibility to follow. The convention to represent the boundary conditions are the following: the arrows represent enforced displacements whereas the lines ended by a stroke represent fixed nodes. The value of the displacement as a function of the time is chosen so that the correct order of magnitude is obtained for the strain rate in comparison to classical values known for continuous casting problems. This condition equates to an imposed displacement velocity of 2 10^{-3} mm s^{-1}, which corresponds to strain rates of the order of magnitude of 10^{-3} s^{-1} to 10^{-4} s^{-1} in the structure. The same displacements field is used for all the presented examples.

Figure 3.22 illustrates the different structures analysed introducing complexity along the analysis process. Structure 1 is the first structure that has been defined for the simulations. This structure has been used to make choices with regard to the modelling of the interface as described in point 3.5.2. Structure 2 is made of a single grain zone in which a middle crack can propagate up to the centre. Structure 3 has been created in order to analyse the effect of a change of orientation of the crack propagation path, while in structure 4, the objective is to analyse which path the model chooses among several possible propagation paths. Structure 5 is a transition case between the simple

cells and an actual microstructure case. Those meshes have been realised using the automatic mesh generator GMAILL. A higher density of elements is imposed along the interface zones in comparison with the inside of the grains. Using this method, the mesh is sufficiently well refined along grain boundaries while the total number of elements remains reasonable. More details about the utilisation of this programme to define the mesh of the mesoscopic cell are given in section 3.5.2.3.

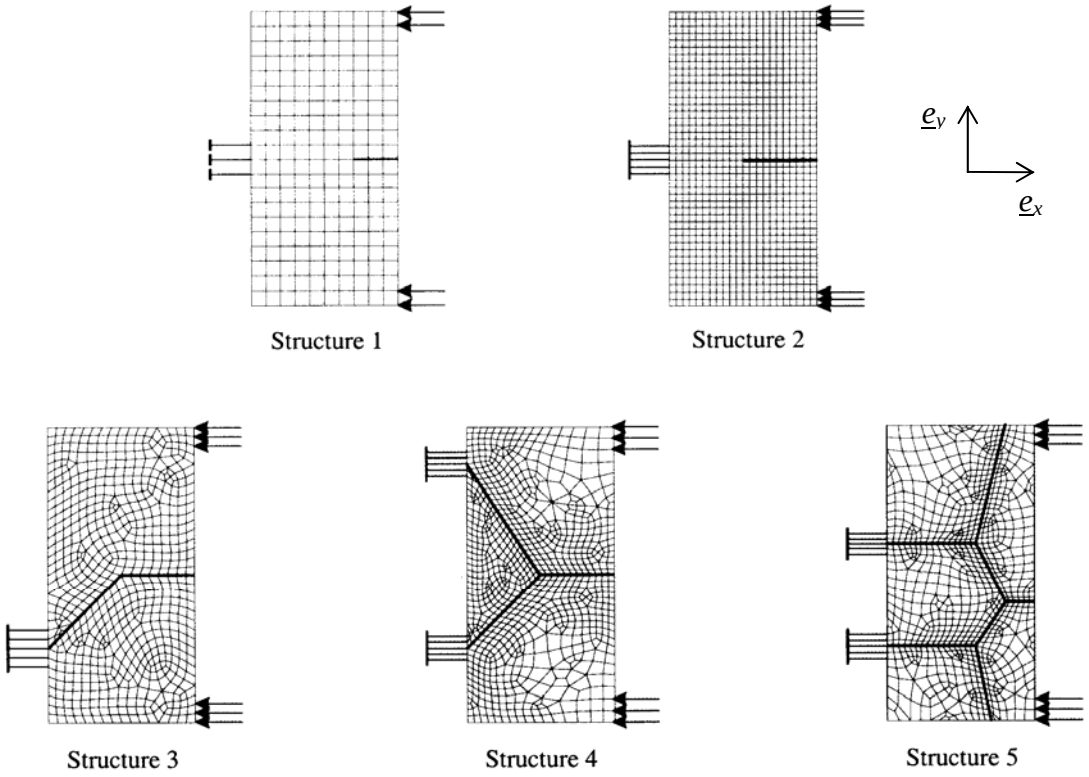

Figure 3.22. Simple mesoscopic cells.

3.6.2 CHOICE OF THE PARAMETERS OF THE MODEL

In all the examples discussed in this chapter, the thermal degrees of freedom have been fixed in order to concentrate only on the damage law at constant temperature. The temperature chosen for the simulations is 900°C and the thermal transfers with the environment and inside the cell are not considered.

Tables 3.2 and 3.3 indicate the values of the different parameters used for the purely elastic or elastic-viscous-plastic law used for the grains (Table 3.2) and for the damage law used for the grain boundaries (Table 3.3). The data used for the elastic-viscous-plastic law are identical to those used for the macroscopic continuous casting

simulations (Pascon 2003) while the damage law parameters are based on the data published by Onck and van der Giessen (1998, 1999). These data were presented in a non-dimensional form and have been scaled to be related to an average half grain boundary length of 0.01 mm.

Table 3.2. Parameters of the elastic-viscous-plastic grain law at 900 °C.

Parameter	Description	Value
E	Elastic Young's modulus	32400 MPa
ν	Poisson's ratio	0.3
p_1	Softening parameter (equation (3.1))	0.0
p_2	Curve level parameter (equation (3.1))	178.3 MPa
p_3	Viscosity parameter (equation (3.1))	0.112
p_4	Hardening parameter (equation (3.1))	0.217

Table 3.3. Parameters for the grain boundary damage law.

Parameter	Description	Value
d	Grain size (diameter)	$0.364\ 10^{-1}$ mm
n	Creep exponent	5.0
B	Creep coefficient	$0.474\ 10^{-11}$ MPa^{-n} s^{-1}
$\dot{\varepsilon}_e / \dot{\varepsilon}_B$	Grain viscosity parameter	10
F_n	Nucleation parameter	$0.169\ 10^{9}$ mm^{-2}
N_I	Cavity density for nucleation	127300 mm^{-2}
N_{max}	Maximum cavity density	1273000 mm^{-2}
Σ_0	Normalization stress	29.16 MPa
D	Diffusion parameter	$0.3429\ 10^{-17}$ mm^5 N^{-1} s^{-1}
ψ	Cavity angle	75°
a_0	Initial void size	$0.67\ 10^{-5}$ mm
b_0	Initial void spacing	$0.16\ 10^{-2}$ mm
d_{lim}	Damage threshold	0.7

The complete set of data relative to the specific material studied in the next chapters of this thesis was not available when the numerical model was being developed, which is the reason why the initial tests have been realised using data from the literature.

3.6.3 RESULTS

For each structure of Figure 3.22, the stress σ_y (stress in the *y*-direction, which is the stress in the vertical direction for these examples) or σ_m (mean stress) is represented. It is particularly interesting to represent the stress σ_y for structure 1 as it is the stress in the direction perpendicular to the crack, i.e. the stress which plays the most important role in the initiation and propagation of this crack. For non horizontal cracks, the stress σ_y does not have a direct physical signification any longer, that is why the mean stress σ_m is used for the last examples as it is still interesting to analyse how the stresses relax when the crack propagates. In all these examples, the numerical results in terms of stresses or strains are not important but the major objective is to analyse how the crack propagates for the different configurations using the interface element presented in section 3.4.2. These simulations are also used to resolve numerical problems and to start the analysis of certain parameters of the model using simple examples.

For simplicity reasons, the first developments and tests have been made using a linear elastic constitutive law inside the grains. Then, the elastic law has been replaced by the actual elastic-viscous-plastic law.

3.6.3.1 Elastic material law in the grain

Determination of the penalty coefficient using structure 2

The penalty coefficients k_s and k_n have a great influence on the results as they introduce a certain amount of loss of rigidity in the model. The higher these coefficients the smaller the influence, nevertheless too high values lead to convergence problems. It is then necessary to start by defining acceptable values for k_s and k_n, values that will be kept constant for all the further calibration, validation and exploitation simulations. To analyse the effect of k_s and k_n, simulations have been performed with different values of k_s and k_n compared among themselves and with a reference case where no interface element have been introduced (a), which corresponds to a case where $k_s = k_n = \infty$. Using these simulations, it is confirmed that when interface elements using a penalty method are introduced, it produces a zone of lower rigidity in the model. This effect is amplified if the penalty coefficients are lower and it is then necessary to take them as high as the convergence permits it to avoid perturbation of the results.

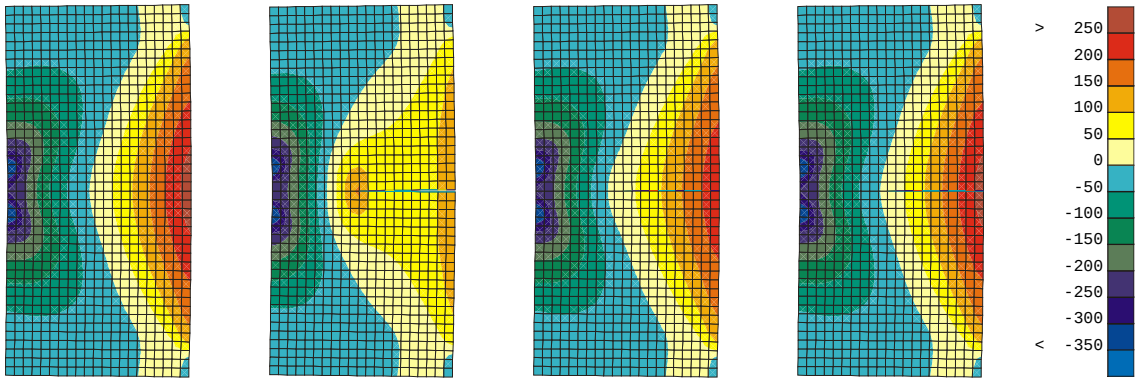

Figure 3.23. Stress results (σ_y) before the initiation of the crack, elastic case, a) without interface element, b) with interface elements $k_s = k_n$ = 10 000 MPa/mm, c) $k_s = k_n$ = 100 000 MPa/mm, d) $k_s = k_n$ = 1 000 000 MPa/mm.

Analysing results from Figure 3.23, it can be concluded that using $k_s = k_n$ = 10 000 MPa/mm (b) is clearly insufficient. Indeed, with these values, even before the initiation of the crack as predicted by the fracture criterion, the zone around the crack lips is already relaxed. The crack seems to be open but this effect is only due to a too small penalty effect. For the two other cases, ($k_s = k_n$ = 100 000 MPa/mm (c) and $k_s = k_n$ = 1 000 000 MPa/mm (d)), the results present similar patterns than for the reference case without interface elements (a).

A simulation up to crack propagation with $k_s = k_n$ = 1 000 000 MPa/mm did not give any results due to convergence problems, this is the reason why the higher values of k_s and k_n presented are for $k_s = k_n$ = 100 000 MPa/mm.

Crack propagation

Figure 3.24 illustrates the crack propagation in structure 2 for $k_s = k_n$ = 100 000 MPa/mm. For this value of the penalty coefficients, the comparison of the results with the reference case before crack initiation has shown that the perturbation introduced by the presence of interface elements was limited and therefore acceptable.

Crack propagation is detected in Figure 3.24 and it can be seen that the stresses decrease along the lips of the crack during the propagation phase. Only several stages of the propagation have been represented: initially there is no crack (Figure 3.24(a)), then four elements are de-bonded (Figure 3.24(b)), then eight elements are de-bonded (Figure 3.24(c)) and finally the crack has propagated along the whole available zone (Figure 3.24(d)). To improve convergence, it is necessary to let the system stabilise itself each time an integration point is detached. Therefore, too big time steps, which

would allow several integration points to detach at the same time, have to be avoided. In this example, the maximum time step was fixed at $t = 0.1$ s.

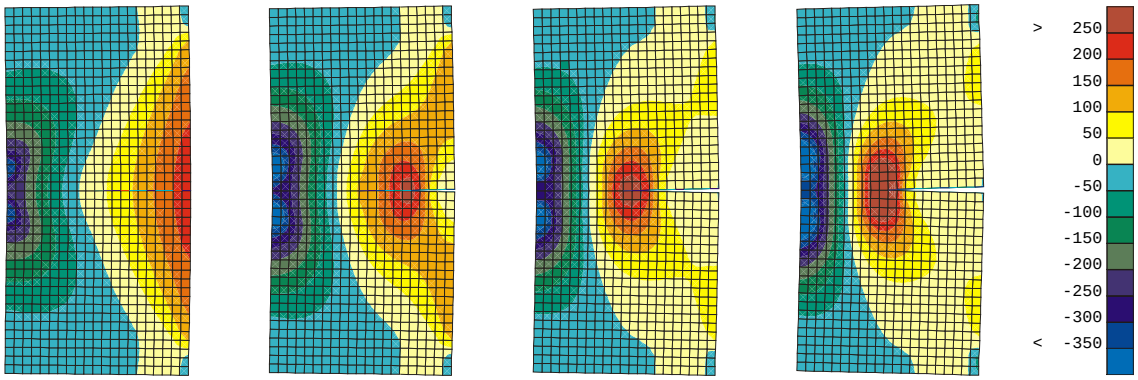

Figure 3.24. Stress results (σ_y) and crack propagation for structure 2.
Elastic case with $k_s = k_n = 100\,000$ MPa/mm.

3.6.3.2 Elastic-viscous-plastic law in the grain

When the elastic-viscous-plastic law is used in the zone representing the grains, the global rigidity of the structure is less than for the elastic case. The difference in the order of magnitude of the terms of the rigidity matrix can then be more important and it is then necessary to analyse the results of the reference simulations carefully before fixing definitively the values of the penalty coefficients.

Adaptation of the penalty coefficients for the elastic-viscous-plastic case

Like for the elastic case, it has been necessary to test different values of the penalty coefficients when an elastic-viscous-plastic law is used to model the grains and to compare the results with a reference case without interface elements. The first simulations have been realised with $k_n = k_s = 100\,000$ MPa/mm; no smaller values have been tested. Figure 3.25 shows that for all the values of k_n and k_s greater or equal to 100 000 MPa/mm, the results are in accordance with the reference case (a) with regard to the value of the stress σ_y before the crack initiation. To obtain the best results for the simulation, the penalty coefficients will have to be fixed at the maximum possible value for which the reference case can be reproduced but without introducing convergence difficulties.

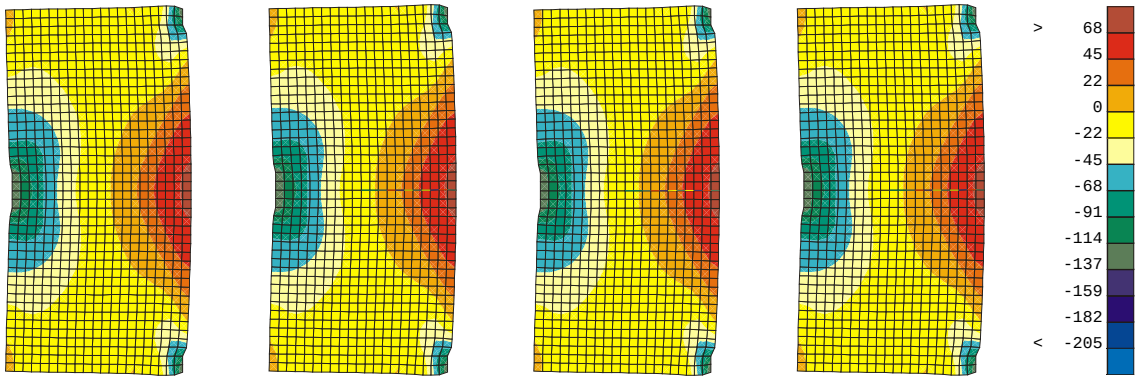

Figure 3.25. Stress results (σ_y) before the initiation of the crack, viscous-plastic case a) without interface element, b) with interface elements $k_s = k_n = 100\ 000$ MPa/mm, c) $k_s = k_n = 1\ 000\ 000$ MPa/mm, d) $k_s = k_n = 10\ 000\ 000$ MPa/mm.

Crack propagation

In this section, the crack propagation in structures 2 to 5 is analysed. The initial results on structure 2 have shown that a value of $k_s = k_n = 100\ 000$ MPa/mm for the penalty coefficients is adequate with regard to the pre-crack behaviour in comparison with the reference case (Figure 3.25(b)) and first tests have shown that convergence is smooth with this value when the crack propagates.

Figure 3.26 shows the crack propagation for structure 2 with $k_s = k_n = 100\ 000$ MPa/mm. The crack propagation path is detected both by the physical opening within the mesh but also by the stress concentration zone around the crack tip.

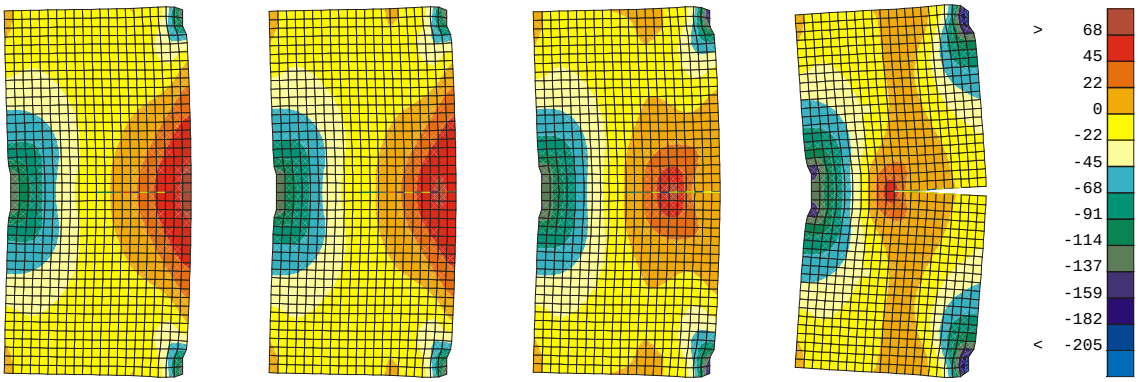

Figure 3.26. Stress results (σ_y) and crack propagation for structure 2. Viscous-plastic case with $k_s = k_n = 100\ 000$ MPa/mm.

Figure 3.27 illustrates the case of structure 3 where a change in the crack orientation is imposed. With the elastic-viscous-plastic law, it is proved that the change of direction in the crack path is well managed by the finite element code. The crack continues to propagates after the bifurcation without any convergence problem for k_s = k_n = 100 000 MPa/mm.

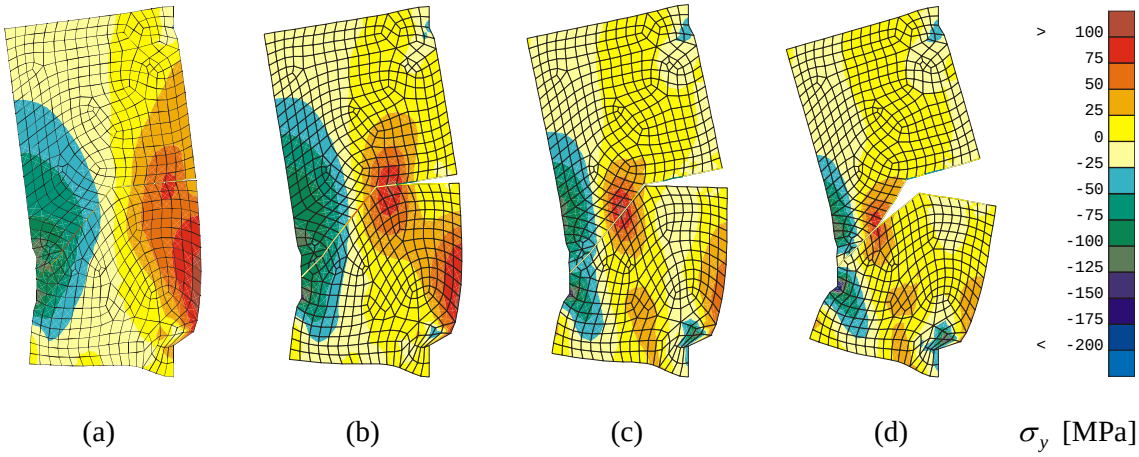

Figure 3.27. Stress results (σ_y) and crack propagation for structure 3.
Viscous-plastic case with $k_s = k_n$ = 100 000 MPa/mm.

For structures 4 and 5, several crack propagation paths are possible and the crack has to choose in which direction it will grow first, which adds another complication to the model. Figure 3.28 and Figure 3.29 show the crack propagation only and not the crack initiation as the interest of these cases is to show how the model deals with the modelling of a crack path passing through the intersection of three grains.

Figure 3.28 illustrates the crack propagation in structure 4, in chronological order from stage (a) to (h). The passage of the triple point does not present any particular difficulties regarding convergence. After the intersection point, the crack starts to propagate towards the bottom of the cell, in the direction which corresponds to the smallest change of direction of the crack compared to the initial horizontal propagation path (Figure 3.28(e)). As the external load is along the horizontal direction, the bottom leg of the possible crack path, which is closer to the horizontal than the top leg of the path, also corresponds to the side where the normal stress is the highest. After that, the crack continues to propagate both in the lower and upper side of the predefined possible path. At each step, the zone of stress concentration at the crack tip is well marked.

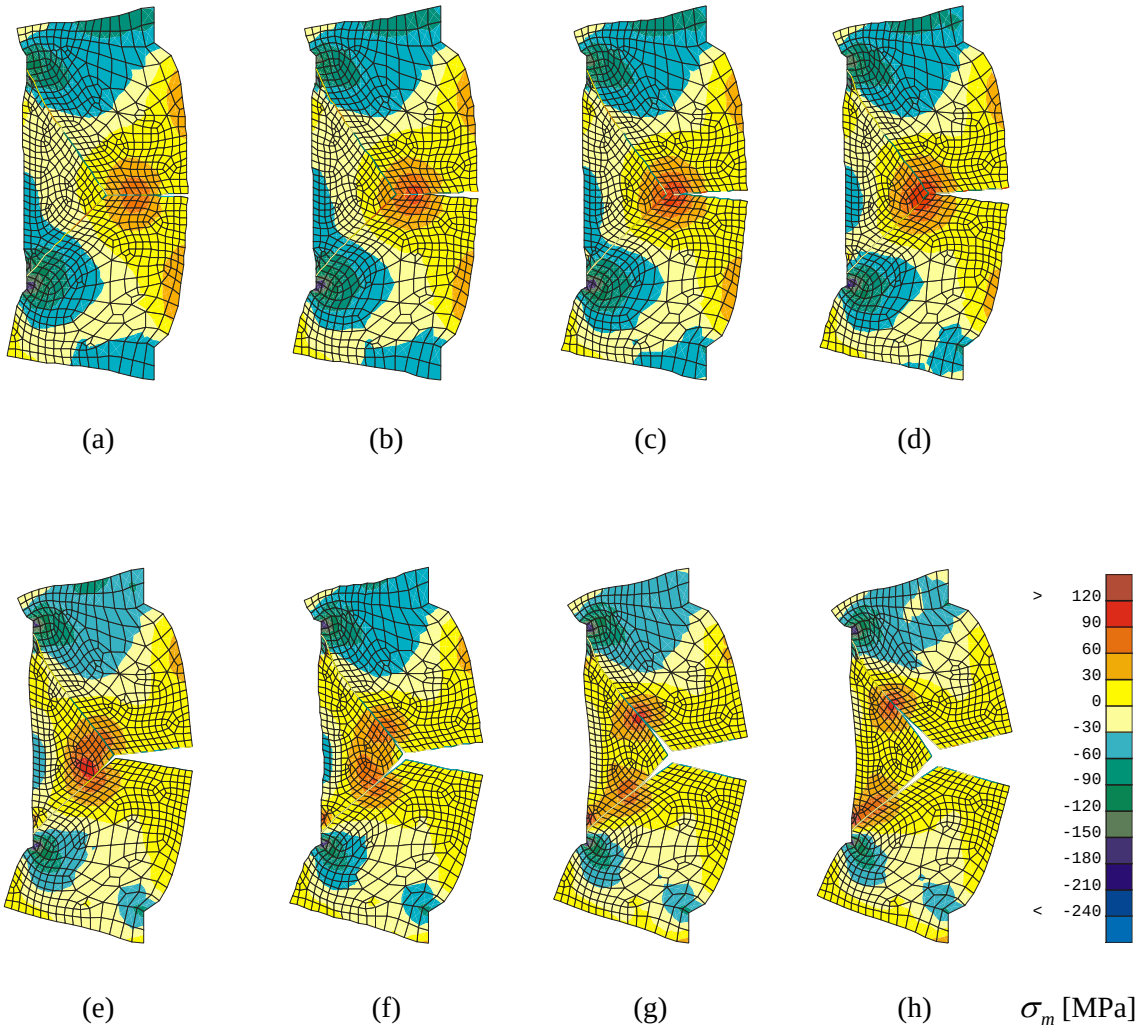

Figure 3.28. Stress results (σ_m) and crack propagation for structure 4.
Viscous-plastic case with $k_s = k_n$ = 100 000 MPa/mm.

Figure 3.29 illustrates cracks propagation in structure 5 which contains five grains. The stages are represented at constant intervals in chronological order from (a) to (n). Like in the previous simulations, the model shows that the stresses around the crack lips decrease when the crack propagates.

Through this example, it has been demonstrated that the cracks propagate along all the possible paths without showing any convergence difficulties with the proposed set of parameters. Shear between grains before de-bonding has also been detected in this example and in particular between the two lower grains at stages (g) and (h). At the end of the simulation, several independent cracks have appeared and progressed within the cell.

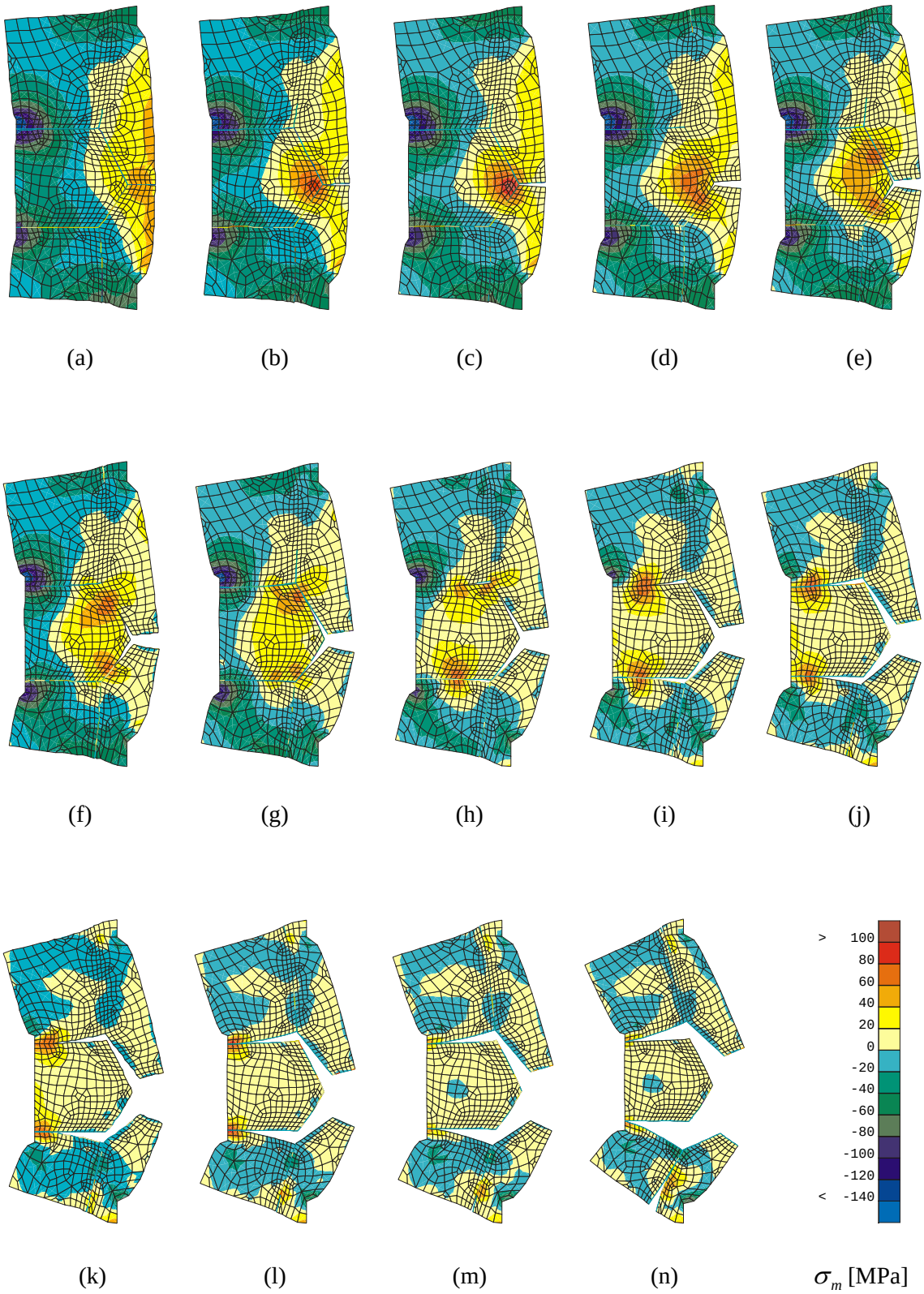

Figure 3.29. Stress results (σ_m) and crack propagation for structure 5.
Viscous-plastic case with $k_s = k_n = 100\,000$ MPa/mm.

Although the number of grains has been increased, none of them are totally free; either one of the nodes of the grain boundary is fixed or displacements are enforced on some of the grain boundary nodes. When actual microstructure will be modelled, some of the internal grains will only be linked to the rest of the structure through the bond made via interface elements.

The de-bonding technique, which has been applied to grains and grain boundaries in this section, is general and could be applied to other types of structures where possible paths for the crack growth are initially known. Different damage constitutive laws could also be associated with the interface without influencing the numerical implementation of the de-bonding mechanism. For example, the interface element developed in this thesis has been used in a research project studying fatigue cracks in welded beam-to-column connections (Lequesne *et al.* 2005). In this project, a cohesive zone law described crack propagation by analysing damage micro-phenomena behind the crack tip and the energy released during the creation of new surfaces.

3.6.3.3 Influence of the penalty coefficients on the crack propagation

The choice of the penalty coefficients is a critical step which has to be resolved before calibrating all the other damage parameters as it may influence the results. In Figure 3.30, the propagation of the crack is shown in structure 3 for two values of the penalty coefficients at two distinct instants.

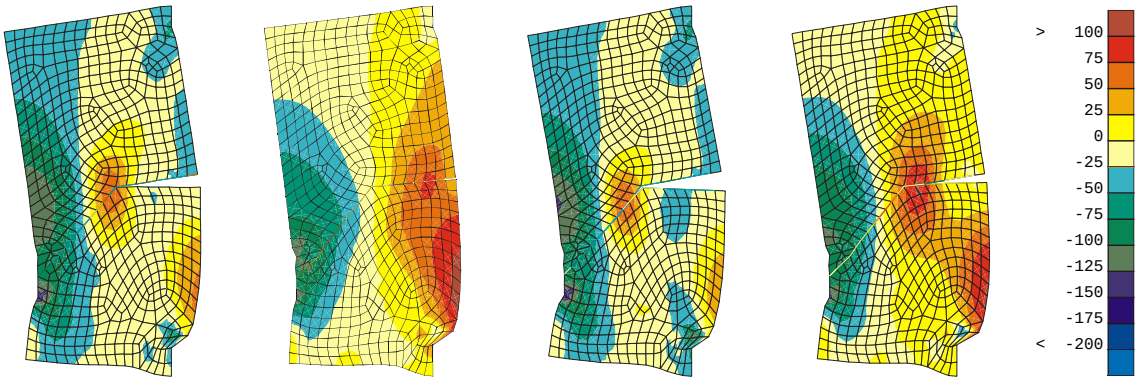

Figure 3.30. Stress results (σ_y) and crack propagation for structure 3. Viscous-plastic case with $t_1 = 100$ s, $t_2 = 120$ s, $k_1 = k_s = k_n = 10\,000$ MPa/mm and $k_2 = k_s = k_n = 100\,000$ MPa/mm.

It can be seen that for a higher value of the penalty coefficients, the crack progresses more slowly. This behaviour can be explained by the higher parasite deformations introduced locally in the model when lower penalty coefficients are used.

As mentioned earlier, the penalty coefficients have to be as high as possible to avoid perturbations in the solutions compared to a case without interfaces but stay small enough to allow a smooth convergence of the simulation. Experience and best practice rules have shown that in most problems $k_s = k_n$ = 100 000 MPa/mm is a suitable value. Once this value has been fixed, it has to stay constant for all the calibration and application simulations using a defined set of damage parameters.

3.7 MACRO-MESO DATA TRANSFER

It is necessary to define a methodology for the linkage between the macroscopic and mesoscopic simulations which allows the user to collect data issued from the macroscopic model and to transfer them to the mesoscopic mesh. In practice, stress and strain fields extracted from the macroscopic simulations are transformed in forces and/or displacements to be applied on the edges of the mesoscopic cell.

Unlike the stresses and strains, which are calculated at the integration points of the finite elements and are function of the material laws specifically defined at the mesoscopic level, the temperatures can be directly applied on the nodes of the mesoscopic cell. If necessary, temperature gradients from the macroscopic model can be reproduced by interpolation between the nodes at the mesoscopic scale whereas the temporal variation of the temperature field is directly modelled via an imposed external temperature data file. The degrees of freedom corresponding to the temperatures are fixed at each time step and thermal exchanges have not to be calculated during the modelling at the mesoscopic scale as they have already been taken into account during the modelling at the macroscopic scale. Using this technique, it is possible to simplify the calculations and to avoid the difficulties encountered for fully-coupled or semi-coupled staggered thermomechanical analysis. Only the thermal dilatations are taken into account via the thermal strain ε_{th} which was included in the thermo-mechanical model when implementing the modified Norton-Hoff law (Pascon *et al.* 2006). The temperature field is then used to calculate the thermal strain ε_{th} and to define the proper set of parameters to be used for the analysis as they are function of the temperature.

Whatever the data to be transferred (temperatures, forces, displacements, strains or stresses), it is important to reproduce accurately the evolution of these fields in

function of the time as the constitutive laws used are non-reversible and strain rate dependant. In the illustration examples presented in this chapter, the loads are applied in a radial way for simplicity reasons. Nevertheless, for the actual continuous casting simulations, the real history of stresses, strains and temperatures will have to be followed.

3.7.1 FROM THE SLAB TO THE MESOSCOPIC CELL

The axes system used in this work has been chosen to be consistent with the macroscopic continuous casting model from which the macroscopic data will be extracted (Pascon 2003): the *x*-axis is parallel to the width of the slab, the *y*-axis is in the direction of the thickness of the slab and the *z*-axis corresponds to the casting direction as represented in Figure 3.31.

For the macroscopic case, a slice model is developed in the plane $x-y$ (type 1 section). The strains in the *z*-direction are modelled using the generalized plane state. As the slice moves in the continuous machine at a predefined velocity, it is possible to reconstitute a complete 3D solution, giving the total history of stresses, strains, strain rates and temperatures in the slab. In the mesoscopic model, slices in the $x-z$ plane (type 2 section) or in the $y-z$ plane (type 3 section) are of particular interest as they allow the study of the effect of oscillation marks, which is not the case for the macroscopic model where the studied slice is parallel to the oscillation marks.

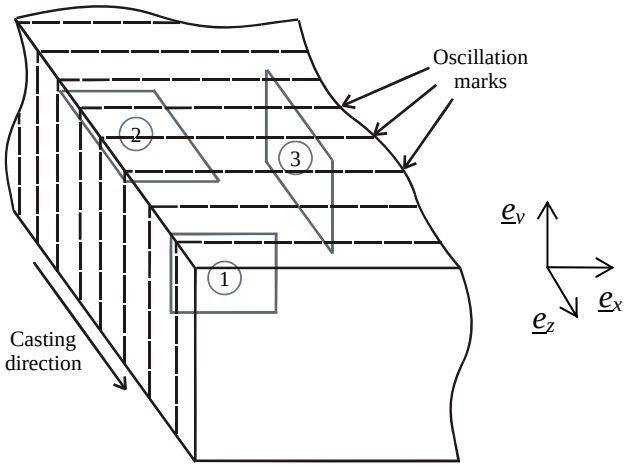

Figure 3.31. Part of slab: studied sections.

Using a generalized plane state approach at the mesoscopic scale, it is possible to impose the appropriate loading fields on the representative cell but particular attention must be paid to the definition of the axes.

3.7.2 COMPARISON OF RESULTS WITH OR WITHOUT INTERFACE ELEMENTS

Test have been realised on a simple homogeneous mesh and hexagonal mesh with or without interface elements. Theses meshes are represented in Figure 3.32. The bold lines within the cell represent grain boundaries. Interface elements, i.e. contact elements and associated foundations, are defined along these lines in case of modelling with interface elements. Each cell has a dimension of 15 mm × 15 mm, which corresponds to a grain diameter of the order of 3 mm for the hexagonal mesh. The objective is to analyse the accuracy of the data transfer and the impact of the interface elements on the global behaviour.

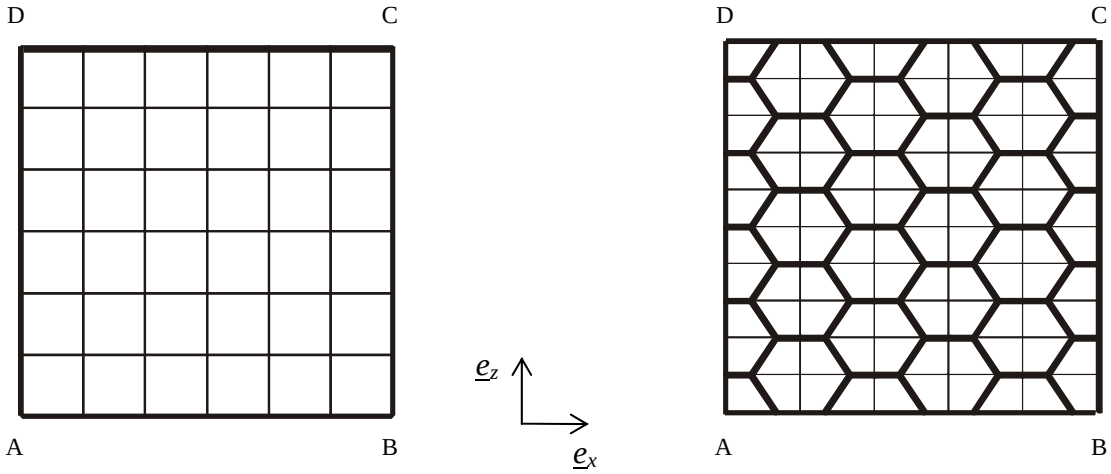

(a) (b)

Figure 3.32. a) Homogeneous mesh, b) hexagonal mesh.

3.7.2.1 Displacements driven simulations

For this example, the applied strain field is constant on the cell but variable with time. It is given by $\varepsilon_x = 10^{-3}t$, $\varepsilon_z = 10^{-3}t$ and $\gamma_{xz} = 0$, where t is the time. If small displacements are considered, the compatibility equations (3.53) can be used to compute the displacements field directly from the strains field:

$$\varepsilon_x = \frac{\partial u}{\partial x}$$
$$\varepsilon_z = \frac{\partial w}{\partial z} \qquad (3.53)$$
$$\gamma_{xz} = \frac{\partial u}{\partial z} + \frac{\partial w}{\partial x}$$

The displacements to be applied along the edges of the cell obtained by integration of equations (3.53) are $u = 10^{-3} t\, x$ along the *x*-axis and $w = 10^{-3} t\, z$ along the *z*-axis. A radial loading history is imposed. Displacements are applied on the four edges of the cell (Figure 3.33).

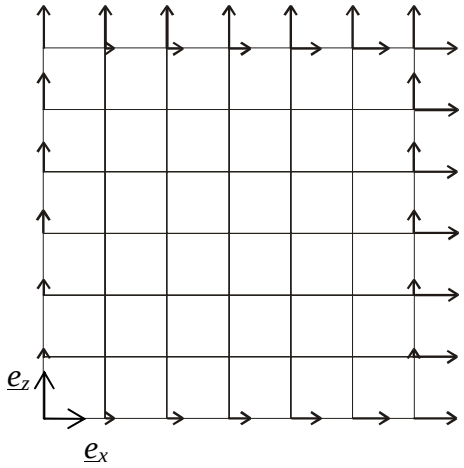

Figure 3.33. Illustration of the displacements imposed on the structure.

As the displacements are enforced, the first verification aims at checking the stress level for the different meshes. Table 3.4 presents the results at $t = 2$ s.

Table 3.4. Comparison of σ_x, σ_z, ε_e et $\dot{\varepsilon}_e$ for the three meshes at $t = 2$ s.

Mesh type	σ_x **[MPa]**	σ_z **[MPa]**	ε_e	$\dot{\varepsilon}_e$ **[s^{-1}]**
Homogeneous mesh without interface elements	120	120	$0.2\ 10^{-2}$	$0.67\ 10^{-3}$
Hexagonal mesh without interface elements	120	120	$0.2\ 10^{-2}$	$0.67\ 10^{-3}$
Hexagonal mesh with interface elements	103	102	$0.18\ 10^{-2}$	$0.57\ 10^{-3}$

For the meshes without interface elements, the stresses are strictly constant in the cell and vary only with time. For the mesh with interface elements, the stresses present small variations over the cell and the value given in Table 3.4 corresponds to a point localised in the middle of the mesh. A reduction in the stress level of 15% is measured for the case with interface elements compared to the case without interface elements. This phenomenon appears despite the fact that the same penalty coefficients

(k_n = k_s = 100 000 MPa/mm) as those defined in section 3.6.3.2 for the elastic-viscous-plastic case to limit the perturbation of the stress field due to the presence of interface elements in the mesh, have been used. The proportion between interface elements and solid elements is higher in the present case than for the simple structures of section 3.6.1, which can explain the variation in the stress level encountered here, the mesh being less rigid due the large amount of interface elements. Looking at the differences observed on the strains and strain rates, it is also concluded that part of the deformation is concentrated in the interface elements, which implies that the corresponding point on the ($\sigma - \varepsilon$) curve for the solid elements in the middle of the mesh is different. Likewise, the strain rate is also smaller, which corresponds to another ($\sigma - \varepsilon$) curve (see also Figure 3.6).

3.7.2.2 Forces driven simulations

The following total forces are applied uniformly on the edges of the cell: $F_x = 150t$ N on BC and $F_z = 150t$ N on CD, where t is the time. No vertical displacements are allowed on AB while no horizontal displacements are allowed on AD (see Figure 3.34).

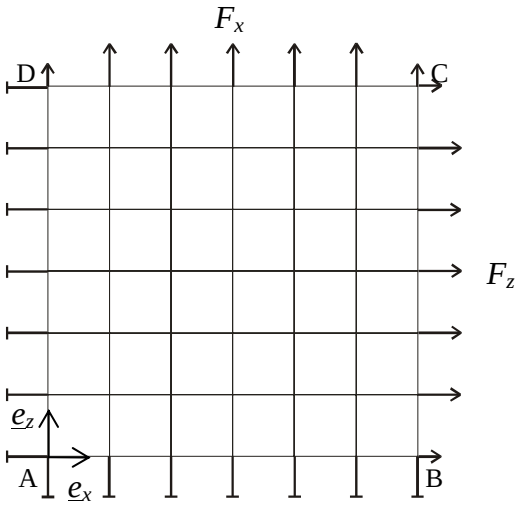

Figure 3.34. Illustration of the forces imposed on the structure.

Table 3.5 compares the results for $t = 10$ s for nodes localised in the middle of the edges BC and CD. The results of Table 3.5 show that for forces driven simulations, the displacements at the edges of the cell are almost 15% higher when interface elements are introduced in the model compared to the case without interface element. Like for the displacements driven simulations, the structure is less rigid due to the presence of interface elements associated with a penalty method.

Table 3.5. Comparison of the displacements along the *x*- and *z*-axes for the three meshes at $t = 10$ s.

Mesh type	Node (15, 7.5)		Node (7.5,15)	
	x **[mm]**	***z*** **[mm]**	***x*** **[mm]**	***z*** **[mm]**
Homogeneous mesh without interface elements	0.025	0.013	0.013	0.025
Hexagonal mesh without interface elements	0.025	0.013	0.013	0.025
Hexagonal mesh with interface elements	0.029	0.015	0.015	0.030

For one element at the centre of the mesh, results in terms of stresses and deformations are equal for the three meshes: $\sigma_x = \sigma_z = 100$ MPa, $\varepsilon_{eq} = 0.16\ 10^{-2}$ and $\dot{\varepsilon}_{eq} = 0.12\ 10^{-3}\ \mathrm{s}^{-1}$. The differences on the displacements for the elements at the boundaries do not have any influence on these variables. It can be verified that by choosing an adequate value for the force increment as a function of the time, it was possible to impose a strain rate of the right order of magnitude compared to the range usually found in continuous casting applications.

3.7.2.3 Summary

The previous analyses have shown that the use of interface elements introduces perturbations on the level of stresses and strains in the solid elements of the structure, even when no crack has appeared. This effect, which is due to the lower stiffness of the interface elements compared to the solid elements, is inevitable and is a function of the value of the penalty coefficients. Limiting the proportion of interface element compared to the solid element also reduced the impact.

The differences are present on both the stresses and strains for a displacements driven simulation, while for a forces driven simulation, only the displacements along the edges of the cell are significantly influenced.

3.7.3 TRANSITION ZONE

By analysing the results of the simulations of section 3.7.2 it has been highlighted that boundary effects appear when forces or displacements are imposed on the edges of the cell. The objective of this section is to analyse these phenomena and to define best practice rules for the definition of the boundary conditions. In particular, the necessity to introduce a transition zone is verified.

3.7.3.1 Cell without transition zone

The first example analyses the boundary effects on a cell without transition zone where forces drive the simulations. A distributed force is applied in the *z*-direction and varies linearly along *x*.

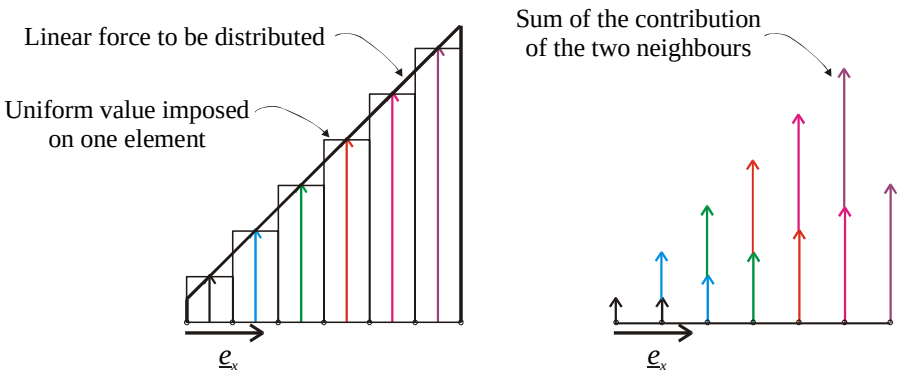

Figure 3.35. Distributed forces in the *z*-direction.

To compute the concentrate force to be applied on each node of a first degree element when a distributed force has to be modelled, the value at the middle of the element is first defined, as shown in Figure 3.35 for the particular case of a linear distributed force. Then, this value is multiplied by the length of the element and one half of the total load is applied on each node of the element. Apart from the nodes at the edges of the structure, each node receives the contribution of its two neighbour elements.

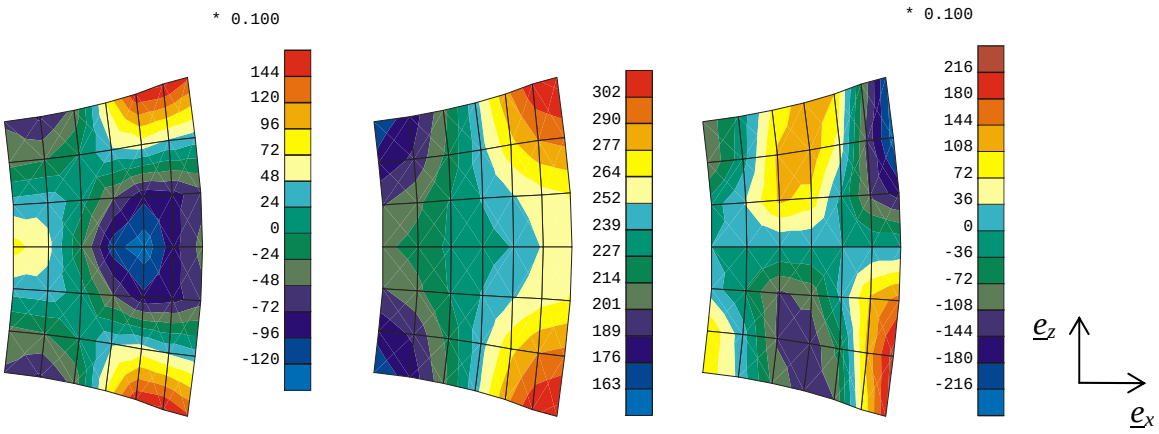

(a) σ_x [MPa] (b) σ_z [MPa] (c) τ_{xz} [MPa]

Figure 3.36. Stress state in a cell without transition zone for a forces driven simulation.

For the example presented in Figure 3.36, a total load of $210t$ N, where t is the time, has been applied. The forces are applied using a radial distribution. Figure 3.36 corresponds to the instant $t = 5$ s.

It can be noticed that for a case of linear loads, important perturbations appear along the boundaries of the cell, close to the nodes where the forces are applied. The stress field that was supposed to be modelled is not accurately reproduced throughout the cell. As this effect is less important for displacements driven simulations (see Figure 3.40(a)), one hypothesis is that the perturbations can be due to the fact that the method to distribute the forces on the individual nodes is not adequate because the simulation corresponds to a case of large displacements.

3.7.3.2 Cell with transition zone

To limit the problems encountered in the previous section relative to the perturbations of the stress field along the boundaries, a transition zone has been added to the model. The boundary conditions (forces or displacements) are applied along the edges of this transition zone, which reduces the boundary effect on the cell itself.

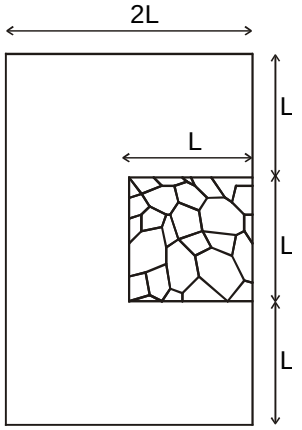

Figure 3.37. Representative cell with a transition zone.

For the following simulations, the representative cell is surrounded by a transition zone whose size is calculated as represented in Figure 3.37. Each zone is meshed independently in order to facilitate the imposition of adequate mesh densities within the different part of the structure. The same number of divisions is imposed on the boundaries of each zone to allow the connection of the different meshes. If the mesh for the representative cell contains x elements, the numbering of the nodes for the transition zone will start at $x+1$. A technique using 'duplicata' nodes is then used to

realise the bonding between the two meshes, i.e. that the two nodes that are localized at the same geometrical position will be allocated the same degree of freedom numbers within the global finite element vector of unknowns, although the nodes numbers are different. During the finite element calculation, the displacements associated to the two nodes will be identical, i.e. that from the finite element point of view the two nodes are considered as a single one.

For testing purpose, the simulations have been initially realised using a structured mesh without interface elements. Then a mesh with interface elements has been created. In order to be as close as possible to realistic case studies, a grain structure based on an actual steel microstructure has been modelled.

Structured mesh without interface elements

The cell of Figure 3.36 has been surrounded by a transition zone as defined by Figure 3.37. The same loading case has been applied as in section 3.7.3.1, i.e. a linear distributed force. The total load is $780t$ N, where t is the time. Figure 3.38 corresponds to the instant $t = 5$ s.

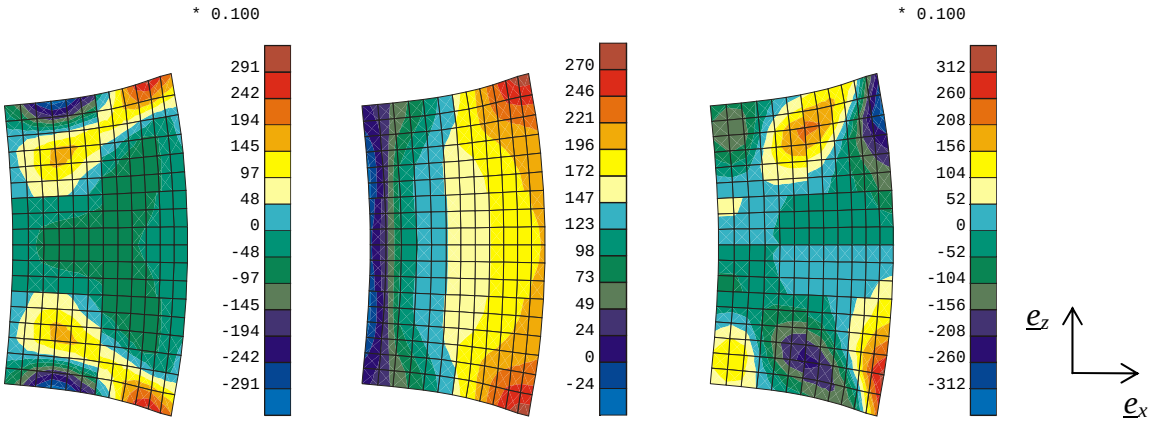

(a) σ_x [MPa] (b) σ_z [MPa] (c) τ_{xz} [MPa]

Figure 3.38. Forces driven simulation on an homogeneous cell with transition zone.

The results obtained with the transition zone show a better accuracy than those obtained without the transition zone. Perturbations are still present around the edges but the imposed stress field is well represented in the middle of structure where the representative cell is located. However, the evolution of the stress σ_z is not strictly linear. This is due to the fact that the calculations of the distribution of the forces have been done using the hypothesis of small deformations but the example of Figure 3.38 is

actually in large deformations. Given the levels reached, the stresses σ_x and τ_{xz} are considered to be equal to zero as required in the zone corresponding to the representative cell.

Realistic mesh with interface elements

Initially, a linear displacements distribution has been applied to the structure as shown in Figure 3.39. In this case the objective was not to apply a given strain field but to produce conditions favourable to crack initiation and propagation for testing purpose. The value of the enforced displacement is $w = \pm 10^{-3} t\, x$, where w is the displacement along the *z*-axis, *t* the time and *x* the coordinate in the horizontal direction. The $\pm$ sign is used to differentiate between the upper $(+)$ and lower $(-)$ edge of the structure. The loading history is radial, i.e. that the displacements field is applied following constant displacement rate. The horizontal displacements are free. One single node is fixed horizontally (middle node of left vertical edge) to avoid rigid body motion.

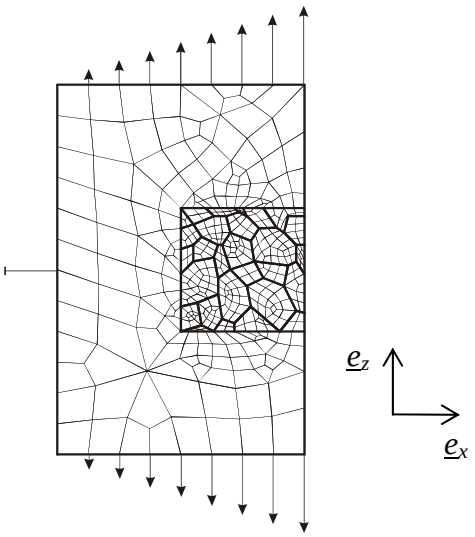

Figure 3.39. Mesh and enforced displacements for a realistic representative cell surrounded by a transition zone.

The results of the simulation are shown in Figure 3.40, which represents the stress σ_z at different times between $t = 45$ s and $t = 70$ s. An automatic strategy is used for the choice of the time step with a maximum step $\Delta t = 1\, s$. The time step is then updated automatically during the simulation to optimize the convergence. The automatic procedure for the choice of time step checks the number of successive iterations before convergence and updates the time step by dividing or multiplying it according to the input parameters provided by the user (maximum and minimum time

step, maximum number of iterations in one step before reducing the time step, number of successive converged iterations without reducing the step before increasing the time step, number by which the time step has to be divided in case of non convergence). In this specific example, it can be noticed that the time step is automatically reduced when a major change appears in the simulation, e.g. when a new crack initiates or when several integration points reach the fracture threshold at the time. These events introduce perturbations in the simulation and the use of smaller time steps usually improves the convergence. When the perturbation has been handled, the step size increases usually automatically. In the example of Figure 3.40, the total number of steps for the simulation (whose total duration is $70\,\mathrm{s}$) is 500 steps, i.e an average step $\Delta t = 0.14\,\mathrm{s}$.

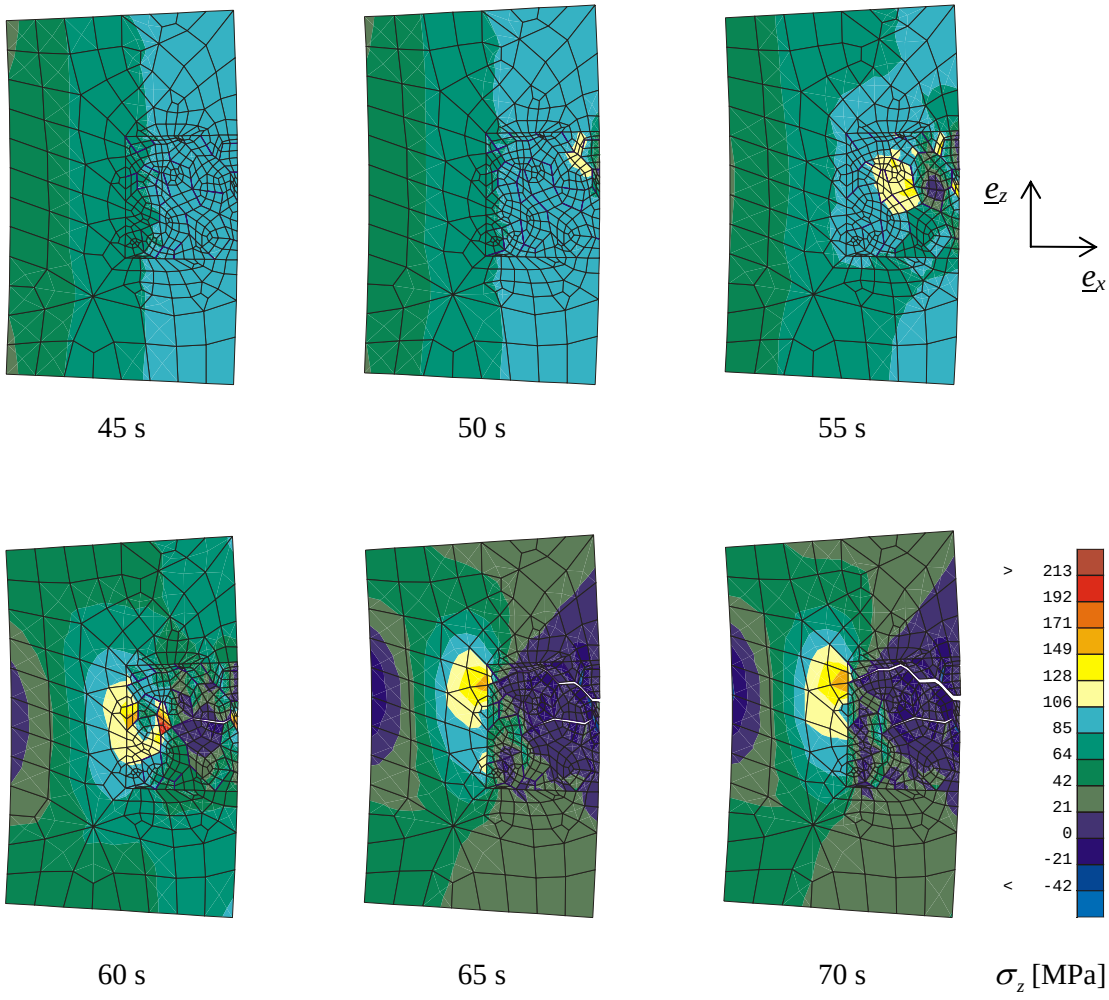

Figure 3.40. Crack initiation in a cell with transition zone for a displacements driven simulation.

The analysis of Figure 3.40 shows that several cracks initiate successively in the structure. Before the crack initiates, at $t = 45$ s, it can be checked that the stress distribution in the mesh is consistent with the applied load, i.e. close to a constant along *z* and presenting a linear variation along *x*. The small deviation from linearity is due to the fact that large deformations are imposed and that a non-linear constitutive law is used. At $t = 50$ s, a first crack initiates along a grain boundary that is perpendicular to the direction of the maximum principal stress. At $t = 55$ s, a second crack has appeared as shown by the zero stress zone in the figure. The propagation of the two cracks can be followed on from *t* = 55 s to *t* = 70s. The stresses concentrate around the crack tip and decrease on the border of the crack. The size of the mesoscopic cell was initially chosen to analyse the initiation of the cracks. To analyse properly the propagation phase, a larger cell would be necessary. Indeed, in the present case, perturbations in the stress levels appear at the junction between the representative cell and surrounding zone when cracks are propagating. This is due to the fact that no propagation is allowed in the transition zone, which does not contain any interface elements by definition. Nevertheless, this example proves the stability of the code when interface elements are de-bonding and constitutes a first demonstration of the ability of the code to handle crack initiation and propagation.

Figure 3.41 corresponds to a forces driven simulation. For initial testing purpose, the objective is to apply a distributed force in the *z*-direction that varies linearly along *x*. In this example, it can be seen that the deformations have to reach a relatively high value before leading to crack initiation.

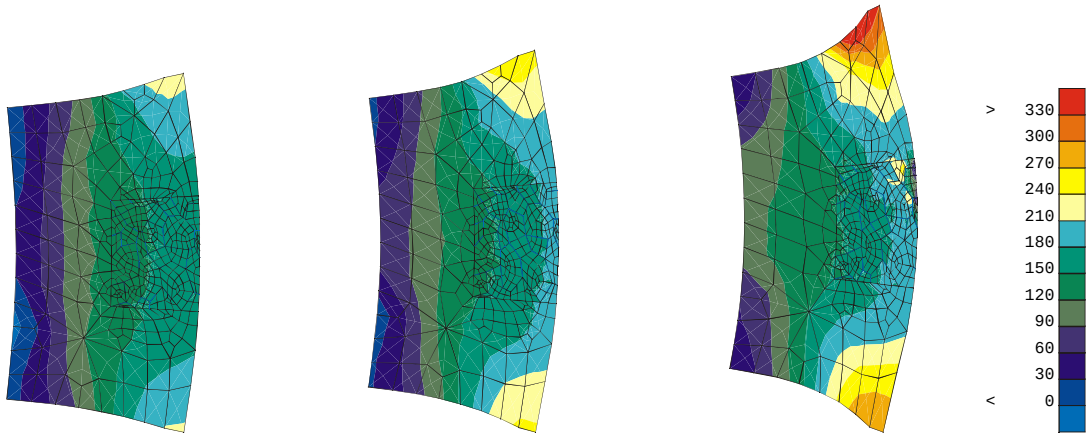

Figure 3.41. Crack initiation in a cell with transition zone for a forces driven simulation.

The conditions in terms of stresses and strains are totally different than those modelled in Figure 3.40. The objective was not to reproduce the same loading history in both cases but just to apply a linear load that leads to stresses and strain rates in a range corresponding to a continuous casting application. As for the previous model, the deviations from the linear case are due to the fact that a non-linear constitutive law is used and that large deformations, for which no corrections have been made with regard to the forces distribution in this demonstration example, occur.

Crack initiation is detected at time $t = 70$ s in Figure 3.41 but after that event, the simulation presents convergence difficulties and it is not possible to proceed further. The calculation is less stable for forces driven simulations that for displacements driven simulations because the perturbation introduced after one integration point has disconnected from its foundation is not restrained by the imposed geometry. Therefore, it can be concluded than crack initiation can be analysed by force driven simulations but that it is better to used displacements driven simulations whenever possible because they have better convergence properties, especially when the crack propagation path has to be followed.

Other advantages of the transition zone

The necessity to use a transition zone has been confirmed through the previous examples. Indeed, the transition zone eliminates the boundary effect and assures that the correct stress, strain and strain rates fields are reproduce inside the representative cell. Another advantage is that when the displacements and forces to be applied to the edges of the transition zone have been defined to reproduce the desired loading fields, it is possible to place another representative cell inside the model without having to redefine the boundary conditions. This allows to run comparative simulations with different representative cells easily.

If the external nodes of the transition zone match nodes of the macroscopic simulation, it is possible to transfer the displacements or forces directly from the macroscopic model to the mesoscopic model without having to recalculate the stresses and strains. This approach, which is illustrated in Figure 2.7(a), has been used by Kiss and Dunai (2002). It can be useful if the size of the zones to be studied mesoscopically is large enough compared to the size of the mesoscopic model and if the surface of the cell where the crack initiates is free.

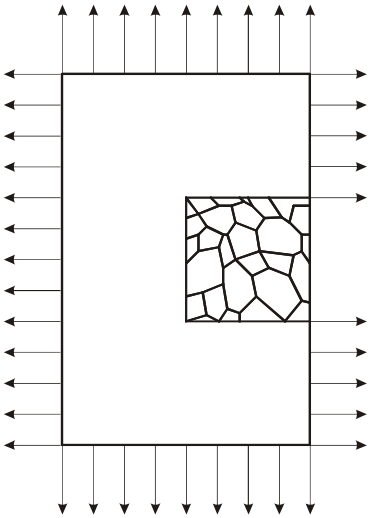

Figure 3.42. Example of enforced displacements on a cell with transition zone.

For the crack to propagate, it is necessary to leave the edge of the mesoscopic cell free of any enforced displacements, otherwise the movements are limited and the crack does not open itself. The transition zone allows to reproduce the displacements of the edge of the slab just above and underneath the representative cell as shown in Figure 3.42. Then, the free edge of the representative cell follows the general movement of the slab.

3.8 SUMMARY AND CONCLUSIONS

This chapter has focused on the presentation of the mesoscopic finite element model which comprises solid and interface elements. The solid elements are associated with a modified Norton-Hoff constitutive law that describes the elastic-viscous-plastic material behaviour at elevated temperature. This law is used for the modelling of the material inside the grains and also as the macroscopic constitutive law for the parent simulations. The interface elements are used for the modelling of the damage at the grain boundaries, they are associated with a damage law that includes grain boundary sliding and voids nucleation, growth and coalescence by diffusion and creep deformations.

Preliminary simulations have been performed on simple representative cells to study and validate the mesoscopic model. The penalty coefficients k_s and k_n have been defined so that the softer zone introduced in the finite element mesh due to the presence of interface elements does not influence the results before damage occurs. It has been

shown that this condition is respected for $k_s = k_n$ = 100 000 MPa/mm and that these values lead to good convergence properties.

It has been demonstrated through simulations with a mesh representing real grains that it is possible to follow the initiation and propagation of cracks with the approach developed. Generally, displacements driven simulations give better stability in terms of convergence and crack propagation than forces driven simulations. Finally, the necessity to introduce a transition zone for the transfer of data between the macroscopic and mesoscopic models has been highlighted.

Chapter 4

Identification of the material parameters

4.1 DESCRIPTION OF THE PARAMETERS IDENTIFICATION METHOD

The elaboration of the model and the definition of the material parameters require microscopic, macroscopic and damage experiments. The experimental program is summarized in Figure 4.1, which also defines the relations between the experimental analyses and the numerical developments.

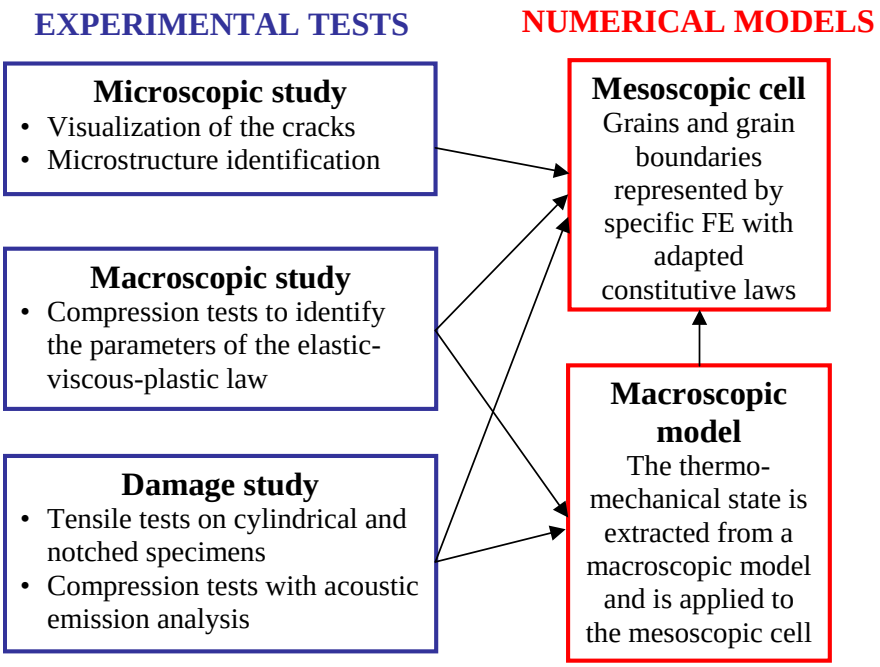

Figure 4.1. Links between the experimental and numerical studies.

The microscopic study comprises metallographical analyses which are used to visualize existing cracks on a rejected industrial product and to establish the microstructure of the material to be modelled. The determination of the actual size and shape of the grains is an essential step towards the definition of the mesoscopic numerical model as it defines the geometrical characteristics of the mesoscopic cell.

The macroscopic study consists in compression tests which are used to identify the elastic-viscous-plastic constitutive law of the studied steel. This material law is introduced within the macroscopic and mesoscopic numerical models for both the simulations of the damage tests and the continuous casting applications.

The damage study comprises tensile tests on cylindrical and notched specimens that are used to check the low ductility zone for the studied steel and acoustic tests that allow the determination of the moment of initiation of the first crack in the specimen using an acoustic emission technique. The finite element simulations of the acoustic tests give the macroscopic data to be applied on the mesoscopic cell for the identification of the damage law parameters.

After a brief description of the characteristics of the material provided for the analysis, the three parts of the experimental study are presented successively in the next sections together with the information that can be extracted from the analyses. Finally, the identification of the parameters specific to the interface law for the studied material is carried out in the last section using the data gathered throughout this chapter.

4.2 THE STUDIED MATERIAL

The study concerns micro-alloyed steels with carbon content inferior to 0.1 wt% (weight percentage). Two different steel grades have been provided successively by the industrial partner. The chemical composition of the two variants is given in Table 4.1.

Table 4.1. Chemical composition in wt%[1].

Steel grade	C	Mn	N	Al	Nb	V	S
A	0.06-0.09				≅ 0	0.04-0.06	
B	0.07-0.1				0.03-0.045	≅ 0	

[1]Values for some elements have been hidden in the published version for proprietary reasons.

Initially, two blocks of material cut from a rejected slab, whose composition corresponds to steel grade A, have been provided. The critical element responsible for

transverse cracking present in this alloy is the vanadium. The dimensions of the two blocks are the following: 200 mm wide (along the width of the slab cross section), 220 mm high (along the height of the slab cross section) and 100 mm thick (along the casting direction). They were localized on each side of the original slab and they include the corner and the lateral surface of the slab which are the critical zones for transverse crack initiation (see Figure 4.2). Cracks were visible to the unaided eye on the block extracted from the left hand side of slab. Therefore, the first microscopic observations have been made using a cut out of this particular block.

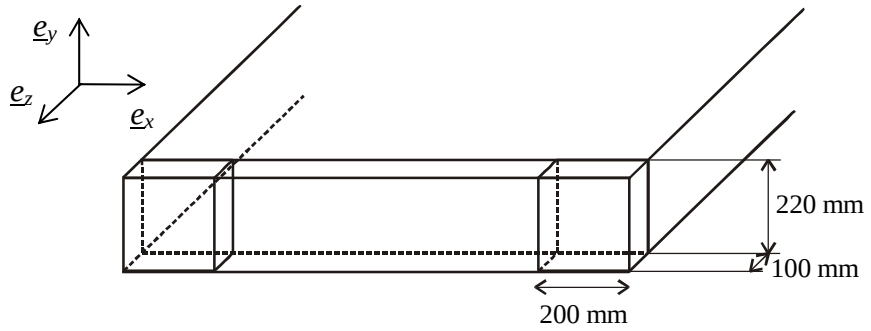

Figure 4.2. Position of the first two blocks extracted from the slab of steel grade A.

Later on, a second steel, whose composition corresponds to steel grade B, has been chosen in consultation with the industrial partner to pursue the analysis. The reason invocated to use another alloy is that it is a more representative material with regard to crack appearance (presence of niobium) within the company; indeed among the various steel grades produced by the industrial partner at the beginning of the project, steels containing niobium were more numerous. The use of this second steel grade is also relevant due to the higher availability of the material. It has been provided in the form of a 100 mm thick slice of slab. The slice has been cut into several blocks of roughly 200 mm width to facilitate the transport. The height of the blocks is 220 mm corresponding to the height of the slab itself.

The analysis of the chemical composition of the material informs on the nature of the precipitates which could be present at the grain boundaries and influence the fracture behaviour of the material as mentioned in section 2.2.1. As the effects of the vanadium and niobium constituents on transverse cracking are similar, i.e. the formation of precipitates at the grain boundaries that constitute initiation sites for cracks, it is supposed that the cracks observed on the first steel grade (A) can be used as a reference for the study, the way of propagation should be the same for the two variants.

4.3 MICROSCOPIC STUDY

The experimental analyses at the microscopic level aim at visualizing transverse cracks on actual continuous casting specimens and at observing the grain microstructure for the definition of the mesoscopic finite element model. They have been carried out in the laboratory of Metallurgy at the University of Liège using two types of microscopes: an optical microscope (stereo microscope) for initial visualization and definition of the grains size and shape; and a scanning electron microscope (S.E.M.) for further analysis of the crack content.

4.3.1 OPTICAL MICROSCOPY

4.3.1.1 Crack observations

Observations have been made by optical microscopy in order to analyze more precisely the cracks that were detected on the surface of the left hand side block extracted from the slab of steel grade A.

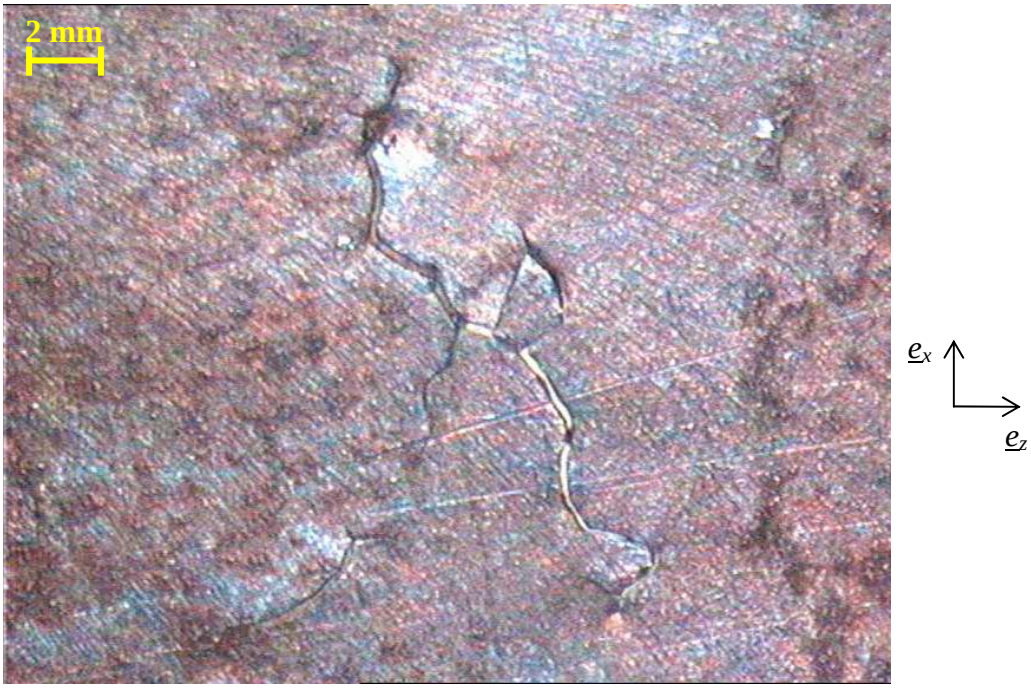

Figure 4.3. Transverse crack.

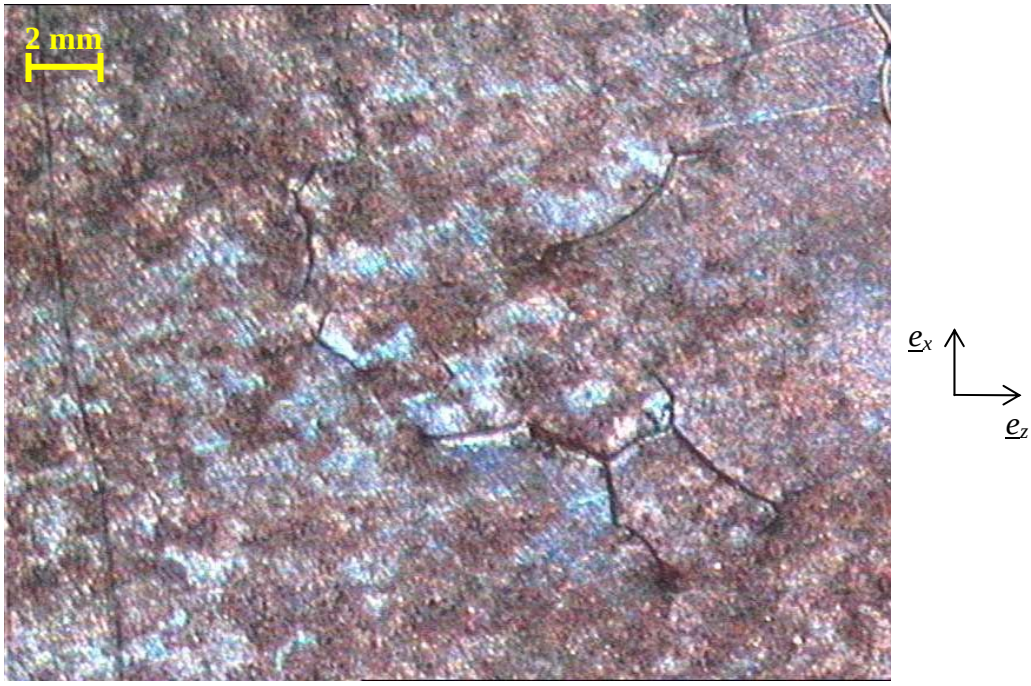

Figure 4.4. Star crack.

Two types of cracks have been visualized: a star crack and a transverse crack as shown in Figure 4.3 and Figure 4.4, respectively. They were localized on the upper surface, close to the corner of the slab, within a distance of 30 mm from the edge. The photos confirm that the cracks propagate along the grain boundaries; indeed the cracks path is constituted of broken lines which reflect a grain boundaries pattern. A complete grain contour is also distinguishable in Figure 4.3. As creep cracks in continuous casting arise at high temperature when the steel is in the austenite phase, the grain boundaries observed through the crack path are austenitic grain boundaries. These observations give a first estimation of the austenitic grain size of the order of magnitude of the millimetre. This is surprisingly high for an austenitic grain whose diameter is usually closer to 50 microns according to metallurgy experts, although the existence of very coarse grains may be explained by the particularity of the solidification process in continuous casting.

4.3.1.2 Determination of the austenite grain size and microscopic structure

Metallographic analyses have been carried out to establish the microstructure of the material and to deduce a suitable representative mesh for the finite element simulations. These analyses have been performed using the second batch of specimens (steel grade B).

The objective of the microscopic observations is also to determine the austenitic grain size along different orientations in the slab; therefore various sections of the slab need to be observed. The different surfaces analysed by optical microscopy are represented in Figure 4.5. Sections A and B are localized in the critical zone for crack initiation, i.e. on the lateral face or close to the corner on the upper surface of the slab. Sections C and D are localized further towards the middle of the slab. The combination of the different observations will inform on the three-dimensional aspect of the grains microstructure.

In order to reveal the austenitic grain boundaries, each of the surfaces defined in Figure 4.5 have been etched using picric acid. This particular chemical treatment has been realized following the modified Bechet-Beaujard instructions as described in Appendix B. Initially, the chemical treatment has been applied for 3 minutes on each of the specimens. After the picric acid etching, the four surfaces have been analysed using an optical microscope at low magnification with a view to observing the austenitic grains.

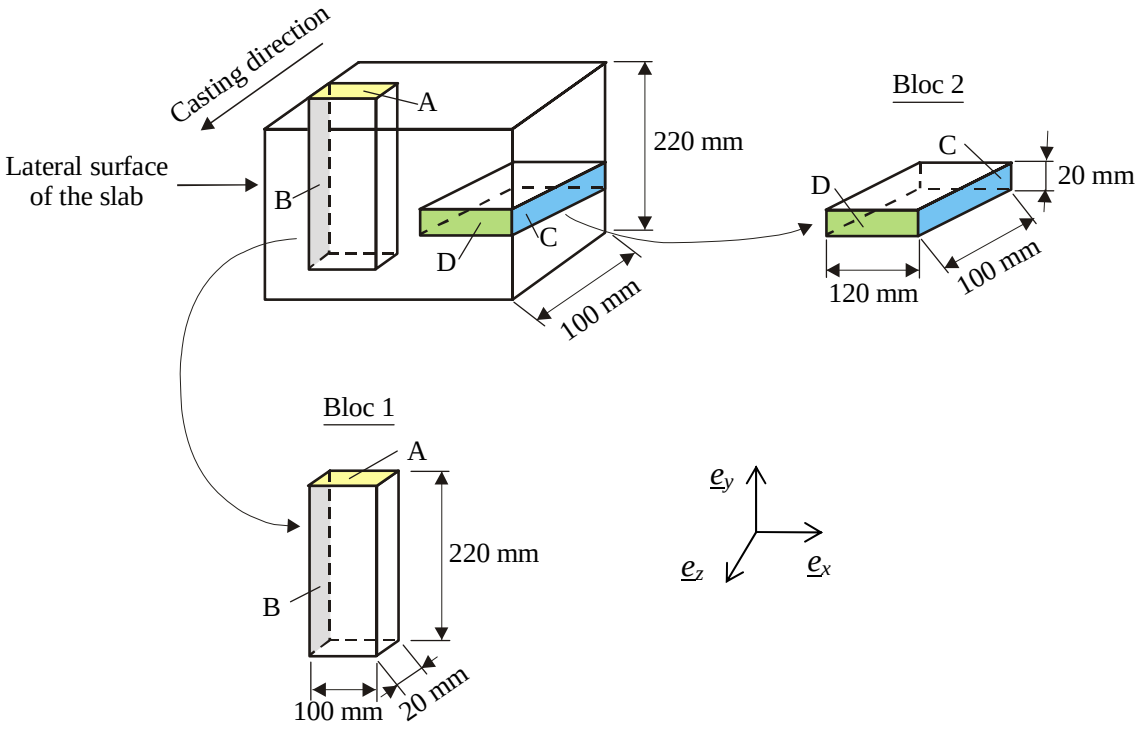

Figure 4.5. Observed surfaces.

For surfaces B and D, the boundaries of the austenitic grains are clearly marked; but this is not the case for surface A and C although the experiment has been exactly done in the same conditions as for surfaces B and D. As the micrographs obtained for

surfaces A and C did not reveal the austenitic microstructure after the initial chemical etching, the treatment with picric acid has been prolonged up to 12 minutes but the austenitic grains structure still did not appear after the prolonged treatment and surfaces A and C had to be excluded from the analysis.

The micrographs obtained by optical microscopy after the successful chemical treatment on surfaces B and D are presented in Appendix B. A total of 44 images have been taken to scan the two surfaces B and D; Figure 4.6 and Figure 4.7 indicate the position of these images for sample B and D, respectively.

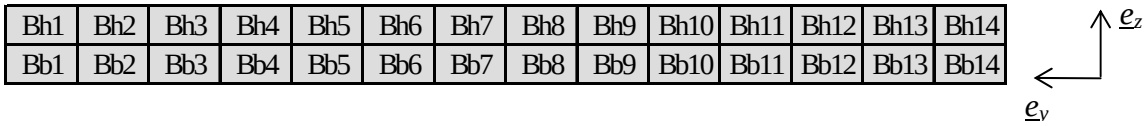

Figure 4.6. Division of the sample and numbering of the images for surface B.

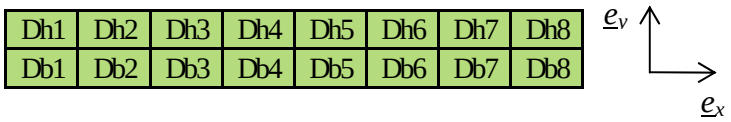

Figure 4.7. Division of the sample and numbering of the images for surface D.

Considering surface B, the whole slab is scanned through its height, from top to bottom, close to the lateral surface. Actually, the images are taken at a few millimetres under the surface as the specimen has been machined to obtain flat surfaces before being polished and prepared for the chemical treatment. The 2D model will be built using the images taken from surface B, which corresponds to the plan $y-z$ of the slab, i.e. to the type 3 section of Figure 3.31. Using the complete set of images for surface B (Figure 4.6), it is possible to analyse the grain size gradient along the height of the lateral surface of the slab. The images corresponding to the two zones close to the upper surface of the slab (Bh1 and Bb1) are particularly useful for the creation of a realistic representative mesh for the simulation. Indeed, these images correspond to a zone that is close to both the lateral and upper surfaces of the slab.

The analysis of surface D gives the grain size in the centre of the slab in an $x-y$ plan, which is useful for the estimation of a 3D grain size.

Analysis of the images

Standard used

The ASTM E112-63 standard published by the American Society for Testing and Materials has been followed to measure the grain size. Three different methods are proposed in this standard: the method by comparison, the method by intercepts and the planimetric method.

The *comparison method* consists in comparing the images with a data base of images, each of those images corresponding to a predefined grain size.

The *intercept procedure* consists in counting the number of grains intercepted by one ore more straight lines, sufficiently long to yield at least 50 intercepts. By averaging on several lines and accounting for the appropriate scale used to plot the images, it is possible to obtain an average grain size for the particular location analysed in the sample. For non-equiaxed structures, it is possible to measure the grain size using lines oriented along the three principal directions of the sample.

The *planimetric method* consists in counting the number of grains inside a circle or rectangle whose area equals 5000 mm^2, this area being the actual area on the plotted image and being independent of the scale at which the image has been plotted. The grains that cut the boundary are counted as half a grain. Knowing the scale used to plot the images, it is possible to calculate the equivalent number of grains by square millimetre of material and consequently the average grain diameter.

Observation of the grain boundaries and determination of the austenite grain size

The planimetric technique has been used for the analyses of the grain size and its gradient as it appears to be the most precise of the three methods. In the one hand, it includes a much larger number of grains in the count compared to the intercept method, which leads to a better average; and on the other hand it is more reliable than a comparison method where expert judgement is necessary.

After having drawn circles of area 5000 mm^2 on each image, the grains contours have been highlighted using black ink before counting them. Generally, the grain boundaries were immediately visible on the images from the centre of the slab while it was more difficult to see them on some of the images corresponding to area close to the upper or lower surface of the slab. The contrasts on the images were better perceived using additional light. In this case, finer contours appeared on all the images and all the actual austenitic grains were highlighted. To calculate the gradient, it is necessary to measure the size along the whole height of the sample but for the purpose of the

modelling, it is also essential to have a measure close to the upper and lower surfaces, which are the most critical zones for crack initiation.

Results of the measurements

Table 4.2 and Table 4.3 comprise the number of grains observed for each zone as well as the calculated grain diameters. The image numbers have been defined in Figure 4.6 and Figure 4.7.

Table 4.2. Measurement of the grain size for surface B
(on the lateral face, from the upper to the lower face of the slab).

Position for the measure [mm]	Image number	Number of grains	Average number of grains	Average grain diameter [mm]
7.69 (Top)	Bh1	135	134.25	1.06
	Bb1	133.5		
23.08	Bh2	116.5	103.5	1.21
	Bb2	90.5		
38.46	Bh3	108.5	107.25	1.19
	Bb3	106		
53.85	Bh4	123.5	112	1.16
	Bb4	100.5		
69.23	Bh5	67	69.25	1.48
	Bb5	71.5		
84.62	Bh6	77.5	82.25	1.35
	Bb6	87		
100.00 (Middle)	Bh7	57.5	66.5	1.51
	Bb7	75.5		
115.38	Bh8	58.5	69.75	1.47
	Bb8	81		
130.77	Bh9	75.5	93.25	1.27
	Bb9	111		
146.15	Bh10	82	127.75	1.09
	Bb10	173.5		
161.54	Bh11	92.5	116	1.14
	Bb11	139.5		
176.92	Bh12	120.5	144.5	1.02
	Bb12	168.5		
192.31 (Bottom)	Bh13	150	161	0.97
	Bb13	172		

Table 4.3. Measurement of the grain size for surface D
(at a constant height in the middle of the slab, variation along the *x*-axis).

Position for the measure [mm]	Image number	Number of grains	Average number of grains	Average grain diameter [mm]
7.23	Dh1	71.5	99.75	1.23
	Db1	128		
20.77	Dh2	95.5	122.75	1.11
	Db2	150		
34.62	Dh3	94	121.25	1.11
	Db3	148.5		
50.00	Dh4	94.5	125.75	1.09
	Db4	157		
66.15	Dh5	73.5	118.25	1.13
	Db5	163		
82.31	Dh6	78	104.5	1.20
	Db6	131		
97.69	Dh7	110	119.25	1.12
	Db7	128.5		
110.77	Dh8	106	114.75	1.15
	Db8	123.5		

Two micrographs were available for each location and the grain size has been calculated as an average between the two images. The position of the measure corresponds to the distance from the side of the specimen as defined in Figure 4.5 to the centre of the image, going from top to bottom for specimen B and from left to right for specimen D.

Conclusions

The measurement of the grain size is not a straightforward task. In the particular example of the austenitic microstructure, it is also affected by the quality of the images after the etching process and by the capacity of the observer to perceive the contrasts on the images.

From the measurements on surface B, it emerges that the grain size presents a gradient along the height of the slab (Table 4.2). For the surface D, the grain size observed is almost constant (Table 4.3), which is logical as the measures are taken in the middle of the slab, far from the lateral surface and at a constant depth. This tendencies are illustrated in Figure 4.8 where the points corresponding to the surface B

show large variations, with a maximum at mid-height, and those measured on surface D are localized around 1.1 mm.

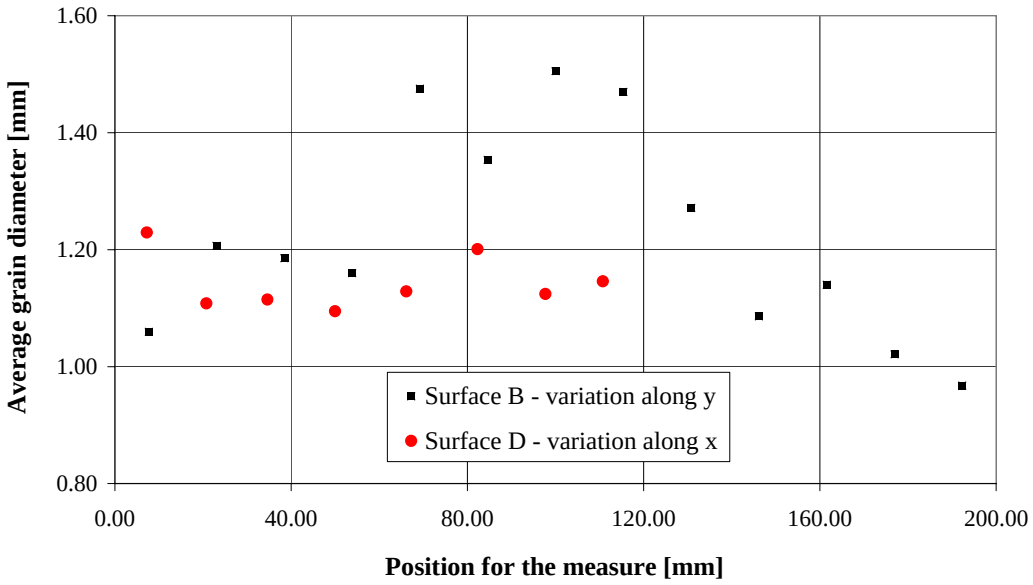

Figure 4.8. Average grain diameter measured on surface B and D.

Finally, it can be concluded that the observed grain size is approximately 1 mm for the zone close to the surface analysed in this study, which confirms the rough estimate of section 4.3.1.1.

4.3.2 S.E.M. ANALYSIS

The analyses of the surface of steel A with the optical microscope have revealed that the cracks were filled in with an unknown interstitial substance in certain areas (see Figure 4.3). It has been necessary to determine the composition of this substance by S.E.M. analysis because its presence was not expected in these specimens. Indeed, if this substance comes from the slag that could contradict the assumption that the cracks appear in the unbending zone of the continuous casting machine.

An X-ray spectral analysis has been carried out on the specimen (Lecomte-Beckers and Tchoufang 2000). A couple of points have been analysed in the first instance to define qualitatively the global composition of the steel. In a second phase, the focus has been on several points inside the cracks to check if their content was different from the elements found in the first observations.

The results of the spectral analysis show that the substance inside the crack is composed in the majority of calcium, sodium, potassium, chlorine and titanium. These elements are present mostly in the interstitial substance and are quasi absent from the original alloy.

After discussion with continuous casting process experts, it appears that those elements could come from all the environment of the continuous casting machine and especially from the cooling water which streams on the slab surface during the whole process. So the assumption that the cracks appear during the unbending phase is not contradicted.

4.4 MACROSCOPIC STUDY

The objective of the macroscopic analysis is to provide experimental results to be used for the calibration of the modified Norton-Hoff law presented in section 3.3.2. To obtain representative characteristic curves of the material for this study, experiments have been carried out at various temperatures and strain rates which have to cover the ranges encountered in continuous casting and especially in the unbending zone of the machine.

The macroscopic study consists in compression tests of cylindrical specimens during which force-displacement curves are recorded and post-processed to provide stress-strain curves. Various strain rates ($\dot{\varepsilon}$ = 10^{-2}, 10^{-3} and 10^{-4} s^{-1}) and temperatures (T = 700, 800, 900, 1000, 1100 and 1200 °C) have been tested and compared with analytical computations in order to identify the parameters p_1 to p_4 of equation (3.1). A thermal treatment that aimed at reproducing the thermal cycle of continuous casting had been applied on each test sample before compression.

4.4.1 PREPARATION OF THE SPECIMENS

The macroscopic compression experiments have been carried out on steel grade B (see Table 4.1). The specimens for testing have been machined out of the blocks provided by the industrial partner as shown in Figure 4.9. As the cracks appear on the surface of the slab, only the upper and lower surfaces of the block were used for sampling to assure that the surface material chemical composition was recovered for the experimental testing. Only two of the blocks containing part of the lateral surface of the slab were available, so it has been decided to use only the upper and lower surfaces of

the middle blocks for reproducibility, one of the lateral block having already been used for the microscopic analysis.

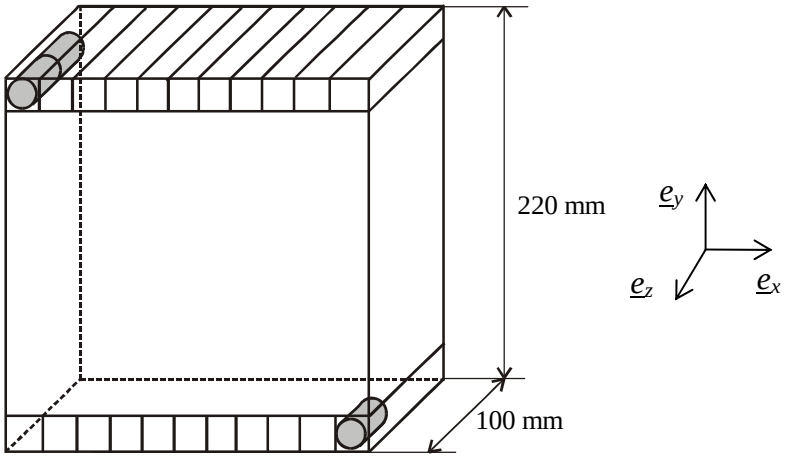

Figure 4.9. Sampling of test specimens.

Before testing, the specimens have been heated up to a temperature above the testing temperature. This step is necessary to dissolve the precipitates which are present in the ferritic phase of the steel at room temperature and to recover an austenitic microstructure close to the one existing in the continuous casting. The objective is to be in *as-cast* conditions for the mechanical testing (Bernard *et al.* 1978, Revaux *et al.* 1994, Mintz 1999). Figure 4.10 shows an example of heating cycle used during the study, where typical heating rates are proposed. The particular conditions applied before each specific experiment are specified hereafter when discussing the tests themselves as the same cycle could not be used for all the experiments due to the various characteristics of the different equipments available in each laboratory.

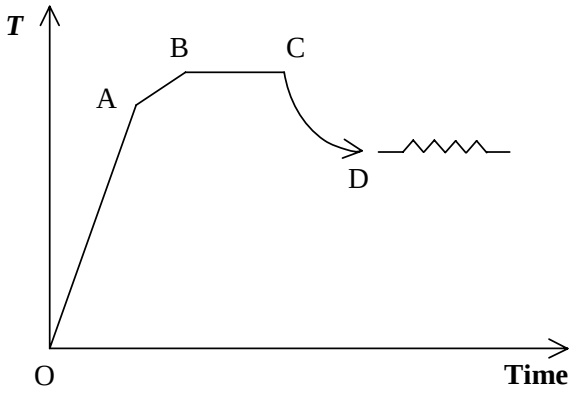

OA : 25 °C/min
AB : 10 °C/min
BC : 1 min
CD : ≅ 50 °C/min

A = 1100 °C
B = 1375 °C
D = test temperature

Figure 4.10. Thermal cycle applied before the experiments to simulate *as-cast* conditions.

4.4.2 DESCRIPTION OF THE COMPRESSION TESTS

Two sets of uniaxial compression tests have been performed: the first one has been carried out at the Institute for Metal Forming (IBF) – RWTH Aachen – as a prelude to the acoustic tests that are described in section 4.5.2; and the second one in house at the laboratory of Materials and Structures of the University of Liège in order to complete the data set. Throughout this section, the letter A refers to the tests realised in Aachen, whereas the letter L refers to those realised in Liège.

Cylindrical specimens have been machined in the respective laboratories in accordance with the standard size used for this type of tests. The specimen size is of the same order of magnitude in both laboratories although slightly different: diameter × height = 14 mm × 21 mm for A specimens and 13 mm × 20 mm for L specimens.

The A tests have been carried out in an compression machine equipped with an induction furnace. The thermal cycle shown in Figure 4.10 has been respected for these specimens, which were maintained at a temperature of 1375 °C for 1 minute before cooling down to the test temperature.

The L tests have been carried out in an compression machine equipped with a radiation furnace. Due to the characteristics of the furnace available in Liège, L specimens could only be heated up to a temperature of 1150 °C before the compression tests. A thermal history similar to the one defined in Figure 4.10 has been applied but with the plateau BC at 1150 °C. In practice, the reproduction of the temperature cycle is well respected. This affirmation has been checked by recording the temperature in the specimen during the tests using thermocouples. For example, it has been verified that the variations in the temperature level during the compression test at 800 °C and $\dot{\varepsilon} = 10^{-3}\ s^{-1}$ were inferior to 0.5 °C (Moureaux 2001), which indicates that the temperature regulation is very precise.

All compression tests have been carried out on vertical upsetting machines equipped with a regulation system allowing the application of a constant strain rate. The vertical displacement of the upsetting plates is controlled in order to impose the given strain rate. During the tests, the variation of the load is recorded as a function of the time. Each laboratory has its own evaluation piece of software which allows converting the load – displacement curves recorded during the tests into true stress – true strain curves. These conversion programs incorporate corrections to account for the barrel effect on the cylindrical specimens due to both the deformation and thermal expansion and allow the definition of the physical stresses and strains in the material.

Table 4.4 summarizes the experimental conditions for all the compression tests carried out as well as the number of specimens tested for each parameters combination. The observation of the specimens of type A after compression indicates that the composition of the material after the thermal cycle of Figure 4.10 may have been inhomogeneous for some of the specimens. Indeed, due to inhomogeneities in the material microstructure, no homogeneous deformation was realizable during the compression tests for several of the specimens and the flow curves recorded had to be considered critically. This affirmation is confirmed by the observation of the deformed specimens which show an asymmetric geometry. In particular, the A test at 1100 °C and $\dot{\varepsilon} = 10^{-3}$ s^{-1} had to be rejected due to an irregular behaviour at the beginning of the curve probably due to a strong inhomogeneity within the sample (Tschirnich 2000); the A test at 1100 °C and $\dot{\varepsilon} = 10^{-2}$ s^{-1} was also rejected because the level of the curve was incoherent with the other data collected (see Figure 4.11). Some of the A tests at the lowest strain rates and highest temperatures failed (Tschirnich 2000) and no results were provided for these tests. It is assumed that the limitation of the machine is reached at $\dot{\varepsilon} = 10^{-4}$ s^{-1} and therefore all the A tests at this strain rate have been excluded from the analysis except for the test at 700 °C which presents a coherent behaviour when compared with the tests at the other strain rates (see Figure 4.13).

Table 4.4. Summary of the experimental tests carried out.

T [°C]	$\dot{\varepsilon} = 10^{-2}$ s^{-1}	$\dot{\varepsilon} = 10^{-3}$ s^{-1}	$\dot{\varepsilon} = 10^{-4}$ s^{-1}
700	1 × A	1 × A	1 × A
800	1 × A	1 × A	1 × A (failed)
	-	2 × L	2 × L
900	1 × A	1 × A	1 × A (rejected)
	-	2 × L	2 × L
1000	1 × A	1 × A	1 × A (failed)
	-	-	2 × L
1100	1 × A (rejected)	1 × A (rejected)	-
	2 × L	2 × L	2 × L
1200	1 × A (failed)	1 × A (failed)	1 × A (failed)

The choice of the combination parameters for the L tests has been initially dictated by the missing data. The L tests at $\dot{\varepsilon} = 10^{-3}$ s^{-1} (800 °C and 900 °C) have been added to the experimental program in order to analyse the sensibility of the stress-strain

curves to the strain rate and temperature for the specific testing conditions available in Liège. The L tests at $\dot{\varepsilon} = 10^{-2}$ s^{-1} and 10^{-3} s^{-1} have been carried out on a compression machine whose maximum load is 40 tons; whereas the L tests at $\dot{\varepsilon} = 10^{-4}$ s^{-1} have been carried on another compression machine, whose maximum load is 10 tons, allowing a better regulation of the velocity at very low strain rates. The analysis of the deformation curves as a function of the time shows that the recorded strain rates are constant and correspond to the imposed values within a 10% error band (Moureaux 2001). Two tests have been carried out for each of the combinations tested.

4.4.3 ANALYSIS OF THE FLOW CURVES

The results of the compression tests have been provided directly in terms of flow curves, i.e. stress – strain curves (Tschirnich 2000, Moureaux 2001). Figure 4.11 to Figure 4.13 show the complete set of experimental data available for the analysis, each figure corresponding to one strain rate. The curves that were finally rejected from the analysis, as mentioned in Table 4.4, are also presented on these graphs.

A first comment on the results is that the testing conditions were not the same in the two laboratories and therefore it is not surprising to get differences in the curves obtained. In particular, the annealing at 1375 °C for the A tests must be sufficient to dissolve the carbonitrides present in the original alloy whereas they are probably not dissolved for the L tests where the maximum temperature reached before testing is only 1150 °C and this could lead to different rigidities of the specimens. Discussions with experts have confirmed that dispersion of the results between different laboratories is frequent and that tests at very low strain rates are always challenging. They also agree that the rigidity at low strains for the A tests seems unusual and that the L tests are in better correspondence with the behaviours normally observed for this type of curves.

The analysis of the results confirms that globally, the rigidity of the material decreases with the temperature, apart from the L tests at T = 800 °C for $\dot{\varepsilon} = 10^{-3}$ s^{-1} and 10^{-4} s^{-1} where a different behaviour is observed. At $\dot{\varepsilon} = 10^{-3}$ s^{-1}, the L tests at 800 °C present a lower rigidity than those at 900 °C for the larger strains as illustrated in Figure 4.12. At $\dot{\varepsilon} = 10^{-4}$ s^{-1}, the L tests at 800 °C present a rigidity similar to those at 1000 °C for the entire range of strains, as shown in Figure 4.13. The austenite – ferrite transformation that occurs around 800 °C may explain this type of behaviour, the two microstructures leading to different rigidities of the material.

Some of the L tests present a profile that is characteristic of the recrystallisation process. In particular, the oscillations observed at T = 1000 and 1100 °C in Figure 4.13

($\dot{\varepsilon}$ = 10^{-4} s^{-1}) are typical of a recrystallisation behaviour. This phenomenon is also observed for the maximum equivalent stress at the beginning of the curve for the L tests at T = 1100 °C in Figure 4.11 ($\dot{\varepsilon}$ = 10^{-2} s^{-1}) and for the L tests at T = 1100 °C in Figure 4.12 ($\dot{\varepsilon}$ = 10^{-3} s^{-1}). Such recrystallisation patterns are not observed for the A tests in the austenitic phase (i.e. when T = 900, 1000 and 1100 °C).

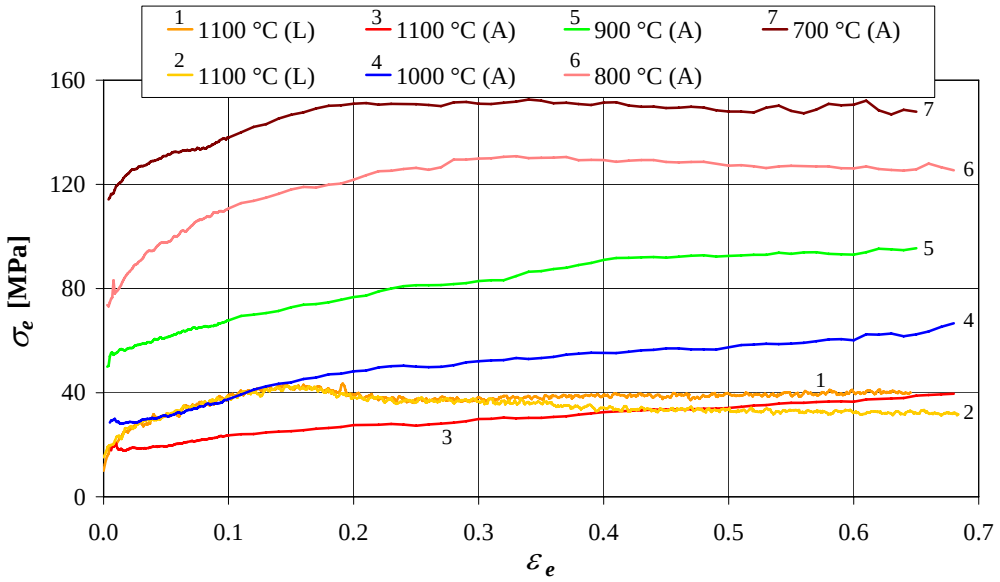

Figure 4.11. Experimental flow curves at $\dot{\varepsilon}$ = 10^{-2} s^{-1}.

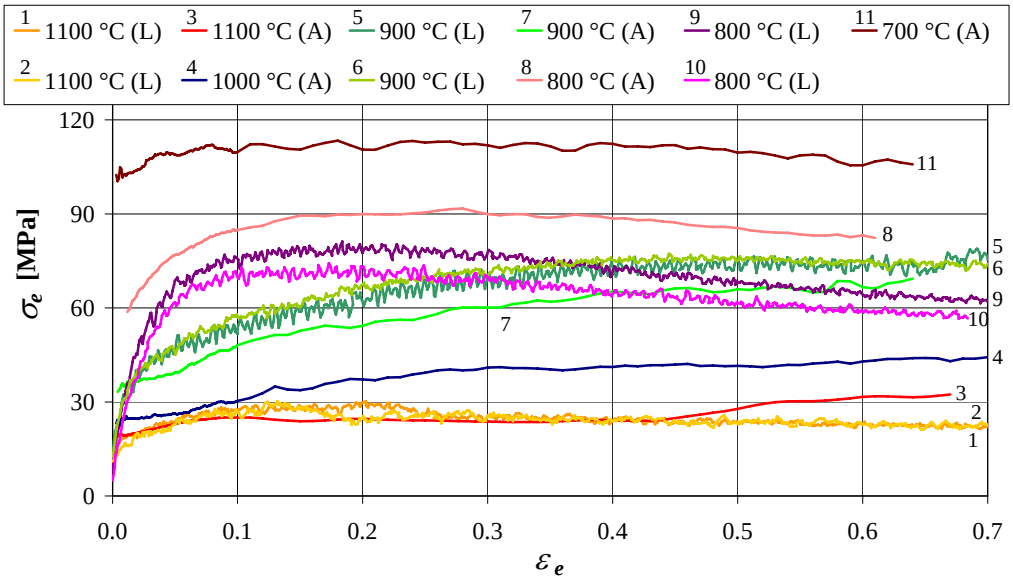

Figure 4.12. Experimental flow curves at $\dot{\varepsilon}$ = 10^{-3} s^{-1}.

A softening effect is observed for the experiments at T = 700 and 800 °C for the A tests. At these temperatures, the material comprises a mixture of austenite and ferrite and the decreasing of the curves at the higher strains suggests a recrystallisation process. For the other temperatures, the equivalent stress continues to increase slightly with the equivalent strain for the whole range of strain tested. For the L tests, all the curves present at least a small softening effect or a plateau.

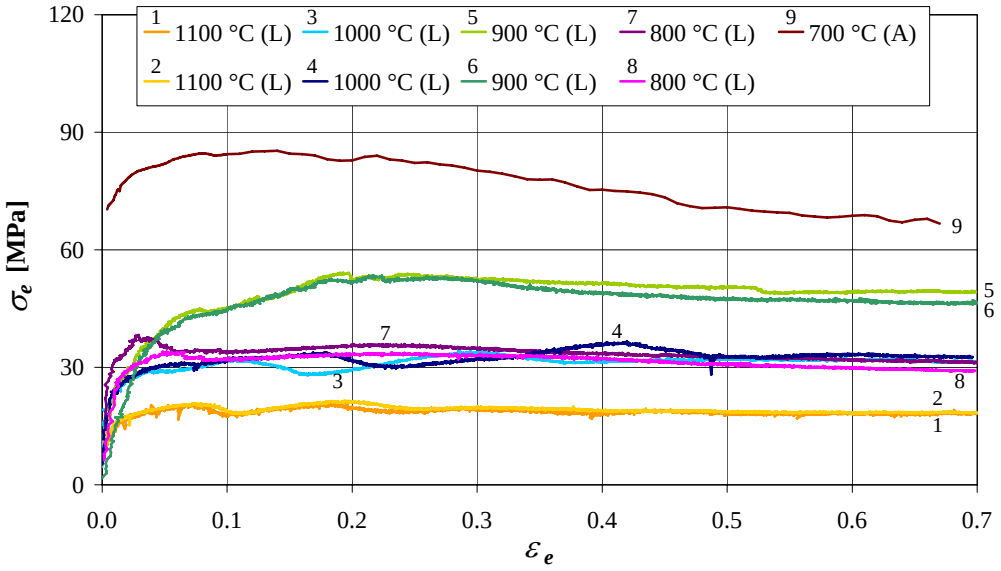

Figure 4.13. Experimental flow curves at $\dot{\varepsilon} = 10^{-4}$ s^{-1}.

As highlighted here before, lots of physical phenomena come into play when carrying out compression experiments within the range of temperatures and strain rates necessary for this analysis. It is admitted that it is not possible to define with certitude which results are the closest to the actual continuous casting behaviour but it is also acknowledged that the experimental curves are in a whole representative of the material to be modelled and, in this respect, suitable for the definition of a typical constitutive law to be used for the modelling of the material analysed in this study.

4.4.4 IDENTIFICATION OF THE PARAMETERS OF MODIFIED NORTON-HOFF LAW

The parameters identification has been done using a least squares method for each temperature to determine the parameters p_1 to p_4 of the modified Norton-Hoff law given by equation (3.1) (Remy 2002a). R^2 is the variable that is minimized in the problem. It is a measure of the difference between the experimental data and the simulated curves. R^2 is given by the normalized sum of the quadratic differences

between the experimental data and equation (3.1) for all the experimental curves available at each temperature. The normalization is carried out by dividing the sum of the quadratic differences by the number of data point minus the number of parameters to be fitted (i.e. 4 in the present case). To avoid privileging the L tests in comparison with the A tests, a weight factor of 0.5 is used when accounting for the L tests as two experiments of type L where carried out for each combination of temperatures and strain rates tested whereas only one of type A was realised for each combination.

The results of the identification can be found in Table 4.5. *R* is also given in this table; it is a different value for each temperature which gives an idea of the quality of the identification. *R* becomes zero when the difference between the data points and the fitted curve is zero.

Table 4.5. Parameters of the modified Norton-Hoff law (Pecquet 2003); units consistent with an equivalent stress σ_e measured in MPa.

T [°C]	p_1	p_2	p_3	p_4	R
700	0.2476	156.107	0.115	0.067	9.737
800	0.7749	303.085	0.231	0.203	19.762
900	0.0465	125.001	0.155	0.210	15.119
1000	0.0014	53.692	0.099	0.193	5.612
1100	0.8429	65.402	0.148	0.193	3.585

The softening parameter p_1 should not influence the results of the macroscopic continuous casting model as it has principally an effect in the large strains that will not appear in this process. Nevertheless, it is important to have an accurate model at larger strains for the acoustic tests simulations used to identify the damage parameters and in case of localised higher strains due to the grain configuration in the mesoscopic cell. The parameter p_2 influences the maximum value of the stress but the global effect on the curve level is also strongly linked to the hardening and softening parameters. The viscosity parameter p_3 and the hardening parameter p_4 lie almost in the interval 0.1 – 0.2, which fits with usual values found for steel. p_3 does not increase monotonously as could have been expected for the majority of steel grades. This type of behaviour has also been found in the literature for several low carbon steel grades (Altan *et al.* 1983), which is the type of steel used in this study.

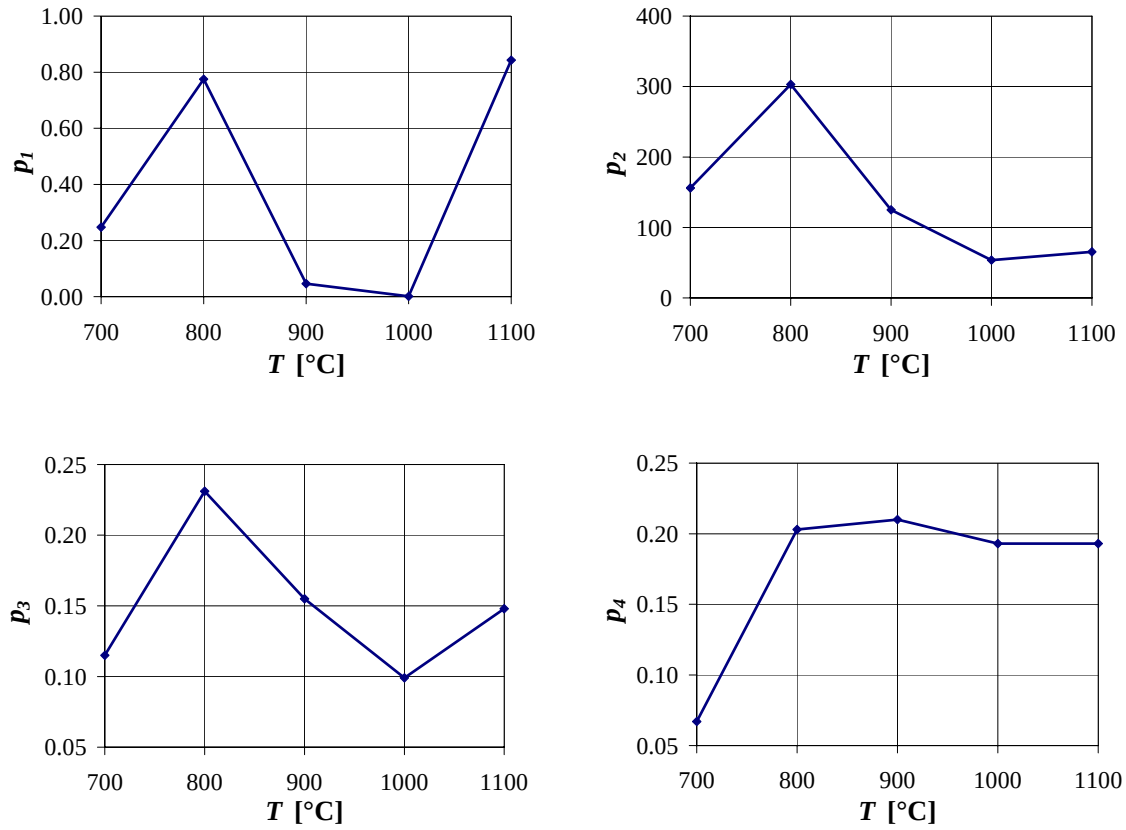

Figure 4.14. Variation of the four parameters given in Table 4.5 with the temperature; units consistent with an equivalent stress σ_e measured in MPa.

The four parameters of the modified Norton-Hoff constitutive law are plotted in Figure 4.14 as a function of the temperature. The linear interpolation, which is automatically carried out within the finite element code to calculate these parameters at temperatures between the data points, are also shown on the graphs. The non-monotonous variations of the parameters with the temperature is not surprising. Indeed, phase transformations occur during the cooling of steel between 1100 and 700 °C and the data points defined by the compression experiments may correspond to different phases of the material.

Figure 4.15 to Figure 4.19 show the results of the calibration per temperature for the three strain rates. The oscillating (coloured) lines correspond to the experimental results presented before and the smooth (black) lines to the modified Norton-Hoff curves (equation (3.1)) using the parameters of Table 4.5.

The fitted curves approach the experimental results quite well, taking into account the dispersion of the later. Even if the curves shape suggests that some recrystallisation occurs, this phenomena is not represented explicitly in the model.

Nevertheless, softening is clearly modelled at 700 °C (Figure 4.15), 800 °C (Figure 4.16) and 1100 °C (Figure 4.19) as can be visualised on the figures; the decrease of the stress for the higher strains matches the indications given by the evolution of the parameter p_1.

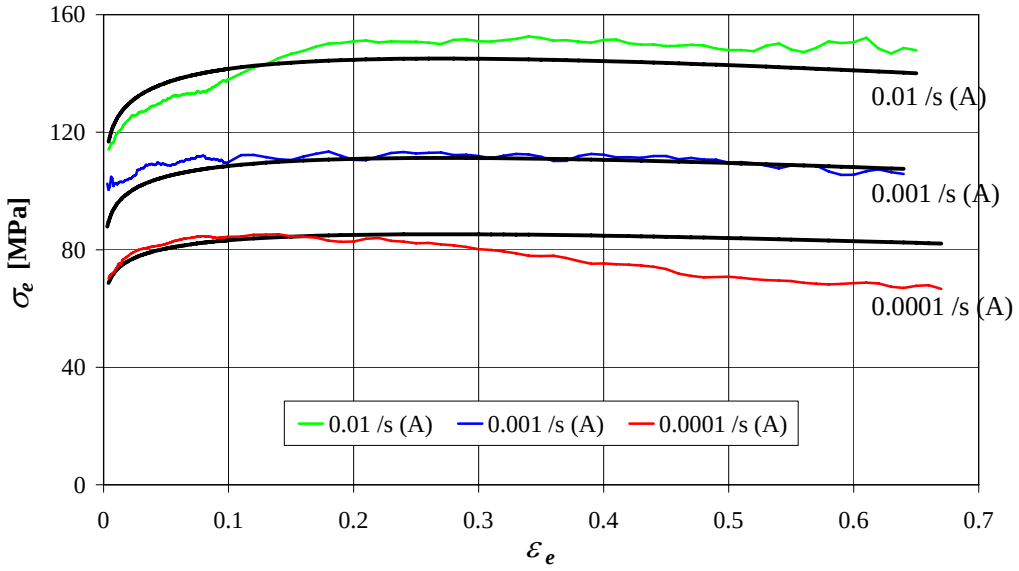

Figure 4.15. Experiments (colour) and modified Norton-Hoff (black) curves at T = 700 ºC.

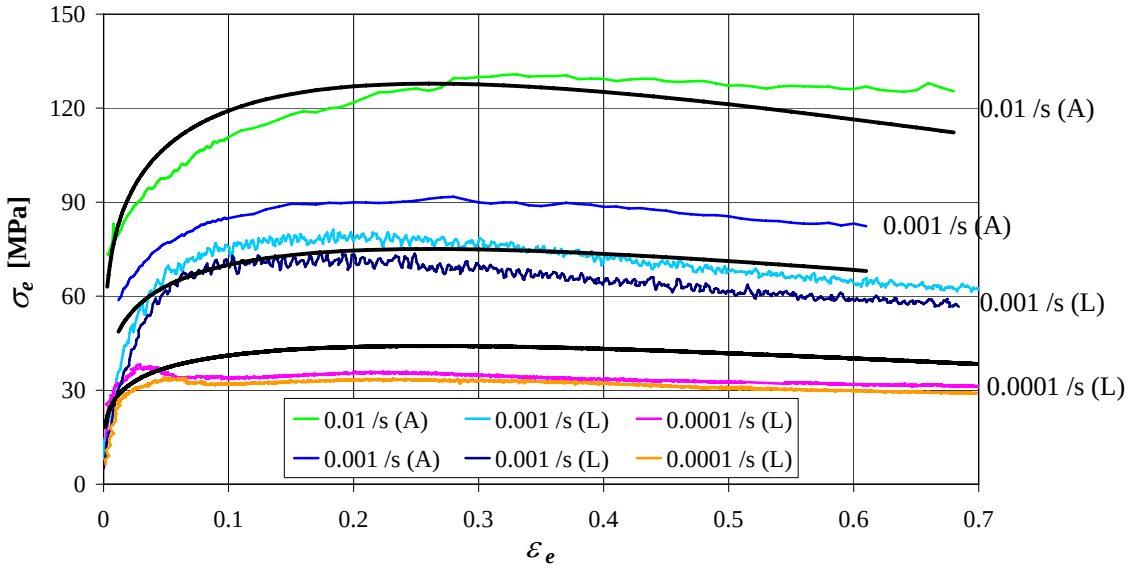

Figure 4.16. Experiments (colour) and modified Norton-Hoff (black) curves at T = 800 ºC.

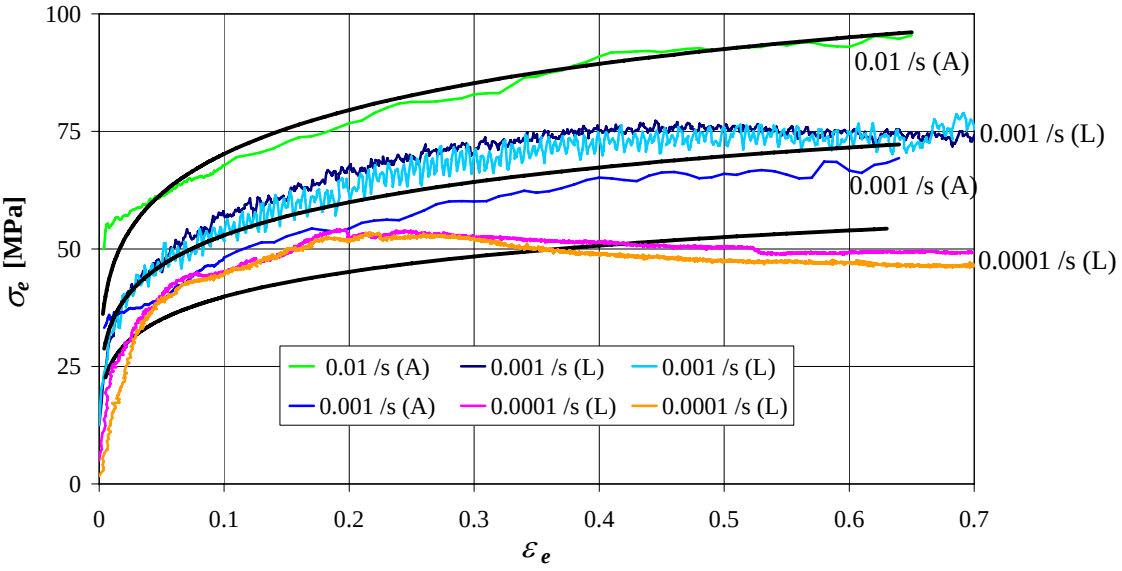

Figure 4.17. Experiments (colour) and Norton-Hoff (black) curves at T = 900 ºC.

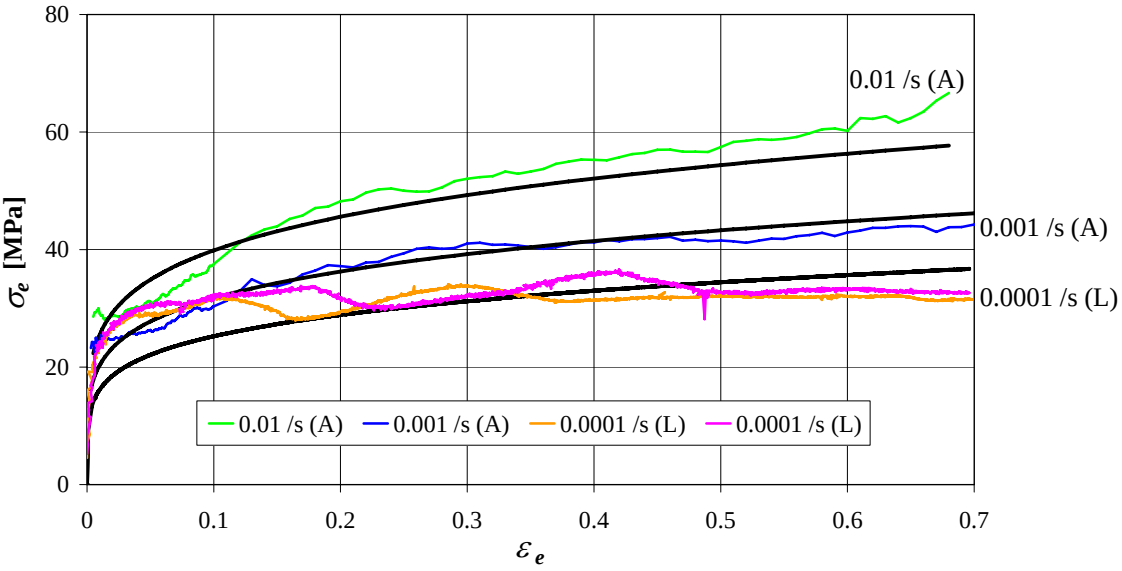

Figure 4.18. Experiments (colour) and modified Norton-Hoff (black) curves at T = 1000 ºC.

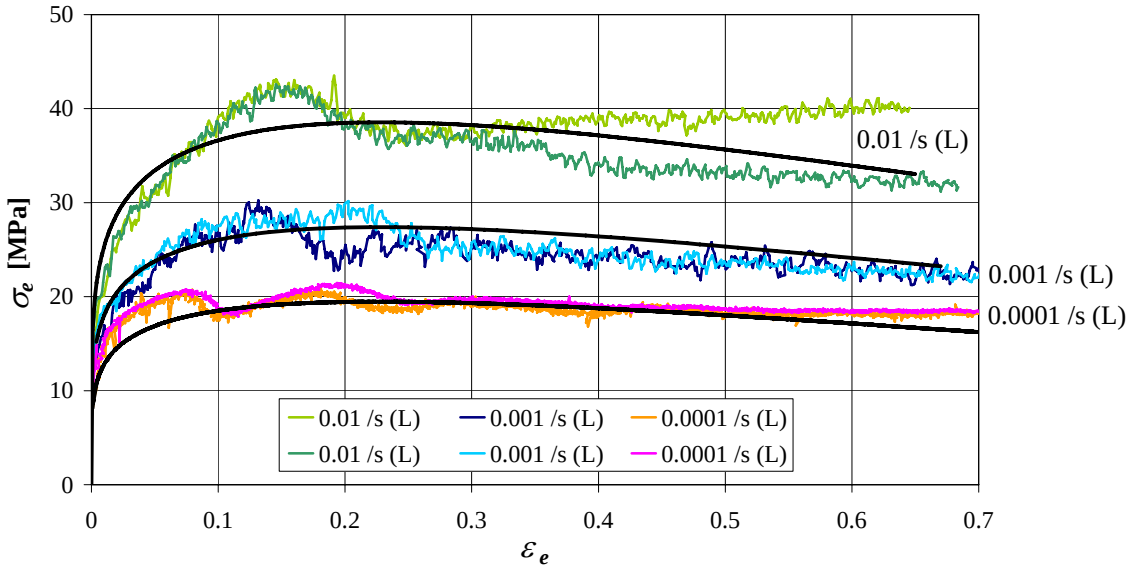

Figure 4.19. Experiments (colour) and modified Norton-Hoff (black) curves at T = 1100 ºC.

4.5 DAMAGE STUDY

The damage study comprises two types of experiments: tensile tests, which are carried out to analyse the effect of a notch on the ductility of the material at elevated temperatures; and acoustic compression tests, which will be used for the determination of the parameters of the interface damage law.

4.5.1 TENSILE TESTS AND DUCTILITY ANALYSIS

At elevated temperature, tensile tests can be used to define the ductility curve of the material. The ductility characterizes the capacity of a material to withstand large deformations without fracture.

For this study, tests have been carried out on a thermo-mechanical machine using plain cylindrical specimens (see Figure 4.20(a)) and notched cylindrical specimens (also referred to as the notched specimens, Figure 4.20(b)). The notched specimen is designed to analyze the effect of an oscillation mark in the context of the continuous casting process. Therefore, the characteristics of the notch are the following:

- V shaped notch
- width = 0.75 mm
- notch radius = 0.08 mm
- angle = 40°

These dimensions are representative of an oscillation mark apart from the angle, which in actual slabs is closer to 120°. This angle has been chosen according to the machining possibilities and the global dimensions of the notch are representative enough to provide a comparison between the two cases (with and without notch).

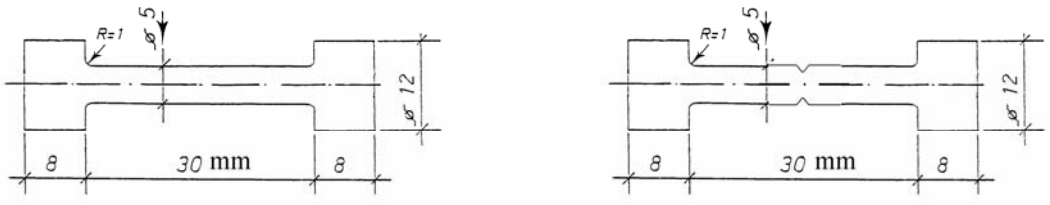

(a) (b)

Figure 4.20. a) Plain cylindrical specimen, b) notched specimen.

Contrarily to the compression tests, where the displacement can be automatically adjusted to maintain a constant strain rate in the direction of the loading of the specimen, the experimental set up for the tensile tests is not designed to control directly the strain rate but only the speed at which the heads of the specimen are pulled away from one another. During the first series of tests, the specimens where pulled apart up to fracture at a constant head speed of 0.1 cm/min, which corresponds to an initial strain rate of 5.55 10^{-4} s^{-1}. Due to the elongation of the specimen and to the necking effect, the strain rate during the experiment becomes non uniform and can not be directly predicted.

The results of the first series of tests are summarized in Table 4.6 for three temperatures. In this table, the tensile strength is the maximum tensile stress reached before necking, the elongation is the maximum deformation reached at rupture and the reduction of area (RA) is a measure of the necking effect which is calculated as follows:

$$RA = \frac{S_0 - S_f}{S_0} \tag{4.1}$$

where S_0 is the initial cross section in the middle plane of the specimen and S_f the final cross section at this same location after fracture. The results show that the tensile strength decreases with the temperature whereas the elongation increases, both for notched and plain specimens. This observation is expected as the material naturally loses stiffness when the temperature increases. By comparing the case with and without notch, it can be seen that for each temperature, the tensile strength and elongation are lower for notched samples. This fact is due to the geometry that induces a higher

triaxiality of the stress tensor applied on the material, which implies that notched specimens break earlier. Indeed, it is well known that higher damage is related to higher triaxiality (Brocks *et al.* 1995, Gologanu *et al.* 2001).

Table 4.6. Results of tensile tests at a constant head speed of 0.1 cm/min.

Specimen type	*T* [°C]	Tensile strength [MPa]	Elongation [%]	*RA* [%]
Without notch	800	93	23.5	31.0
	900	64	22.7	27.7
	1000	38	42.6	40.9
With notch	800	75	8.1	31.3
	900	51	13.0	30.1
	1000	32	19.5	45.0

No significant differences were found regarding the reduction of area for notched and plain specimens; the necking effect is analysed in more details hereafter in relation with the ductility at elevated temperatures.

A typical ductility curve comprises three distinct zones as illustrated in Figure 4.21 (Mintz *et al.* 1991).

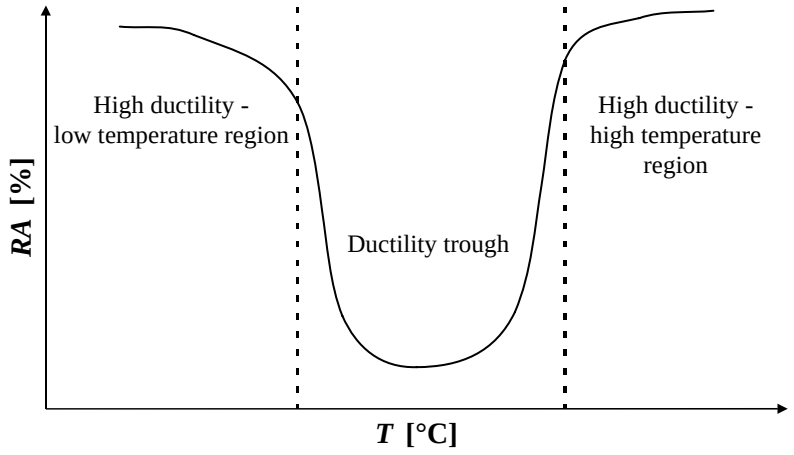

Figure 4.21. Typical hot ductility curve showing the three characteristic ductility regions.

The ductility trough is characterized by an embrittlement due to grain boundary sliding and to strain concentration and microvoid coalescence at the grain boundaries where soft thin ferrite films and/or precipitate free zones usually form. In the lower temperature region, recovery in ductility occurs because the fraction of ferrite present

increases which reduces the embrittlement due to strain concentration at grain boundaries. At higher temperatures, the ductility improves when grain boundary migration takes place during the process of dynamic recrystallisation, leaving the micro-cracks isolated inside the grains. The absence of thin ferrite film around the austenite grains and the lower precipitation level at these higher temperatures also reduce the embrittling mechanisms.

To define the ductility trough experimentally, additional tests have been performed at intermediate temperatures and for another head speed. The complete set of results in term of reduction of area (RA) is presented in Figure 4.22 at head speeds of 0.1 cm/min and 0.01 cm/min and for temperatures going from 800 °C to 1050 °C with an increment of 50 °C. Although the experimental results do not include data corresponding to the high ductility – low temperature region, the experience confirms that there is a gap of ductility localized between 800 °C and 1000 °C for the studied material. This range corresponds to the temperature of the slab surface during the unbending phase in continuous casting, so that in the continuous casting process the unbending zone corresponds actually to the more critical condition as far as ductility is concerned. Although, the damage effect due to the notch clearly influences the tensile strength and elongation, there is no major effect of the notch on the reduction of area itself. Nevertheless, the notch produces stress concentrations, which implies that notched specimens reach the plasticity domain and break earlier during the test.

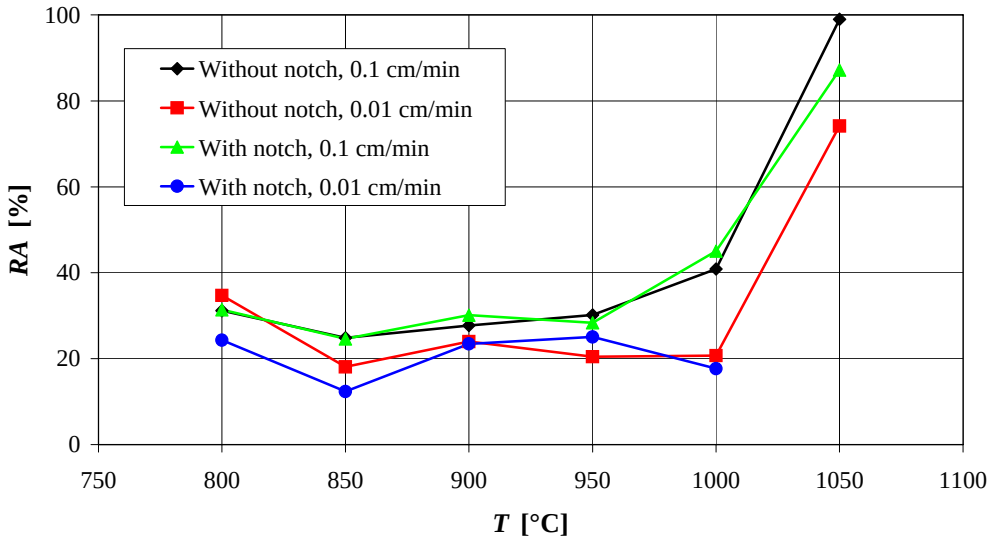

Figure 4.22. Ductility curves.

Figure 4.22 also shows that the trough is slightly deeper at the lower loading speed, which indicates that the ductility is reduced at smaller strain rates. Although this is in accordance with the literature (Mintz *et al.* 1991), it is not possible to raise a formal conclusion linking continuous casting speed and ductility on the basis on these experimental results as only two loading speeds were tested.

4.5.2 ACOUSTIC TESTS

The Institute for Metal Forming (IBF) – RWTH Aachen – has developed a technique for the analysis and prediction of material failure based on the detection of acoustic emissions occurring during cracking. The experimental set up was initially designed to predict metal formability at room temperature according to basic tests; it has then been adapted to the conditions prevalent during hot forming (Kopp and Bernrath 1999). The methodology consists in using finite element simulations of the basic tests in parallel with the experiments to plot formability limit curves for the material. Once determined, these curves are used for the forecasting of material failure associated with practical production processes.

4.5.2.1 Goal of the acoustic tests in the context of this thesis

In this study, the acoustic tests are carried out in order to provide a set of experimental data for the determination of the damage parameters of the interface law. The goal is to correlate the instant of initiation of the first crack, determined through acoustic emission during the compression of steel specimens, and the damage parameters of the interface law via finite element simulations of the compression tests. The full description of the method and its application to the identification of the damage parameters are presented in the following sections.

4.5.2.2 Description of the acoustic tests

Acoustic emissions: origin and capture

If the internal stresses in a crystal are exceeding locally a critical threshold during forming, a sudden change appears (the initiation of a micro-crack), which allows the material to return to an equilibrium state with a lower potential energy. The energy emitted is dissipated in the form of elastic waves that can be detected in the surrounding area as sound pulses. Piezoelectric sensors are used to record the sound signals. These signals, that have a very low intensity, are pre-amplified, filtered to separate the sound

associated with the damage process from the interferences and amplified again before being introduced in the data acquisition system.

Experimental set up

As for the other mechanical experiments, a thermal cycle is applied to the specimens before testing in order to simulate the continuous casting conditions and to recover, as closely as possible, the austenitic microstructure of the steel pertaining during this process. The specimens are first heated up to 1375 °C in an external radiation furnace and maintained at this temperature for ten minutes before cooling down to test temperature as described in Figure 4.10. To protect the sample material against surface oxidation, the furnace is rinsed with argon inert gas. Afterwards, the samples are manually placed in the upsetting machine; the surrounding furnace having been heated up to test temperature within the argon atmosphere. Finally the samples are compressed up to crack initiation with a constant strain rate while upcoming acoustic emission events caused by material failure are recorded.

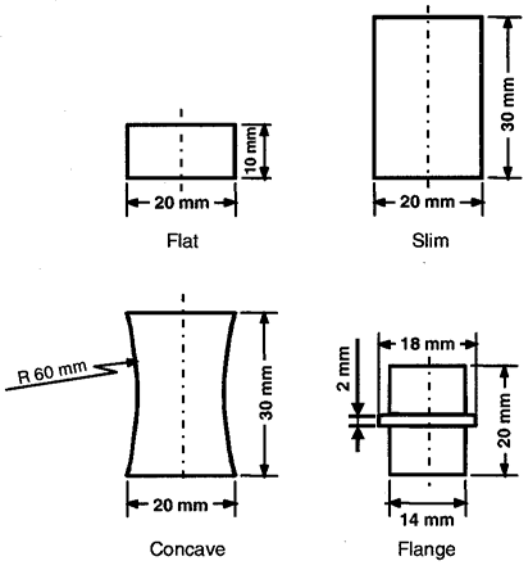

Figure 4.23. Geometry of the specimens for the acoustic tests.

Several sets of acoustic tests have been done with different sample geometries as shown in Figure 4.23 (two cylindrical: flat and slim and two non-cylindrical: flange and concave shapes) to generate different stress-strain histories at the critical point of the samples. The critical point is the point where the crack is supposed to appear due to the mechanical loading, i.e. where the stresses and strains are the most severe during the deformation of the specimen (on the outer edge at mid-height for the flat, slim and

concave samples and at the intersection of the outer edge of the cylindrical part with the ring for the flange sample). Figure 4.24 shows the critical point location for each specimen; the critical point is represented in the first quadrant only for illustration purpose in this 2D view. The location of the critical point has been determined experimentally for various samples at the time of the development of the technique at IBF. It is well defined for each geometry and corresponds to the point where the crack usually initiates as it can be visualized on the specimens after testing. Abnormalities of the results are often linked to the fact that the specimen already contained defects before the test, in this case the initiation site can not be defined properly and the test has to be rejected.

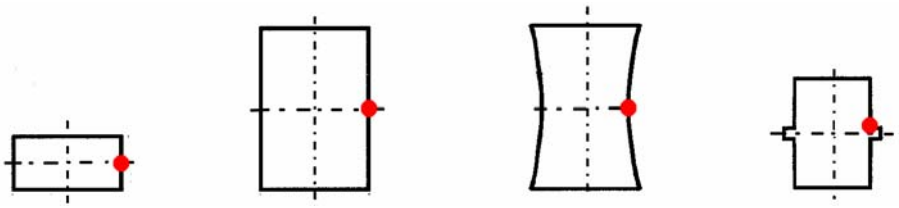

Figure 4.24. Critical point for crack initiation for each geometry.

To cover the range of loading and temperature conditions corresponding to crack initiation during the continuous casting process, compression tests have been carried out at three temperatures (800, 900 and 1000 °C) and two strain rates ($1\ 10^{-3}$ and $5\ 10^{-4}\ s^{-1}$); with at least three samples for each combination and for each geometry to ensure statistically relevant results.

The experiments have been carried out at the IBF following the experimental schedule and the specifications defined as part of this work. More details regarding the experimental set-up can be found in the report provided by the IBF together with a first discussion of the results and an analysis of the reproducibility of the tests (Wolske 2001). The finite element simulations relative to these tests have been done as part of this thesis and are presented hereafter.

4.5.2.3 Numerical simulations

The finite element simulations of the acoustic tests allow the determination of the formability curves for the material but they also predict the stress, strain and temperature fields in the whole specimen and in particular in the region where the crack is expected to appear. The stresses, strains and temperatures histories at the critical point can then be collected during the simulations to be used as macroscopic data for the

mesoscopic simulations to be carried out for the identification of the damage law parameters.

The material law used for these simulations is the elastic-viscous-plastic law that is also used to model the grains behaviour of the mesoscopic model (see equation (3.1)). The temperature is fixed at the corresponding test temperature for each simulation. The compression load is modelled using a tool whose displacement produces a vertical logarithmic strain in the sample corresponding to the required constant strain rate. A contact law with friction is used between the sample and the tool.

Description of the simulations

Due to the revolution symmetry of the problem, axisymmetric models can be created to limit the size of the simulations. There is also a horizontal plane of symmetry in the middle of the specimen which allows reducing the model to only half the height of the specimen. The meshes are realised using standard 8-node thermo-mechanical elements with four integration points. The upper right element of each mesh is divided into two 6-node compatible triangular elements with three integration points; this refinement was necessary to avoid a complete crushing of the quadrangular element when the side of the specimen comes in contact with the foundation during the simulation. A mesh sensitivity analysis is carried out for each geometry, focusing on the accurate modelling of the critical zone as presented in the next section.

For each analysis, the temperature of the nodes is fixed to the test temperature and kept constant during the whole simulation. The movement of the horizontal tool, i.e. the foundation, drives the simulation. It is imposed via the definition of its vertical position which is calculated so that the logarithmic strain rate is constant and corresponds to the specifications of the experiment for each particular test. Classical contact finite elements associated with a Coulomb's contact law are placed on the top and side of the specimen to assure a proper modelling of the contact between the solid and the foundation during the compression. The boundary conditions and contact elements are presented in a generic way in Figure 4.25, they are similar for the four specimens studied.

Initial simulations have shown that the results are strongly function of the friction coefficient between the tool and the sample. Therefore, further experiments performed at IBF using the same procedure as for the acoustic tests have been necessary to determine the actual friction coefficient. The chosen tests were ring tests at 800 °C and with a constant displacement rate of the tool of $8\ 10^{-3}$ mm s^{-1}. The friction

coefficient found is 0.2 (Volles 2003). This value is supposed to be independent of the temperature in the range corresponding to the acoustic tests.

The modified Norton-Hoff law is used to model the material behaviour. The parameters used are those defined in Table 4.5.

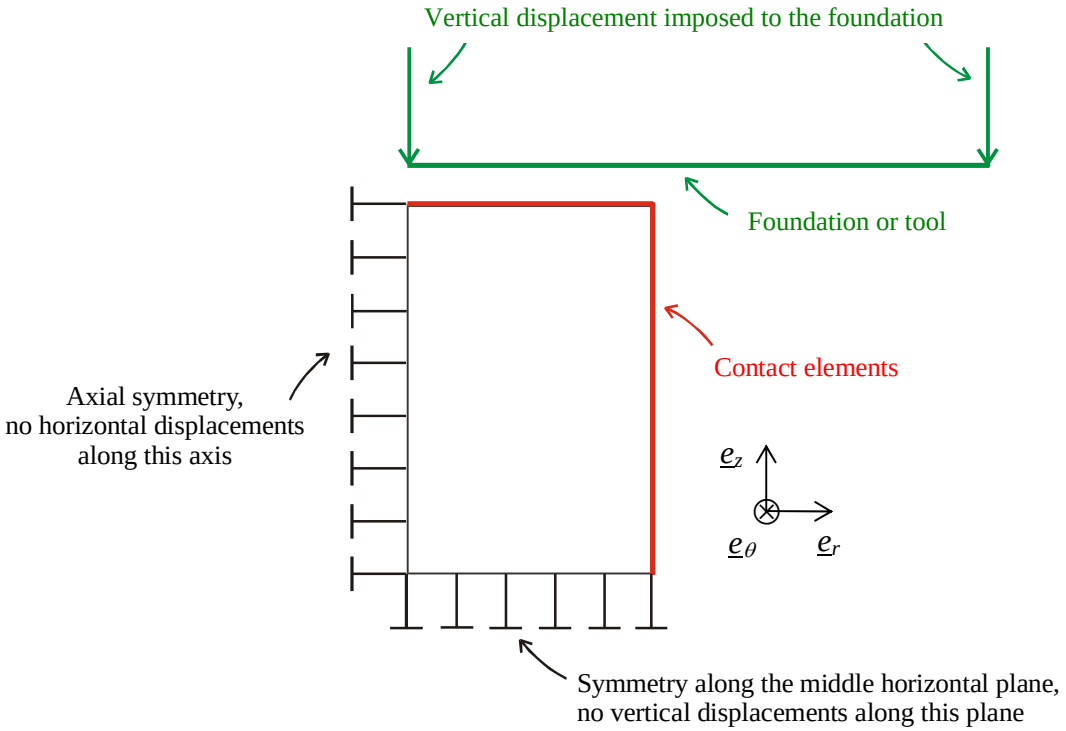

Figure 4.25. Boundary conditions and contact elements for the compression tests.

Mesh sensitivity

Analysing the sensitivity of the results to the mesh is a recommended step of any finite element simulation but it is particularly important in the context of this study as reliable local results are required for the parameters identification phase.

At least two meshes have been created for each of the geometry of Figure 4.23. The characteristics of these meshes are summarized in Table 4.7. The meshes have been realised using an automatic mesh generator which can use two different meshing strategies. The meshing type is given to differentiate between the different cases tested. The frontal meshing technique starts by dividing the contours of the zone to be meshed and then progress towards the inside of the zone by defining the elements along an advancing front according to the density of elements required. The structured mesh creates a regular arrangement of the elements which can be defined through number of elements on the contours and/or densities. The technique, which only works if the zone

to be meshed has an even number of sides, is particularly appropriate for rectangular surfaces. Therefore, the best results are achieved by dividing the zone to be meshed into rectangles before running the structured mesh generator.

Other data in Table 4.7 are the number of nodes and elements, which give an insight into the size of the problem whereas the area of the critical element is used to compare the refinement of the different meshes in the critical zone. The last column of the table indicates the representative element length ratio between the critical elements of the different meshes, the coarser critical element for each geometry being taken as a reference. This ratio is given by the square root of the ratio between the areas of the critical elements for the two meshes compared. It is a simple way to visualise the ratio between the elements sizes as it represents the ratio of the length of these critical elements if they where perfectly square.

Table 4.7. Characteristics of the different meshes[1].

Specimen type	Meshing type	Number of elements	Number of nodes	Area of critical element [mm^2]	Length ratio
Flat	Frontal	603	1760	$5.292\ 10^{-3}$	1
	Structured 1	**698**	**2032**	**$2.996\ 10^{-3}$**	0.75
	Structured 2	1723	5071	$1.129\ 10^{-3}$	0.46
Slim	**Frontal**	**716**	**2103**	**$6.601\ 10^{-3}$**	0.21
	Structured	1071	3144	$1.500\ 10^{-1}$	1
Concave	Frontal	698	2049	$5.775\ 10^{-3}$	0.38
	Structured	**630**	**1817**	**$4.048\ 10^{-2}$**	1
Flange	Frontal	715	2136	$6.782\ 10^{-3}$	1
	Structured	1028	3071	$3.616\ 10^{-3}$	0.73

[1]Data in bold characters indicate the meshes that have been retained after the mesh sensitivity analysis.

The criteria to establish the quality of the mesh is based on the analysis of the stress field in the critical zone. The reproducibility of the results for various elements sizes ensures that the mesh is refined enough in the critical zone to give an accurate solution. Comparing the reaction forces on the tool for the different meshes is a technique that is often used to validate a mesh but it is not appropriate here as it does not imply that the solution is locally accurate.

The created meshes and the stress fields in the critical zone are reported hereafter for each specimen's geometry. The figures also show the location of the

critical element, which is highlighted in red for each mesh after zooming on the critical zone. The scale used is consistent between all the figures presented in this section so that the size of the elements can be visually compared. Although the same standard procedure is used in each case to validate the quality of the mesh, i.e. the comparison of the stresses in the critical element, the tested models are progressively improved based on the lessons learned throughout the previous analyses and additional verifications are presented individually to clarify some of the results.

For the mesh sensitivity analysis, only one temperature and one strain rate have been used (T = 900 °C and $\dot{\varepsilon}$ = 5 10^{-4} s^{-1}).

Flat specimen

The frontal mesh and the two structured meshes created for the flat geometry are shown in Figure 4.26.

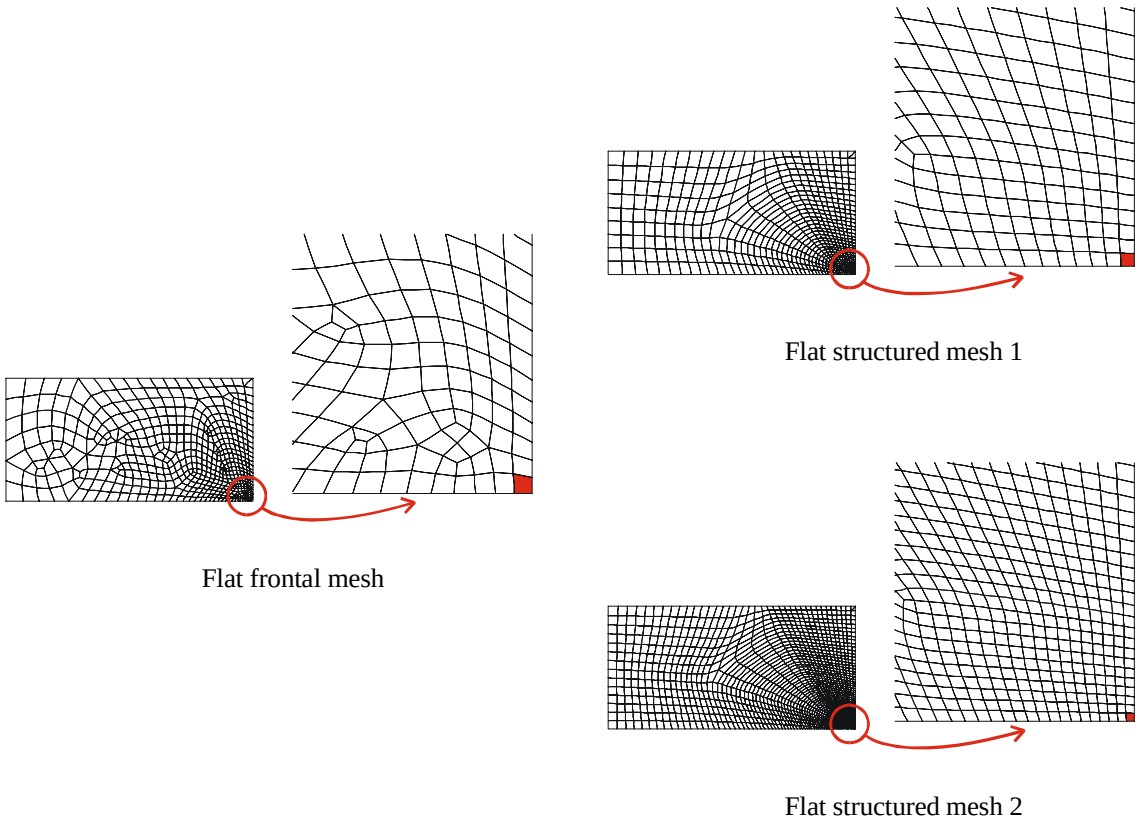

Figure 4.26. Frontal and structured meshes for the flat specimen.

In order to accurately conclude on the convergence of the results relative to the mesh size, it is recommended to divide the elements side length at least by two when refining the meshes. For the flat example, the critical element length ratio between the

first structured mesh and the frontal mesh is 0.75 (see Table 4.7); i.e. a reduction of 25% only of the length of the elements side between the two meshes. Therefore, a second structured mesh for which the length ratio is less than 0.5 has been created.

The stress history in the critical element is represented in Figure 4.27 for the three meshes (frontal (fr), structured 1 (str1) and structured 2 (str2)). The stresses recorded are calculated by averaging the values obtained for the four integration points of the element. For all the graphs of this chapter, *r* refers to the radial direction, *z* to the axial direction and *c* to the circumferential direction (also referred to as θ). It is verified that σ_r is close to zero as the critical point is localized on the surface of the specimen; that σ_θ is positive as the specimen is in tension in the circumferential direction around the critical point; and that σ_z is negative as the specimen sustains an axial compression load. The shear stresses are not represented as they are close to zero and will not be modelled in the parameters identification simulations

Although small jumps in the curves occur after t = 750 s, Figure 4.27 shows that the stress histories obtained with the different meshes are almost identical. The jumps are correlated with the progressive contact interaction between the foundation and the contact element of the side of the specimen during the crushing of the specimen, which explains why they do not appear simultaneously for all the meshes. These jumps do not represent any physical behaviour and will be smoothed before using the results as input data for the damage parameters identification phase.

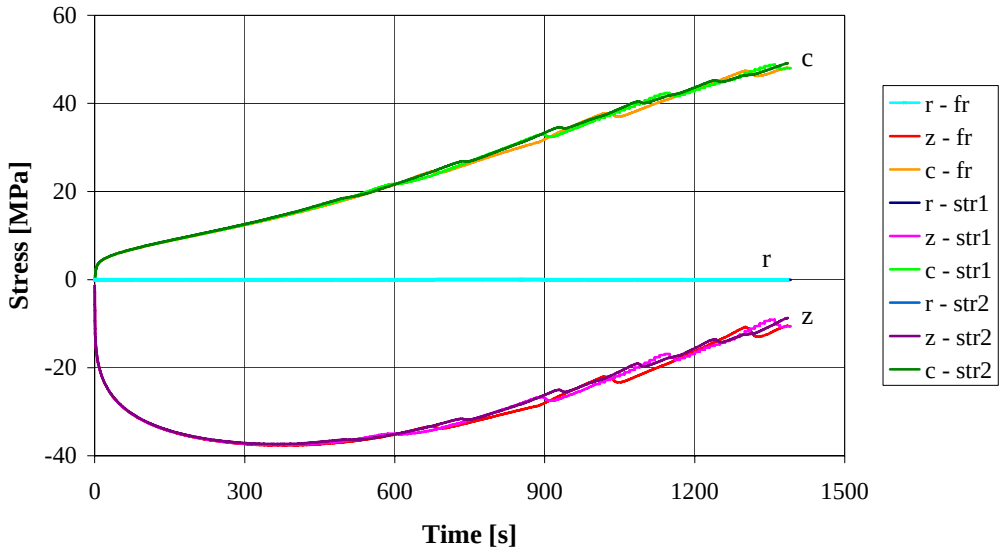

Figure 4.27. Mesh sensitivity analysis for the flat specimen: stresses in the radial (r), axial (z) and circumferential (c) directions in the critical element for the three meshes of Figure 4.26.

The sensitivity analysis has proved that the three meshes were converging to the same results, which is an indication that the mesh quality in each case is appropriate for the problem. In order to limit the computation time, the subsequent simulations will be carried out using the structured mesh 1 because it contains a relatively small number of elements and nodes compared to the structured mesh 2 and provides a slightly finer discretization of the contact surface of the specimen compared to the frontal mesh.

Slim specimen

Figure 4.28 represents the frontal (fr) and structured (str) meshes created for the modelling of the slim specimen. The structured mesh has been created using rectangular elements of size 0.2 mm × 0.75 mm. The objective of this configuration is to analyse the impact of starting with elongated elements on the deformed mesh after crushing. The length ratio between the meshes as defined in Table 4.7 is 0.21, i.e. that the area of the critical element of the structured mesh is about 25 times higher than the area of the critical element of the frontal mesh.

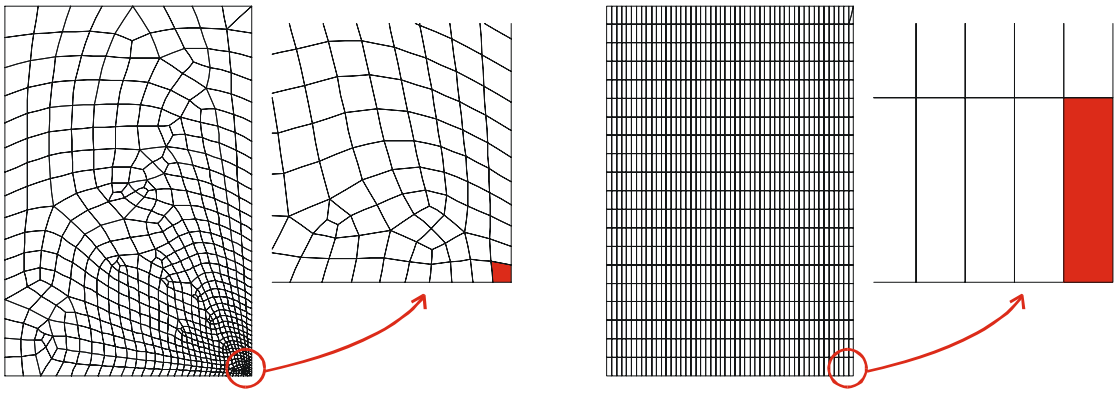

Slim frontal mesh Slim structured mesh

Figure 4.28. Frontal and structured meshes for the slim specimen.

Figure 4.29 shows the stress fields in the critical element for both meshes. Apart from the oscillations due to the contact behaviour between the foundation and the side of the specimen, the two curves are consistent. It can be concluded that both meshes are suitable for the simulations. The choice is then to use the frontal mesh for this specimen geometry as it contains less elements and nodes. Moreover, the deformed mesh obtained at the end of the simulation is acceptable with regards to the shape of the elements as can be seen in Figure 4.30(a). The distortion of the structured mesh at the end of simulation presents a similar pattern although elongated elements have been used to model the initial configuration.

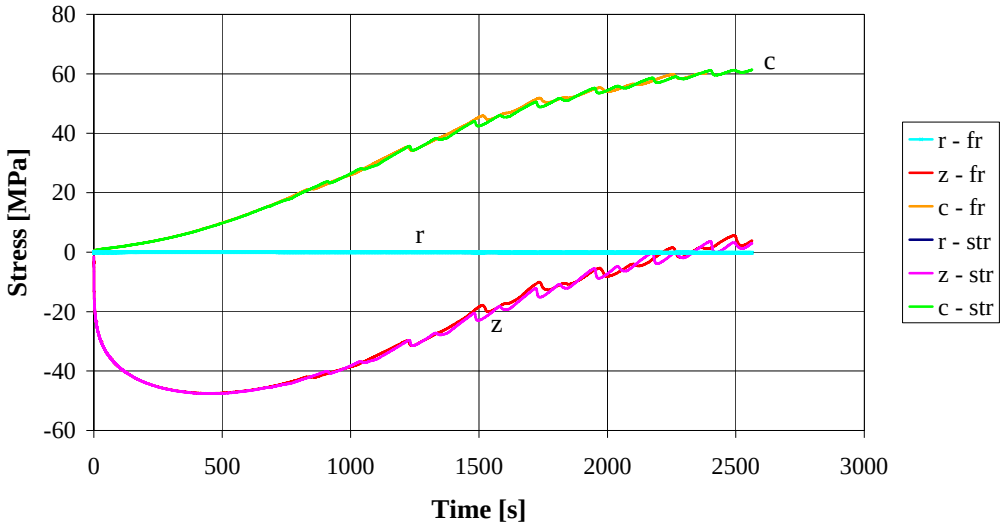

Figure 4.29. Mesh sensitivity analysis for the slim specimen: stresses in the radial (r), axial (z) and circumferential (c) directions in the critical element for the two meshes of Figure 4.28.

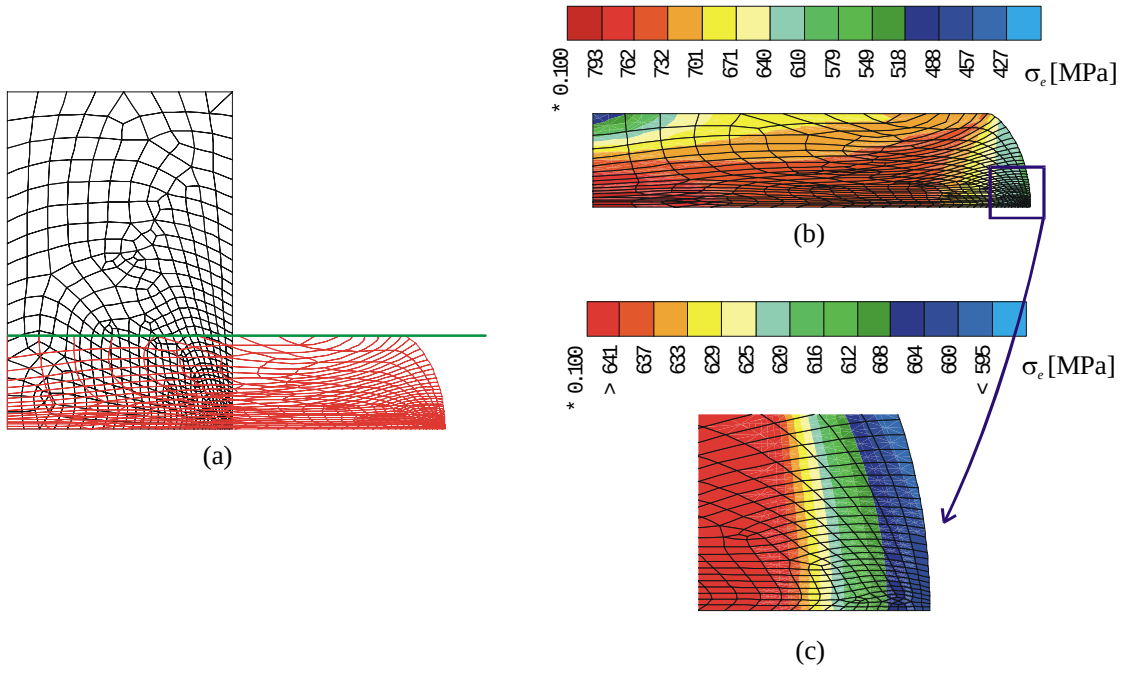

Figure 4.30. Analysis of the slim specimen after compression (t = 2563 s). a) Deformation of the frontal mesh, b) von Mises equivalent stress in the whole specimen, c) von Mises equivalent stress after zooming on the critical zone.

Figure 4.30(b) also shows the von Mises equivalent stress in the whole specimen after compression. A zoom on the critical area confirms that the stress gradients in this zone are not important and that the data obtained with different element sizes can be relied on for the parameters identification simulations. In particular, the variation of the

von Mises equivalent stress along the radial axis is less than 1% over at least three elements when progressing from the external surface to the inside of the specimen (Figure 4.30(c)).

Concave specimen

Figure 4.31 shows the frontal and structured mesh for the concave geometry specimen. The structured mesh has been created by dividing the meshing area in four zones. The objective is to keep coarse elements in the zones that are not so much affected by the deformation and to put refined elements close to the critical point and on the side of the specimen so that the progressive contact between this part of the specimen and the foundation is accurately modelled.

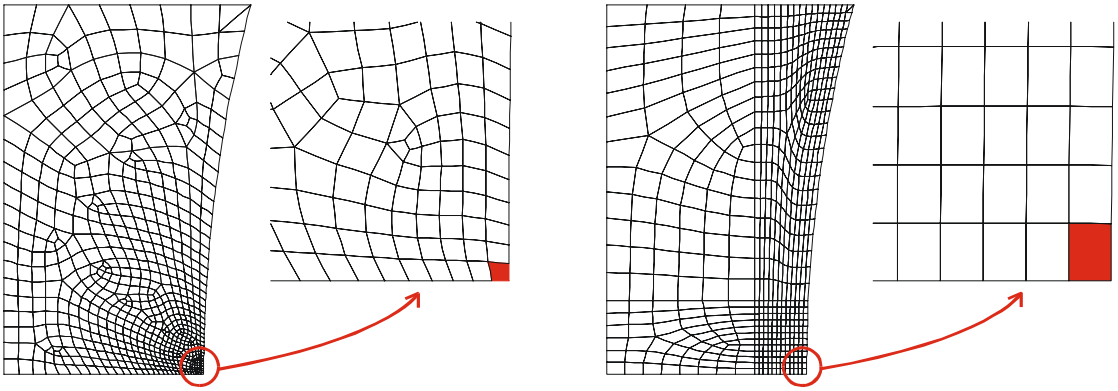

Concave frontal mesh Concave structured mesh

Figure 4.31. Frontal and structured meshes for the concave specimen.

An additional layer of contact and foundation elements has been introduced on the side of concave frontal mesh (see Figure 4.32) as it appeared that the some elements of this part of the specimen came in contact with each other during the simulation.

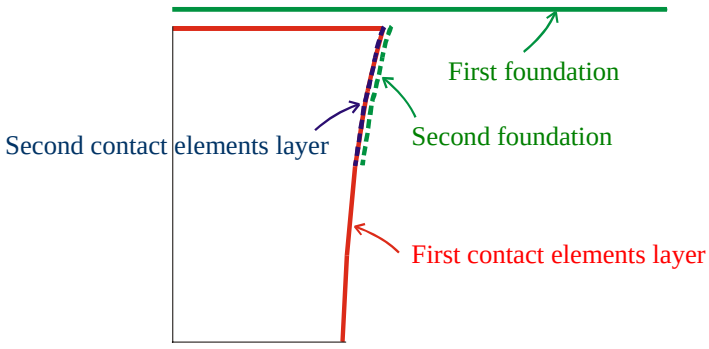

Figure 4.32. Concave model with additional layer of contact and foundation elements.

The stress field histories for the first frontal mesh (fr), the frontal mesh with the additional layer of contact and foundation element (frc) and the structured mesh (str) are presented in Figure 4.33. Up to t = 2300 s, the three meshes give almost identical results and it can be concluded that the three of them are acceptable based on the mesh sensitivity criterion. As in Figure 4.27 and Figure 4.29, the different curves corresponding to the radial stresses are superimposed along the x-axis. The circumferential stress σ_θ and the axial stress σ_z present a smooth behaviour with the structured mesh but jumps are observed with the two frontal meshes after t = 2300 s.

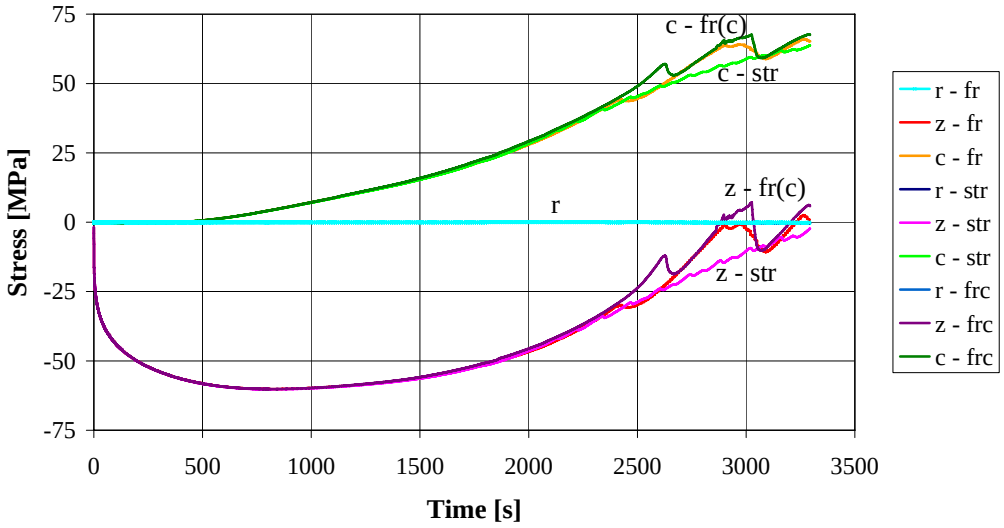

Figure 4.33. Mesh sensitivity analysis for the concave specimen: stresses in the radial (r), axial (z) and circumferential (c) directions in the critical element for the two meshes of Figure 4.31.

Figure 4.34 shows the deformed frontal and structured meshes at the end of the simulation. Globally, it is observed that the elements of the structured mesh have deformed shapes less distorted than those of the elements at the same location in the frontal mesh. A detailed analysis of the deformed meshes leads to the conclusion that the jumps appearing in the stress fields do not represent the physical behaviour of the material but are linked to numerical problems. This is illustrated in Figure 4.35 where a zoom close to the foundation is shown at t = 2980 s; i.e. when the jumps are observed. For the first frontal mesh, it is clearly shown that the elements of the side of the specimen penetrate in each other (Figure 4.35(a)).

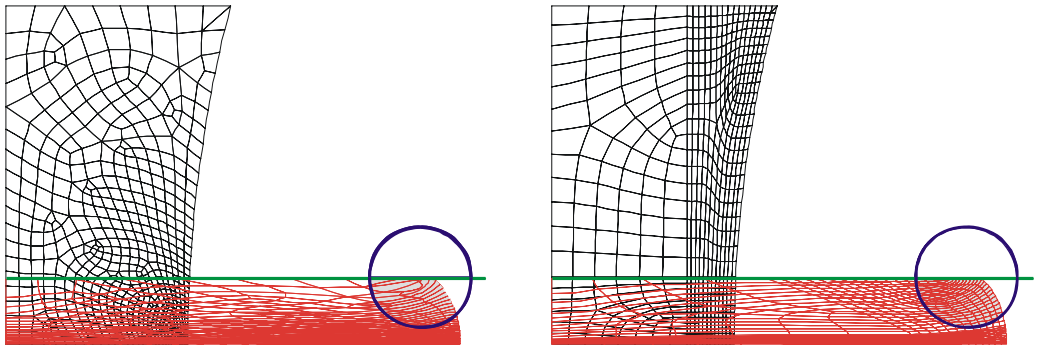

Concave frontal mesh Concave structured mesh

Figure 4.34. Deformation of the frontal and structured meshes for the concave specimen at the end of the simulation (t = 3294 s) and location of the zoom area for Figure 4.35.

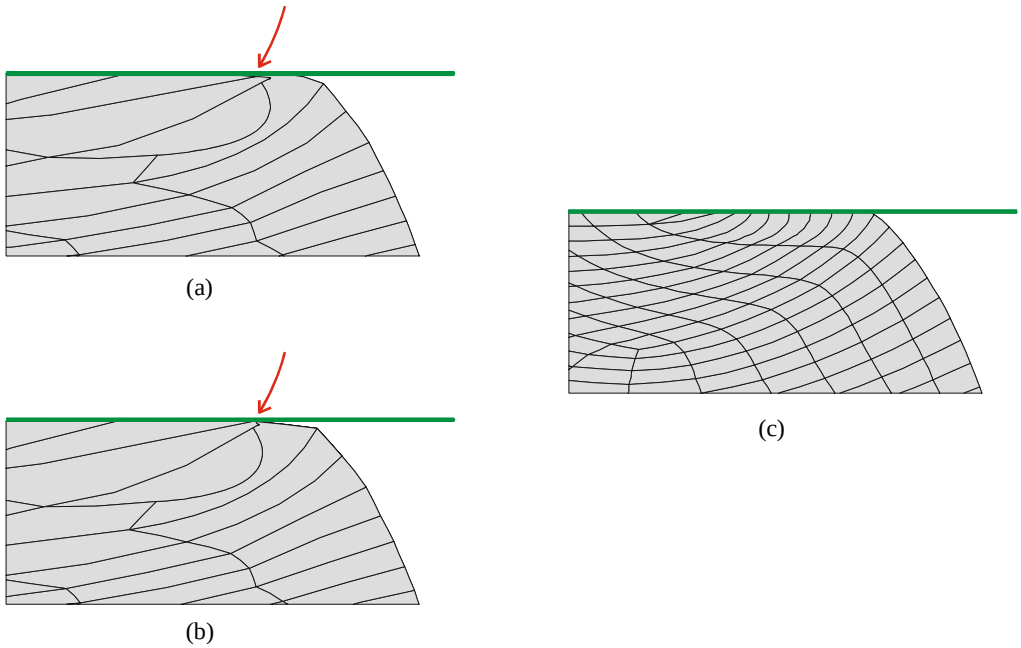

(a)

(b)

(c)

Figure 4.35. Zoom on the deformed mesh next to the foundation for the concave specimen at t = 2980 s. a) Frontal mesh with one layer of contact and foundation elements, b) frontal mesh with two layers of contact and foundation elements, c) structured mesh.

With an additional layer of contact and foundation elements, the behaviour of the mesh is slightly better although a small penetration is still observed due the penalisation method used to model the contact behaviour. Nevertheless, the numerical inconstancies are not resolved as three nodes belonging to the same element side collapse in a single point after coming in contact with the foundation (Figure 4.35(b)). By comparison, the deformation of the structured mesh as shown in Figure 4.35(c) is smooth and the final shape of the elements is correct; i.e. close to a square shape. Finally, as accurate results are obtained with the structured mesh only, it is obvious that this mesh has to be used for the other simulations.

Flange specimen

Figure 4.36 shows the frontal and structured mesh for the flange geometry specimen.

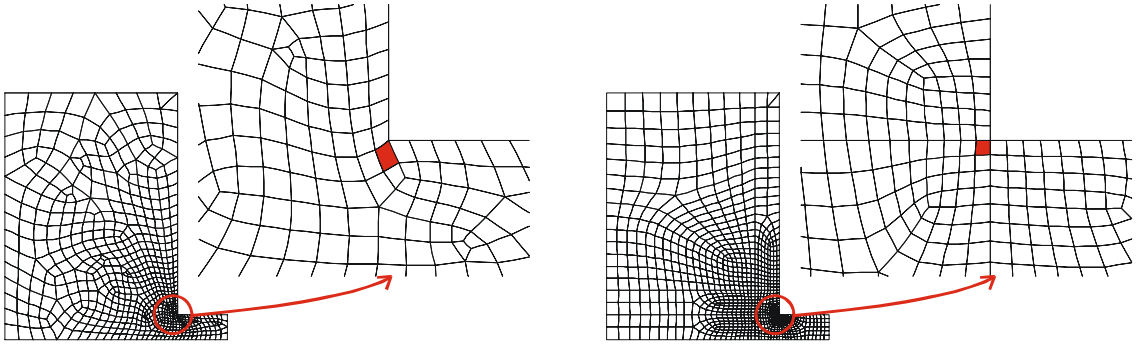

Flange frontal mesh Flange structured mesh

Figure 4.36. Frontal and structured meshes for the flange specimen.

Higher element densities are imposed close to the critical zone to create the pattern of the mesh for both the frontal and structured mesh. As the form of the specimen is not rectangular, the structured mesh created by the mesh generator is an hybrid form which uses both the structured and frontal algorithms. The two meshes produced are different and can be used to test the mesh sensibility.

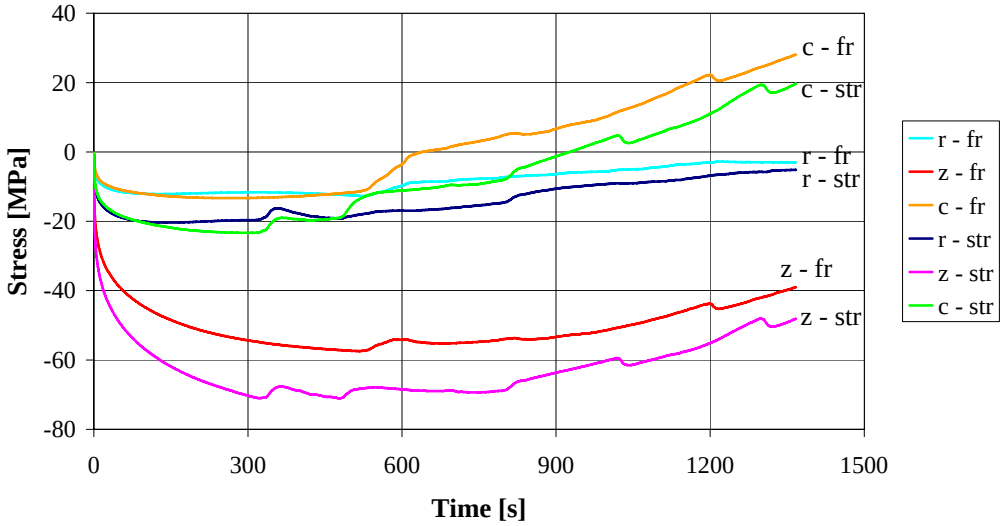

Figure 4.37. Mesh sensitivity analysis for the flange specimen: stresses in the radial (r), axial (z) and circumferential (c) directions in the critical element for the two meshes of Figure 4.36.

The stress fields in the critical element are shown in Figure 4.37 for the frontal (fr) and structured (str) meshes. For the flange specimen, it observed that the stress histories do not match for the two meshes although the critical element is localised in the same area and the element size is similar in both cases for this particular example.

Like for the other specimens shapes, the results represented in Figure 4.37 are the average values of the respective stresses at the four integration points of the critical element. In order to confirm the sensitivity to the mesh, results have been plotted using a second set of integration points. The three integration points used for the second analysis are shown in Figure 4.38. They are represented by black crosses and correspond to the closest integration points that surround the critical area; i.e. the connection between the cylindrical part of the specimen and its flange.

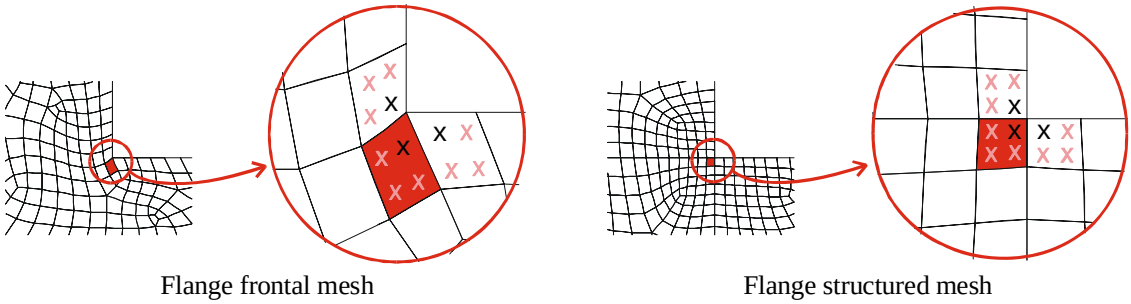

Figure 4.38. Zoom around the critical zone for the flange specimen. Crosses symbolize integration points; black crosses indicate the second set of integration points used.

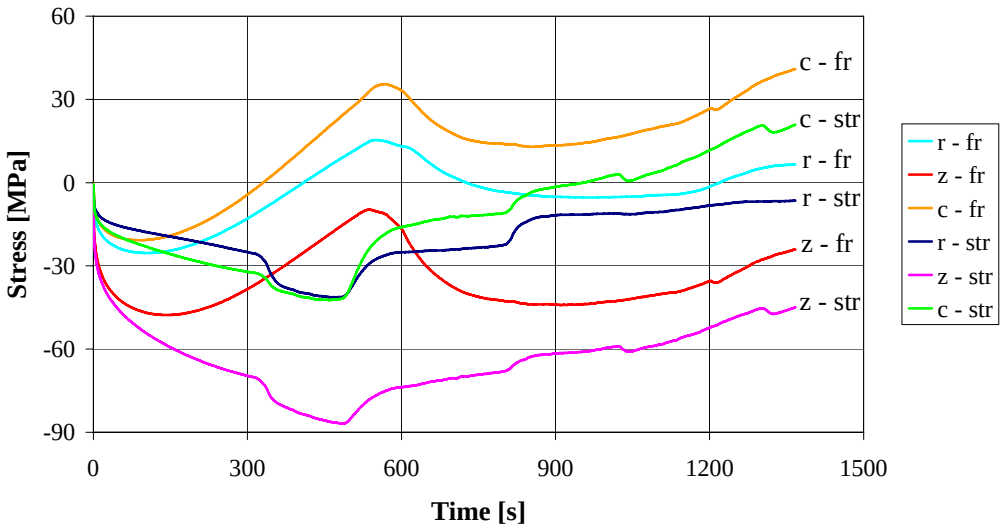

Figure 4.39. Mesh sensitivity analysis for the flange specimen: average stresses in the radial (r), axial (z) and circumferential (c) directions at the three integrations points closest to the critical point for the two meshes of Figure 4.36 using the integration points defined in Figure 4.38.

The stress fields histories are shown in Figure 4.39 using an average on the three integration points defined in Figure 4.38. It is observed that the differences between the two meshes are even bigger than with the initial method.

For the flange specimen, the high stress concentration level in the critical zone is responsible for the sensitivity of the results to the mesh. This conclusion is confirmed in Figure 4.40 where the von Mises equivalent stress in the critical zone is represented for each of the meshes; a steep equivalent stress gradient is observed in the figure. The stress concentration is due to the presence of a sharp angle at the connection between the flange and the cylindrical part of the specimen. When the experiments are used to define formability curves, it is possible to specify a representative mesh density in this area and to use the results of the acoustic tests simulations for the formability analysis of parts presenting a similar geometry by using a mesh of equal density. For the application foreseen here, i.e. the definition of the damage parameters of the interface law, the stresses and strains histories have to be precisely defined. Therefore, due to the outcomes of the mesh sensitivity study, it has been decided to exclude the flange specimen from the analysis as no local results can be uniquely defined with this specific geometry.

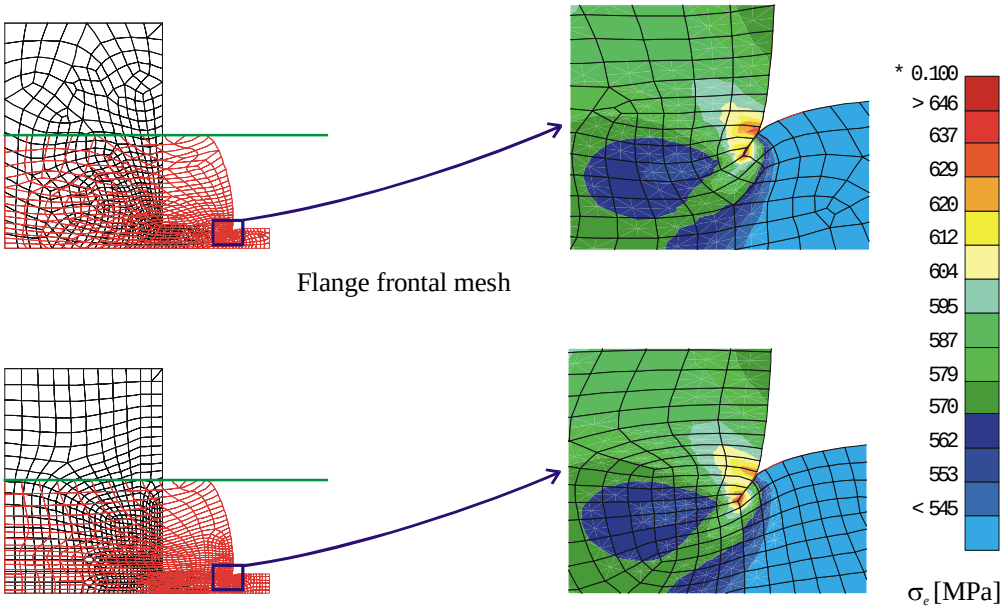

Figure 4.40. Deformed mesh and von Mises equivalent stress in the critical zone for the flange frontal mesh structured mesh.

Summary

Different element sizes have been tested in the critical zone and the stress and strain fields have been compared in order to analyse the mesh dependence of the results. For the slim, flat and concave samples, the analysis has identified meshes for which the results of the simulations in terms of stress and strain distributions have converged; these meshes are highlighted in bold characters in Table 4.7. For the flange sample, the stress concentration is so high in the critical zone that it was not possible to find a mesh with a reasonable number of elements for which the results converged with a sufficiently high accuracy. Therefore, it has been decided to keep only the three first samples, which give reliable results, for the identification stage.

Results of the acoustic simulations

The standard technique for the determination of the formability consists in presenting the results of the acoustic tests using $\left(\frac{\sigma_1}{\sigma_e}, \varepsilon_e\right)$ curves defined by finite element simulations, where σ_1 is the maximal principal stress, σ_e the von Mises equivalent stress and ε_e the equivalent strain at the critical point of the specimen (Kopp and Bernrath 1999). That way, the results are represented in a normalized form that can then be used to assess the formability of the material for other processes.

For each of the tests, the height (h_{crack}) of the specimen at the instant of acoustic emission (i.e. the first crack initiation) was given in the IBF report (Wolske 2001). The corresponding time (t_{crack}) can be calculated using equation (4.1) when the strain rate $\dot{\varepsilon}$ is known:

$$h_t = h_0 \cdot \exp\left(-\dot{\varepsilon} t\right) \tag{4.1}$$

where h_0 is the initial height of the specimen, h_t its height at time t and $\dot{\varepsilon}$ the logarithmic vertical strain rate for the experiments; i.e. $\dot{\varepsilon}=10^{-3}$ s^{-1} and $\dot{\varepsilon}=5\ 10^{-4}$ s^{-1} in this study. The finite element simulations are driven by the displacement of the foundation which is also calculated using equation (4.1).

The specimen height (h_{crack}) at crack initiation and the corresponding time (t_{crack}) for the two strain rates and three temperatures tested are indicated in Table 4.8 for the concave geometry, Table 4.9 for the slim geometry and Table 4.10 for the flat geometry. The results corresponding to the flange geometry are not presented as they are not used for the parameters identification.

For most of the tests, visible cracks were found on the specimen after compression, these results are presented using regular fonts. Data presented in italic in

the results tables correspond to experiments for which no visible cracks were found after compression although acoustic emissions had been recorded; whereas data which are underlined correspond to cases where it was impossible to define with certitude if a crack was present at the critical point or not after compression with acoustic emission. Failed tests are referred to as “no data recorded” in the results tables.

Table 4.8. Instant of crack initiation for the concave specimen.

T [°C]	$\dot{\varepsilon} = 10^{-3}\ s^{-1}$		$\dot{\varepsilon} = 5\ 10^{-4}\ s^{-1}$	
	h_{crack} [mm]	t_{crack} [s]	h_{crack} [mm]	t_{crack} [s]
800	17.79	522.56	*15.62*	*1305.29*
	16.71	*585.19*	13.46	1602.95
	15.83	639.29	13.01	1670.96
900	14.81	705.89	6.76	2980.35
	14.29	741.64	6.57	3037.37
	14.14	752.19	5.78	3293.59
1000	*8.79*	*1227.58*	10.97	2012.07
	7.5	1386.29	10.73	2056.31
	No data recorded		8.5	2522.26

Table 4.9. Instant of crack initiation for the slim specimen.

T [°C]	$\dot{\varepsilon} = 10^{-3}\ s^{-1}$		$\dot{\varepsilon} = 5\ 10^{-4}\ s^{-1}$	
	h_{crack} [mm]	t_{crack} [s]	h_{crack} [mm]	t_{crack} [s]
800	13.85	772.91	18.31	987.50
	13.54	795.55	16.92	1145.40
	No data recorded		13.49	1598.50
900	15.18	681.22	9.63	2272.63
	14.66	716.07	9.07	2392.45
	10.35	1064.21	8.33	2562.67
1000	12.5	875.47	14.62	1437.61
	11.08	996.06	11.23	1965.22
	No data recorded		*No data recorded*	

Table 4.10. Instant of crack initiation for the flat specimen.

T [°C]	$\dot{\varepsilon} = 10^{-3}$ s^{-1}		$\dot{\varepsilon} = 5\ 10^{-4}$ s^{-1}	
	h_{crack} [mm]	t_{crack} [s]	h_{crack} [mm]	t_{crack} [s]
800	4.63	770.03	7.38	607.62
	3.95	*928.87*	*6.59*	*834.06*
	2.81	1269.40	5.43	1221.29
900	*5.13*	*667.48*	6.53	852.36
	4.74	746.55	6.28	930.43
	4.41	818.71	5.29	1273.53
	4.27	850.97		
1000	5.62	576.25	5.88	1062.06
	5.18	657.78	5.85	1072.29
	4.74	746.55	*No data recorded*	

Generally, t_{crack} for the cases without visible cracks are smaller than for the regular cases with visible cracks and this could indicate that the first cracks have initiated inside the specimen, at a location were a flaw was initially present. This behaviour is observed for the concave specimen at $\dot{\varepsilon}$=10^{-3} s^{-1} and T = 1000 °C or at $\dot{\varepsilon}$=5 10^{-4} s^{-1} and T = 800 °C (Table 4.8), or for the flat specimen at $\dot{\varepsilon}$=10^{-3} s^{-1} and T = 900 °C (Table 4.10). Therefore, these data have to be considered critically when defining the interface law damage parameters.

The curves $\left(\frac{\sigma_1}{\sigma_e}, \varepsilon_e\right)$ for the critical point of each specimen are presented in Figure 4.41 to Figure 4.43, they have been compiled from the results of finite elements simulations using the meshes defined in the previous section. On these curves, symbols indicate the instant of first crack initiation for each of the specimens tested, keeping in mind that at least three tests were carried out for each combination of parameters (geometry, temperature and strain rate). A colour code is used to indicate the data points for which no visible cracks could be observed on the surface of the compressed specimens and those for which it could not be defined with certainty whether or not a crack was present; the former being represented in red and the later in orange.

The presentation of the results in terms of normalized stress eliminates the possibility to observe the viscosity effect included in the formulation of the modified Norton-Hoff law (equation (3.1)). No general conclusion can be made regarding the effect of the strain rate on the stress or strain level at crack initiation either. For

example, the cracks in the flat specimens always initiate at a lower equivalent strain for the slowest strain rate compared to the highest strain rate but it is the other way round for the concave specimens at T = 800 and 900 °C. It is to be noted that the ratio between the two strain rates tested is only ½ and that it was not possible to use strain rates below $\dot{\varepsilon}$ =5 10^{-4} s^{-1} due to the limitations of the machine. If they had been carried out, tests at lower strain rates could have led to a different conclusion.

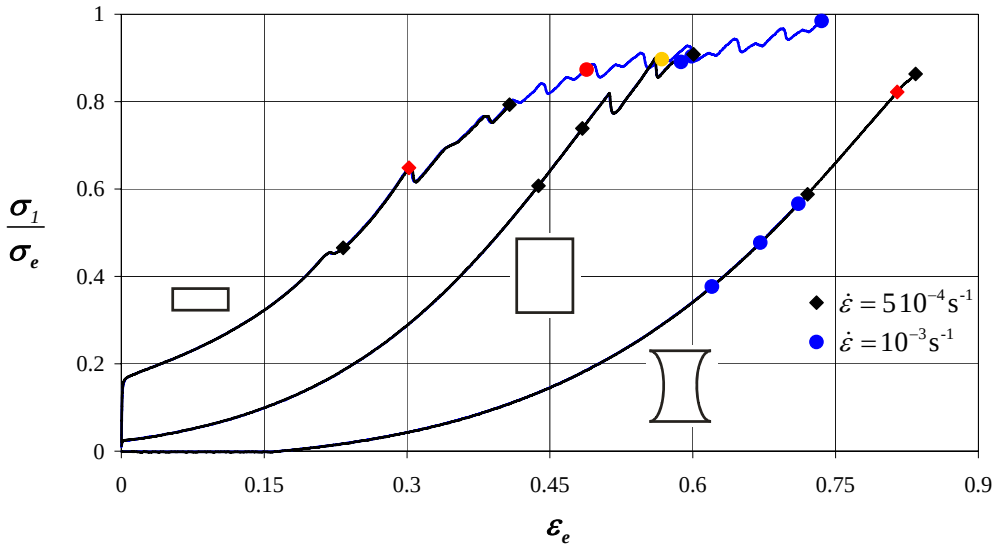

Figure 4.41. Instant of first crack initiation determined by acoustic emission at T = 800 °C.

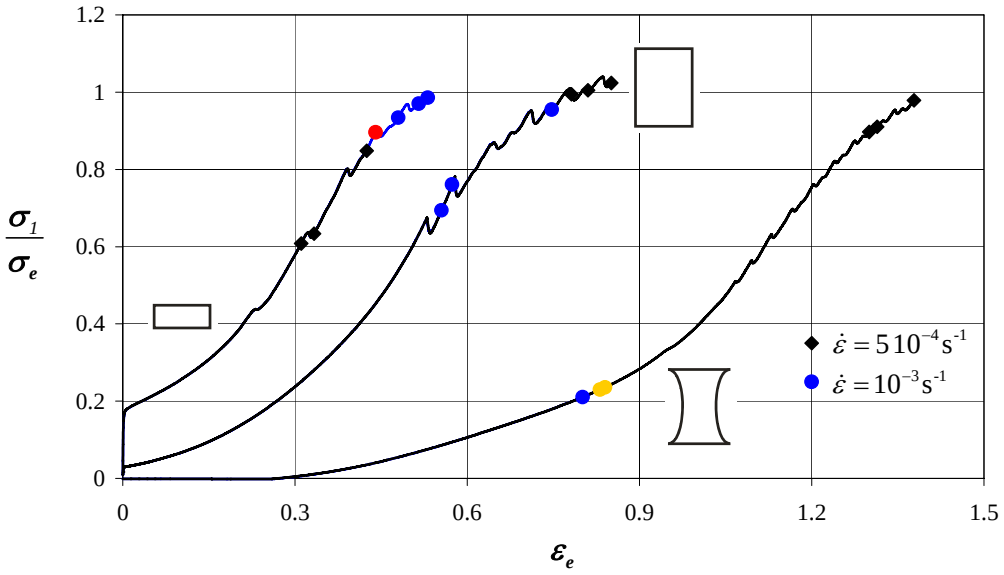

Figure 4.42. Instant of first crack initiation determined by acoustic emission at T = 900 °C.

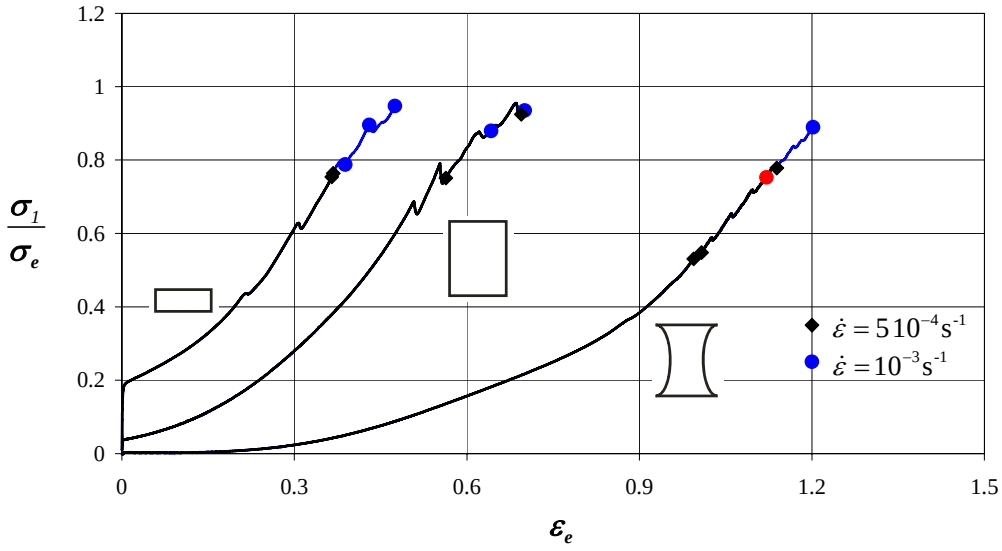

Figure 4.43. Instant of first crack initiation determined by acoustic emission at T = 1000 °C.

The experiments at 800 °C present the biggest dispersion pattern in terms of first crack initiation (Figure 4.41); this case is also the one for which most of the data points have to be considered critically. For the other temperatures, the crack initiation moment is more reproducible as shown in Figure 4.42 at 900 °C and Figure 4.43 at 1000 °C.

The presentation of the finite element data under the form proposed by IBF is used here to visualize the repartition of the experimental results in terms of crack initiation but the definition of formability limit curves is not here considered as a deliverable of the research.

4.6 PARAMETERS OF THE INTERFACE LAW

A table summarizing the parameters to be defined for the interface damage law has been presented in Chapter 3 before describing the first simulations carried out during the development phase of the model (see Table 3.3). These parameters can be categorized in three different groups with regard to the identification methodology. Firstly, several parameters are defined using the data gathered trough the microscopic and macroscopic experiments of sections 4.3 and 4.4. The details of the procedures applied are presented in section 4.6.1. Then a second batch of parameters is directly issued from a literature survey as shown in section 4.6.2. Finally, the remaining parameters are defined using the results of the acoustic tests which were part of the damage analysis of section 4.5. The identification method for the definition of those parameters is detailed in section 4.6.3.

4.6.1 PARAMETERS DEFINED EXPERIMENTALLY

4.6.1.1 Grain size

The first parameter that has been experimentally defined is the grain size. Its value is based on the observation of the austenitic microstructure of the material. The details of the analysis are presented in section 4.3.1.2. The average grain size obtained is 1 mm.

The grain size is indirectly introduced in the model through the geometric definition of the representative mesh for the material but it also directly appears in the equations modelling the grain boundary sliding as detailed in section 3.4.3.1.

4.6.1.2 Creep parameters

The creep parameters *B* and *n* that appear in the classical creep law can be extracted from the modified Norton-Hoff law. These two laws have been defined in Chapter 3 by equations (3.25) and (3.1) respectively. The classical creep law is not directly used to model the macroscopic material behaviour as the more detailed modified Norton-Hoff law is available for this purpose. Nevertheless, the parameters of the classical creep law are directly used in the damage law for the modelling of the grain boundary sliding (section 3.4.3.1) and void growth (3.4.3.2).

The formulation of the modified Norton-Hoff law is not identical to the classical creep law but it is possible to make the link between the two equations using several simplification hypotheses.

$$\text{Eq. (3.1)} \quad \rightarrow \quad \sigma_e = \varepsilon_e^{p_4}.exp\left(-p_1\varepsilon_e\right).p_2.\sqrt{3}.\left(\sqrt{3}.\dot{\varepsilon}_e\right)^{p_3}$$

$$\text{Eq. (3.25)} \quad \rightarrow \qquad \dot{\varepsilon}_e = B\left(\sigma_e\right)^n$$

The modified Norton-Hoff law links the equivalent stress to the equivalent strain and strain rate and takes the hardening and softening effects into account whereas the classical Norton creep law only links the equivalent stress to the equivalent strain rate. Therefore, if the softening and hardening effects are neglected, i.e. if $p_1 = p_4 = 0$, equation (3.1) becomes:

$$\sigma_e = p_2.\sqrt{3}.\left(\sqrt{3}.\dot{\varepsilon}_e\right)^{p_3} \quad \Rightarrow \quad \dot{\varepsilon}_e = \frac{1}{\sqrt{3}}\left(\frac{1}{p_2\sqrt{3}}\right)^{\frac{1}{p_3}} \sigma_e^{\frac{1}{p_3}} \tag{4.2}$$

Comparing equations (3.1) and (4.2), it possible to extract the values of *B* and *n*:

$$B = \frac{1}{\sqrt{3}}\left(\frac{1}{p_2\sqrt{3}}\right)^{\frac{1}{p_3}} \tag{4.3}$$

$$n = \frac{1}{p_3} \tag{4.4}$$

In practical cases, $p_1 \neq p_4 \neq 0$ and the value of B is a function of ε_e which implies that only the creep exponent can be uniquely defined by equation (4.4).

For the present application, the creep coefficient B is determined for a chosen value of ε_e which is representative of the equivalent strain in the simulated process. During the continuous casting process, the deformations of the slab are very small and the simulations indicate that they are generally close to 7%. The Norton-Hoff curves for the material represented in Figure 4.15 to Figure 4.19 show that after the elastic domain, the stress for a given strain rate and temperature reaches a representative level and stays almost constant afterwards apart from the hardening and softening effects that can be present. This means that if the strain reaches a higher value locally in the model, the approximation made on using a specific value of ε_e to calculate B is still valid as the variations of the stress level are small. Therefore, calculating B at an equivalent strain $\varepsilon_e = 7\%$ is a realistic compromise, which corresponds to a representative stress level for the material during the deformation process.

Table 4.11 indicates the values of B and n as a function of the temperature T. The units are consistent with a stress measured in [MPa].

Table 4.11. Values of the creep parameters as a function of the temperature.

***T* [°C]**	***n***	***B* (7%)**
700	8.696	$2.263\ 10^{-21}$
800	4.329	$1.270\ 10^{-11}$
900	6.452	$1.821\ 10^{-14}$
1000	10.081	$1.461\ 10^{-18}$
1100	6.757	$3.642\ 10^{-13}$

As for the modified Norton-Hoff law, the parameters are given at several discrete temperatures and a linear interpolation is realized within the code to calculate the values at the temperature of the interface as show in Figure 4.44 and Figure 4.45.

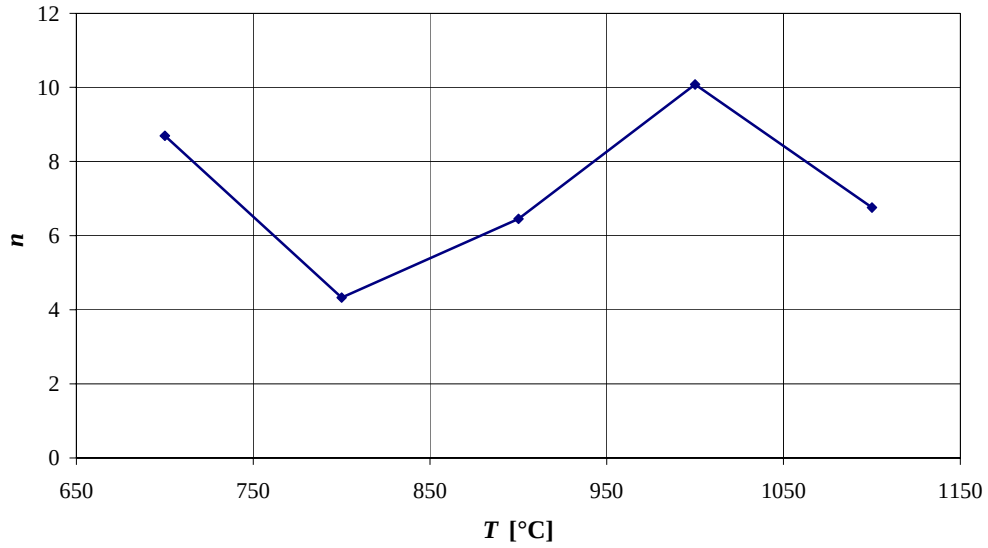

Figure 4.44. Variation of the creep parameters *n* with the temperature.

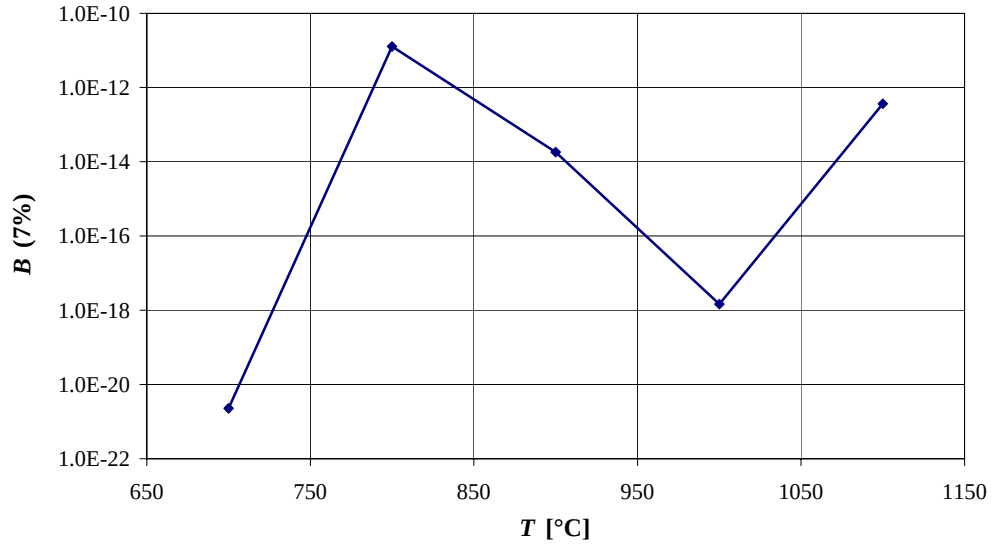

Figure 4.45. Variation of the creep coefficient *B* (7%) with the temperature.

4.6.1.3 Normalization stress

The normalization stress is used in the interface damage model when defining the nucleation behaviour (section 3.4.3.2). It is defined using the same conditions than for the definition of the creep parameters, i.e. for an equivalent strain rate $\varepsilon_e = 7\%$. As the objective is to define a value that is representative of the stress in the material during the continuous casting simulation, an intermediate equivalent strain rate equal to 10^{-3} s^{-1} as been imposed. Table 4.12 indicates the value of Σ_0 for five different temperatures.

Table 4.12. Normalization stress Σ_0 as a function of the temperature.

T [°C]	Σ_0 [MPa]
700	106.955
800	66.683
900	46.202
1000	29.625
1100	24.941

During the numerical simulation, the program interpolates between those values according to the temperature of the interface as shown in Figure 4.46. The normalization stress decreases with the temperature, which is a consistent behaviour as the material becomes less rigid when the temperature increases.

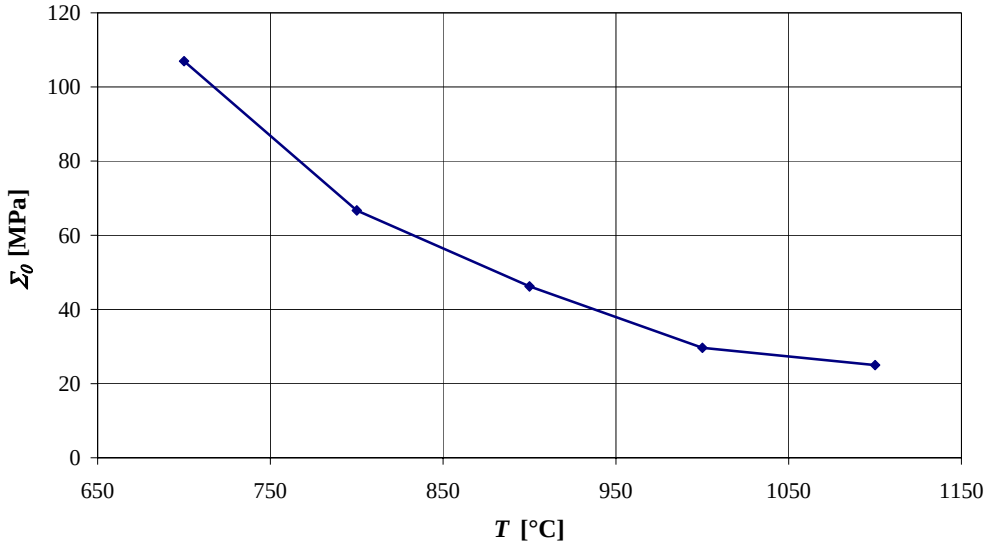

Figure 4.46. Evolution of the normalization stress Σ_0 with the temperature.

4.6.2 PARAMETERS BASED ON LITERATURE

4.6.2.1 Diffusion parameter

The diffusion parameter D is one of the most important driving parameters of the grain boundary diffusion model. Its expression was given by equation (3.37) which is retranscribed here below.

Eq. (3.37) $\rightarrow$ $$D = \frac{D_{b0}\delta_b\Omega}{kT}\cdot exp\left(-\frac{Q_b}{RT}\right)$$

For the initial simulations of Chapter 3, a single value of D was introduced in the data file because the temperature was uniform and constant during the calculation. For practical examples, it is useful to use the full definition of D, given by equation (3.37) as the temperature varies spatially and with time. For austenitic steel, the particular values of the parameters of equation (3.37) that have to be introduced in the input file are the following: the grain boundary diffusion coefficient $D_{b0}\delta_b = 7.5\ 10^{-14}$ m^3 s^{-1}, the atomic volume $\Omega = 1.21\ 10^{-29}$ m^3 and the activation energy $Q_b = 159$ kJ mol^{-1} (Needleman *et al.* 1980). The temperature T has to be defined in Kelvin to be consistent with the definition of the Boltzmann's constant $k = 1.3807\ 10^{-23}$ J K^{-1} and of the universal gas constant $R = 8.3145$ J mol^{-1} K^{-1}.

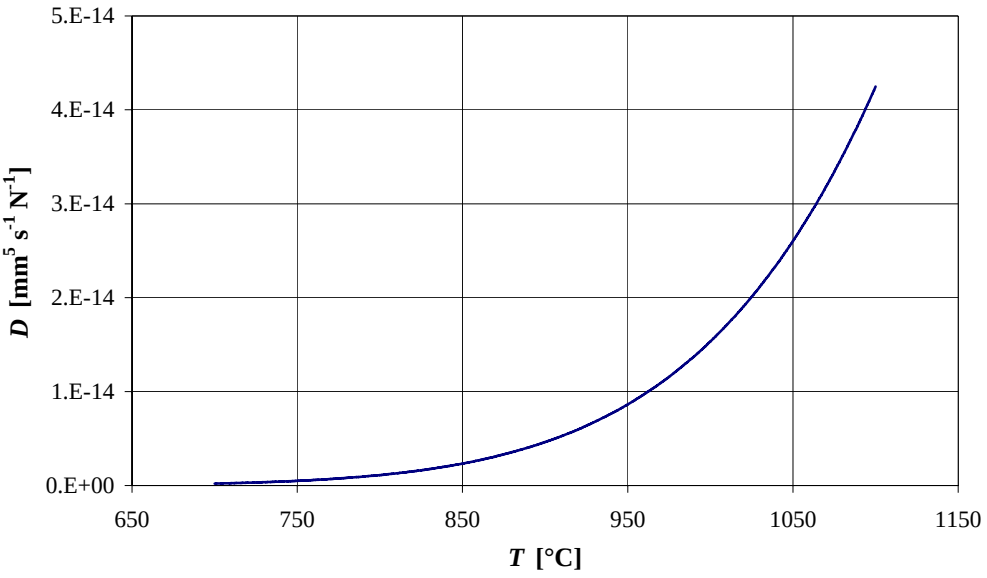

Figure 4.47. Diffusion parameter D as a function of the temperature.

Figure 4.47 shows the evolution of the diffusion parameter as a function of the temperature for the austenitic steel, the diffusion is enhanced when the temperature increases. During the simulation, the diffusion parameter is calculated according to equation (3.37) for the particular temperature of the interface.

4.6.2.2 Cavity angle

The cavity angle influences the void growth (section 3.4.3.2). This parameter is chosen on the basis of the value found in literature for a similar void growth law (Onck and van der Giessen 1998). It is fixed at $\psi = 75°$.

4.6.2.3 Grain viscosity parameter

The grain viscosity parameter $\dot{\varepsilon}_e / \dot{\varepsilon}_B$ defined by the ratio between the grain deformation rate $\dot{\varepsilon}_e$ and the boundary deformation rate $\dot{\varepsilon}_B$ and which characterizes the intergranular sliding (section 3.4.3.1), is chosen equal to an intermediate value of 10 (Onck *et al.* 1999). The grains can slide along each others but not without a certain resistance.

4.6.3 PARAMETERS BASED ON THE ACOUSTIC EXPERIMENTS SIMULATIONS

The remaining parameters, i.e. those which have not been fixed by the literature or by the initial set of experiments, are defined in this section following a calibration method that uses the results of the acoustic experiments presented in section 4.5.2 and finite element simulations.

The simulation of the acoustic test experiments is used to retrieve the stress-strain history at the critical point for each specimen type and strain rate and temperature combination. These loads have to be applied on the representative mesoscopic cell to analyse the effect of the different parameters of the damage law and to compare the damage level with the experimental results. The objective is to define a set of parameters that is compatible with the experimental results.

4.6.3.1 Link between the macroscopic simulations and the mesoscopic cell

The transfer of the stress, strain and temperature fields from the macroscopic model to the mesoscopic cell is not straightforward. This section starts by a description of how the macroscopic and mesoscopic model are related to each other from a geometric point of view. Then, the technique for the data collection and transfer between the two models is presented.

Orientation of the mesoscopic representative cell

The mesoscopic cell is bi-dimensional and is orientated along a plane perpendicular to the axis of the specimens. From a mechanical point of view, the cell is defined in generalized plane state in order to account for the tri-dimensional loading state that has to be transferred from the macroscopic simulations. This formulation allows applying non null stresses and strains simultaneously in the out-of-plane direction (see section 3.3.1.3). The mesoscopic cell is oriented so that its axes system corresponds to the one defined for a type 2 section of the macroscopic continuous

casting model (see Figure 3.31). The correspondence of the axis between the axisymmetric macroscopic model and the mesoscopic cell is illustrated in Figure 4.48.

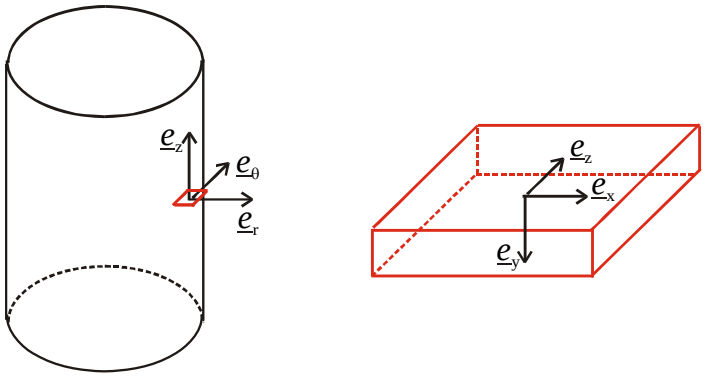

Figure 4.48. Orientation of the mesoscopic cell with regard to the macroscopic models.

Cracks are known to initiate on grain boundaries that are perpendicular to the maximum principal stress. Therefore, the maximum tensile stress that is recorded during the simulation of the acoustic experiments is responsible for the crack initiation and propagation and has to be reproduced accurately. During the compression of the cylinders, this stress corresponds to the circumferential stress σ_θ. At the critical point, i.e. close to the surface of the specimen, the radial stress σ_r is equal to zero. At that point, the shear stresses are also close to zero and are not taken into account during the data transfer. The axial compression stress σ_z is not negligible and has to be transferred, which confirms the necessity to use the generalized plane state to model the reduction of the cell thickness during compression.

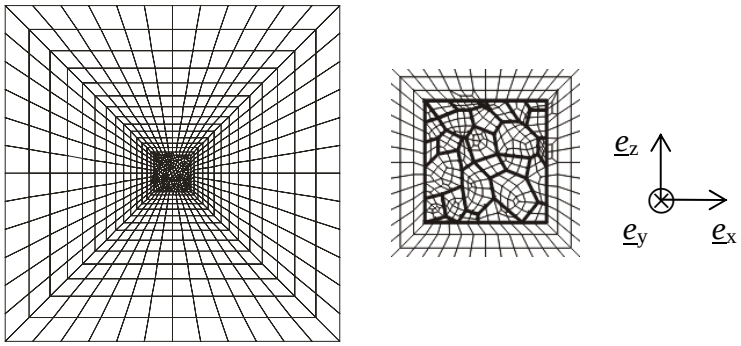

Figure 4.49. Left: mesoscopic cell surrounded by a transition zone (50 mm × 50 mm). Right: zoom on the grains zone (5.45 mm × 5.45 mm).

A surrounding transition zone is used to transfer the data from the macroscopic model to the mesoscopic model (Figure 4.49). The history of stresses and strains are

determined by running macroscopic simulations and are converted into forces and displacements to be used as boundary conditions imposed on each node of the periphery of the transition zone. As an elastic-viscous-plastic constitutive law is used in the grains and as the damage variables at the interfaces grow during the loading, it is important to follow the whole forming process. During the damage law parameters identification phase, the objective is to analyse and define the initiation of the crack and not its propagation. Therefore, it is not necessary to leave a free surface as required for the continuous casting simulations. The surrounding zone can be defined all around the mesoscopic cell, which implies a more precise reproduction of the loads inside the cell itself.

For the acoustic tests simulations, the temperature is fixed and is constant in the specimen. Nevertheless, the method could be used for simulations with variable temperatures; the temperature of each node of the mesoscopic cell should be fixed at each time step according to the results of the parent macroscopic simulation. No thermal exchange is computed at the mesoscopic scale as the thermal problem has already been solved by the macroscopic model.

Data collection and transfer

The stress and strain fields at the critical element are recorded for each of the macroscopic simulations. They are then directly converted into loads or boundary conditions. They are then transferred to the representative cell using two external files, the first one containing imposed forces and the second one imposed displacements as a function of the time.

During the data transfer, the objective is to reproduce in the mesoscopic cell the stress and strain tensors histories recorded at the critical point of the parent macroscopic simulation. These mechanical fields are assumed to be uniform on the cell with small variations in the grains zone due the grains pattern and to the damage initiating at the grain boundaries. The loads can be applied using forces or displacements or a combination of the two. The stress-strain fields are three-dimensional in the macroscopic simulations, with compression in the axial direction and tension in both radial and circumferential directions. In the critical element, the radial stress vanishes as the edge of the sample is reached but the strain field remains three-dimensional.

The compression stress is reproduced on the mesoscopic cell in the direction normal to the plane (y-direction) using the properties of the generalised plane strain state. The tensile stress, which is responsible for the apparition of the crack, is applied

in the *z*-direction of the mesoscopic cell. The stress in the *x*-direction and the shear stresses have to be equal to zero.

Extraction of the data from the macroscopic parent simulation

The process of data transfer is presented in detail using the simulation of the compression test for the concave specimen at T = 900 °C and $\dot{\varepsilon}$ =5 10^{-4} s^{-1} (structured mesh) as an example. The results in terms of stresses have been presented in Figure 4.33 in the section relative to the mesh sensitivity analysis.

As large deformations are involved, it also is necessary to record the history of deformation in the critical element for the radial, circumferential and axial directions in order to have all the information required for the data transfer between the macroscopic and mesoscopic models. The deformations are calculated from the displacements of the nodes of the element, using the logarithmic or natural formulation of the strain given by equation (4.5), where L_0 and L are the lengths of the element in the direction for which the strain is calculated, for the initial and deformed state, respectively.

$$\varepsilon = ln\left(\frac{L}{L_0}\right) \tag{4.5}$$

Figure 4.50 shows the evolution of the strain in the critical element for the three directions (r – radial, z – axial and c – circumferential).

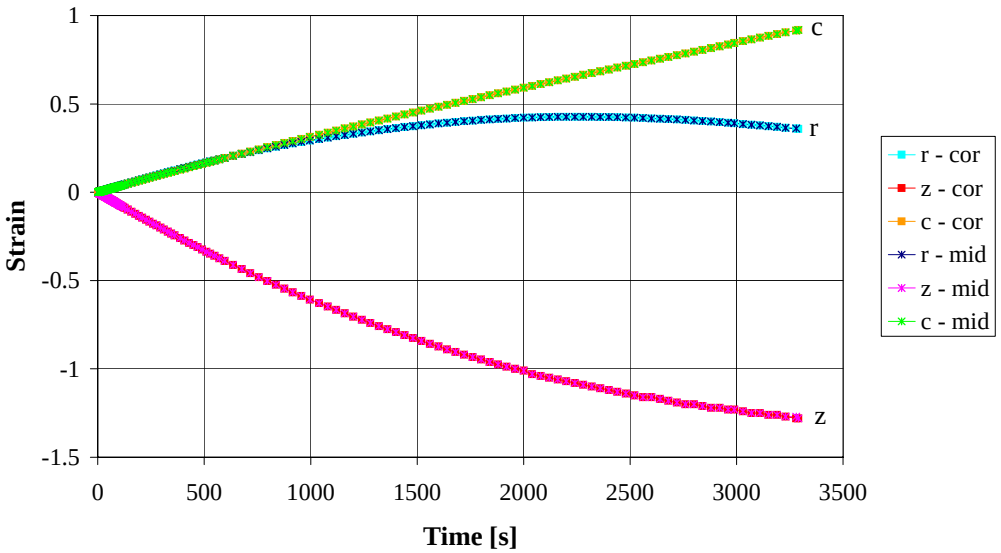

Figure 4.50. Calculated strains using the displacements of the middle nodes (mid) or corner nodes (cor); concave specimen at T = 900 °C and $\dot{\varepsilon}$ =5 10^{-4} s^{-1}.

Two approaches have been compared to calculate the strains. The first one considers the coordinates of corner nodes of the element (cor) to calculate the variables L_0 and L of equation (4.5) and the second one uses the middle nodes (mid). They both give the same results as confirmed by Figure 4.50.

Calculation of the boundary condition to be applied on the mesoscopic cell

For the first trial, displacements were imposed in the three directions as the simulations usually have a better convergence when the loadings are imposed through displacements only. Although the correct equivalent stress was computed in the mesoscopic cell, it appeared that the stress components distribution was not correct. This is due to the formulation of the elastic-viscous-plastic law, which is given in terms of equivalent stress and strain. Indeed, different stresses distributions may correspond to the same equivalent stress. By testing the different possible combinations, it has been found that the correct stress and strain tensors can be reproduced if a displacement is imposed in the *x*-direction of the mesoscopic cell and forces in the *y* and *z*-directions.

As already mentioned before, it is necessary to take the deformation of the cell into account to reproduce the accurate stress field. Equations (4.6), (4.7) and (4.8) calculate the deformed dimensions of the cell based on the strain. ε_θ, ε_r and ε_z are the strains calculated for the three directions of the macroscopic model and which have to be transferred to the mesoscopic cell. L_{i_0} and L_i with i = z, x, y are the initial and deformed length of the mesoscopic cell in the three corresponding directions as defined by Figure 4.48.

$$\varepsilon_\theta = ln\left(\frac{L_z}{L_{z_0}}\right) \quad \Rightarrow \quad L_z = L_{z_0} \cdot exp\left(\varepsilon_\theta\right) \tag{4.6}$$

$$\varepsilon_r = ln\left(\frac{L_x}{L_{x_0}}\right) \quad \Rightarrow \quad L_x = L_{x_0} \cdot exp\left(\varepsilon_r\right) \tag{4.7}$$

$$\varepsilon_z = ln\left(\frac{L_y}{L_{y_0}}\right) \quad \Rightarrow \quad L_y = L_{y_0} \cdot exp\left(\varepsilon_z\right) \tag{4.8}$$

Knowing the deformed sizes of the cell, equation (4.9) calculates the displacement Δ_x along the *x*-direction, while equations (4.10) and (4.11) calculate the forces F_y and F_z to apply in the *y* and *z*-directions of the cell respectively, σ_z and σ_θ being the stresses issued from the macroscopic simulation in the corresponding directions. Only discrete points from the curves issued from the macroscopic simulation

(Figure 4.33 and Figure 4.50) are used for the data transfer; this results in smoothing these curves, especially with regards to the stresses where non-physical oscillations were observed (see Figure 4.33).

$$\Delta_x = L_x - L_{x_0} \quad \Rightarrow \quad x = x_0 + \Delta_x \tag{4.9}$$

$$F_y = L_x \cdot L_z \cdot \sigma_z \tag{4.10}$$

$$F_z = L_x \cdot L_y \cdot \sigma_\theta \tag{4.11}$$

Figure 4.51 shows how the displacements and forces defined by equations (4.9) to (4.11) are applied on the mesoscopic cell. The coordinates of the side AB of the cell are fixed in the *x*-direction and imposed displacements applied on the side CD. The total force in F_y the *y*-direction (i.e. in the thickness direction) is applied on the node defining the degree of freedom specific to the generalized plane state (see section 3.3.1.3). The force F_z in the *z*-direction has to be uniformly distributed on the elements of sides BC and DA.

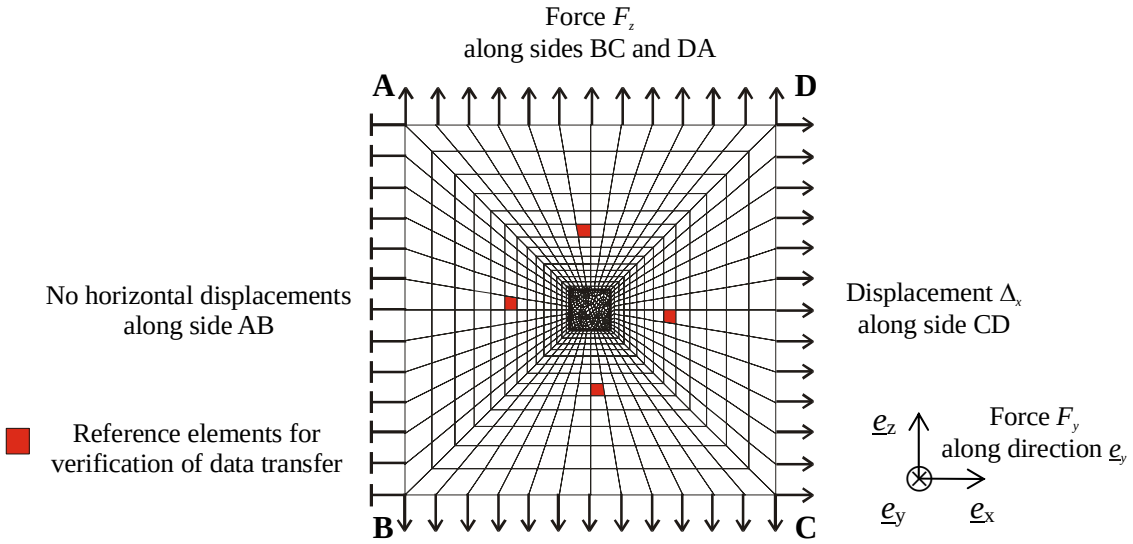

Figure 4.51. Boundary conditions on the mesoscopic cell.

The actualised coordinate *x* as defined by equation (4.9) is shown in Figure 4.52 for the treated case; in this example, the origin of the axes system is localised in the centre of the cell. The maximum situated around *t* = 2250 s can be directly correlated to the maximum shown in Figure 4.50 for ε_r.

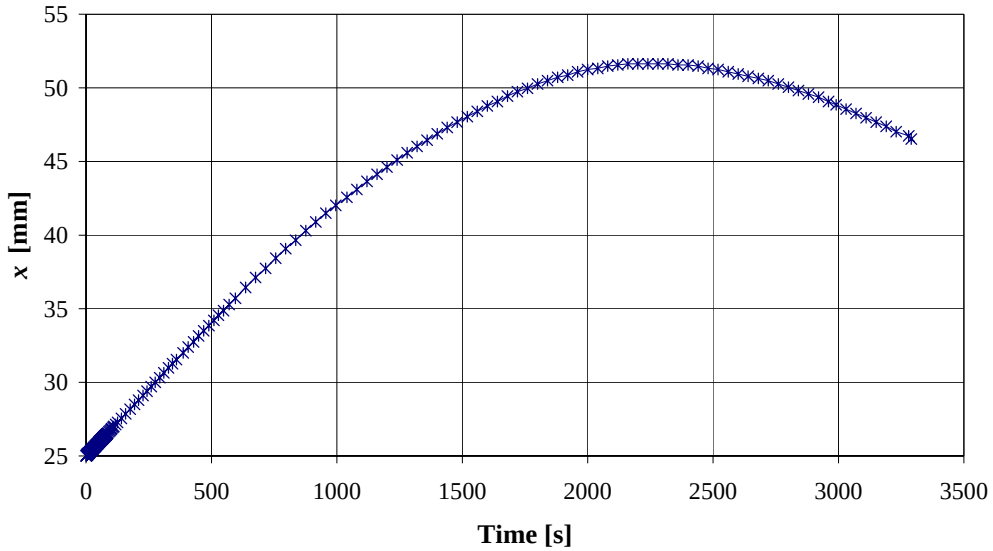

Figure 4.52. Imposed coordinate along the *x*-axis (side CD);
concave specimen at T = 900 °C and $\dot{\varepsilon}$ =5 10^{-4} s^{-1}.

The evolution of the forces F_y and F_z are represented in Figure 4.53 and Figure 4.54, respectively. It can be verified that a compression force is applied along the thickness of the cell and a tensile force along the *z*-direction, the latter being responsible for the crack initiation in the cell.

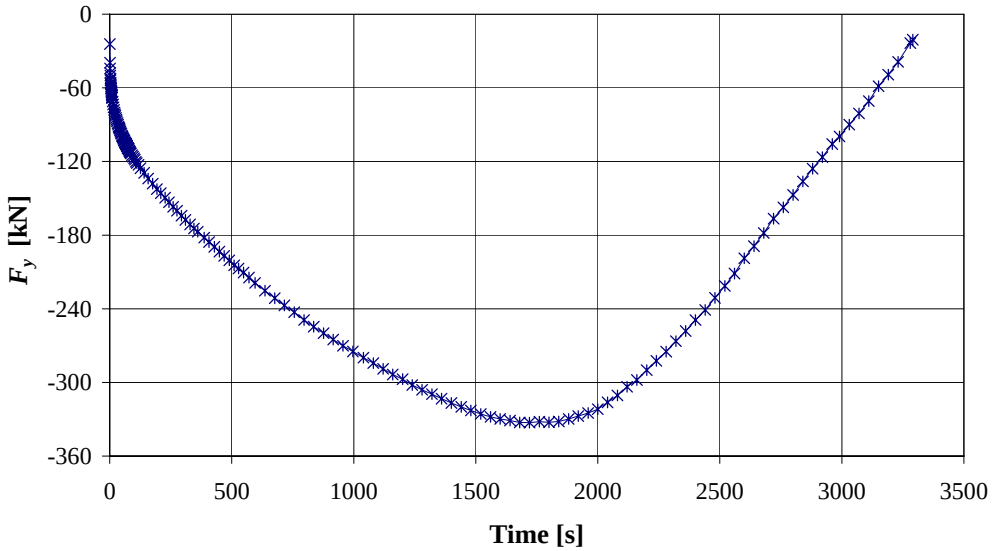

Figure 4.53. Imposed force along the *y*-axis (thickness);
concave specimen at T = 900 °C and $\dot{\varepsilon}$ =5 10^{-4} s^{-1}.

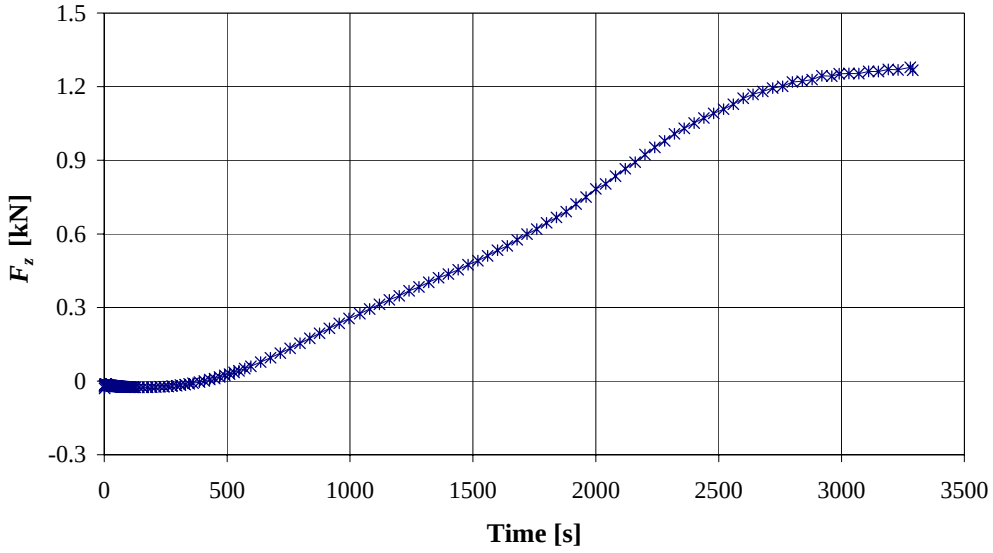

Figure 4.54. Imposed force along the *z*-axis (side DA, $-F_z$ on side BC); concave specimen at T = 900 °C and $\dot{\varepsilon}$ =5 10^{-4} s^{-1}.

Verification of the data transfer

Comparisons of the stresses and strains in the two models are done to verify that the data transfer between the macroscopic and mesoscopic models is correct. As the fields inside the grains zone are not uniform by nature due to the presence of a non-homogenous structure, the verification is done by comparing the average results of four elements chosen around the grains zone in the homogeneous surrounding area. These elements have been highlighted in Figure 4.51.

In Figure 4.55, the imposed stresses issued from Figure 4.33 are compared with the ones recorded during the mesoscopic simulation. Although some oscillations are present, it can be verified that the stresses are well reproduced for the three directions. Even the stress σ_x, which is equal to zero in the macroscopic case, is transferred correctly although it is the deformation that has been applied along that direction.

Regarding the strains, the state variables directly available from the simulation are the equivalent strain and the cell thickness. Those values are represented in Figure 4.56 for both the macroscopic and mesoscopic simulations. It can be checked that the values issued from the mesoscopic simulation after the data transfer match perfectly those given by the parent macroscopic simulation. The displacement in the *x*-direction consists in a direct transfer from the macroscopic to the mesoscopic model which does not involve the calculation of stresses. Comparing the thickness and the equivalent

strain assures that the data in terms of strains for the three individual directions are correctly transferred.

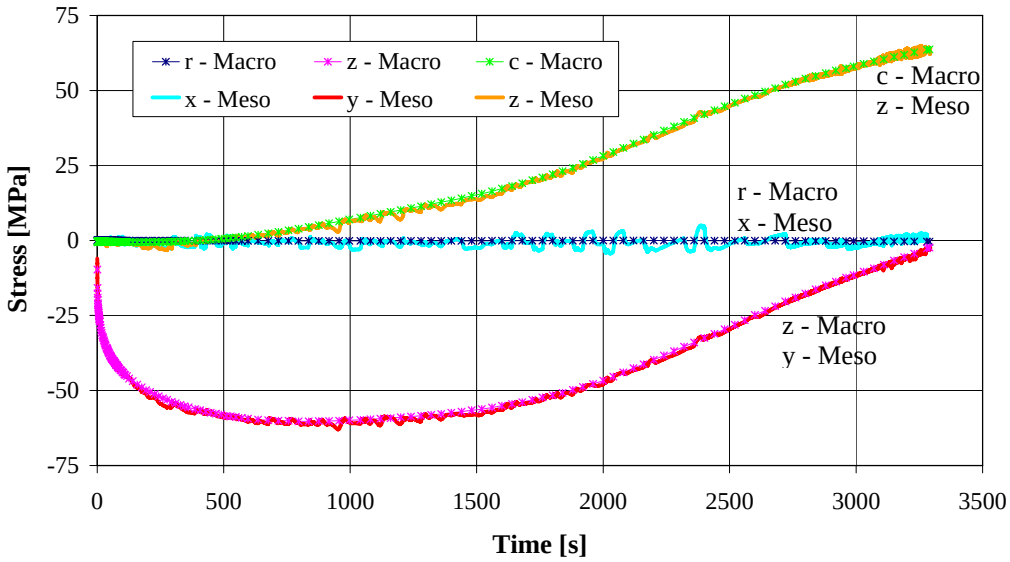

Figure 4.55. Verification of the data transfer for stresses; concave specimen at T = 900 °C and $\dot{\varepsilon}$ = 5 10^{-4} s^{-1}.

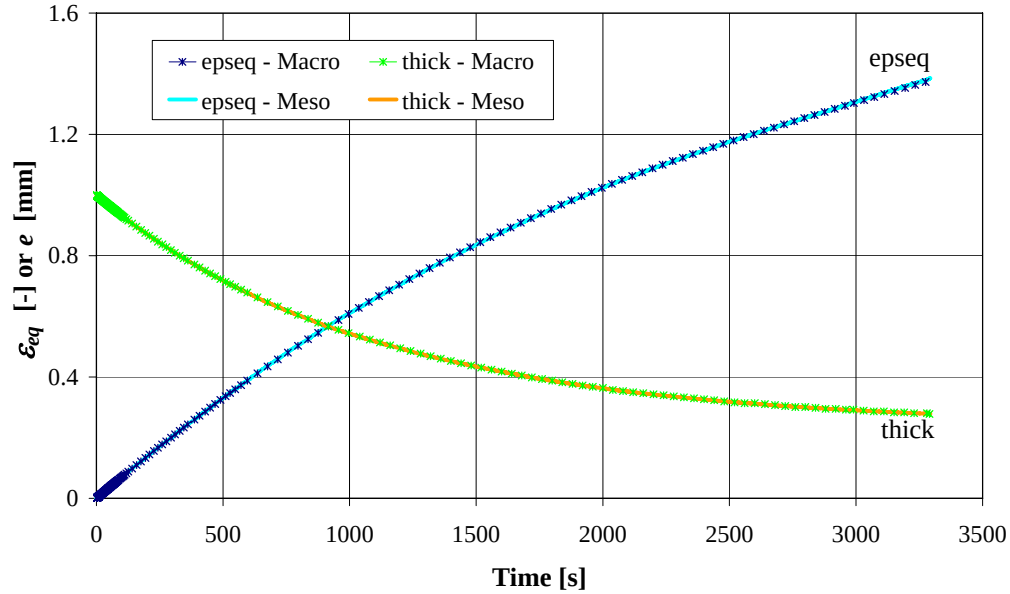

Figure 4.56. Verification of the data transfer for strains; concave specimen at T = 900 °C and $\dot{\varepsilon}$ = 5 10^{-4} s^{-1}.

Maps of the stresses and strains inside the grains zone and surrounding area have also been plotted to verify the distribution of these fields in the homogeneous and non-

homogeneous areas. In particular, the results have been plotted for t = 2980 s. Figure 4.57 represents the stress distribution for σ_x (a), σ_z (b), τ_{xz} (c) and σ_y (d). The stress level in the surrounding area matches the data represented in Figure 4.55 at the given time, which confirms that the data used to plot Figure 4.55 have been correctly extracted.

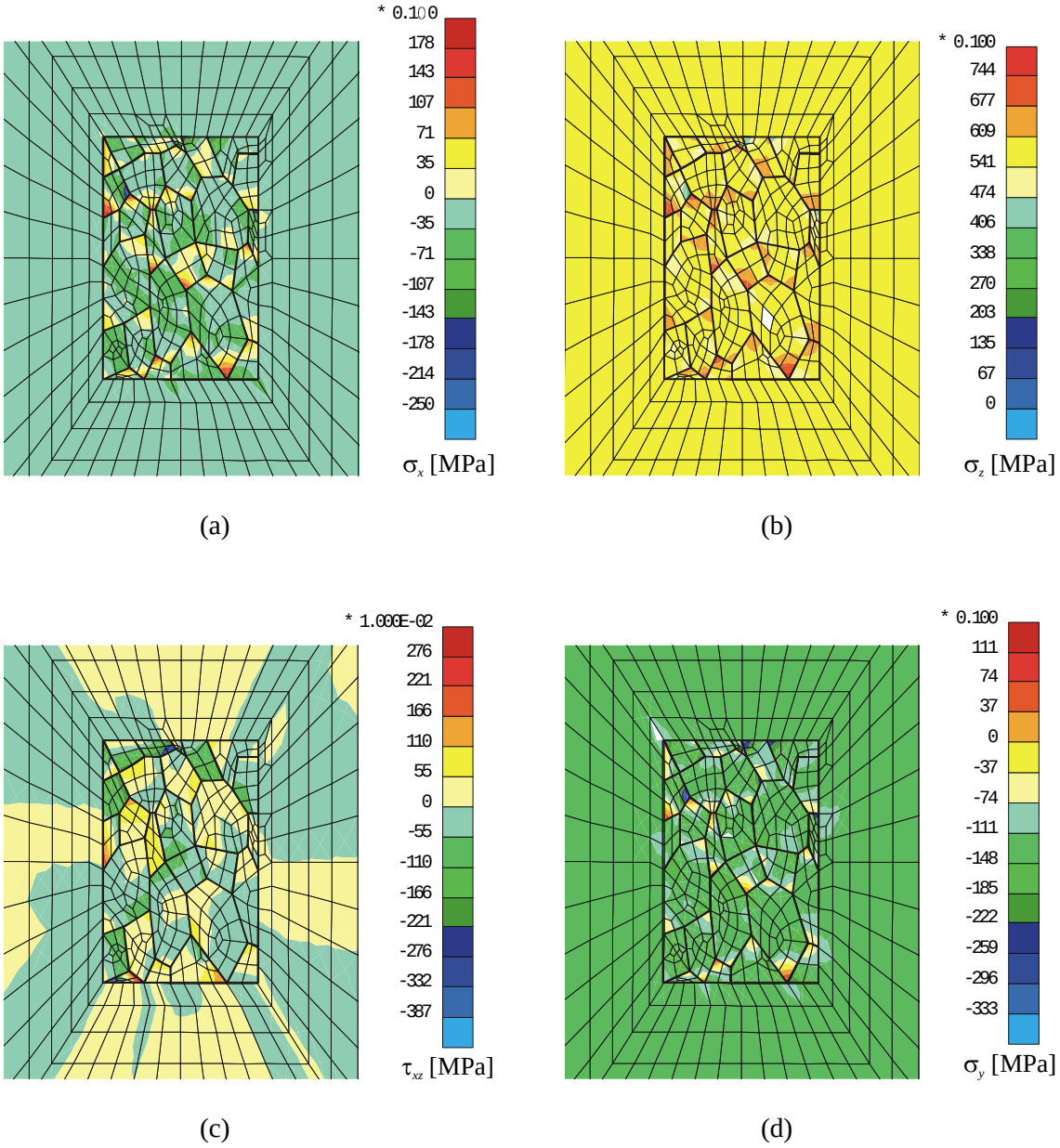

Figure 4.57. Stress distribution in the mesoscopic cell and in the transition zone at t = 2980 s; concave specimen at T = 900 °C and $\dot{\varepsilon}$ = 5 10^{-4} s^{-1}.

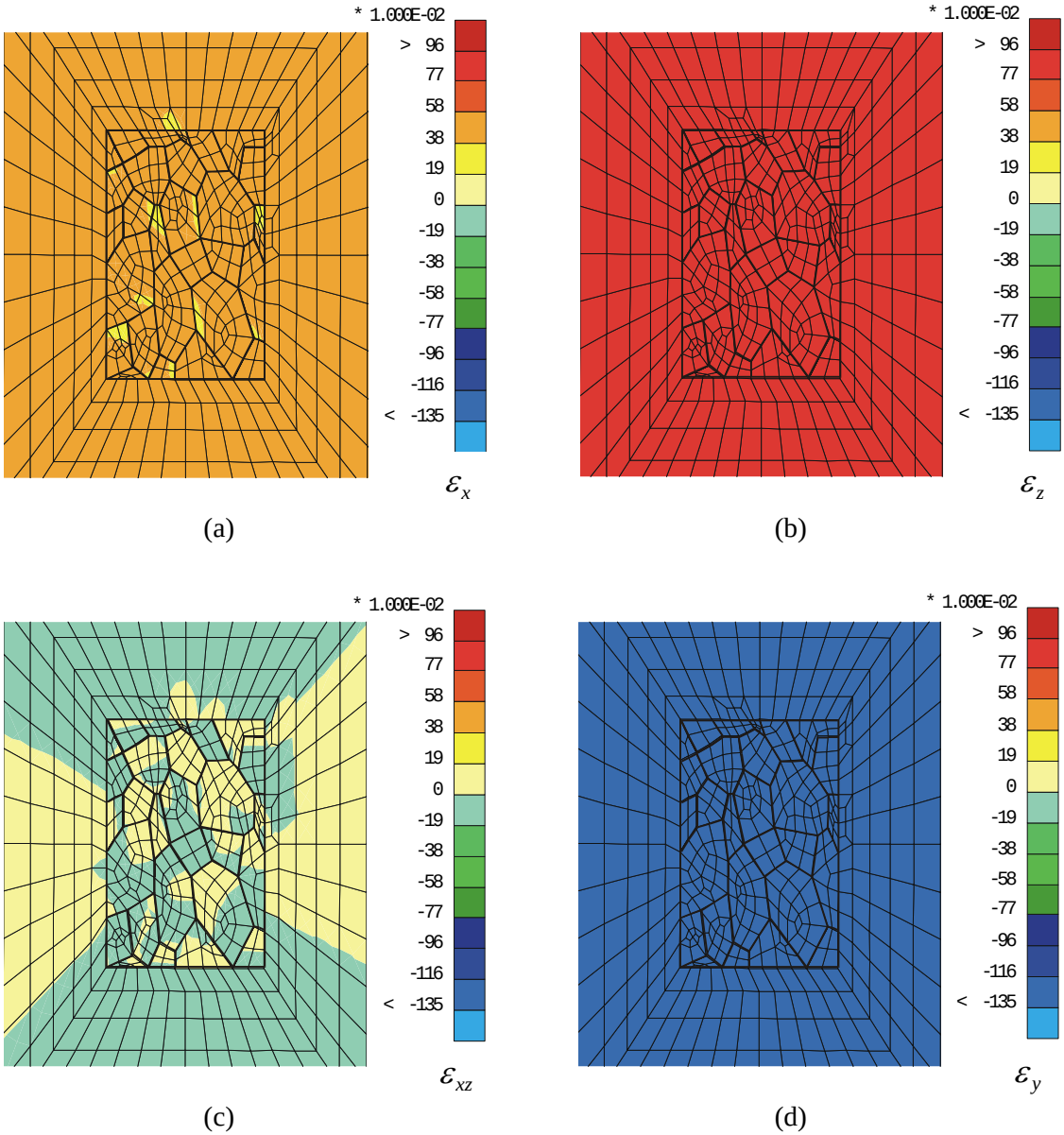

Figure 4.58. Strain distribution in the mesoscopic cell and in the transition zone at t = 2980 s; concave specimen at T = 900 °C and $\dot{\varepsilon}$ = 5 10^{-4} s^{-1}.

Stresses variations are present within the grains zone, especially at the junction between grains. Although it is not possible to certify that the amplitude of these variations are in accordance with the physics of the problem, it is acknowledged that due to the grains pattern, the model at the grain scale can not be considered as a continuum any longer. Therefore, the non-homogeneity of the stresses is representative of the physical reality. Moreover, for each direction, the average of the stresses on the grains zone correspond to the respective macroscopic stress, which confirms that the grains zone is a representation at the mesoscopic scale of the behaviour represented by the continuum at the macroscopic scale. The shear stress τ_{xz} has been represented to

prove that the level of shear in the model is negligible; the values obtained are generally less than 0.1 MPa as shown in Figure 4.57(c).

Figure 4.58 represents the strain distribution in the grains zone and surrounding area at the same instant t = 2980 s. Maps relative to strains do not present the same variations patterns as those relative to stresses and are usually homogeneous within both the grains zone and surrounding area. This is due to the fact that the variations of the deformation, which may appear during the loading of the specimen, are concentrated in the grain boundaries according to the model developed here. The grain boundaries are represented by one-dimensional interface elements associated with a penalty method and for these elements it is not possible to visualize the deformations directly through strains maps like for the solid elements. Regarding the shear behaviour, Figure 4.58(c) confirms that the level of deformations in shear is much smaller that the other strain components and very close to zero.

According to the results presented in Figure 4.57 and Figure 4.58, a surrounding zone made of only three layers of elements is large enough to serve as a transition between the grains zone and the applied boundary conditions for the identification simulations. For the continuous casting simulations, one surface has to be left free to allow crack initiation and propagation, so a larger transition has still to be use to assure a proper modelling of the displacements in the x-direction.

4.6.3.2 Damage parameters identification

Sensitivity analysis

Before starting the identification process, it is necessary to remind the parameters of the interface law that still need to be defined and to analyse their effect on the damage evolution. This first analysis is done by interpreting the equations presented in section 3.4.3 for the damage evolution law. The detailed calibration method and results are discussed afterwards

Figure 4.59 represents a typical damage evolution. Three phases can be defined. First the damage increases very slowly due the diffusion and growth of the voids that are already present (A-B). Then the nucleation threshold is reached, new voids are created and the damage increases more rapidly (B-C). Finally, the saturation state is reached, no more cavities can be created and the growth of the damage slows down until final rupture (C-D).

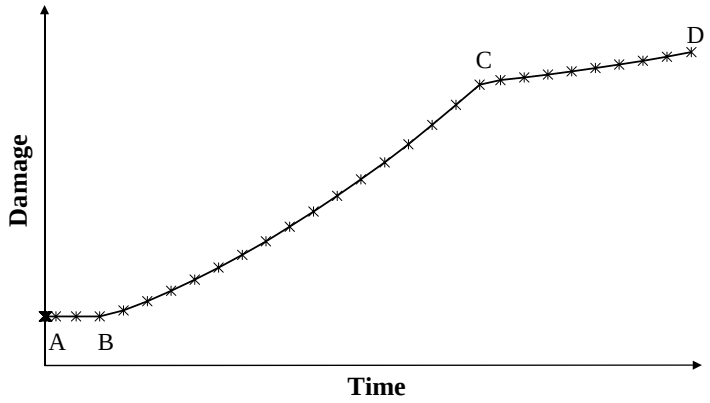

Figure 4.59. Typical damage evolution.

The damage parameter is the ratio between the voids diameter *2a* and the average spacing between voids *2b*. The initial damage value depends on the initial values a_0 and b_0. The initial density of cavities for nucleation by unit length N_I and the nucleation activity parameter F_n determine the position of point B; increasing N_I and/or reducing F_n delays the onset of damage progression and moves point B towards the right. The slope of the curve between B and C partially depends on the value of F_n; reducing F_n slows down the nucleation process and consequently the damage increase, leading to a smaller slope for the portion BC of the curve. The maximum density of cavities N_{max} influences strongly the position of point C; increasing N_{max} allows to prolong the nucleation process and therefore to move point C towards the left.

These five parameters (a_0, b_0, N_I, F_n and N_{max}), which appear in the void evolution equations of section 3.4.3.2, have not been fixed yet. Together with the damage threshold for crack appearance d_{lim}, which is defined at point D on the damage curve, they can be used for the calibration of the model.

Calibration method

The damage tests with acoustic emission at T = 900 °C and $\dot{\varepsilon} = 5\ 10^{-4}\ s^{-1}$ have been chosen as a reference at the start of the identification process because they correspond to an intermediate temperature value. Moreover, at this temperature and strain rate, the reproducibility of the results is very good and all the data points are associated to the visualization of an actual crack on the specimens (see Figure 4.42).

The identification process is carried out in three steps. First, a series of simulations is realized at T = 900 °C and $\dot{\varepsilon} = 5\ 10^{-4}\ s^{-1}$ for the three specimens types (flat, slim and concave) taking a reference set of values for the unknown damage law parameters. Then, these values are manually adapted, taking into account their influence on the sensitivity of the results as described here before, with a view to approaching a

set of parameters that is consistent with results of the acoustic tests in terms of damage evolution in the mesoscopic cell. Finally, when a set of parameters is established for the reference strain rate and temperature, the other combinations of strain rates and temperatures are simulated as a validation exercise; at this stage, the damage parameters can be fine tuned if necessary.

The choice to perform the identification process manually has been driven by three considerations:

- the automatic optimiser OPTIM associated with the finite element code LAGAMINE was only at the early stage of its development phase when the present work started; therefore, no reliable optimisation tools was available at the beginning of this project,
- experience with automatic optimisers has proved that the choice of the initial set of parameters has a great influence on the results and that some of the parameters have to be manually restrained to ensure a correct physical meaning of the data set; moreover, the number of parameters to be optimised and the number of experimental cases tested are quite high in the present application (6 parameters and 18 different experiments), which would lead to a tremendous computation time for the optimiser,
- automatic optimisers require extremely robust direct finite element computations to allow a smooth automatic optimisation process; this condition is not easily fulfilled with non-linear model such as the damage and crack propagation model used in this study.

The main drawback of the manual optimisation method is that only a limited set of parameters are tested. Nevertheless, this technique leads to a solution that respects the physics of the problem and which is representative of the material behaviour.

Details of the analysis and results

In practice, it has been decided to start the analysis by combining three possible values for each parameter, the reference set of data constituting the intermediary level.

Table 4.13. Initial values used for the damage law parameters

a_0 [mm]	b_0 [mm]	F_n [mm^{-1}]	N_I [mm^{-1}]	N_{max} [mm^{-1}]
$2.75\ 10^{-3}$	$2.75\ 10^{-1}$	$4.21\ 10^{3}$	84.2	$40 \times N_I$
$2.75\ 10^{-4}$	*$2.75\ 10^{-2}$*	*$4.21\ 10^{4}$*	*168.4*	*$100 \times N_I$*
$2.75\ 10^{-5}$	$2.75\ 10^{-3}$	$4.21\ 10^{5}$	336.8	

Only two values have been used for N_{max} as the results with these inputs were satisfactory. Table 4.13 summarizes the values that have been used for the initial simulations at T = 900 °C and $\dot{\varepsilon} = 5\ 10^{-4}\ s^{-1}$. The reference values are indicated in italic in the table; their order of magnitude has been defined using normalized data found in literature (Onck *et al.* 1999) and a grain size equal to 1 mm.

Numerous combinations of these parameters have been tested, taking into account the results obtain from the simulations already carried out to decide which combination to test next. A method of trial and error has been applied to converge towards a solution for which the first crack appears at approximately the expected time for each geometry for the case at T = 900 °C and $\dot{\varepsilon} = 5\ 10^{-4}\ s^{-1}$. The damage threshold d_{lim} is not imposed during the parameters identification simulations but the value of the damage variable d reached at the cracking instants predicted by the experiments is observed for each combination of parameters. The set of parameters retained after this first step is the following: $a_0 = 2.75\ 10^{-3}$ mm, $b_0 = 2.75\ 10^{-2}$ mm, $N_I = 336.8\ mm^{-2}$, $F_n = 4.21\ 10^5\ mm^{-2}$, $N_{max} = 40\ N_I$ and $d_{lim} = 0.7$.

As this stage, the other combinations of temperatures and strain rates have been simulated. During this phase, the parameters have been further manually optimized in order to match as best as possible the whole set of experimental results.

Table 4.14. Parameters determined by acoustic analysis.

Parameter	Description	Value
a_0	Initial void size (radius)	$2.75\ 10^{-3}$ mm
b_0	Initial void spacing	$2.75\ 10^{-2}$ mm
N_I	Cavity density for nucleation	$380\ mm^{-2}$
F_n	Nucleation parameter	$1.5\ 10^5\ mm^{-2}$
N_{max}	Maximum cavity density	$40\ N_I$
d_{lim}	Damage threshold	0.7

Even if the numerical model allows a temperature dependence of these parameters, a unique set of parameters could be established; the temperature dependence being already modelled through the diffusion and creep parameters. Finally, the parameters determined by the acoustic analysis are given in Table 4.14. Other values of d_{lim} did not permit to find a better set of parameters that could reproduce the different cases tested experimentally.

Figure 4.60 to Figure 4.62 present the time for crack initiation measured during the damage experiments with acoustic emission analysis together with the time for crack initiation predicted by the finite element simulations using the final set of damage parameters identified.

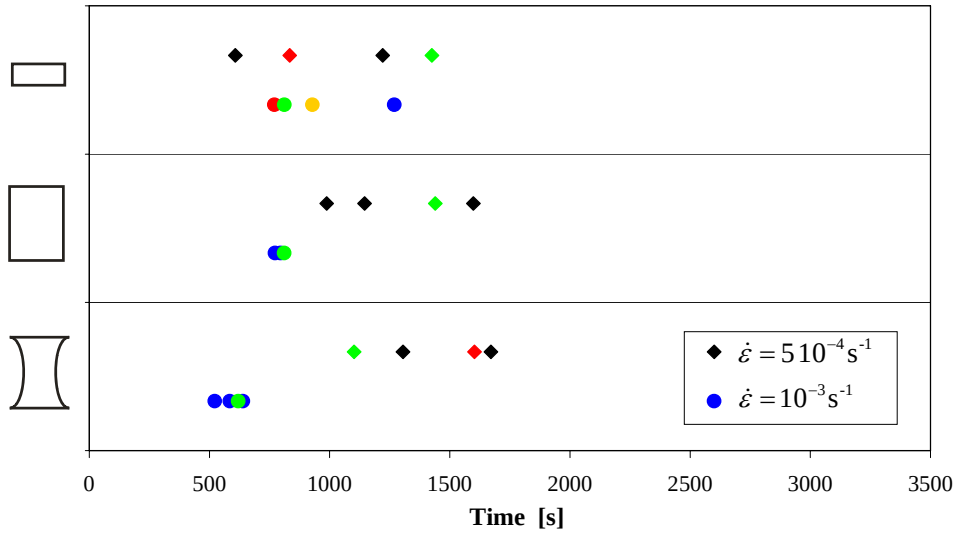

Figure 4.60. Instant of crack appearance: comparison model (green symbols) and experiments (other symbols) for T = 800 °C.

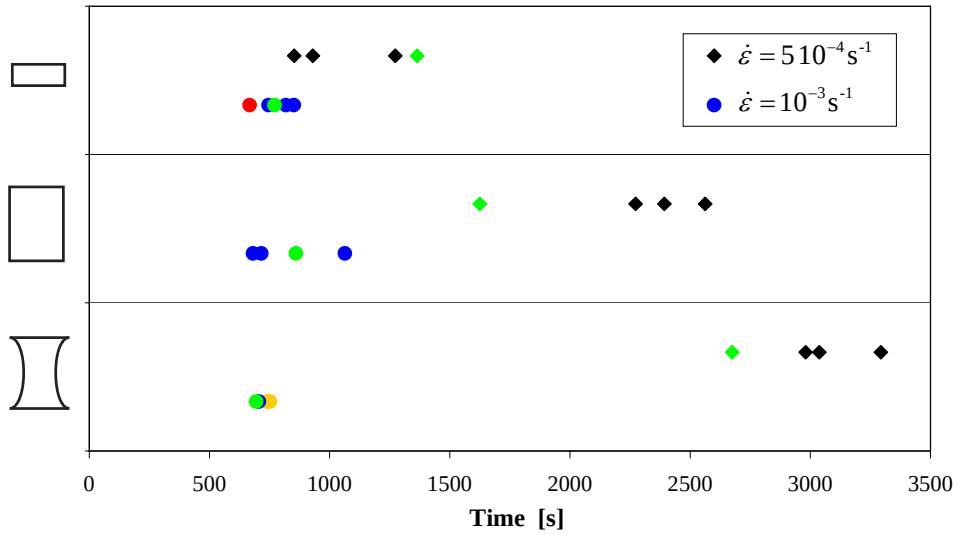

Figure 4.61. Instant of crack appearance: comparison model (green symbols) and experiments (other symbols) for T = 900 °C.

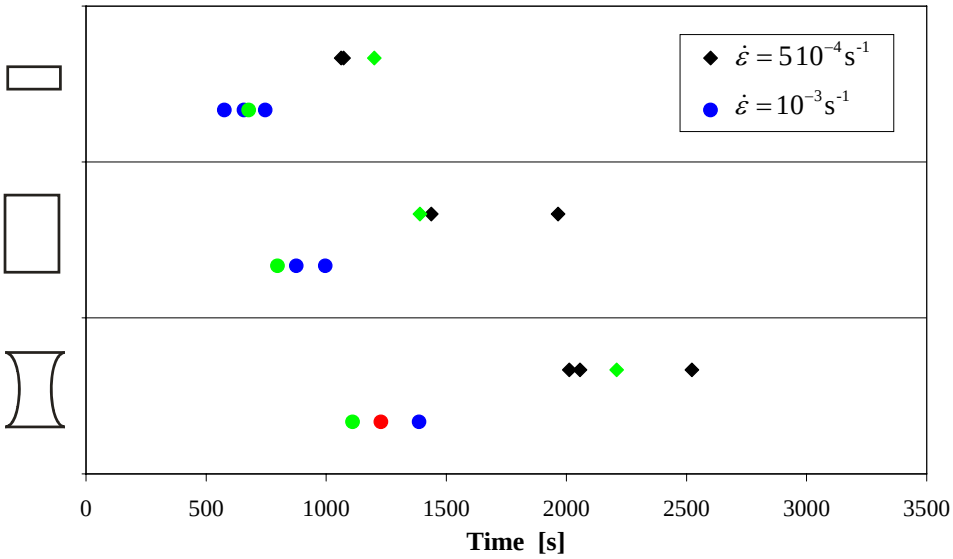

Figure 4.62. Instant of crack appearance: comparison model (green symbols) and experiments (other symbols) for T = 1000 °C.

For the experimental results, the same colour code as defined in section 4.5.2.3 is used (blue and black when a crack is visible after the compression test, red when no crack is visible and orange for indeterminate results). The crack initiation instants predicted by the model are represented by green symbols. Although a single set of parameters has been defined for all the temperatures, one figure has been plotted for each temperature in order to simplify the visualization of the results.

With this set of parameters, the model predictions match the experiments quite well. The largest differences are for the concave and slim samples at T = 900 °C and $\dot{\varepsilon}$ = 5 10^{-4} s^{-1} for which the model predicts the crack too early (see Figure 4.61). For the other combinations of parameters, the simulations results correspond to the data points except for the flat sample at $\dot{\varepsilon}$ = 5 10^{-4} s^{-1} for which the model predicts the crack a little bit later than what has been experimentally observed. The variations appearing at T = 900 °C and $\dot{\varepsilon}$ = 5 10^{-4} s^{-1} come from the fact that, although this case has been privileged during the first phase of identification process, it was no longer focused on during the last optimization steps. In global, the set of parameters is considered to be representative of the experiments and the chronology of cracks appearance for the different combinations of specimen type, strain rate and temperature is well respected.

4.6.4 COMPLETE SET OF PARAMETERS FOR THE DAMAGE LAW

Table 4.15 summarizes the list of parameters to be introduced in the model to define the grain boundary damage law for the interface element. The penalty coefficients k_n and k_s used in equation (3.21) have also been reminded in this table; they had been defined in Chapter 3 as part of the first development examples and have been kept constant in all the simulations of this chapter.

Table 4.15. Parameters for the grain boundary damage law.

Parameter	Description	Value
d	Grain size (diameter)	1 mm
n	Creep exponent	Function of T (see Table 4.11)
B	Creep coefficient	Function of T (see Table 4.11)
$\dot{\varepsilon}_e / \dot{\varepsilon}_B$	Grain viscosity parameter	10
F_n	Nucleation parameter	$1.5\ 10^5$ mm^{-2}
N_1	Cavity density for nucleation	380 mm^{-2}
N_{max}	Maximum cavity density	15200 mm^{-2}
Σ_0	Normalization stress	Function of T (see Table 4.12)
D	Diffusion parameter	Function of T (see section 4.6.2.1)
ψ	Cavity angle	75°
a_0	Initial void size (radius)	$2.75\ 10^{-3}$ mm
b_0	Initial void spacing	$2.75\ 10^{-2}$ mm
d_{lim}	Damage threshold	0.7
k_n	Normal penalty coefficient	100 000 MPa/mm
k_s	Shear penalty coefficient	100 000 MPa/mm

4.7 SUMMARY AND OUTCOMES OF THE EXPERIMENTAL PROGRAM

The parameters of the constitutive laws to be used for the modelling of the continuous casting process at the mesoscopic scale have been identified on the basis of experiments results and literature data. The experiments have been realised on specimens extracted from rejected material provided by the industrial partner.

Metallographic analyses combining optical microscopy and picric acid etching at room temperature have been performed on steel specimens to determine the original austenitic grain size and morphology.

As part of the macroscopic study, compressions of cylindrical specimens have been carried out and the corresponding stress-strain curves recorded. Several strain rates and temperatures have been tested in order to identify the parameters of the modified Norton-Hoff law representative of the thermo-mechanical behaviour of the material.

Finally, a damage study has been used to complete the set of data extracted from the literature review, the microscopic analyses and the compression tests. The damage study consists in the definition of the ductility curve and in compression tests with acoustic emission analysis realised on steel specimens in order to determine the apparition of the first crack during compression. Finite element simulations of the acoustic tests have been used to define the remaining parameters of the damage law using an inverse method.

The full set of parameters defined for the studied material is summarized in Table 4.5 and Table 4.15.

Chapter 5

Application to continuous casting

5.1 INDUSTRIAL CONTEXT

As highlighted in section 2.2, the formation of transverse cracks remains a major problem in steel continuous casting. In particular, the oscillation marks which are caused by the vertical oscillations of the mould, constitute an important factor responsible for cracks initiation. The macroscopic model developed in a previous study to analyse the thermo-mechanical behaviour of the strand during the cooling of continuous casting proposes indicators that predict the risk of transverse cracking (Pascon *et al.* 2006). Nevertheless, the influence of the oscillations marks is not directly included in this model, therefore the capacity to account for the presence of oscillation marks is one of the interests of the mesoscopic modelling. Other benefits of the mesoscopic simulations are the possibility to analyse the effects of various mesoscopic factors such as the grain size and its gradient or the precipitation state.

Before analysing the continuous casting process at the mesoscopic scale, it is important to briefly describe the macroscopic model which provides the data to be transferred to the mesoscopic cell. The localisation, size and shape of the oscillation marks encountered on industrial products also need to be defined. These two points are discussed in the following sections.

5.1.1 MACROSCOPIC MODELING OF THE CONTINUOUS CASTING PROCESS

The data required for the mesoscopic analysis are extracted from the macroscopic thermo-mechanical continuous casting model developed by Pascon *et al.* (2006). This model has been used to study the risk of transverse cracking during bending and straightening of steel slabs. It is a bi-dimensional finite element slice model which accounts for the thermal and mechanical behaviour of the steel solidifying shell moving down through the caster at the casting speed (Figure 5.1). Heat transfer equations model the temperature evolution and solidification process, while an elastic-viscous-plastic constitutive law predicts the stresses and strains occurring in the strand due to the solidification, cooling and applied forces. A ferrostatic pressure is applied on the solidified shell as long as the liquid core is present. The contact between the slab and the tool (i.e. the rolls) is represented by thermo-mechanical contact elements associated with a penalty method and a friction Coulomb's law. The thermal boundary conditions are based on a thermal resistance approach to model conduction when contact occurs; when no contact occurs, convection and radiation are taken into account. The model also takes advantage of the generalized plane strain formulation to apply the extraction force on the slice of material and to account for its deformation in the casting direction. Another feature of the model is the specific bulging control methodology introduced in the analysis using springs.

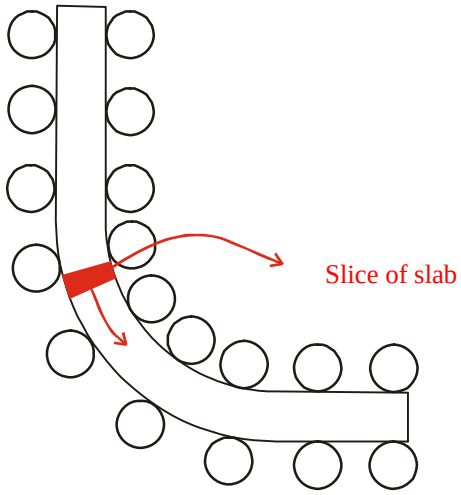

Figure 5.1. Schematic representation of a slice of slab moving through the caster.

The major outputs of the macroscopic model are the temperature, stress, strain and strain rate fields during the whole continuous casting process. Two transverse

cracking indicators, whose value increases when the risk of crack appearance increases, are also proposed:

$$I_1 = \begin{cases} \max\left(0, \sigma_z\right) & \text{if} \quad T_1 < T < T_2 \\ 0 & \text{otherwise} \end{cases} \tag{5.1}$$

$$I_2 = \begin{cases} \max\left(0, \dot{\varepsilon}_z\right) & \text{if} \quad T_1 < T < T_2 \\ 0 & \text{otherwise} \end{cases} \tag{5.2}$$

The first indicators I_1 is based on the longitudinal stress (equation (5.1)) and the second indicators I_2 on the longitudinal strain rate (equation (5.2)). They also account for the existence of a low ductility trough for the material (see Figure 4.21), T_1 and T_2 being the temperatures delimiting this zone.

5.1.2 CHARACTERISATION OF THE OSCILLATION MARKS

The localisation, size and shape of the oscillations marks to be modelled have been defined by observation of the pieces of slab provided for the experimental analysis. The following characteristics could be determined (see also Figure 5.2):

- inter-distance between two oscillation marks = 12 to 15 mm,
- depth of the oscillation marks < 1 mm,
- width of the oscillation marks = 2 to 3 mm.

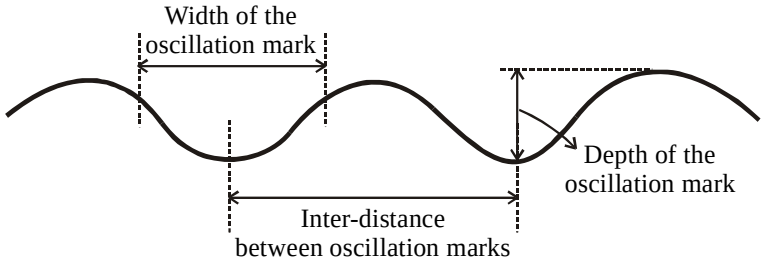

Figure 5.2. Schematic representation of the characteristics of the oscillation marks.

These values are in agreement with measurements carried out by the industrial partner (Condamin *et al.* 2000). By analysing ten samples issued from five different continuous casting batches, they found average values for the inter-distances between two oscillation marks varying from 7.7 to 10.2 mm and average values for the depth of the oscillation marks varying from 0.3 to 0.6 with maximum values up to 1.4 mm for some extreme but rare cases. The steel grades tested have a carbon content approximately equal to 0.1 wt%, which is similar to the material used in this study.

Mathematical models can also be used to calculate the characteristics of the oscillation marks based on the deformations of the solidified shell within the mould and on parameters such as the amplitude and frequency of the mould oscillations and the casting speed. Generally, the depth of the oscillation marks decreases for higher oscillations frequencies because the marks have less time to form. For known continuous casting conditions, a theoretical inter-distance can be calculated by dividing the casting speed by the oscillations frequency of the mould. In particular, a mechanical model proposed Schwerdtfeger and Sha (2000) predicts oscillation marks depths varying between 0.05 and 0.45 mm; these results are also compared to experimental data which confirm the observations made on the slab used for the present analysis.

5.2 CHOICE OF THE CELL SIZE WITH REGARD TO OSCILLATION MARKS

The last step before applying the actual continuous casting loads as boundary conditions on the mesoscopic model is to define the size required for the representative cell. The main objective is to check if the oscillation marks interact with each others from a mechanical point of view and to decide whether or not it is necessary to model several oscillation marks.

5.2.1 DEFINITION OF THE MODEL

A large grains zone (10.9 mm × 21.8 mm) has been built on the basis of the initial cell (5.45 mm × 5.45 mm) already used in sections 3.7.3.2 and 4.6.3.1. Practically, the process was the following:

- the grains zone of the initial mesoscopic cell (see Figure 3.39 or 4.49) has first been duplicated eight times and translated appropriately,
- the junctions between the individual meshes have been checked and properly fixed,
- all the nodes have been translated randomly so that all the grains are slightly different,
- a transition zone has been added, the final mesh dimension is 21.8 mm × 65.4 mm,
- the final mesh has been checked to detect and correct distorted elements.

The final mesh is presented in Figure 5.3(a); it constitutes the reference case for comparison purpose when introducing oscillation marks. This mesh contains approximately 5000 nodes and 4000 elements, 1050 of which are interface elements that

describe the grain boundaries. Figure 5.3(b) is a zoom in the upper half of the cell; it shows the localisation of the elements that are used to compare the stress level between the cases with different types of oscillation marks.

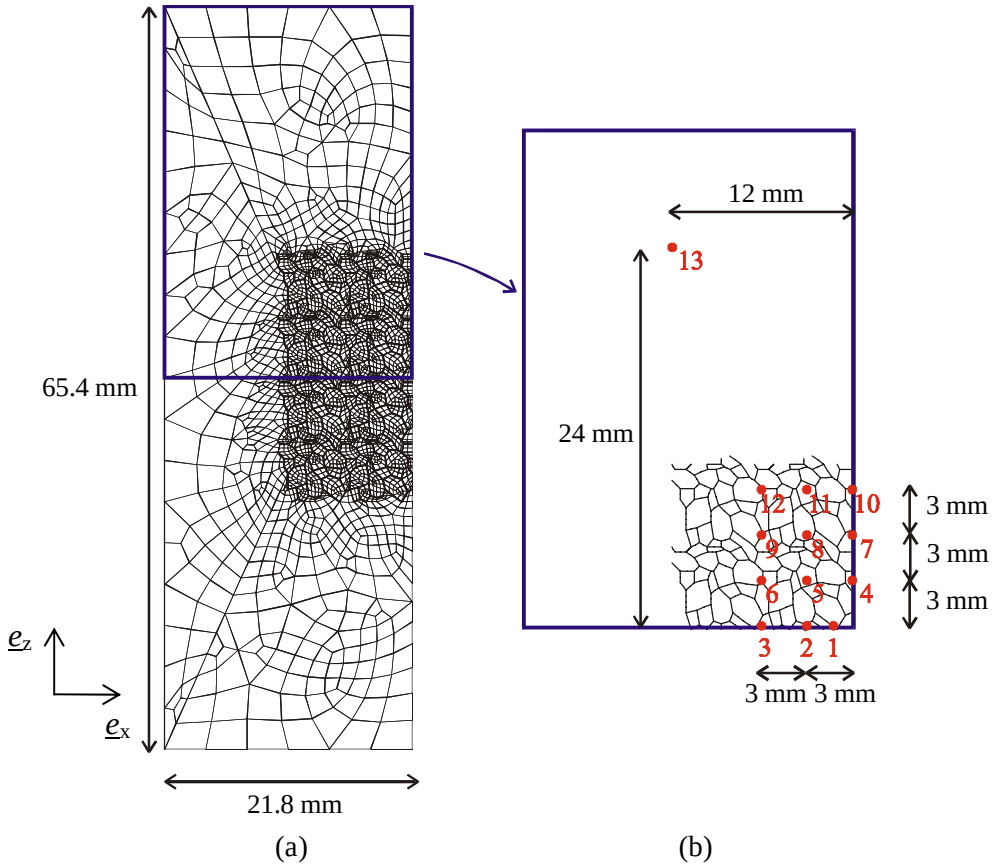

Figure 5.3. a) Mesh for the analysis of the oscillation marks influence: reference case, b) zoom on the upper half of the mesh and localisation of the elements used for comparison.

The cell is bended by a non-uniform tensile field applied in the vertical direction (*z*-direction). Displacements that are representative of the continuous casting process are imposed on the cell upper and lower boundaries to recover a maximum strain rate of approximately 10^{-3} s^{-1}. These displacements have a triangular shape as illustrated on Figure 5.4(a). No loads are applied along the *x*-direction or along the thickness. The loading state has been chosen to simulate the bending process occurring during the continuous casting process and to enforce a higher stress level on the right edge of the cell where the crack is known to initiate. This choice produces a conservative model for the analysis of the oscillation marks spacing.

To test the effect of the oscillation marks, two types of analysis are made: first, the stress distributions with two different geometries of oscillation marks are compared

and then, the number of oscillation marks are increased. The shape and size of the oscillation marks have been chosen using observations made on the slab provided for the analysis, experimental data collected by the industrial partner and information available in the literature as summarized in section 5.1.2.

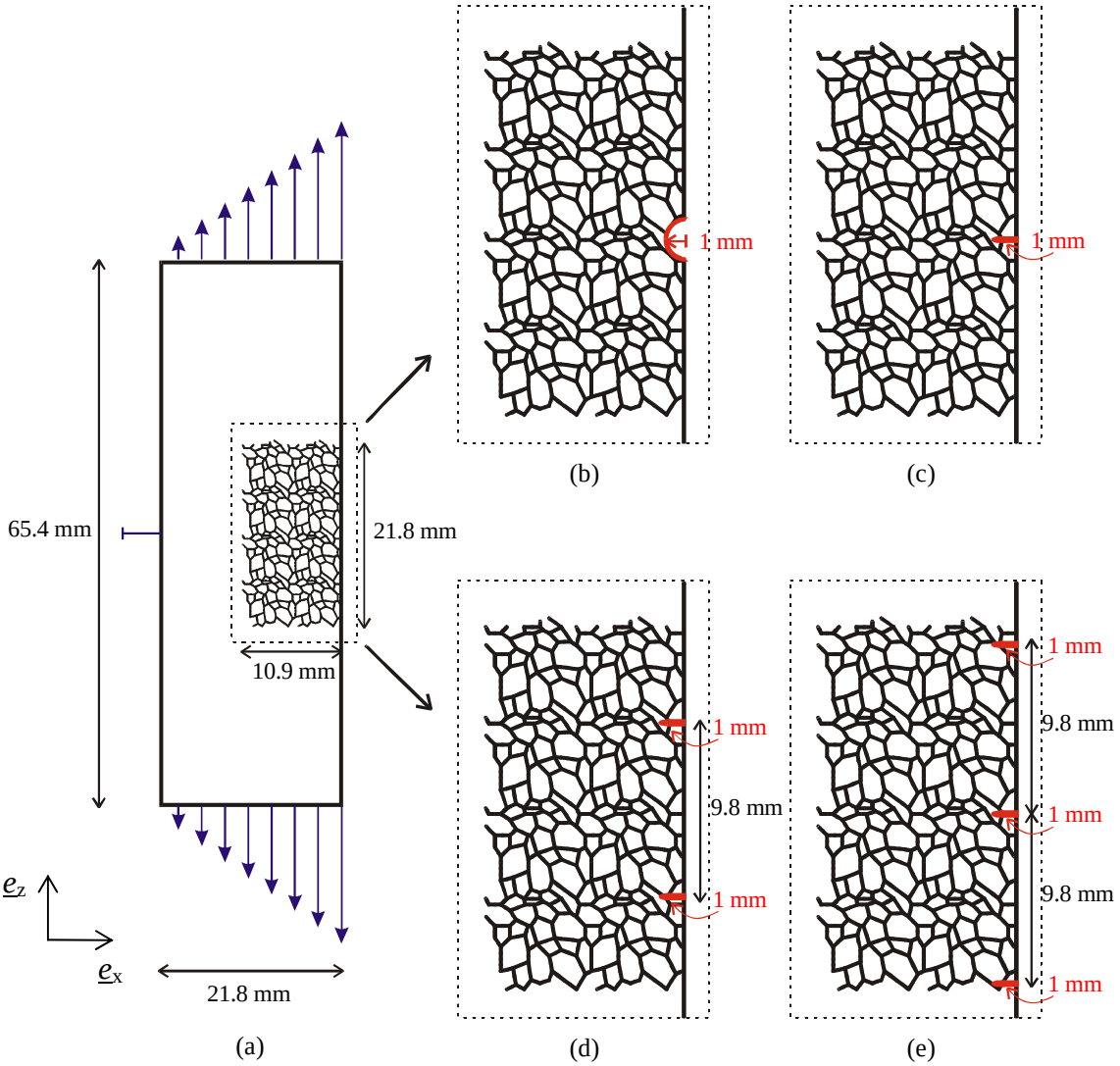

Figure 5.4. a) Dimensions of the cell and applied boundary conditions; geometry and position of the oscillation marks: b) one circular oscillation mark, c) one sharp oscillation mark, d) two sharp oscillation marks, e) three sharp oscillation marks.

The two geometries tested are a circular (Figure 5.4(b)) and a sharp (Figure 5.4(c)) oscillation mark. In both cases, the oscillation mark is localised at mid-height of the cell and its depth is 1 mm. Figure 5.4(d) and Figure 5.4(e) show the localisation of the oscillation marks for the cases with two and three sharp oscillation marks, respectively. The distance between the oscillation marks, which is equal to 9.8 mm, has

been chosen so that at least three of them could be represented in the existing mesh. As this distance is smaller than the distance experimentally observed (i.e. from 12 to 15 mm), the model is conservative. The combination of parameters presented in Figure 5.4 regarding the localisation, size and shape of the oscillation marks allows to cover the range of cases experimentally encountered.

The material law representing the grains and the surrounding zone is the modified Norton-Hoff law with the parameters defined in Table 4.5. For the damage interface law modelling the grain boundaries, the parameters used are those identified by the acoustic tests simulations and summarized in Table 4.15. A uniform temperature of 900 °C is fixed and kept constant during the simulations.

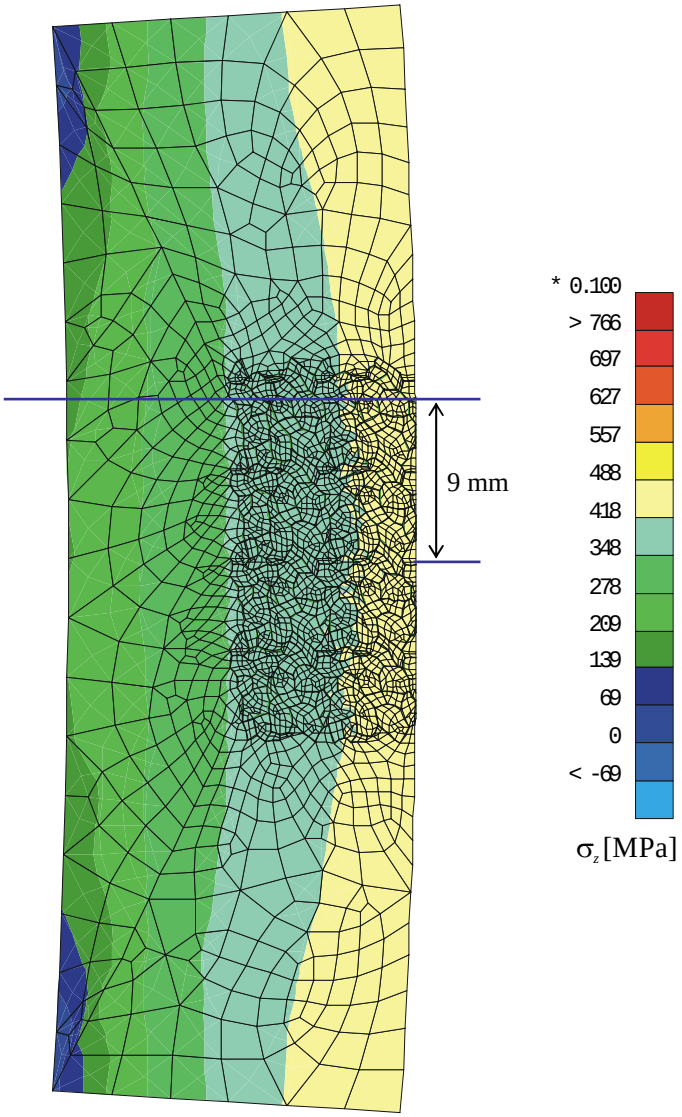

Figure 5.5. σ_z at time t = 60 s (before initial crack appears) for the reference case.

5.2.2 RESULTS FOR THE REFRENCE CASE

Maps of the stress σ_z (vertical direction) before the initiation of the first crack are plotted for the different cases illustrated in Figure 5.4 and used for comparison purpose. The choice of σ_z as the comparison variable is justified by the fact that it is the stress that is directly imposed to the cell through the boundary conditions and that this stress is mainly responsible for crack initiation and opening.

Figure 5.5 shows the stress distribution σ_z in the deformed cell for the reference case without oscillation mark at t = 60 s. The pattern observed is regular in both the surrounding and grains zones with a maximum tensile stress on the right side of the cell where the oscillation marks are localised for the other cases. This stress distribution pattern is correlated to the bending loads imposed.

5.2.3 INFLUENCE OF THE GEOMETRY OF THE OSCILLATION MARKS

Figure 5.6 presents the results with the two types of oscillation marks at the instant t = 60 s for the circular (a) and sharp (b) geometries. The same legend is used for all the stress maps presented in this chapter so that the plots can directly be compared. A first observation is that the regular stress pattern is recovered in the grains zone at a vertical distance from the notch approximately equal to 9 mm as highlighted by the horizontal line in Figure 5.5 and Figure 5.6.

A stress concentration is observed at the tip of the oscillation mark for both geometries. For the sharp oscillation mark, the stress concentration is more localized, the circular oscillation mark producing a smoother variation. Compared to the reference case, the general stress distribution is mostly disturbed in an circle of radius approximately equal to 6 mm around the tip of the oscillation mark (see Figure 5.6). Nevertheless, when comparing the two cases presented in Figure 5.6, it can be seen that the geometry of the oscillation mark itself only influences the stress pattern in the close vicinity of the notch tip. Therefore, there is no need to analyse the effect of introducing several oscillations marks using the two geometries.

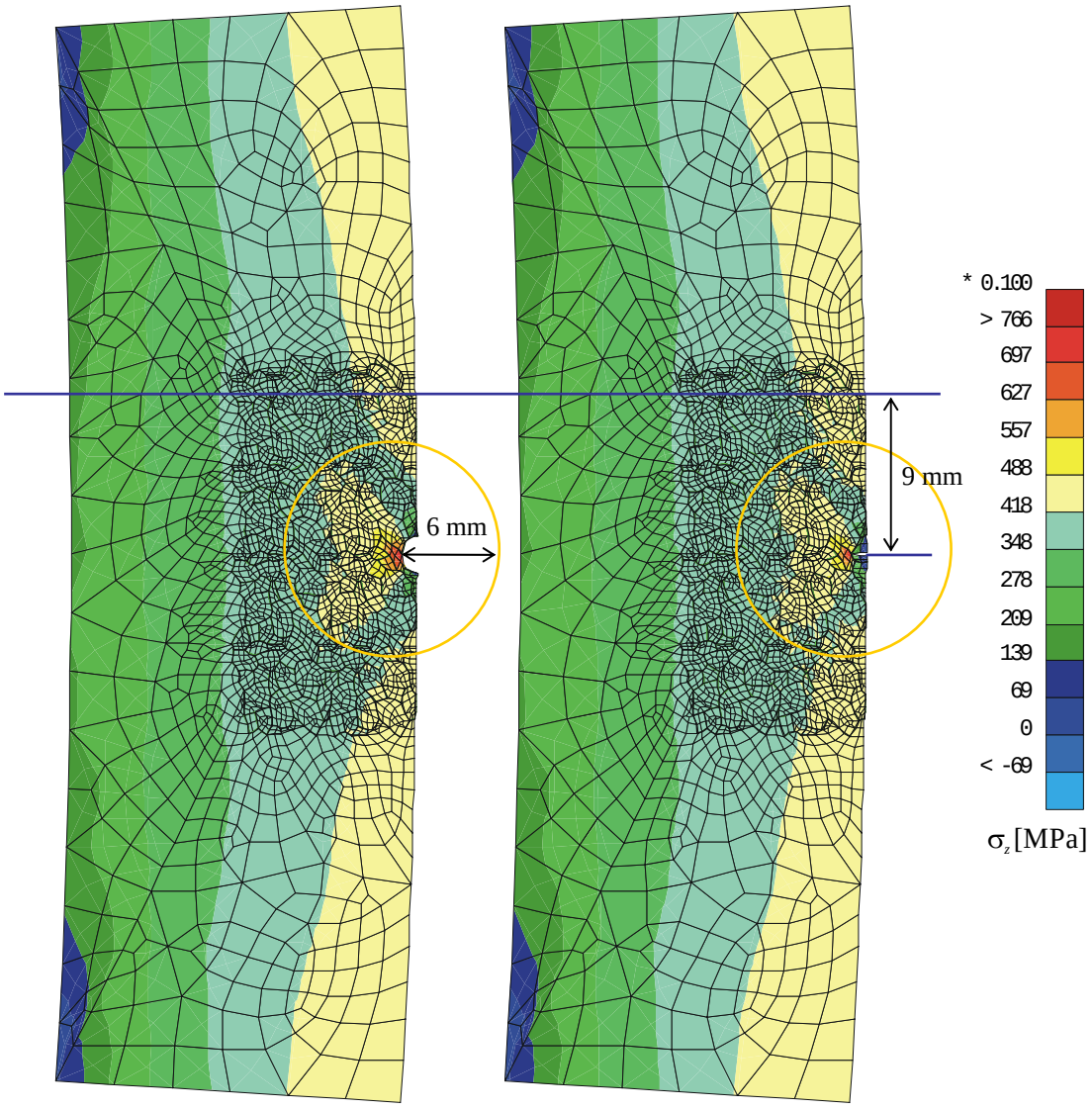

Figure 5.6. σ_z at time t = 60 s (before initial crack appears) for a circular (a) and a sharp (b) oscillation mark (depth of the oscillation mark = 1 mm).

Table 5.1 presents more detailed results in terms of the stress σ_z at specific locations in the cell for the reference case, circular oscillation mark and sharp oscillation mark. A sketch showing the localisation of the elements used for the comparison has been presented in Figure 5.3(b). The first element (location 1) is localised at the position of the tip of the oscillation mark. Locations 2 to 12 form a grid of regular interval equal to 3 mm on the upper half of the cell; although the model is not perfectly symmetric due to the grains pattern, the general behaviour in the upper and lower half of the mesh is similar and there is no need to study both. The last line in the table (location 13) corresponds to an element localised completely outside the disturbed

zone and which is used as a reference. The percentage of variation of σ_z between the case with one oscillation mark (circular or sharp) and the reference case is also indicated in Table 5.1.

Table 5.1. Comparison of the stress σ_z for the three cases of Figure 5.5 and Figure 5.6.

Position of the element[1]	Reference case	One circular oscillation mark		One sharp oscillation mark	
	σ_z [MPa]	σ_z [MPa]	Variation	σ_z [MPa]	Variation
1	43.26	*75.82*	75.25%	*85.41*	97.41%
2	39.25	44.09	*12.35%*	41.01	*4.49%*
3	39.48	40.14	1.68%	39.81	0.86%
4	44.53	35.12	*-21.14%*	39.71	*-10.83%*
5	42.73	44.16	3.34%	43.47	1.73%
6	39.57	41.58	5.08%	40.79	3.08%
7	45.67	44.06	-3.54%	44.73	-2.07%
8	42.70	40.88	-4.28%	41.64	-2.50%
9	40.16	40.56	1.00%	40.36	0.51%
10	45.76	45.11	-1.43%	45.37	-0.85%
11	42.84	41.98	-2.01%	42.34	-1.17%
12	40.46	39.82	-1.57%	40.09	-0.92%
13	36.20	35.91	-0.80%	36.03	-0.46%

[1]Localisation of the elements defined on Figure 5.3(b).

The detailed results confirm the observation already made by global vizualisation of the stress maps. The stress concentration at the crack tip is more important for the sharp geometry with a maximum stress $\sigma_z = 85\,\text{MPa}$ compared to $\sigma_z = 75\,\text{MPa}$ for the circular geometry; but the disturbed zone spreads further for the circular geometry, the stress variation compared to the reference case being 12% for the circular case and only 4.5% for the sharp case at point 2. There is a stress relaxation along the lips of the oscillation marks as shown by the data highlighted at point 4. For the circular geometry, this effect starts and extends further due to the shape of the notch. Points 10, 11 and 12 are localised on the horizontal line drawn at a distance of 9 mm from the centre of the oscillation mark as illustrated in Figure 5.5 and Figure 5.6. For

these locations, the variations of σ_z compared to the reference case are less or equal to 2%. This low value allows to consider that the original stress pattern is recovered. For comparison, the variations at point 13, which is outside the disturbed zone and not strongly affected by the perturbation, lie between 0.5 and 0.8%.

As it has been established that the global stress pattern is fully recovered at a distance equal to 9 mm from the centre of the oscillation mark, it is necessary to check if 18 mm (2 × 9 mm) is the minimum distance required between two oscillation marks in order to prevent any interaction concerning the initiation of cracks; this point is investigated in the next section.

5.2.4 ANALYSIS OF THE INTERACTIONS BETWEEN THE OSCILLATION MARKS

Figure 5.7 is used to check in which zone the oscillation marks will interact and to decide whether or not it is necessary to model a few of them. The distance between the oscillation marks (9.8 mm) has been chosen so that at least three of them can be represented in the existing mesh and is therefore smaller that 18 mm but conservative.

Looking at the stress patterns in Figure 5.6 and Figure 5.7, it can be seen that the stress distribution for σ_z has the same shape and size, corresponding to two lobes or 'wings', in the zones around the oscillations marks for all the cases, i.e. with one, two or three oscillation marks. This is a first indication that the presence of several oscillation marks does not strongly influence the local stress distribution around each oscillation mark. This conclusion is reinforced by the fact that in reality the inter-distance between the oscillation marks for practical cases is greater than the 9.8 mm modelled in these examples.

The calculated stress field corresponds to the characteristic pattern predicted by the standard equations of fracture mechanics for the stress distribution around the crack tip. The differences observed in the shape and size of the lobes in Figure 5.7 when the transition zone is reached, occur because the mesh becomes more rigid in this zone. Indeed, in the transition zone, the elements size increases and there is no boundary elements that release the degrees of freedom of the displacement field.

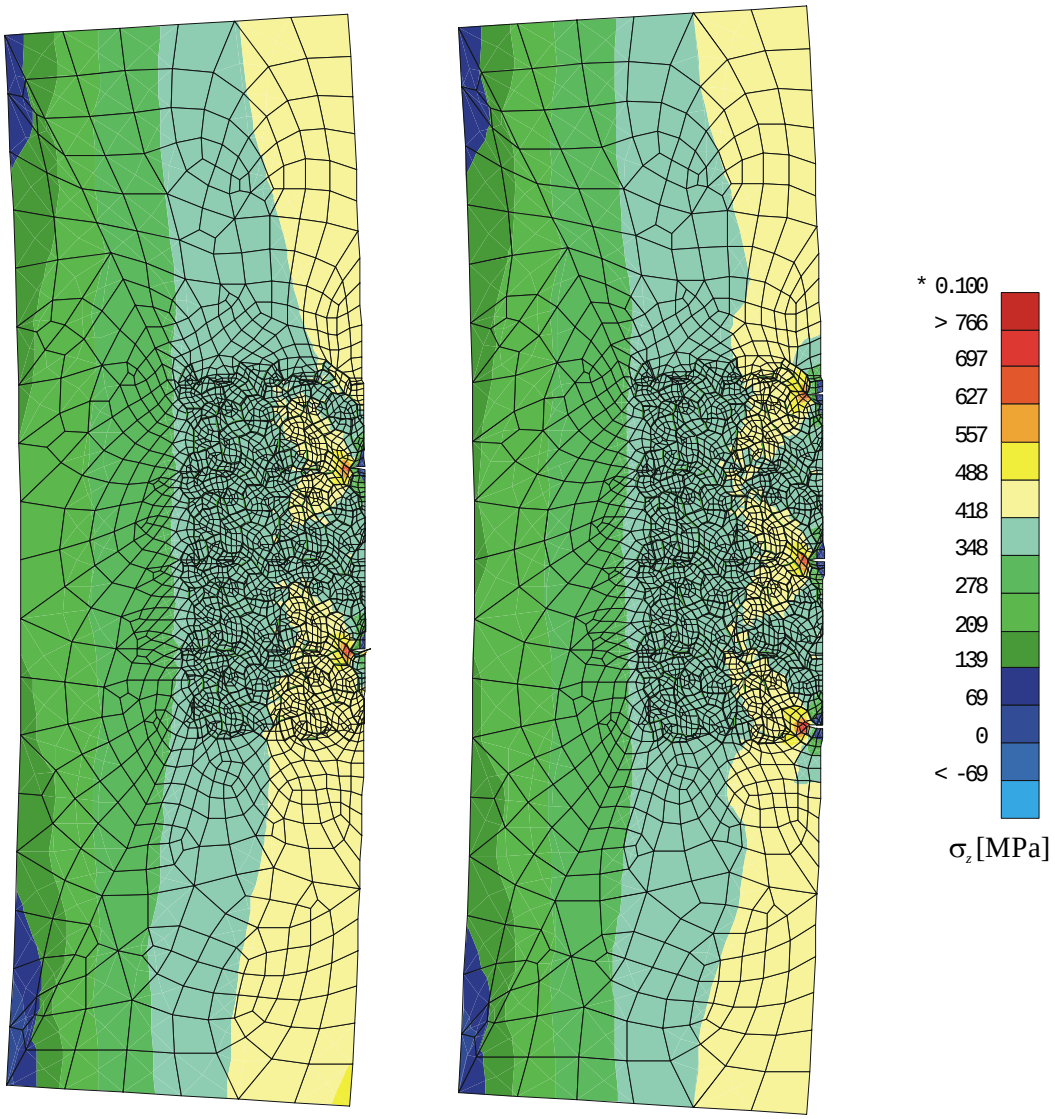

(a) (b)

Figure 5.7. σ_z at time t = 60 s (before initial crack appears) for two (a) or three (b) sharp oscillation marks (distance between the oscillation marks = 9.8 mm).

Table 5.2 indicates the instant of first crack initiation around each oscillation mark for all the cases tested. All the simulations have been carried out up to t = 100 s except for the reference case simulation which has been extended up to t = 200 s.

Looking at the results in Table 5.2, it is important to underline the fact that the first crack initiation appears almost simultaneously for the cases with one (t = 65 s), two (t = 64 s) or three (t = 67 s) sharp oscillation marks. It can then be concluded that, even if the oscillation marks influence each other, there is no need to model more than one of them in the final simulations. Indeed, for each defined oscillation mark geometry, the perturbation is only concentrated in between the oscillations marks and has no real

effect near the notch tip where it is essential to model the stresses correctly to detect crack appearance. The last calculations will then be done using the smaller cell as defined in Figure 3.39. This choice will induce major computation time savings.

Table 5.2. Time at crack initiation for the different meshes[1].

Mesh type	Localisation of the crack	Time at crack initiation
No OM (reference)	Right side, centre	154 s
One circular OM	Tip of circular OM	72 s
One sharp OM	Tip of sharp OM	65 s
Two sharp OMs	Tip of lower sharp OM	86 s
	Tip of upper sharp OM	64 s
Three sharp OMs	Tip of lower sharp OM	no crack at t = 100 s
	Tip of middle sharp OM	67 s
	Tip of upper sharp OM	85 s

[1]OM stands for oscillation mark.

Of course as sharp and circular geometries strongly modify the stress and strain fields at the tip of the oscillation mark, the cracks do not start to propagate at the same time when the geometry changes. Not surprisingly the sharp oscillation mark induces early crack propagation. For the reference mesh, there is no stress concentration induced by an oscillation mark; stress variations in the mesh are only due to the grains patterns and the crack initiate later on a grain boundary element perpendicular to the loading direction. The crack is localised on the free edge of the cell, where the stress level in the vertical direction is globally higher.

When the cracks propagate, the comparison between the different meshes is no longer possible as each crack evolves differently, depending on the grains pattern. Moreover, when a crack initiates, the global stiffness of the cell is reduced and therefore the opening of the second crack is delayed. This behaviour is linked to the fact that during crack propagation, although there is a stress concentration at the crack tip, there is also an important unloading effect along the lips of the crack and a lower, but existing, unloading effect in the surrounding area of the crack. It can also be noticed in Table 5.2 that the initiation of the second crack for the cases with two or three

oscillation marks also appears simultaneously around t = 85 s. This effect has not been investigated further.

5.3 DESCRIPTION OF THE MACROSCOPIC SIMULATIONS

The major features of the macroscopic continuous casting finite element model have been presented in section 5.1.1. The objective of the present section is to describe the application of this model to the specific continuous casting process analysed in this study with a view to collect the macroscopic results required for the modelling at the mesoscopic scale.

5.3.1 GEOMETRY OF THE PROBLEM AND MATERIAL PARAMETERS

The product used for the analysis is a slab of cross section 1200 mm × 220 mm which is cast at a casting speed equal to 1.2 m/min. The problem being symmetric along the y-axis, only half of the slab is modelled for the macroscopic analysis (Figure 5.8).

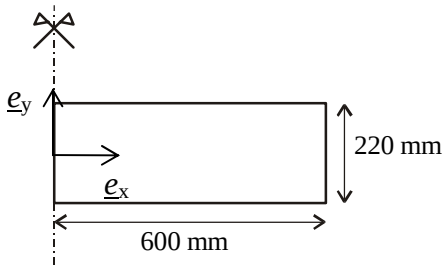

Figure 5.8. Half slab cross-section used for the macroscopic modelling.

The modelling conditions, geometry of the caster, material parameters and heat transfer coefficients are identical to those used by Pascon (2003); the detailed inputs are not published here as they are industrial proprietary data but they are considered to be representative of the behaviour of a low carbon steel similar to the one modelled throughout this thesis. An exception is for the modified Norton-Hoff law in the temperature range between 700 and 1100 °C, where the parameters summarized in Table 4.5, which have been specifically identified for the steel grade provided by the industrial partner, are substituted to Pascon's data.

The caster is a vertical-curve machine which presents five successive zones: a vertical zone under the mould, a bending zone, a curved zone of constant radius, a straightening zone and an horizontal zone.

5.3.2 DESCRIPTION OF THE LOCAL DEFECT

The mesoscopic model is tested using a reference configuration where the continuous casting process takes place without a hitch and a configuration presenting a local defect. The modelled defect is a misalignment of one pair of rolls localised just before the beginning of the straightening zone of the continuous casting machine. The amplitude of the misalignment is 2 mm perpendicularly to the casting axis towards the centre of curvature of the caster (Figure 5.9). Although the amplitude of the defect seems small compared to the dimension of the caster, whose radius of curvature is 8 m, it introduces large local bending and straightening effects which are damageable to the final product. In practice, the position of the rolls are controlled at a precision of the order of the millimetre.

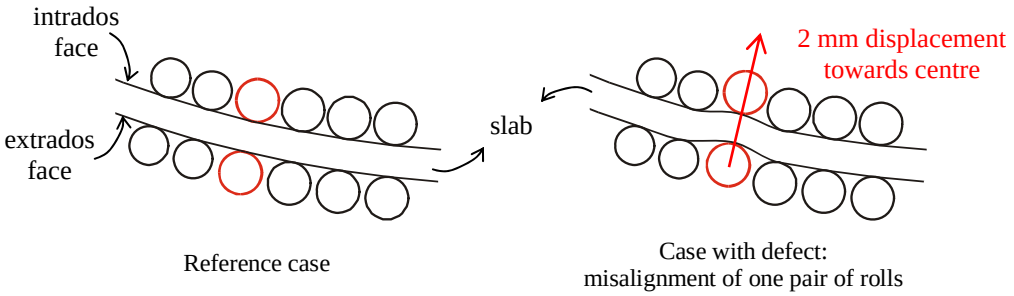

Figure 5.9. Illustration of the local defect relative to the reference case.

5.4 METHODOLOGY FOR THE DATA TRANSFER

The technique applied to transfer data from the macroscopic to the mesoscopic model has already been described when modelling the acoustic experiments in section 4.6.3.1. Basically, the stresses, strains and temperatures in the critical zone are recorded all along the simulation and transformed into boundary conditions to be applied to the mesoscopic cell. The adaptation of the method to the continuous casting slice model is presented hereafter.

5.4.1 EXTRACTION OF THE DATA

The results of the macroscopic model have identified the corner of the slab as the critical zone for crack initiation and propagation, the intrados side being the more exposed (Pascon 2003). These results are in agreement with on-site observations, which also show that the cracks more often initiate on the lateral face of the slab. Based on

these findings, two critical areas are chosen for the mesoscopic analysis, they are positioned close to the corner of the slab, either for the intrados or the extrados. These locations have been circled in Figure 5.10. To analyse a crck initiating on the lateral face of the slab, a section of type 2 has to be used.

Contrarily to the acoustic experiments, the temperature in the critical zone varies during the simulation of the continuous casting problem. Therefore, the temperature evolution has also to be transferred to the mesoscopic cell; this is done by imposing the temperature of each node of the mesoscopic cell at every time step following the data recorded from the macroscopic model. Similarly to the stress and strain fields, the temperature varies with time but is considered uniform on the cell, the objective being to reproduce the characteristic thermo-mechanical behaviour recorded macroscopically and not the spatial gradients.

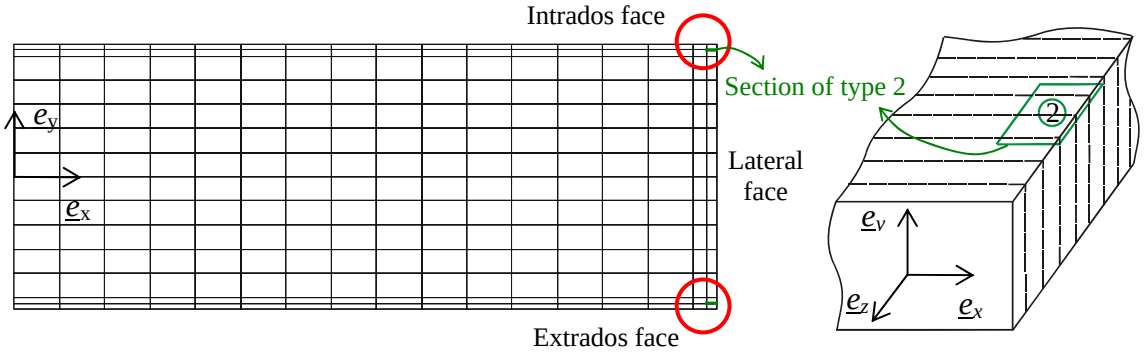

Figure 5.10. Mesh used for the macroscopic simulations, identification of the critical zones on the intrados and extrados faces and localisation of a section of type 2.

As the temperature is defined at the nodes and not at the integration points, it has been decided to focus on one node for the data collection and to use the results from the integration points surrounding it to calculate representative stresses at that node.

The localisation of the interesting nodes and integration points is illustrated in Figure 5.11 for the particular case of the intrados. The node where the stress, strain and temperature fields are recorded is node 1, which is common to the two elements in the corner (black dot). The displacements of the nodes labelled 2 to 5 (grey dots) are used to define the logarithmic strain along the *x* and *y*-axes in this zone. The strain along the *z*-axis is calculated directly using the information relative to the thickness of the slice of material modelled in generalized plane state.

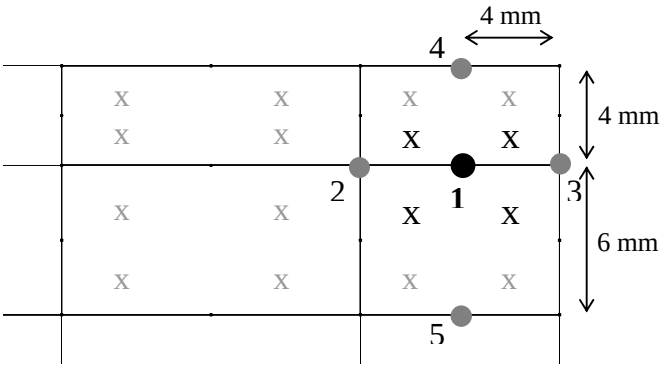

Figure 5.11. Zoom on the critical zone (intrados face) and identification of the nodes used in the calculations, nodes are represented by dots and integration points by crosses.

The stresses at node 1 are calculated by interpolation of the stresses recorded at the four integration points that surround the central node as highlighted in Figure 5.11 (black crosses). An interpolation in $1/R^2$ is used. It consists in calculating a weighted average of the stresses attaching more weight to the integration points that are closer to the central node where the interpolation is made. The exact formulation for the stresses interpolation is given by equation (5.3):

$$\sigma_{x,y,z} = \frac{\sum_{i=1}^{4} \frac{\left(\sigma_{x,y,z}\right)_i}{\left(R_i\right)^2}}{\sum_{i=1}^{4} \frac{1}{\left(R_i\right)^2}} \tag{5.3}$$

where R_i is the distance between the central node and the integration point *i* in the initial configuration and $\left(\sigma_{x,y,z}\right)_i$ the stress σ_x, σ_y or σ_z at the integration point *i*.

For illustration purpose, Figure 5.12 to Figure 5.14 show the stresses, strains and temperatures collected in the critical zone of the intrados face before being applied to the mesoscopic cell. The results for the reference case and for the case with defect are presented. These data have been extracted from the macroscopic simulations using the data collected at and around node 1 as explained before.

Globally, the stresses, strains an temperature curves present large oscillations all along the process due to the succession of rolls and water sprays in the caster. For the intrados face, apart from the variations at the beginning of the curve, i.e. just under the mould, the stress σ_z in the casting direction has a negative value during the first two thirds of the process; the upper face of the slab stays in compression until the straightening phase where it is in tension. The stresses σ_x and σ_y are close to zero

except at the end of the simulation after the straightening phase where compression occurs in the *y*-direction. The strains evolution plotted in Figure 5.13 can be easily correlated with the bending and straightening zones of the caster. In particular, it can be noted that for the intrados face, ε_z decreases sharply during the bending phase, then presents a smooth variation when the slab cools down in the zone of constant curvature of the caster, and finally increases sharply during the straightening phase.

The misalignment of one pair of rolls introduces large variations in the stress σ_z compared to the reference case. The evolution of σ_z in case of defect indicates a succession of local bending/straightening/bending behaviours as shown in Figure 5.12. The effect of the misalignment is also directly observed on the strains (see Figure 5.13). Nevertheless, the mechanical defect has almost no influence on the stresses σ_x and σ_y; the same comment can be done regarding the temperature but this is expected as the cooling conditions are not dramatically affected by the displacement of the pair of rolls. Moreover, all the variables plotted in Figure 5.12 to Figure 5.14 go back to values almost identical to the ones recorded for the reference case when the zone with defect is passed.

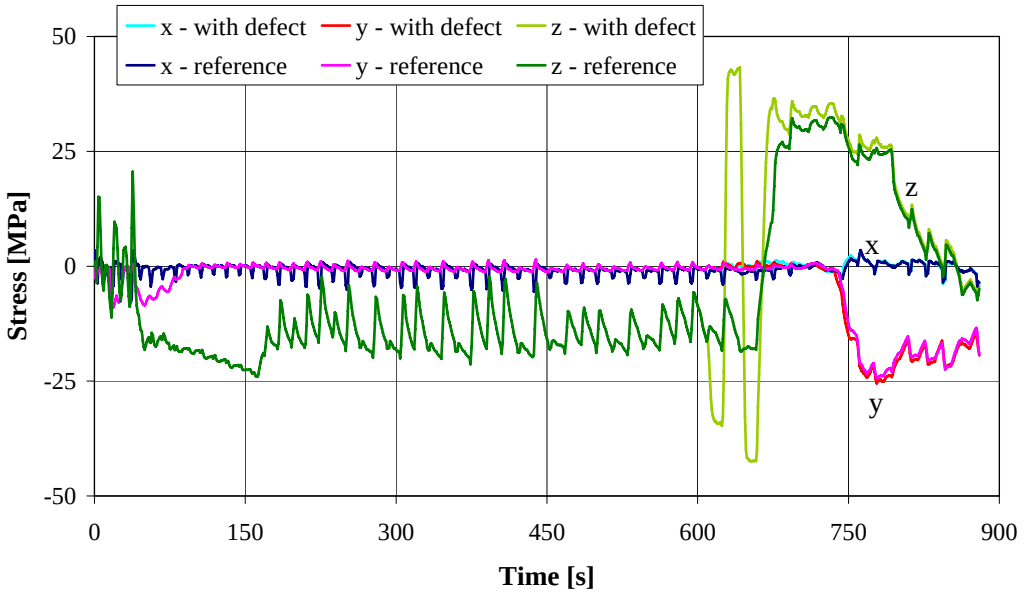

Figure 5.12. Stresses in the critical zone of the intrados side for the reference case and case with defect (misalignment of one pair of rolls).

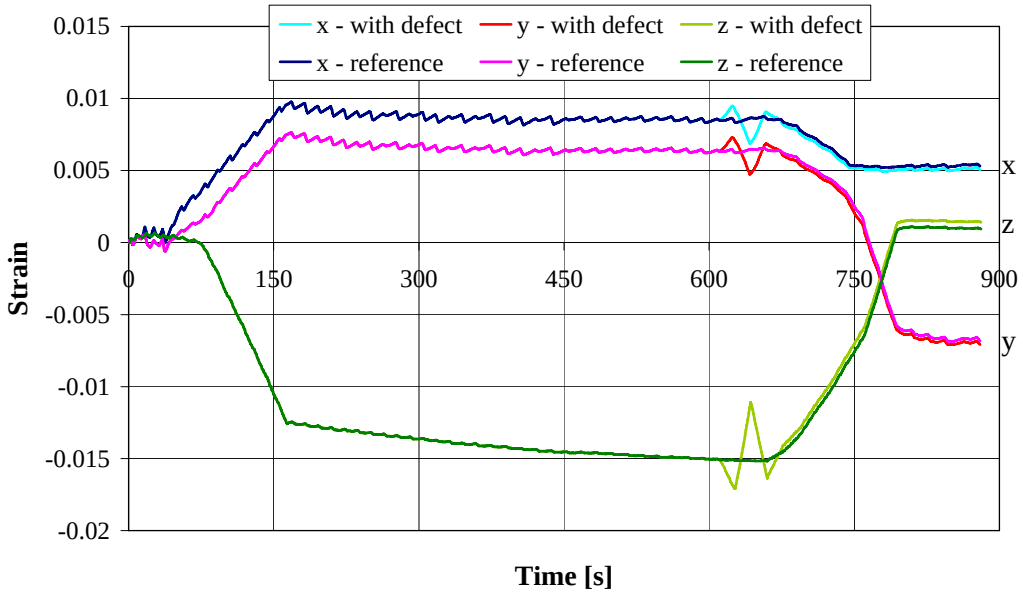

Figure 5.13. Strains in the critical zone of the intrados side for the reference case and case with defect (misalignment of one pair of rolls).

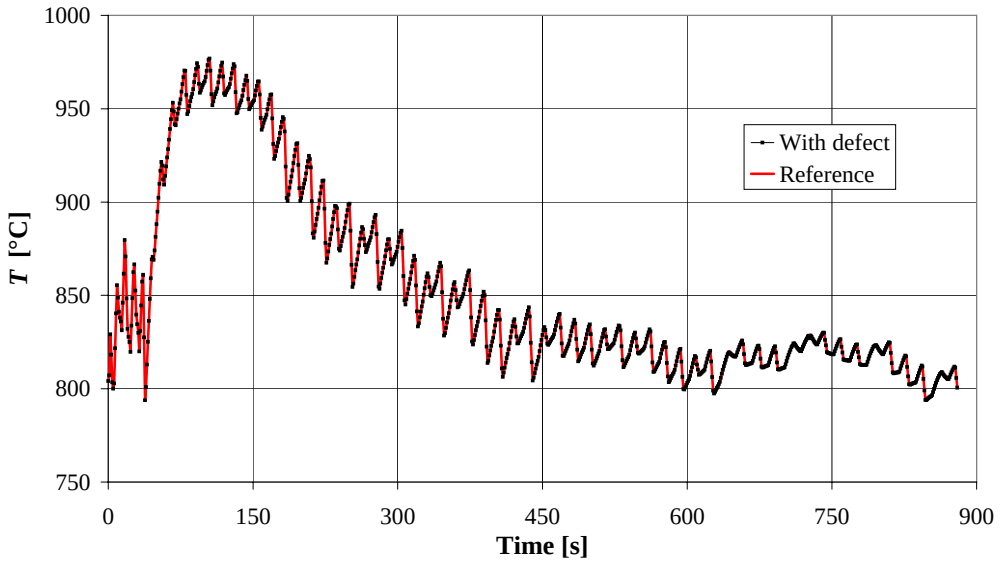

Figure 5.14. Temperatures in the critical zone of the intrados side for the reference case and case with defect (misalignment of one pair of rolls).

Similar curves can be drawn for the extrados. On the extrados side, the stress σ_z in the casting direction is in tension in the bending zone and in compression in the

constant curvature and straightening zones. The effect of the bending and straightening phases on the strains are inverted compared to the intrados face.

5.4.2 DEFINITION OF THE MESOSCOPIC CELL BOUNDARY CONDITIONS

The stresses and strains extracted from the macroscopic continuous casting simulations are used to define the forces and displacements to be applied as boundary conditions on the mesoscopic cell. The details of the conversion method have been described in section 4.6.3.1. The same equations are used in the present case after having been adapted to the proper the axes systems used for the continuous casting slice model and for the corresponding mesoscopic model.

It has been shown in Chapter 4 that it is possible to reproduce the correct macroscopic stress-strain behaviour on the mesoscopic cell when forces F_y and F_z are imposed in the *y*-direction (thickness) and *z*-direction (vertical) and displacements Δx in the *x*-direction (horizontal) as shown on Figure 5.15.

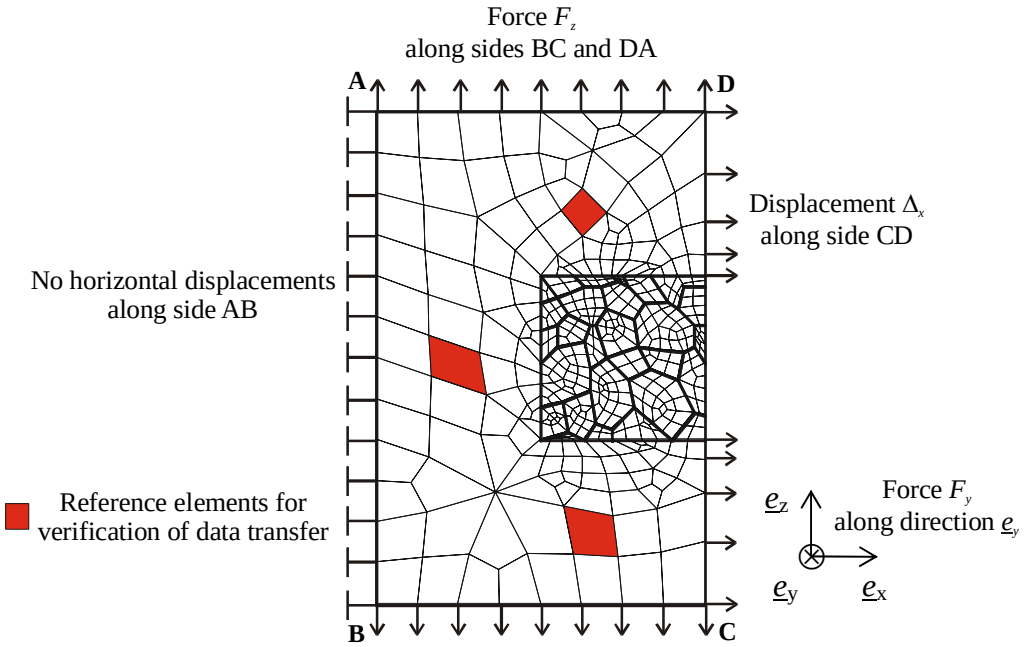

Figure 5.15. Boundary conditions on the mesoscopic cell.

The displacements along the *x*-direction are equal to zero on side AB. A free edge is kept along the grains zone to allow crack initiation and propagation. For the calculation of the forces based on the stresses, the actualised section has to be taken into account; the latter being known via the strains. The axes system of the mesoscopic cell

has been chosen to be directly transposable to the macroscopic model as defined in Figure 3.31. In the example presented in Figure 5.15, the section studied is a section of type 2 which means that the cracks initiate on the lateral face of the slab. To study a section of type 3 where the cracks initiate on the upper or lower face of the slab, the axes *x* and *y* of the mesoscopic cell have to be switched but the *z*-axis remains unchanged.

5.5 RESULTS OF THE MESOSCOPIC SIMULATIONS

5.5.1 VERIFICATION OF THE DATA TRANSFER

Before analysing the results in terms of damage progression and crack initiation for various continuous casting conditions, a verification that the correct stresses distribution is reproduced on the mesoscopic cell has been carried out. To perform the verification, the average of the stresses for the three elements highlighted in Figure 5.15 have been recorded and compared with the imposed data. In Figure 5.16, which corresponds to the reference case for the critical zone of the intrados side, it can be seen that the data are correctly reproduced for each stress all along the simulation.

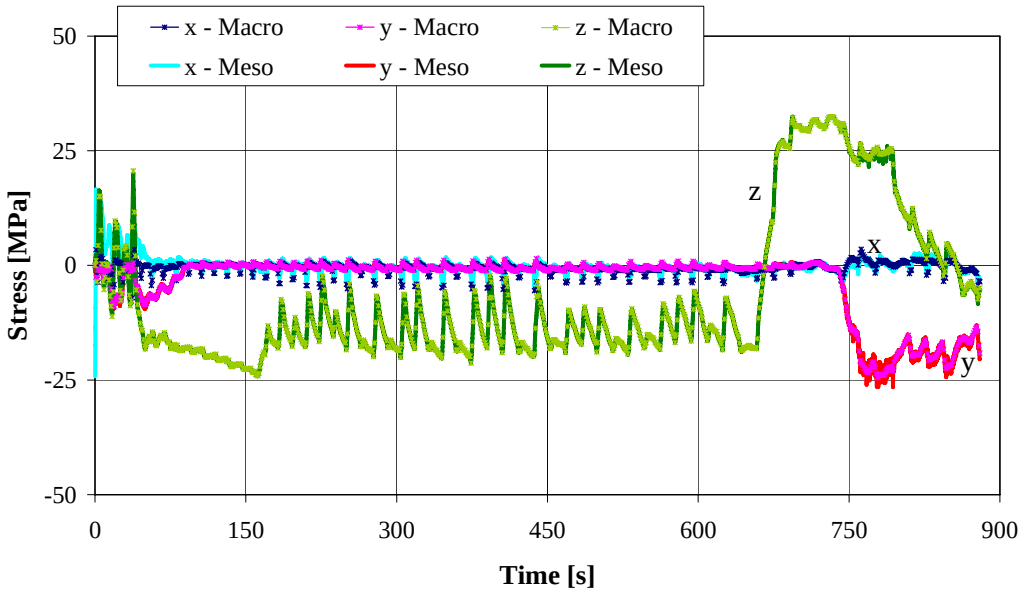

Figure 5.16. Verification of the stresses transfer between the macroscopic and mesoscopic models for critical point on the intrados side.

The detailed calculation has not been made here regarding the verification of the transfer for the strains, but it has been proved in Chapter 4 that the transfer method was reliable. As the deformations are directly imposed along the *x*-axis and as it has been checked that the stresses are correctly reproduced, the strains along the *y* and *z*-axes will be correct as they are fixed by the constitutive law.

The transfer of the temperature field is straightforward and does not required any verification as it is directly imposed to the nodes of the mesoscopic cell.

5.5.2 ANALYSIS OF THE DAMAGE

The level of damage in the cell has been analysed for the different cases studied. The conditions that have been tested are the following:

- internal (intrados) and external (extrados) surface of the slab,
- cases with and without oscillation marks,
- reference case and case with defect (misaligned rolls).

The combinations of these conditions leads to the realisation and analysis of eight different simulations.

Figure 5.17 shows the meshes defined for the case with and without oscillation mark. The cell without oscillation mark is the one that has been previously used for the initial simulations and whose dimensions are 5.45 mm × 5.45 mm for the grains zone and 10.9 mm × 16.35 mm when the surrounding zone is included.

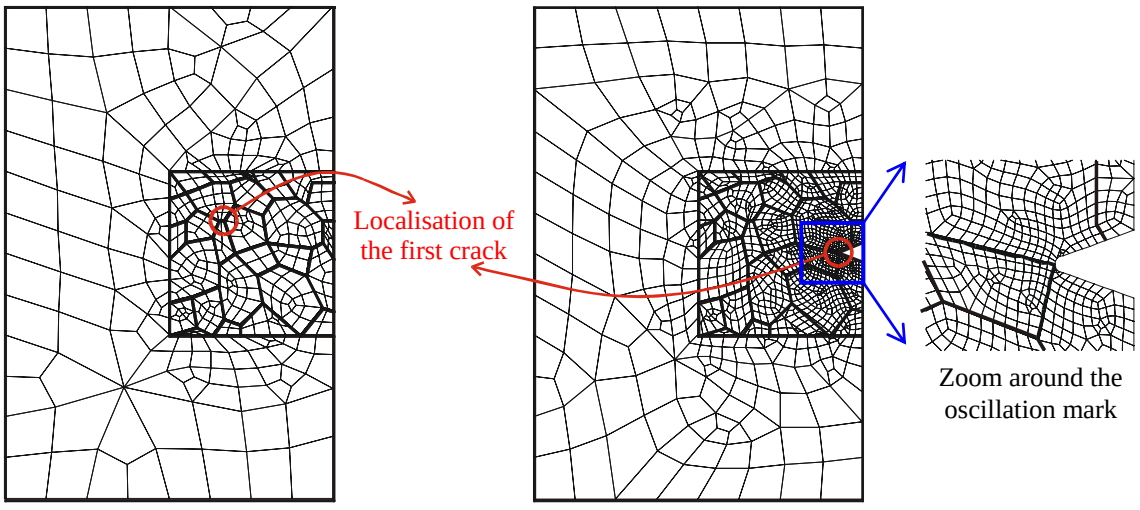

Figure 5.17. Meshes used for the final simulations, the red circle indicates the localisation of the critical element for crack initiation.

For the case without oscillation mark, as the loads are applied uniformly on the cell, the maximum damage value does not automatically appear on the edge of the grains zone. Therefore, the critical locations for crack initiation have been identified during the mesoscopic simulations and are represented in Figure 5.17: inside the grains zone, on a grain boundary perpendicular to the direction of the maximal principal stress, for the case without oscillation mark, and at the tip of the oscillation mark for the case with oscillation mark.

The initial mesh has been modified for the case with oscillation mark to allow a suitable modelling of the geometry of the oscillation mark. For this example, the oscillation mark corresponds to a V-shape indentation of depth equal to 0.75 mm as described in Figure 5.18, which indicates the exact geometry of the oscillation mark inserted in the mesh of Figure 5.17.

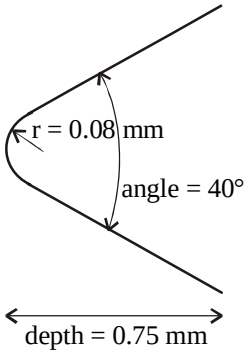

Figure 5.18. Geometry of the oscillation mark.

Table 5.3 indicates the results in terms of damage and the instant of the first crack initiation for the different cases analysed. With the mesoscopic damage law, the damage accumulates all along the simulation until it reaches the damage threshold indicating crack initiation. Such a criterion is different that the one proposed with the macroscopic model, where the risk indicators as defined by equations (5.1) and (5.2) correspond to instantaneous values.

For the mesh without oscillation mark, the maximal damage values d_{max} reached at the end of the simulations are indicated in Table 5.3. These values are around 0.2 which is much smaller than the critical threshold of 0.7 identified for crack initiation with the acoustic experiments simulations. Without oscillation mark, the spatial stresses variations inside the grains zone are only due to the shape, localisation and movements of the grains. There is no stress concentration effect that triggers the damage increase like for the case with oscillation mark. Nevertheless, it can be noted that for the case

without oscillation mark, the damage is slightly more important on the extrados face. This observation is due to the fact that the damage increases more when the cell is in tension and that the extrados face is in tension during most of the simulation whereas the intrados face is only in tension during the straightening phase. For both faces, the introduction of the defect induces a larger increase of the damage level.

Table 5.3. Maximum damage values for the eight cases studied.

Simulation	Mesh type	Intrados	Extrados
Reference	Without oscillation mark	d_{max} = 0.18	d_{max} = 0.23
	With oscillation mark	d_{max} = 0.5 (crack) t_{crack} = 783 s	d_{max} = 0.23 t_{crack} = no crack
With defect (misalignment of one pair of rolls)	Without oscillation mark	d_{max} = 0.22	d_{max} = 0.25
	With oscillation mark	d_{max} = 0.5 (crack) t_{crack} = 756 s	d_{max} = 0.47 t_{crack} = no crack

For the mesh with oscillation mark, a maximum damage threshold of 0.5 has been imposed to allow a comparison between the different cases. This choice is slightly smaller than the threshold of 0.7 identified with the simulations of the acoustic experiments but it is representative of the experimental results observed on the slabs. When the damage threshold is reached, a crack initiates. The corresponding time t_{crack} is indicated in Table 5.3.

The difficulty to accurately define the damage threshold using the results of the acoustic experiments can be explained by the fact that during these tests, the critical points in the different specimens are always in tension, whereas in the continuous casting process, the critical points undergo compression and tension loads alternatively. Although the correct strain rates are reproduced, the global loading histories are quite different. At the origin, the acoustic tests have been developed to define forming limit curves (Kopp and Berneath 1999) which have to be used to predict the formability of processes whose loading histories can be correlated with one of the basic tests used for production of these curves. Based on this consideration, it would be interesting to define specific acoustic tests configurations that reproduce cycles similar to those encountered in continuous casting in order to define more quantitative damage thresholds.

In the present case, the results of Table 5.3 for the mesh with oscillation mark indicate that a crack initiate on the intrados side and that the misalignment of one pair of rolls induces earlier cracking than the reference case with a maximal damage threshold of 0.5. Without defect, the damage remains low for the extrados side even with an oscillation mark but it almost reaches the maximal damage threshold on the intrados side, which is experimentally known to be more exposed to cracking problems.

A general conclusion drawn from the analysis is that the mesoscopic model predicts a more important damage level for the cases that are known to be more critical and that the model can be used to rank the different cases with regard to the sensibility to transverse cracking. The final results presented are compatible with the experimental observations and with the results given by the macroscopic model.

5.6 CONCLUSIONS OF THE PRACTICAL APPLICATION

In the context of the application of the mesoscopic damage model to the simulation of the industrial process of continuous casting, it has been shown that the modelling of a single oscillation mark was sufficient to analyse the influence of oscillation marks on transverse cracking. Indeed, no interaction between oscillation marks was observed for the different representative cases tested.

The final application, where various continuous casting conditions were simulated, has proved that the model could rank the different factors tested with regard to the sensitivity to transverse cracking. It has also been highlighted that it was difficult to define a precise damage threshold for crack initiation. To address this problem, specific acoustic test configurations could be developed to identify damage thresholds for the particular loading cases encountered in continuous casting. This approach would help in defining as set of parameters for which the model could be used as a quantitative rather than as a qualitative predictive tool.

Finally, the model has been validated by showing that with a maximum damage threshold of 0.5, the predictions were coherent with the results obtained with the macroscopic model and with the information collected from the industrial partner.

Chapter 6

Conclusions and perspectives

The objective of this research work was to develop a model capable of studying the damage process at elevated temperature and of addressing the problem of transverse cracking in steel continuous casting. To achieve this goal, a mesoscopic finite element model with damage has been developed, implemented and tested before being applied to the modelling of the industrial process of steel continuous casting.

6.1 KEY FINDINGS AND ACHIEVEMENTS

Based on the outcomes of the literature review, it is acknowledge that transverse cracks occurring in steel continuous casting are intergranular. These cracks develop by cavitation at the grain boundaries and by grain boundary sliding. The phenomenon of voids nucleation, growth and coalescence is established, the cavities evolving mainly under diffusion and creep deformations at elevated temperature. Strains concentration in the thin ferrite films formed along the grain boundaries during cooling also enhances the cracking process.

Due to the nature of the cracks to be represented, a mesosocopic approach which comprises solid elements for the grains and interface elements for the grain boundaries appeared to be an appropriate choice for the modelling. Therefore, a 2D grain model was developed and introduced in the finite element code LAGAMINE. In particular, a new interface element and its associated damage law were implemented.

The identification of the parameters of the constitutive laws specific to the studied material was realised using data collected from the literature and from microscopic and macroscopic experiments carried out especially as part of this project. To complete the parameters identification process, an inverse method that uses results from acoustic tests, i.e. compression tests during which crack initiation is detected by acoustic emission, was proposed. Used in parallel with finite element simulations modelling the performed experiments, these tests allowed the calibration of the parameters of the interface damage law that had not been directly defined by the macroscopic and microscopic experiments or by the literature review.

As the location of the critical zone for crack initiation was known for both the acoustic tests and the steel continuous casting applications, it was possible to model these processes at the mesoscopic scale by transferring stress, strain and temperature histories from the macroscopic to the mesoscopic level. Finally, it was shown that the mesoscopic damage model accurately simulated crack initiation for realistic continuous casting cases. When compared with the extrados face, it was verified that the model predicted a higher damage level in the critical zone for the intrados face. The introduction of an oscillation mark in the mesoscopic cell and the simulation of a process defect (misalignment of one pair of rolls) gave rise to earlier crack initiation. These results were correlated with crack risk indicators predicted by the macroscopic continuous casting model and with in-situ observations.

6.2 FUTURE WORK

The new mesoscopic damage model implemented in the LAGAMINE finite element code has been validated by simulating different continuous casting conditions. The model being now available, it is exploitable to test additional practical cases. For example, it is possible to use the model to analyse the effect on transverse cracking of:

- the oscillation marks geometry, by changing the depth and shape of the modelled oscillation mark,
- the grain size and/or its gradient, by defining various grains patterns,
- the precipitation state, by varying the parameters linked to nucleation or to the initial voids characteristics,
- the steel grade, by using appropriate grain and interface constitutive laws, a first comparative analysis could be provided by modifying only the grain law,

- other process defects such as blocked rolls or nozzles, by imposing on the mesoscopic cell the macroscopic stress, strain and temperature fields corresponding to these defects.

The model can also be exploited by defining spatial random variations of the damage parameters in the mesoscopic cell and analysing the results statistically. Likewise, statistically representative simulations can be carried out by modelling and analysing various grain patterns.

As already mentioned during the development phase, additional features can be added to the model. In particular, it is possible to extend the damage evolution law to account for characteristic phenomena linked to fatigue problems and/or to model specifically the austenite-ferrite transformation.

The difficulty to define accurately the damage parameters at elevated temperature by direct measurements imposes to rely on non-direct method. This statement is particularly true for materials cooling down under continuous casting conditions. Therefore, another research stream associated to the mesoscopic damage modelling is the definition of reliable non-direct parameters identification methods. In particular, specific acoustic tests configurations which lead to stress-strain histories that are closer to the loads sustained by the material during the macroscopic industrial process of continuous casting should be investigated to allow the definition of a set of parameters that assures a quantitative prediction of crack initiation.

Finally, the interface element and the damage law developed in this thesis are already applied in the scope of other research projects. More precisely, the complete model is exploited in a research project that aims at widening the developments carried out for microalloyed steels to peritectic and stainless steels (Schwartz *et al.* 2007). In another research project, the interface element is extended to be used in conjunction with a damage cohesive law for the modelling of fatigue crack in welded beam-to-column connection in buildings submitted to earthquake (Lequesne *et al.* 2005).

References

Altan, T., Oh, S., and Gegel, H., *Metal forming fundamentals and applications*, published by ASM International, pp. 60-61, 1983.

Anderson, T.L., *Fracture mechanics - Fundamentals and applications*, Ed. Taylor & Francis, London, 2005.

Anonymous, Standard methods for estimating the average grain size of metals, *ASTM E112-63*, published by ASTM International (American Society for Testing and Materials).

Ashby, M.F., Boundary defects and atomistic aspects of boundary sliding and diffusional creep, *Surface Sci.*, **31**, pp. 498-542, 1972.

Ashby, M.F., Gandhi, C., and Taplin, D.M.R., Fracture-mechanism maps and their construction for F.C.C. metals and alloys, *Acta Metall.*, **27**, pp. 699-729, 1979.

Aria, M., and Ogata, T., Study on mechanical factor of grain boundary cavity nucleation under creep-fatigue condition, *Damage and Fracture Mechanics*, Ed. Carpinteri, A., and Brebbia, C.A., Comp. Mech. Pub., Southampton, pp. 471- 480, 1998.

Bandstra, J.P., Koss, D.A., Geltmacher, A., Matic, P., and Everett, R.K., Modeling void coalescence during ductile fracture of a steel, *Mater. Science Engrg*, **A366**, pp. 269-281, 2004.

Barber, B., Leckenby, B.M., and Lewis, B.A., Finite element analysis of roll misalignement during continuous casting, *Ironmaking and Steelmaking*, **18:6**, pp. 431-436, 1991.

Benzerga, A.A., Micromechanics of coalescence in ductile fracture, *J. Mech. Phys. Solids*, **50**, pp. 1331-1362, 2002.

Benzerga, A.A., Besson, J., and Pineau, A., Anisotropic ductile fracture. Part II: theory, *Acta Mater.*, **52**, pp. 4639-4650, 2004.

Berger, E., Endommagement de matériaux viscoplastiques: étude théorique et simulations numériques, *Thèse de Docteur de l'Ecole Nationale Supérieure des Mines de Saint-Etienne et de l'Institut National Polytechnique de Grenoble*, France, 1998 (in French).

Bernard, G., Birat, J.P., Conseil, B., and Humbert, J.C., Etude de la sensibilité à la crique des aciers coulés en continu à l'aide d'essais de ductilité à chaud, *Revue de Métallurgie*, pp. 467-480, juillet 1978 (in French).

Betten, J., Sklepus, S. and Zolochevsky, A., A microcrack description of creep damage in crystalline solids with different behavior in tension and compression, *Int. J. Damage Mech.*, **8**, pp. 197-232, 1999.

Bille, J.P., Habraken, A.M., and Charlier, R., Numerical approach of contact using an augmented Lagrangian method, *3^{ième} Congrès National Belge de Mécanique Théorique et Appliquée*, Belgium, 1994.

Biwa, S., Finite expansion of an infinitesimal void in elastic-plastic materials under equitriaxial stress, *JSME Int. J. Serie A*, **40:1**, pp. 23-30, 1997.

Bordas, S., and Moran, B., Enriched finite elements and level sets for damage tolerance assessment of complex structures, *Engrg Frac. Mech.*, **73**, pp. 1176-1201, 2006.

Brighenti, R., Application of the element-free Galerkin meshless method to 3-D fracture mechanics problems, *Engrg Frac. Mech.*, **72**, pp. 2808-2820, 2005.

Brimacombe, J.K., and Sorimachi, K., Crack formation in the continuous casting of steels, *Metallurgical Transactions B*, **8**, pp. 489-505, 1977.

Brocks, W., Sun, D.Z., and Honig, A., Verification of the transferability of micromechanical parameters by cell model calculation with visco-plastic materials, *Int. J. Plasticity*, **11:8**, pp. 971-989, 1995.

Broek, D., *Elementary engineering fracture mechanics*, Ed. Kluwer Academic Publishers, Dordrecht, 1986.

Budiansky, B., Hutchinson, J.W. and Slutsky, S., Void growth and collapse in viscous solids, "*Mechanics of Solids" The R. Hill 60th anniversary volume*, Ed. Hopkins H.G., Sewell M.J., pp. 13-44, 1982.

Cannmo, P., Runesson, K., and Ristinmaa, M., Modelling of plasticity and damage in a polycrystalline microstructure, *Int. J. Plasticity*, **11:8**, pp. 949-970, 1995.

Cardoso, G.I.S.L., Mintz, B., and Yue, S., Hot ductility of aluminium and titanium containing steels with and without cyclic temperature oscillations, *Ironmaking and Steelmaking*, **22:5**, pp. 365-377, 1995.

Carpinteri, A., Ferro, G., and Ventura, G., The partition of unity quadrature in element-free crack modelling, *Comp. Struc.*, **81**, pp. 1783-1794, 2003.

Castagne, S., Habraken, A.M., and Cescotto, S., Application of a damage model to an aluminum alloy, *Int. J. Damage Mech.*, **11:4**, pp. 367-392, 2002.

Castagne, S., Remy, M., and Habraken, A.M., Development of a mesoscopic cell modelling the damage process in steel at elevated temperature, *Key Engrg Mat.*, **233**, pp. 145-150, 2003.

Castagne, S., Pascon, F., Bles, G., and Habraken A.M., Developments in finite element simulations of continuous casting, *J. Physique IV*, **120**, pp. 447-455, 2004.

Cepeda L.E., Rodriguez-Ibabe, J.M., Urcola, J.J., and Fuentes, M., Inflence of dynamic recrystallisation on hot ductility of aluminium killed mild steel, *Mat. Science and Tech.*, **5**, pp. 1191-1199, 1989.

Cescotto, S., and Grober, H., Calibration and application of an alastic-visco-plastic constitutive equation for steels in hot-rolling conditions, *Eng. Comput.*, **2**, pp. 101-106, 1985.

Cescotto, S., and Charlier, R., Frictional contact finite element based on mixed variational principles, *Int. J. Num. Meth. Engrg*, **36**, pp 1681-1701, 1993.

Chaboche, J.L., Kruch, S., and Pottier, T., Micromechanics versus macromechanics: A combined approach for the metal matrix composites constitutive modelling, *Eur. J. Mech. A/Solids*, **17**, pp. 885-908, 1998.

Charles, J.F., Zhu, Y.Y., Habraken, A.M., Cescotto, S., and Traversin, M., A fully coupled elasto-plastic damage theory for anisotropic materials, *Advanced methods in material processing defects*, **45**, pp. 33-42, 1997.

Chuang, T.J., Kawaga, K.I., Rice, J.R., and Sills, L.B., Non-equilibrium models for diffusive cavitation of grain interfaces, *Acta Metall.*, 27, pp. 265-284, 1979.

Chu, C.C., and Needleman, A., Void nucleation effects in biaxially stretched sheets, *J. Engrg Mat. Tech.*, **102:3**, pp. 249-256, 1980.

Condamin, L., Kuster, J.M., and Molvinger, J.C., Mesures de rides d'oscillations, *Internal note Ref. F&A n 2000/8511*, Irsid - Groupe Usinor, France, 2000 (in French).

Costes, F., Modélisation thermomécanique tridimensionnelle par éléments finis de la coulée continue d'aciers, *Thèse de Docteur de l'Ecole Nationale Supérieure des Mines de Paris*, France, 2004 (in French).

Daux, C., Moës, N., Dolbow, J., Sukumar, N., and Belytschko, T., Arbitrary branched and intersecting cracks with the extended finite element method, *Int. J. Num. Meth. Engrg*, **48**, pp. 1741-1760, 2000.

de Borst, R., and Remmers, J.J.C., Computational modelling of delamination, *Composites Sc. Tech.*, **66:6**, pp. 713-722, 2006.

Duchêne, L., Godinas, A., Cescotto, S., and Habraken, A.M., Texture evolution during deep-drawing process, *J. Mat. Proc. Techn.*, **126**, pp. 110-118, 2002.

Duchêne, L., and Habraken, A.M., Analysis of the sensitivity of FEM predictions to numerical parameters in deep drawing simulations, *Eur. J. Mech; A/Solids*, **24:4**, pp. 614-629, 2005.

Duflot, M., and Nguyen-Dang, H., Fatigue crack growth analysis by an enriched meshless method, *J. Comp. Appl. Math.*, **168**, pp. 155-164, 2004.

Duva, J.M., and Hutchinson, J.W., Constitutive potentials for dilutely voided nonlinear materials, *Mech. Mater.*, **3**, pp. 41-54, 1984.

Eshelby, J.D., The determination of the elastic field of an ellipsoïdal inclusion and related problem, *Proc. Roy. Soc. London*, **A241**, pp. 376-396, 1957.

Espinosa, H.D., Dwivedi, S., and Lu, H.C., Modeling impact induced delamination of woven fiber reinforced composites with contact/cohesive laws, *Comput. Methods Appl. Mech. Engrg*, **183:3**, pp. 259-290, 2000.

Feyel, F., A multilevel finite element method (FE^2) to describe the response of highly non-linear structures using generalized continua, *Comput. Methods Appl. Mech. Engrg*, **192:28-30**, pp. 3233-3244, 2003.

Foulk, J.W., Allen, D.H., and Helms, K.L.E., Formulation of a three-dimensional cohesive zone model for application to a finite element model, *Comput. Methods Appl. Mech. Engrg*, **183:1**, pp. 51-66, 2000.

François, D., Pineau, A., and Zaoui, A., *Comportement mécanique des matériaux*, Ed. Hermès, Paris, pp. 236-280, 1993.

Frost, H.J., and Ashby, M.F., *Deformation-mechanism maps, the plasticity and creep of metals and ceramics*, Ed. Pergamon Press, New York, 1982.

Fu, J.Y., Garcia, C.I., Pytel, S., and DeArdo, A.J., Hot ductility of continuously cast microalloyed steels, *Processing, Microstructure and Properties of HSLA steels*, The Mineral, Metal and Materials Society, pp. 27-38, 1988.

Gamsjäger, E., Fischer, F.D., Chimani, C.M., and Svoboda, J., Large strain concentrations during continuous casting – A micromechanical study of the diffusional phase transformation, *Proc. 4th International ESAFORM Conference on Material Forming*, Ed. Habraken, A.M., Liège, pp. 871-874, 2001.

Gandhi, C., and Ashby, M.F., Fracture-mechanism maps for materials which cleave: F.C.C., B.C.C. and H.C.P. metals and ceramics, *Acta Metall.*, **27**, pp. 1565-1602, 1979.

Ghosh, S., Lee, K., and Moorthy, S., Two scale analysis of heterogeneous elastic-plastic materials with asymptotic homogenization and Voronoi cell finite element model, *Comp. Meth. Appl. Mech. Engrg*, **132:1-2**, pp. 63-116, 1996.

Ghosh, S., Lee, K., and Raghavan, P., A multi-level computational model for multi-scale damage analysis in composite and porous material, *Int. J. Solids Structures*, **38**, pp. 2335-2385, 2001.

Gologanu, M., Leblond, J.B., and Devaux, J., Approximate models for ductile metals containing non-spherical voids – case of axisymetric prolate ellipsoïdal cavities, *J. Mech. Phys. Solids*, **41:11**, pp. 1723-1754, 1993.

Gologanu, M., Leblond, J.B., Perrin, G., and Devaux, J., Theoretical model for void coalescence in porous ductile solids. I. Coalescence “in layers”, *Int. J. Solids Structures*, **38**, pp. 5581-5594, 2001.

Goldsztein, G.H., Rigid perfectly plastic two-dimensional polycrystals, *Proc. Roy. Soc. London*, **A457**, pp. 2789-2798, 2001.

Gonzales, C., and Llorca, J., A self-consistent approach to the elasto-plastic behaviour of two-phase materials including damage, *J. Mech. Phys. Solids*, **48**, pp. 675-692, 2000.

Griffith, A.A., The phenomena of rupture and flow in solids. *Phil. Trans. Roy. Soc. London*, **A221**, pp.163-198, 1920.

Gurson, A.L., Continuum theory of ductile rupture by void nucleation and growth, *J. Engrg Materials Technology*, **99**, pp. 2-15, 1977.

Guttmann, M., Mécanismes microscopiques de la germination et de la croissance des cavités et des fissures intergranulaires dans les métaux et alliages à haute température sous sollicitation monotone et cyclique, *Communication n°530/MAT/T 41*, Département étude des matériaux, EDF, France, 1982 (in French).

Habraken, A.M., and Bourdouxhe, M., Coupled thermo-mechanical-metallurgical analysis during cooling of steel pieces, *Eur. J. Mech. A/Solids*, **11:3**, pp. 381-402, 1992a.

Habraken, A.M., Radu, J.P., and Charlier, R., Numerical approach of contact with friction between two bodies in large deformations, *Contact Mechanics Int. Symposium*, Lausane, 1992b.

Habraken, A.M., and Cescotto, S., Contact between deformable solids: the fully coupled approach, *Mathl. Comput. Modelling*, **28:4-8**, pp. 153-169, 1998a.

Habraken, A.M., Charles, J.F., Wégria, J., and Cescotto, S., Dynamic recrystallisation during zinc rolling, *Int. J. Forming Processes*, **1:1**, pp. 53-73, 1998b.

Habraken, A.M., Contributions to constitutive laws of metals: micro-macro and damage models, *Thèse d'agrégation*, Université de Liège, Belgique, 2001.

Habraken, A.M., and Duchêne, L., Anisotropic elasto-plastic finite element analysis using a stress-strain interpolation method based on a polycristalline model, *Int. J. Plasticity*, **20:8-9**, pp. 1525-1560, 2004.

Harada, S., Takana, S., Misumi, H., Mizogichi, S., and Horiguchi, H., A formation mechanism of tranverse cracks on CC slabs surface, *ISIJ International*, **30:4**, pp. 310-316, 1990.

Hatanaka, K., Yahya, A.N., Nonaka, I., and Umaki, H., Initiation of high temperature creep voids in notched components, *JSME International Journal*, **42:2**, pp. 280-287, 1999.

Héraud, S., Du polycristal au multi cristal : élaboration d'un mésoscope numérique pour une analyse locale en élastoviscoplasticité, *Thèse de Docteur de l'Ecole Polytechnique*, France, 1998 (in French).

Hiebler H., and Bernhard, C., Mechanical properties and crack susceptibility of steel during solidification, *Steel Research*, **70:8-9**, pp. 349-355, 1999.

Hill, R., The elastic behaviour of crystalline aggregates, *Proc. Phys. Soc.*, **A65-5**, pp. 349-354, 1952.

Hill, R., A self-consistent mechanics of composite materials, *J. Mech. Phys. Solids*, **13**, pp. 213-222, 1965.

Horstemeyer, M.F., and Mosher, D.A., Strain-rate and temperature dependent plasticity-damage evolution, *Proc. of Plasticity '99: The Seventh International Symposium on Plasticity and its Current Applications,* Ed. Akhtar S. Khan, pp. 651-654, 1999.

Huespe, A.E., Cardona, A., and Fachinotti, V., Thermomechanical model of a continuous casting process, *Comp. Meth. Appl. Mech. Engrg*, **182:3-4**, pp. 439-455, 2000.

Hull, D., and Rimmer, E., The growth of grain boundary voids under stress, *Phil. Mag.*, **4**, pp. 673-687, 1959.

Irwin, G.R., Fracture dynamics, *Fracturing of Metals*, Ed. American Society for Metals, Cleveland, pp. 147-166, 1948.

Irwin, G.R., Onset of fast crack propagation in high strength steel and aluminum alloys, *Sagamore Research Conference Proceedings*, Ed. Syracuse University Press, New York, **II**, pp. 289-305, 1956.

Jetteur, P., and Cescotto, S., A mixed finite element for the analysis of large inelastic strains, *Int. J. Num. Meth. Engrg*, **31**, pp. 229-239, 1991.

Ju, J.W., On energy-based coupled elastoplastic damage theories: Constitutive modelling and computational aspects, *Int. J. Solids & Structures*, **25:7**, pp. 803-833, 1989.

Kachanov, L.M., On the creep fracture time, *Izv Akad*, Nauk USSR Odt, Tekh., **8**, pp. 26-31, 1958 (in Russian).

Kiss, K., and Dunai, L., Fracture mechanics based fatigue analysis of steel bridge decks by two-level cracked models, *Computer and Structures*, **80**, pp. 2321-2331, 2002.

Kopp, R., and Bernrath, G., The determination of formability for cold and hot forming conditions, *Steel Research*, **70:4-5**, pp. 147-153, 1999.

Kouznetsova, V., Geers, M.G.D., and Brekelmans, W.A.M., Multi-scale constitutive modelling of heterogeneous materials with a gradient-enhanced computational homogenization scheme, *Int. J. Numer. Meth. Engng*, **54**, pp. 1235-1260, 2002.

Lankford, W.T., Some considerations of strength and ductlity in the continuous-casting process, *Metallurgical Transactions,* **3**, pp. 1331-1357, 1972.

Lassance, D., Scheyvaerts, F., and Pardoen, T., Growth and coalescence of penny-shaped voids in metallic alloys, *Engrg Fracture Mech.*, **73**, pp. 1009-1034, 2006.

Lassance, D., Fabrègue, D, Delannay, F., and Pardoen, T., Micromechanics of room and high temperature fracture in 6xxx Al alloys, *Progress Mat. Sc.*, **52**, pp. 62-129, 2007.

Leblond, J.B., Perrin, G., and Devaux, J., An improved Gurson-type model for hardenable ductile metals, *Eur. J. Mech. A/Solids*, **14**, pp. 499-527, 1995.

Leblond, J.B., *Mécanique de la rupture fragile et ductile*, Lavoisier, Paris, 2003.

Lecomte-Beckers, J., and Tchoufang Tchuindjang, J., Etude micro-macro de l'endommagement à haute température des aciers de construction, *Impulsion Project - Internal report n° 1*, Université de Liège, Belgique, 2000 (in French).

Lee, B.J., and M.E. Mear, M.E., Axisymmetric deformation power-law solids containing a dilute concentration of aligned spherical voids, *J. Mech. Phys. Solids*, **40**, pp. 1805-1836, 1992.

Lemaitre, J., and Chaboche, J.L., *Mécanique des matériaux solides*, Dunod, Paris, 1985.

Lemaitre, J., Coupled elasto-plasticity and damage constitutive equations, *Comp. Meth. Appl. Mech. Engrg*, **51:1-3**, pp. 31-49, 1985.

Lemaitre, J., and Desmorat, R., *Engineering damage mechanics*, Ed. Springer-Verlag, Berlin Heidelberg, 2005.

Lequesne, C., Gerday, A.F., Plumier, A., and Habraken, A.M., Modeling of fatigue crack in welded beam-to-column connection of steel moment frame buildings submitted to earthquake, *Advances in Fracture and Damage Mechanics IV*, Eds. Aliabadi, M.H., Buchholz, F.G., Alfaiate, J., Planas, J., Abersek, B., and Nishida, S.I., EC, Ltd. Publications, Eastleigh, UK, pp. 233-238, 2005.

Li, C.S., and Thomas, B.G., Thermomechanical finite-element model of shell behavior in continuous casting of steel, *Metal. Mat. Trans. B*, **35:6**, pp. 1151-1172, 2004.

Li, K.P., Habraken, A.M., and Bruneel, H., Simulation of square cup deep drawing with different finite elements, *J. Mat. Proc. Techn.*, **50:1-4**, pp. 81-91, 1995.

Li, K.P., and Cescotto, S., A 8-node brick element with mixed formulation for large deformation analyses, *Comp. Meth. Appl. Mech. Engrg*, **141**, pp. 157-204, 1997a.

Li, X.K., and Cescotto, S., Finite element method for gradient plasticity at large strains, *Int. J. Num. Meth. Engrg*, **39**, pp. 619-633, 1996.

Li, X.K., and Cescotto, S., A mixed element method in gradient plasticity for pressure dependent materials and modelling of strain localization, *Comp. Meth. Appl. Mech. Engrg*, **144**, pp. 287-305, 1997b.

Liang, Y., and Sofronis, P., On hydrogen-induced void nucleation and grain boundary decohesion in nickel-base alloys *J. Engrg Mat. Tech.*, **126**, pp. 368-377, 2004.

Lim, L.G., and Dunne, F.P.E., Modelling void nucleation and growth processes in a particle-reinforced metal matrix composite material, *Comp. Mater. Science*, **5**, pp. 177-186, 1996.

Liu, Y., Kageyama, Y., and Murakami, S., Creep fracture modeling by use of continuum damage variable based on Voronoi simulation of grain boundary cavity, *Int. J. Mech. Sci.*, **40:2-3**, pp. 147-158, 1998.

Louhenkilpi, S., Laitinen, E., and Nieminen, R., Real-time simulation of heat transfer in continuous casting, *Metallurgical Transactions B*, **24**, pp. 685-693, 1993.

Maehara, Y., Yasumoto, K., Sugitani, Y., and Gunji, K., Effect of carbon on hot ductility of as-cast low alloy steels, *Transactions ISIJ*, **25**, pp. 1045-1052, 1985.

Maehara, Y., Tomono, H., and Yasumoto, K., Effect of notch geometry on hot ductility of austenite, *Transactions ISIJ*, **27**, pp. 103-109, 1987.

McLean, M., and Dyson, B.F., Modeling the effects of damage and microstructural evolution on the creep behavior of engineering alloys, *J. Engrg Mat. Tech.*, **122**, pp. 273-278, 2000.

Michel, B., Formulation of a new intergranular creep damage model for austenitic stainless steel, *Nuc. Engrg Design*, **227**, pp. 161-174, 2004.

Mintz, B., Yue, S., and Jonas, J.J., Hot ductility of steels and its relationship to the problem of transverse cracking during continuous casting, *International Material Reviews*, **36:5**, pp. 187-217, 1991.

Mintz, B., and Abushosha, R., Influence of vanadium on hot ductility of steel, *Ironmaking and Steelmaking*, **20**, pp. 445-452, 1993.

Mintz, B., The influence of composition on the hot ductility of steels and to the problem of tranverse cracking, *ISIJ International*, **39:9**, pp. 833-855, 1999.

Miyake, T., Nakayama, K., Morishita, M., and Tai, H., Effects of heat and fluid flow in continuous casting molds on solidification shell growth, *Kobelco Technology Review*, **21**, pp. 7-13, 1998.

Mohan, R., and Brust, F.W., On void growth in elastic-nonlinear viscous solids under creep and cyclic creep conditions, *J. Engrg Mat. Tech.*, **122**, pp. 283-293, 2000.

Moës, N., and Belytschko, T., Extended finite element method for cohesive crack growth, *Engrg Fract. Mech.*, **69:7**, pp. 813-833, 2002.

Mori, T., and Tanaka, K., Average stress in matrix and average elastic energy of materials with misfitting inclusions, *Acta Metall. Mater.*, **21**, pp. 597-629, 1973.

Moureaux, P., Essais de compression – Sylvie Castagne, *M.S.M. Internal report*, Université de Liège, Belgique, 2001 (in French).

Murakami, S., Hayakawa, K., and Liu, Y., Damage evolution and damage surface of elastic-plastic-damage materials under multiaxial loading, *Int. J. Damage Mechanics*, **7:2**, pp. 103-128, 1998.

Murakami, S., Liu, Y., and Mizuno, M., Computational method for creep damage fracture analysis by damage mechanics, *Comput. Methods Appl. Mech. Engrg*, **183**, pp. 15-33, 2000.

Myllykoski, L., and Suutala, N., Effect of solidification mode on hot ductility of austenitic stainless steels, *Metals Technology*, **10**, pp. 453-463, 1983.

Nabarro, F.R.N., and de Villiers, H.L., *The physics of creep*, Ed. Taylor & Francis, London, 1995.

Needleman, A., and Rice, J.R., Plastic creep flow effects in the diffusive cavitation of grain boundaries, *Acta Metall.*, **28**, pp. 1315-1332, 1980.

Needleman, A., and Rosakis, A.J., The effect of bond strength and loading rate on the conditions governing the attainment of intersonic crack growth along interfaces, *J. Mech. Phys. Solids*, **47**, pp. 2411-2449, 1999.

Nguyen, B.N., Onck, P., and van der Giessen, E., A homogenized microstructural approach to creep fracture, *Endommagement, fatigue, rupture*, Ed. C.R. Acad. Sci., Paris, **328-IIb**, pp. 733-739, 2000.

Onck, P., and van der Giessen, E., Microstructurally-based modelling of intergranular creep fracture using grain elements, *Mechanics of Materials*, **29**, pp. 109-126, 1997.

Onck, P., and van der Giessen, E., Micromechanics of creep fracture: simulation of intergranular crack growth, *Comp. Materials Science*, **13**, pp. 90-102, 1998.

Onck, P., and van der Giessen, E., Growth of an initially sharp crack by grain boundary cavitation, *J. Mech. Phys. Solids*, **47**, pp. 99-139, 1999.

Onck, P.R., Nguyen, B.N., and van der Giessen, E., The linkage between microscopic cavitation damage and macroscopic crack growth, *J. Engrg Mat. Tech.*, **122**, pp. 279-282, 2000.

Orowan, E., Fracture and strength of solids, *Reports on Progress in Physics*, **12**, pp. 185-232, 1949.

Pardoen, T., and Hutchinson, J.W., An extended model for void growth and coalescence, *J. Mech. Phys. Solids*, **40**, pp. 2467-2512, 2000.

Park, J.K., Thomas, B.G., and Samarasekera, I.V., Analysis of thermo-machanical behavior in billet casting with different mold corner radii, *Ironmaking and Steelmaking*, **29:5**, pp. 359-375, 2002.

Pascon, F., Habraken, A.M., Bourdouxhe, M., and Labory, F., Modélisation des phénomènes thermomécaniques dans une lingotière de coulée continue, *Mec. Ind.*, **1**, pp. 61-70, 2000 (in French).

Pascon, F., 2D½ thermal-mechanical model of continuous casting of steel using finite element method, *Thèse de Docteur en Sciences Appliquées*, Université de Liège, Belgique, 2003.

Pascon, F., Casotto, S., Bruschi, S., and Habraken, A.M., Thermo-mechanical-metallurgical model to predict geometrical distortions of rings during cooling

phase after ring rolling operations, *Int. J. Mach. Tools Manuf.*, **45**, pp. 657-664, 2005.

Pascon, F., Cescotto, S., and Habraken, A.M., A 2.5D finite element model for bending and straightening in continuous casting of steel slabs, *Int. J. Numer. Meth. Engng*, **68**, pp. 125-149, 2006.

Patrick, B., Short, M.W., Walmsley, R., Barber, B. Hartse, K., Tacke, K.H., and Stinert, I., Crack prevention in continuous casting, ECSC project 7210-CA/167, 7210-CA/168, 7210-CA/833, *Draft final report*, Max Planck Institut, Düsseldorf, Germany, 1997.

Pecquet, E., Commentaires et résultats de la calibration des courbes de Norton-Hoff température par température, *M.S.M. Internal report*, Université de Liège, Belgique, 2003 (in French).

Perzyna, P., Internal state variable description of dynamic fracture of ductile solids, *Int. J. Solids & Structures*, **22:7,** pp. 797-818, 1986.

Pietrzak, G., and Cunier, A., Large deformation frictional contact mechanics: continuum formulation and augmented Lagrangian treatment, *Comp. Meth. Appl. Mech. Engrg*, **177:3-4**, pp. 351-381, 1999.

Ponte Castañeda, P., The effective mechanical properties on nonlinear isotropic composites, *J. Mech. Phys. Solids*, **39**, pp. 45-71, 1991.

Pottier, T., Modélisation multiéchelle du comportement et de l'endommagement de composites à matrice métallique, *Thèse de Docteur de l'Ecole Nationale des Ponts et Chaussées*, France, 1998 (in French).

Ragab, A.R., Creep rupture due to material damage by cavitation, *J. Engrg Mat. Tech.*, **124**, pp. 199-205, 2002.

Raghavan, P., Li, S., and Ghosh, S., Two scale response and damage modelling of composite materials, *Finite Elem. Anal. Design*, **40**, pp. 1619-1640, 2004.

Remy, M., Calibration finale de la loi de Norton-Hoff, *M.S.M. Internal report*, Université de Liège, Belgique, 2002a (in French).

Remy, M., Castagne, S., and Habraken, A.M., Progress in microscopic modeling of damage in steel at high temperature, *Int. J. Forming Processes*, **5:2-4**, pp. 445-455, 2002b.

Ren, J., and Wang, Z., Analysis of bulging and strain for continuously cast slab as thermoelastic continuous beam, *Ironmaking and Steelmaking*, **25:5**, pp. 394-397, 1998.

Revaux, T., Deprez, P., Bricout, J.P., and Oudin, J., *In situ* solidified hot tensile test and hot ductility of some plain carbon steels and microalloyed steels, *ISIJ International*, **34:6**, pp. 528-535, 1994.

Rice, J.R., A path independent integral and the approximate analysis of strain concentration by notches and cracks, *J. Appl. Mech.*, **35**, pp. 379-386, 1968.

Ridoffi, M.R., Thomas, B.G., and Della Foglia, U., The optimization of mold taper for the Ilva-Dalmine round bloom caster, *La Revue Métallurgique – CIT*, pp. 609-620, 1994.

Rabotnov, Y.N., Creep rupture, *Proc. Applied Mechanics Conference*, Eds. Hetenyi, M., and Vicenti, H., Stanford University, pp. 342-349, 1968.

Rousselier, G., Ductile fracture models and their potential in local approach of fracture, *Nuclear Engrg Des*, **105**, pp. 97-111, 1987.

Rousselier, G., Devaux, J.C., Mottet, G., and Devesa, G., A methodology for ductile fracture analysis based on damage mechanics: an illustration of a local approach of fracture, *Non-linear Fracture Mechanics: Volume II - Elastic-Plastic Fracture, ASTM STP 995*, Eds. Landes, J.D., Saxena, A., and Markle, J.G., American Society for Testing and materials, Philadelphia, pp. 332-354, 1989.

Sabirov, I., and Kolednik, O., The effect of inclusion size on the local conditions for void nucleation near a crack tip in a mild steel, *Scripta Mater.*, **53**, pp. 1373-1378, 2005.

Schwerdtfeger, K., and Sha, H., Depth of oscillation marks forming in continuous casting of steel, *Metal. Mat. Trans. B*, **31**, pp. 813-826, 2000.

Seppälä, E.T., Belak, J., and Rudd, R.E., Onset of void coalescence during dynamic fracture of ductile metals, *Phys. Rev. Letters*, **93**, 245503(4), 2004.

Shewmon, P., and Anderson, P., Void nucleation and cracking at grain boundaries, *Acta Mater.*, **46**, pp. 4861-4872, 1998.

Simo, J.C., and Laursen, T.A, An augmented lagrangian treatment of contact problems involving friction, *Comp. Struc.*, **42**, pp. 97-116, 1992.

Sukumar, N., Moran, B., and Belytschko, T., The natural element method in solid mechanics, *Int. J. Num. Meth. Engrg*, **43:5**, pp. 839-887,1998.

Suquet, P., Overall potentials and external surfaces of power-law or ideally plastic composites, *J. Mech. Phys. Solids*, **41**, pp. 981-1002, 1993.

Suzuki, H.G., Nishimura, S., Imamura, J., and Nakamura, Y., Embrittlement of steel occurring in the temperature range from 1000 to 600°C, *Transaction ISIJ*, **24**, pp. 169-177, 1984.

Suzuki, M., Hayashi, H., Shibata, H., Emi, T., and Lee, I.J., Simulation of tranverse crack formation on continuously cast peritectic medium carbon steel slabs, *Process Metallurgy*, **70:10**, pp. 433-419, 1999.

Swan, C.C., and Kosaka, I., Voigt-Reuss topology optimization for structures with non-linear material behaviors, *Int. J. Num. Meth. Engrg*, **40**, pp. 3785-3814, 1997.

Swartz, R., Castagne, S., and Habraken, A.M., Numerical study to identify the material parameters of a damage model, *in Proc. XIV Komplastech Conference, Computer Methods in Materials Science*, Zakopane, Poland, 2007.

Tanguy, B., and Besson, J., An extension of the Rousselier model to viscoplastic temperature dependent materials, *Int. J. Fract.*, **116:1**, pp. 81-101, 2002.

Thomas, B.G., and Ho, B., Spreadsheet model of continuous casting, *Materials processing in the computer age*, Eds. Voller, V.R, Stachwicz, M.S, and Thomas, B.G, The Minerals, Metals & Materials Society, pp. 293-306, 1991.

Thomas, B.G., Modeling of the continuous casting of steel-past, present, and future, *Metallurgical Transactions B*, **33:6**, pp. 795-812, 2002.

Thomson, C.I.A., Worswick, M.J., Pilkey, A.K., Lloyd, D.J., and Burger, G., Modeling void nucleation and growth within periodic clusters of particles, *J. Mech. Phys. Solids*, **47**, pp. 1-26, 1999.

Thomson, C.I.A., Worswick, M.J., Pilkey, A.K., and Lloyd, D.J., Void coalescence within periodic clusters of particles, *J. Mech. Phys. Solids*, **51**, pp. 127-146, 2003.

Tijssens, M.G.A., Sluys, B.L.J., and van der Giessen, E., Numerical simulation of quasi-brittle fracture using damaging cohesive surfaces, *Eur. J. Mech. A/Solids*, **19:5**, pp. 761-779, 2000.

Tschirnich, M., Determination of flow curves, *Final report for R&D Project Nr. IX/2/2000 MSM-IBF*, Rheinisch-Westfälische Technische Hochschule, Aachen, Germany, 2000.

Tvergaard, V., Material failure by void coalescence in localized shear bands, *Int. J. Solids & Structures*, **18:8**, pp. 659-672, 1982.

Tvergaard, V., On the creep constrained diffusive cavitation of grain boundary facets, *J. Mech. Phys. Solids*, **35:5**, pp. 373-393, 1984.

Tvergaard, V., and Needleman, A., Analysis of the cup-cone fracture in a round tensile bar, *Acta Metall.*, **32:1**, pp. 157-169, 1984.

Tvergaard, V., Cohesive zone representation of failure between elastic or rigid solids and ductile solids, *Engrg Fracture Mech.*, **70**, pp. 1859-1868, 2003.

van der Giessen, E., and Tvergaard, V., A creep rupture model accounting for cavitation at sliding grain boundaries, *Int. J. Frac.*, **48**, pp. 153-178, 1991.

van der Giessen, E., and Tvergaard, V., Development of final creep failure in polycrystalline aggregates, *Acta Metall.*, **42**, pp. 959-973, 1994.

van der Giessen, E., van den Burg, M.W.D., Needleman, A., and Tvergaard, V., Void growth due to creep and grain boundary diffusion at high triaxialities, *J. Mech. Phys. Solids*, **43:1**, pp. 123-165, 1995.

van der Giessen, E., Nguyen, B.N., and Onck, P.R., From a microstructural to a continuum model for creep fracture, *Continuous Damage and Fracture*, Ed. Benallal, A., Elsevier, pp. 129-136, 2000.

Vodovipec, F., Influence of precipitation and precipitates of aluminium nitride on torsional deformability of low-carbon steel, Metals Technology, pp. 118-121, 1978.

Volles, R., Friction-coefficient determination, *Final report for R&D Project Nr. IX/01/2003 MSM-IBF*, Rheinisch-Westfälische Technische Hochschule, Aachen, Germany, 2003.

Voyiadjis, G.Z., and Park, T., The kinematics of damage for finite-strain elasto-plastic solids, *Int. J. Engrg Science*, **37:7**, pp. 803-830, 1999.

Voyiadjis, G.Z., and Deliktas, B., A coupled anisotropic damage model for the inelastic response of composite materials, *Comp. Meth. Appl. Mech. Engrg*, **183:3-4**, pp. 159-199, 2000.

Voyiadjis, G. Z., *Damage mechanics*, Ed. Taylor & Francis, London, 2005.

Washizu, K., *Variational methods in elasticity and plasticity*, Ed. Pergamon, Oxford, 1982.

Weisgerber, B., Hecht, M., and Harste, K., Investigations of the solidification structure of continuously cast slabs, *Process Metallurgy*, **70:10**, pp. 403-411, 1999.

Wells, A.A., Application of fracture mechanics at and beyond general yielding, *British Welding Journal*, **11**, pp. 563-570, 1963.

Westwood, C., Pan, J., Le, H., Kucherenko, S., and Crocombe, A., A simplified model for cavity growth along grain-boundary by coupled surface and grain boundary diffusion, *Eur. J. Mech. A/Solids*, **19**, pp. 17-30, 2000.

Wolske, M., Investigations to the formability of micro-alloyed steel, *Final report for R&D Project Nr. IX/3/2000 MSM-IBF*, Rheinisch-Westfälische Technische Hochschule, Aachen, Germany, 2001.

Wu, M.S., and Guo, J., Analysis of a sector crack in a three dimensional Voronoi polycrystal with microstructural stresses, *J. Applied Mech.*, **67**, pp. 50-58, 2000.

Xu, X.P., and Needleman, A., Numerical simulations of fast crack growth in brittle solids, *J. Mech. Phys. Solids*, **42**, pp. 1397-1434, 1994.

Xu, Y., and Bassani, J.L., A steady-state model for diffusion-controlled fracture, *Mat. Sci. & Engrg*, **A260**, pp. 48-54, 1999.

Zienkiewicz, O.C., and Taylor, R.L., *The finite element method for solid and structural mechanics*, 6th edition, Ed. Elsevier Butterworth-Heinemann, Oxford, 2005.

Zhou, F., and Molinari, J.F., Dynamic crack propagation with cohesive elements: a methodology to address mesh dependency, *Int. J. Num. Meth. Engrg*, **59**, pp. 1-24, 2004.

Zhu, Y.Y., Contribution to the local approach of fracture in solid dynamics, *Thèse de Docteur en Sciences Appliquées*, Université de Liège, Belgique, 1992a.

Zhu, Y.Y., A fully coupled elastoplastic damage modeling of contact-impact between two deformable bodies. Structures under shock and impact, *II Computational Mechanics Publications*, Eds. Bulson, P.S., and Telford, T., pp. 113-133, 1992b.

Zhu, Y.Y., and Cescotto, S., Unified and mixed formulation of the 4-node quadrilateral elements by assumed strain method: Application to thermomechanical problems, *Int. J. Num. Meth. Engrg*, **38**, pp. 685-716, 1995.

Appendix A

Derivation of the generalized plane state for the mixed 4-node element

A.1 INTRODUCTION

The developments leading to the definition of the classical rigidity matrix for the mixed 4-node element have been presented by Zhu in his thesis (Zhu 1992a). The additional terms that have to be introduced in the rigidity matrix for the modelling of the generalized plane state are calculated hereafter.

A.2 MATHEMATICAL DERIVATIONS

A.2.1 NODAL FORCES AND RIGIDITY MATRIX

The generalized plane state allows the modelling of a thin slice of material, whose two surfaces are forced to stay plane but can move closer or apart from one another and/or rotate around any axis to be defined in the plane the section.

In practice, an additional node is associated to the element. This node has three degrees of freedom that are linked to the relative movement of the two surfaces of the slice (one displacement and two rotations). For the mixed 4-node element, a fifth node has to be defined. This node is common to all the elements and is then linked to all the nodes of the studied section through the rigidity matrix.

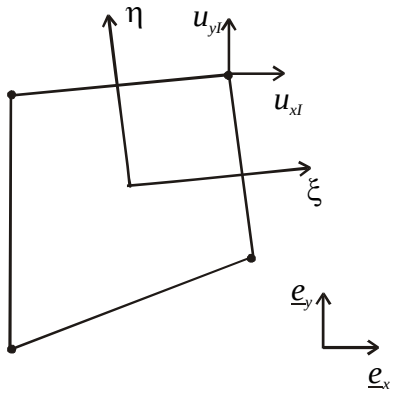

Figure A.1. Representation of the 4-node element.

The displacements (A.1) and the thickness of the slice (A.2) are given by:

$$\begin{aligned} u_x &= \sum_I N_I u_{x_I} \\ u_y &= \sum_I N_I u_{y_I} \end{aligned} \tag{A.1}$$

$$e = \alpha_1 + \alpha_2 x + \alpha_3 y \tag{A.2}$$

where $\underline{u}_x = \left[u_{x1}, u_{x2}, u_{x3}, u_{x4}\right]$ and $\underline{u}_y = \left[u_{y1}, u_{y2}, u_{y3}, u_{y4}\right]$ are the vectors representing the nodal displacements in the plane of the studied section, along $\underline{e}_x$ and $\underline{e}_y$ as shown on Figure A.1; and e the thickness of the slice. The N_I are the interpolation functions in the plane; α_1, α_2 and α_3 are the coordinates of the additional node, α_1 is associated to the translation of the centre of the element, α_2 and α_3 are associated to the rotation around the x and y axes, respectively.

For the mixed 4-node element, the vector representing the interpolation functions in the plane is given by:

$$\underline{N}(\xi,\eta) = \frac{1}{4}\underline{s} + \frac{1}{4}\underline{\xi}\xi + \frac{1}{4}\underline{\eta}\eta + \frac{1}{4}\underline{h}\xi\eta \tag{A.3}$$

with $\underline{\xi} = \left[-1,1,1,-1\right]$, $\underline{\eta} = \left[-1,-1,1,1\right]$, $\underline{s} = \left[1,1,1,1\right]$ and $\underline{h} = \left[1,-1,1,-1\right]$, ξ and η being the reference coordinates in the plane.

The Jacobien matrix for the transformation in the plane is:

$$J = \begin{bmatrix} \dfrac{\partial x}{\partial \xi} & \dfrac{\partial x}{\partial \eta} \\ \dfrac{\partial y}{\partial \xi} & \dfrac{\partial y}{\partial \eta} \end{bmatrix} \tag{A.4}$$

Its inverse is given by:

$$J^{-1} = \begin{bmatrix} \dfrac{\partial \xi}{\partial x} & \dfrac{\partial \xi}{\partial y} \\ \dfrac{\partial \eta}{\partial x} & \dfrac{\partial \eta}{\partial y} \end{bmatrix} = \frac{1}{|J|} \begin{bmatrix} \dfrac{\partial y}{\partial \eta} & -\dfrac{\partial x}{\partial \eta} \\ -\dfrac{\partial y}{\partial \xi} & \dfrac{\partial x}{\partial \xi} \end{bmatrix} \tag{A.5}$$

where $|J|$ is the Jacobien determinant:

$$|J| = \frac{\partial x}{\partial \xi}\frac{\partial y}{\partial \eta} - \frac{\partial x}{\partial \eta}\frac{\partial y}{\partial \xi} \tag{A.6}$$

The expression for the velocity gradient is:

$$\{d\varepsilon\} = [B]\{du, d\alpha\} \tag{A.7}$$

with

$$\{d\varepsilon\} = \left\{ \frac{\partial du_x}{\partial x}, \frac{\partial du_x}{\partial y}, \frac{\partial du_y}{\partial x}, \frac{\partial du_y}{\partial y}, \frac{du_z}{e} \right\} \tag{A.8}$$

$$\{du, d\alpha\} = \left\{ du_x^1, du_y^1, du_x^2, du_y^2, du_x^3, du_y^3, du_x^4, du_y^4, d\alpha_1, d\alpha_2, d\alpha_3 \right\} \tag{A.9}$$

$$[B] = [B_u \vdots B_\alpha] = \begin{bmatrix} B_x^1 & 0 & B_x^2 & 0 & B_x^3 & 0 & B_x^4 & 0 & \vdots & 0 & 0 & 0 \\ B_y^1 & 0 & B_y^2 & 0 & B_y^3 & 0 & B_y^4 & 0 & \vdots & 0 & 0 & 0 \\ 0 & B_x^1 & 0 & B_x^2 & 0 & B_x^3 & 0 & B_x^4 & \vdots & 0 & 0 & 0 \\ 0 & B_y^1 & 0 & B_y^2 & 0 & B_y^3 & 0 & B_y^4 & \vdots & 0 & 0 & 0 \\ 0 & 0 & 0 & 0 & 0 & 0 & 0 & 0 & \vdots & \dfrac{1}{e} & \dfrac{x}{e} & \dfrac{y}{e} \end{bmatrix} \tag{A.10}$$

The notation $\{\ \}$ is used to indicate that the vector has to be considered as a column.

To derive the terms of the matrix *B* relative to the coordinates α_I, the following relation has to be considered: $\dfrac{du_z}{e} = \dfrac{d(e)}{e} = \dfrac{1}{e}\left(d\alpha_1 + d\alpha_2 x + d\alpha_3 y\right)$. The variations of *x* and *y*, which are second order effects, are not taken into account. The detailed calculation of the terms B_x^I and B_y^I can be found in Zhu's thesis (Zhu 1992a) and are not retranscribed here.

The rigidity matrix is obtained by differentiation of the nodal forces. For the degrees of freedom in the plane of the section, the nodal forces are given by:

$$\{F_u\} = \int_V \left[B_u\right]^T \{\sigma\}\, dV \tag{A.11}$$

and for the degrees of freedom relative to the additional node:

$$\{F_\alpha\} = \int_V \left[B_\alpha\right]^T \{\sigma\}\, dV \tag{A.12}$$

where the stress field vector is given by:

$$\{\sigma\} = \begin{Bmatrix} \sigma_x \\ \sigma_{xy} \\ \sigma_{yx} \\ \sigma_y \\ \sigma_z \end{Bmatrix} \tag{A.13}$$

The tangent matrix K has to link the nodal forces increments to the displacements increments:

$$\begin{bmatrix} dF_u \\ dF_\alpha \end{bmatrix} = \begin{bmatrix} K_{uu} & K_{u\alpha} \\ K_{\alpha u} & K_{\alpha\alpha} \end{bmatrix} \begin{bmatrix} du \\ d\alpha \end{bmatrix} \tag{A.14}$$

The differentiation of (A.11) gives the upper part of the matrix, i.e. K_{uu} and $K_{u\alpha}$, while the differentiation of (A.12) gives the lower part, i.e. $K_{\alpha u}$ and $K_{\alpha\alpha}$.

To simplify the presentation, all the matrices that are developed in this chapter comprise only the mechanical degrees of freedom. The coupling thermomechanical terms are identical to those of the strain plane state and are already implemented in the element.

A.2.1.1 Computation of the upper part of the matrix K

To perform the numerical integration, equation (A.11) is written:

$$\{F_u\} = \left[B_u\right]^T \{\sigma\} \left|J\right| e\, w \tag{A.15}$$

where $\left|J\right|$ is the transformation Jacobian in the plane x-y and w the integration weight. The mixed 4-node element developed here has one single integration, otherwise a sum over the integrations points should be introduced in equation (A.15).

The differentiation of (A.15) comprises four terms:

$$\begin{aligned} \{dF_u\} &= [B_u]^T \{d\sigma\} |J| e\, w \qquad (1) \\ &+ d\left([B_u]^T\right)\{\sigma\} |J| e\, w \qquad (2) \\ &+ [B_u]^T \{\sigma\} d\left(|J|\right) e\, w \qquad (3) \\ &+ [B_u]^T \{\sigma\} |J| de\, w \qquad (4) \end{aligned} \tag{A.16}$$

Computation of the first term

$$\{dF_u\}^{(1)} = [B_u]^T \{d\sigma\} |J| e\, w \tag{A.17}$$

Knowing that $\{d\sigma\} = [C]\{d\varepsilon\}$ and $\{d\varepsilon\} = [B]\{du, d\alpha\}$ where $[C]$ is the constitutive matrix, equation (A.17) becomes:

$$\{dF_u\}^{(1)} = [B_u]^T [C][B] |J| e\, w \{du, d\alpha\} \tag{A.18}$$

The part of the tangent matrix due to term (1) is then given by:

$$[K_u]^{(1)} = [B_u]^T [C][B] |J| e\, w = [B_u]^T [C][B_u \vdots B_\alpha] |J| e\, w \tag{A.19}$$

which is composed by the classical tangent matrix (A.20) plus the part to add due to the modelling of the generalized plane state (A.21):

$$[K_{uu}]^{(1)} = [B_u]^T [C][B_u] |J| e\, w \tag{A.20}$$

$$[K_{u\alpha}]^{(1)} = [B_u]^T [C][B_\alpha] |J| e\, w \tag{A.21}$$

The terms of the tangent matrix that couple two nodes *I* and *J* can now be calculated. The term of the matrix $[B_u]$ corresponding to node *I* are:

$$[B_u]_I = \begin{bmatrix} B_x^I & 0 \\ B_y^I & 0 \\ 0 & B_x^I \\ 0 & B_y^I \\ 0 & 0 \end{bmatrix} \tag{A.22}$$

and the matrix $[C]$ can be written:

$$[C]=\begin{bmatrix} C_{11} & C_{12} & C_{13} & C_{14} & C_{15} \\ C_{21} & C_{22} & C_{23} & C_{24} & C_{25} \\ C_{31} & C_{32} & C_{33} & C_{34} & C_{35} \\ C_{41} & C_{42} & C_{43} & C_{44} & C_{45} \\ C_{51} & C_{52} & C_{53} & C_{54} & C_{55} \end{bmatrix} \tag{A.23}$$

Finally, using (A.20), (A.22) and (A.23), the matrix coupling nodes *I* and *J* can be computed as follows:

$$[K_{uu}]^{(1)}_{I,J}=\begin{bmatrix} B^I_x(C_{11}B^J_x+C_{12}B^J_y) & B^I_x(C_{13}B^J_x+C_{14}B^J_y) \\ \quad +B^I_y(C_{21}B^J_x+C_{22}B^J_y) & \quad +B^I_y(C_{23}B^J_x+C_{24}B^J_y) \\ B^I_x(C_{31}B^J_x+C_{32}B^J_y) & B^I_x(C_{33}B^J_x+C_{34}B^J_y) \\ \quad +B^I_y(C_{41}B^J_x+C_{42}B^J_y) & \quad +B^I_y(C_{43}B^J_x+C_{44}B^J_y) \end{bmatrix} |J|\,e\,w \tag{A.24}$$

The matrix $[B_\alpha]$ has to be taken into account to calculate the terms associated with the degrees of freedom of the additional node:

$$[B_\alpha]=\frac{1}{e}\begin{bmatrix} 0 & 0 & 0 \\ 0 & 0 & 0 \\ 0 & 0 & 0 \\ 0 & 0 & 0 \\ 1 & x & y \end{bmatrix} \tag{A.25}$$

The terms of the matrix *K* that couple a node *I* with the additional node, associated with the generalized plane state, are defined using (A.21), (A.22), (A.23) and (A.25):

$$[K_{u\alpha}]^{(1)}_I=\begin{bmatrix} B^I_xC_{15}+B^I_yC_{25} & \left(B^I_xC_{15}+B^I_yC_{25}\right)x & \left(B^I_xC_{15}+B^I_yC_{25}\right)y \\ B^I_xC_{35}+B^I_yC_{45} & \left(B^I_xC_{35}+B^I_yC_{45}\right)x & \left(B^I_xC_{35}+B^I_yC_{45}\right)y \end{bmatrix} |J|\,e\,w \tag{A.26}$$

Computation of the second term

The second term of equation (A.16) is given by:

$$\{dF_u\}^{(2)}=d\left([B_u]^T\right)\{\sigma\}|J|\,e\,w \tag{A.27}$$

with

$$d\left[B_u\right]^T = \frac{\partial\left[B_u\right]^T}{\partial u}\left\{du\right\} \tag{A.28}$$

The nodal forces corresponding to the degrees of freedom *x* and *y* are computed by detailing expression (A.15) by using (A.13) and (A.22):

$$\begin{aligned}\left\{F_u\right\}_{xI} &= \left(B_x^I\sigma_x + B_y^I\sigma_{xy}\right)\left|J\right|e\,w = \left(\frac{\partial N_I}{\partial x}\sigma_x + \frac{\partial N_I}{\partial y}\sigma_{xy}\right)\left|J\right|e\,w \\ \left\{F_u\right\}_{yI} &= \left(B_x^I\sigma_{xy} + B_y^I\sigma_y\right)\left|J\right|e\,w = \left(\frac{\partial N_I}{\partial x}\sigma_{xy} + \frac{\partial N_I}{\partial y}\sigma_y\right)\left|J\right|e\,w\end{aligned} \tag{A.29}$$

The derivation of the extrapolation functions N_I is given by:

$$\begin{aligned}\frac{\partial N_I}{\partial x} &= \frac{\partial N_I}{\partial \xi}\frac{\partial \xi}{\partial x} + \frac{\partial N_I}{\partial \eta}\frac{\partial \eta}{\partial x} = \frac{1}{\left|J\right|}\left(\frac{\partial N_I}{\partial \xi}\frac{\partial y}{\partial \eta} - \frac{\partial N_I}{\partial \eta}\frac{\partial y}{\partial \xi}\right) \\ \frac{\partial N_I}{\partial y} &= \frac{\partial N_I}{\partial \xi}\frac{\partial \xi}{\partial y} + \frac{\partial N_I}{\partial \eta}\frac{\partial \eta}{\partial y} = \frac{1}{\left|J\right|}\left(-\frac{\partial N_I}{\partial \xi}\frac{\partial x}{\partial \eta} + \frac{\partial N_I}{\partial \eta}\frac{\partial x}{\partial \xi}\right)\end{aligned} \tag{A.30}$$

Introducing relations (A.30) in (A.29) leads to the simplification of the term $\left|J\right|$. Due to this simplification it is no longer necessary to calculate the third term of equation (A.16) independently.

The components of equation (A.16) relative to the second and third term are given by:

$$\begin{aligned}\left\{dF_u\right\}_{xI}^{(2)(3)} &= \left(d\left(\frac{\partial N_I}{\partial x}\left|J\right|\right)\sigma_x + d\left(\frac{\partial N_I}{\partial y}\left|J\right|\right)\sigma_{xy}\right)e\,w \\ \left\{dF_u\right\}_{yI}^{(2)(3)} &= \left(d\left(\frac{\partial N_I}{\partial x}\left|J\right|\right)\sigma_{xy} + d\left(\frac{\partial N_I}{\partial y}\left|J\right|\right)\sigma_y\right)e\,w\end{aligned} \tag{A.31}$$

with

$$\begin{aligned}d\left(\frac{\partial N_I}{\partial x}\left|J\right|\right) &= d\left(\frac{\partial N_I}{\partial \xi}\frac{\partial y}{\partial \eta} - \frac{\partial N_I}{\partial \eta}\frac{\partial y}{\partial \xi}\right) = d\underbrace{\left(\frac{\partial N_I}{\partial \xi}\frac{\partial N_J}{\partial \eta} - \frac{\partial N_I}{\partial \eta}\frac{\partial N_J}{\partial \xi}\right)}_{S_{IJ}}y_J \\ d\left(\frac{\partial N_I}{\partial y}\left|J\right|\right) &= d\left(-\frac{\partial N_I}{\partial \xi}\frac{\partial x}{\partial \eta} + \frac{\partial N_I}{\partial \eta}\frac{\partial x}{\partial \xi}\right) = d\underbrace{\left(-\frac{\partial N_I}{\partial \xi}\frac{\partial N_J}{\partial \eta} + \frac{\partial N_I}{\partial \eta}\frac{\partial N_J}{\partial \xi}\right)}_{-S_{IJ}=S_{JI}}x_J\end{aligned} \tag{A.32}$$

Finally the terms of the matrix *K* that couple nodes *I* and *J* are written:

$$\left[K_{uu}\right]_{IJ}^{(2)(3)} = \begin{bmatrix} -S_{IJ}\sigma_{xy} & S_{IJ}\sigma_{x} \\ -S_{IJ}\sigma_{y} & S_{IJ}\sigma_{xy} \end{bmatrix} e\, w \tag{A.33}$$

The matrix (A.33) is called the stress matrix. This matrix appears due the large deformations.

There are no terms $\left[K_{u\alpha}\right]_{I}^{(2)(3)}$.

Computation of the fourth term

The fourth term of equation (A.16) is given by:

$$\left\{dF_u\right\}^{(4)} = \left[B_u\right]^T \left\{\sigma\right\} \left|J\right| de\, w \tag{A.34}$$

The variation of the slice thickness *de* (A.36) is computed using expression (A.2) and the coordinates transformation relations (A.35):

$$x = \sum_I N_I x_I \quad \text{and} \quad y = \sum_I N_I y_I \tag{A.35}$$

$$\begin{aligned} de &= d\alpha_1 + d\alpha_2\, x + d\alpha_3\, y + \alpha_2\, dx + \alpha_3\, dy \\ &= d\alpha_1 + \sum_J N_J \left(d\alpha_2\, x_J + d\alpha_3\, y_J + \alpha_2\, dx_J + \alpha_3\, dy_J\right) \\ &= d\alpha_1 + d\alpha_2\, x + d\alpha_3\, y + \sum_J N_J \left(\alpha_2\, dx_J + \alpha_3\, dy_J\right) \end{aligned} \tag{A.36}$$

The three first terms contribute to the part $K_{u\alpha}$ while the last terms contribute to the part K_{uu} of the stiffness matrix K:

$$\left\{dF_u\right\}_I^{(4)} = \sum_J \left[K_{uu}\right]_{I,J}^{(4)} \left\{du\right\}_J + \left[K_{u\alpha}\right]_I^{(4)} \left\{d\alpha\right\} \tag{A.37}$$

The nodal forces corresponding to the degrees of freedom *x* and *y* are computed by detailing expression (A.34) by using (A.13) and (A.22):

$$\begin{aligned} \left\{dF_u\right\}_{xI}^{(4)} &= \left(B_x^I \sigma_x + B_y^I \sigma_{xy}\right) \left|J\right| de\, w \\ \left\{dF_u\right\}_{yI}^{(4)} &= \left(B_x^I \sigma_{xy} + B_y^I \sigma_y\right) \left|J\right| de\, w \end{aligned} \tag{A.38}$$

Finally, linking equations (A.36), (A.37) and (A.38) gives the expression of K_{uu} and $K_{u\alpha}$ relative the fourth term of equation (A.16):

$$\left[K_{uu}\right]_{I,J}^{(4)} = N_J \begin{bmatrix} \alpha_2 \left(B_x^I \sigma_x + B_y^I \sigma_{xy}\right) & \alpha_3 \left(B_x^I \sigma_x + B_y^I \sigma_{xy}\right) \\ \alpha_2 \left(B_x^I \sigma_{xy} + B_y^I \sigma_y\right) & \alpha_3 \left(B_x^I \sigma_{xy} + B_y^I \sigma_y\right) \end{bmatrix} \left|J\right| w \tag{A.39}$$

$$\left[K_{u\alpha}\right]_I^{(4)} = \begin{bmatrix} B_x^I\sigma_x + B_y^I\sigma_{xy} & \left(B_x^I\sigma_x + B_y^I\sigma_{xy}\right)x & \left(B_x^I\sigma_x + B_y^I\sigma_{xy}\right)y \\ B_x^I\sigma_{xy} + B_y^I\sigma_y & \left(B_x^I\sigma_{xy} + B_y^I\sigma_y\right)x & \left(B_x^I\sigma_{xy} + B_y^I\sigma_y\right)y \end{bmatrix} |J| w \quad \text{(A.40)}$$

A.2.1.2 Computation of the lower part of the matrix K

To perform the numerical integration, equation (A.12) is written:

$$\{F_\alpha\} = [B_\alpha]^T \{\sigma\} |J| e w \quad \text{(A.41)}$$

The differentiation of (A.41) comprises four terms:

$$\begin{aligned} \{dF_\alpha\} \quad &= \quad [B_\alpha]^T \{d\sigma\} |J| e w \qquad (1) \\ &+ \quad d\left([B_\alpha]^T\right)\{\sigma\} |J| e w \qquad (2) \\ &+ \quad [B_\alpha]^T \{\sigma\} d\left(|J|\right) e w \qquad (3) \\ &+ \quad [B_\alpha]^T \{\sigma\} |J| de w \qquad (4) \end{aligned} \quad \text{(A.42)}$$

Computation of the first term

The first term of equation (A.42) is given by:

$$\{dF_\alpha\}^{(1)} = [B_\alpha]^T \{d\sigma\} |J| e w \quad \text{(A.43)}$$

Knowing that $\{d\sigma\} = [C]\{d\varepsilon\}$ and $\{d\varepsilon\} = [B]\{du, d\alpha\}$, (A.43) becomes:

$$\{dF_\alpha\}^{(1)} = [B_\alpha]^T [C][B] |J| e w \{du, d\alpha\} \quad \text{(A.44)}$$

The part of the tangent matrix due to the first term of equation (A.42) is:

$$[K_\alpha]^{(1)} = [B_\alpha]^T [C][B] |J| e w = [B_\alpha]^T [C][B_u \vdots B_\alpha] |J| e w \quad \text{(A.45)}$$

which comprises the two terms of K_α:

$$[K_{\alpha u}]^{(1)} = [B_\alpha]^T [C][B_u] |J| e w \quad \text{(A.46)}$$

$$[K_{\alpha\alpha}]^{(1)} = [B_\alpha]^T [C][B_\alpha] |J| e w \quad \text{(A.47)}$$

The terms of the matrix K that couple a node J with the additional node, associated with the generalized plane state, are defined using (A.22), (A.23), (A.25) and (A.46):

$$\left[K_{\alpha u}\right]_J^{(1)} = \begin{bmatrix} B_x^J C_{51} + B_y^J C_{52} & B_x^J C_{53} + B_y^J C_{54} \\ \left(B_x^J C_{51} + B_y^J C_{52}\right) x & \left(B_x^J C_{53} + B_y^J C_{54}\right) x \\ \left(B_x^J C_{51} + B_y^J C_{52}\right) y & \left(B_x^J C_{53} + B_y^J C_{54}\right) y \end{bmatrix} |J| w \qquad \text{(A.48)}$$

The components of the matrix *K* that couple the degrees of freedom of the additional node are calculated using equation (A.47) associated with equations (A.23) and (A.25):

$$\left[K_{\alpha\alpha}\right]^{(1)} = \frac{1}{e} C_{55} \begin{bmatrix} 1 & x & y \\ x & x^2 & xy \\ y & xy & y^2 \end{bmatrix} |J| w \qquad \text{(A.49)}$$

Computation of the second term

The second term of equation (A.42) is given by:

$$\left\{dF_\alpha\right\}^{(2)} = d\left(\left[B_\alpha\right]^T\right)\{\sigma\}|J|\, e\, w \qquad \text{(A.50)}$$

where

$$d\left(\left[B_\alpha\right]^T\right) = \frac{\partial\left(\left[B_\alpha\right]^T\right)}{\partial x} dx + \frac{\partial\left(\left[B_\alpha\right]^T\right)}{\partial y} dy \qquad \text{(A.51)}$$

and

$$\left[B_\alpha\right]^T = \frac{1}{e}\begin{bmatrix} 0 & 0 & 0 & 0 & 1 \\ 0 & 0 & 0 & 0 & x \\ 0 & 0 & 0 & 0 & y \end{bmatrix} = \frac{1}{e}\begin{bmatrix} 0 & 0 & 0 & 0 & 1 \\ 0 & 0 & 0 & 0 & \sum_J N_J x_J \\ 0 & 0 & 0 & 0 & \sum_J N_J y_J \end{bmatrix} \qquad \text{(A.52)}$$

The partial derivation can be decomposed as follows:

$$\frac{\partial}{\partial x} dx = \sum_I \frac{\partial}{\partial x_I} dx_I \quad \text{and} \quad \frac{\partial x_J}{\partial x_I} = \delta_{IJ} \qquad \text{(A.53)}$$

Introducing expressions (A.53) in (A.51) and (A.52) gives the following result:

$$d\left(\left[B_\alpha\right]^T\right)=\frac{1}{e}\begin{bmatrix} & & & & \\ 0 & 0 & 0 & 0 & 1 \\ & & & & \\ 0 & 0 & 0 & 0 & N_J\sum_I \frac{\partial x_J}{\partial x_I}dx_I \\ & & & & \\ 0 & 0 & 0 & 0 & N_J\sum_I \frac{\partial y_J}{\partial y_I}dy_I \\ & & & & \end{bmatrix}=\frac{1}{e}\begin{bmatrix} 0 & 0 & 0 & 0 & 1 \\ 0 & 0 & 0 & 0 & N_J dx_J \\ 0 & 0 & 0 & 0 & N_J dy_J \end{bmatrix} \quad \text{(A.54)}$$

To avoid too heavy calculations, the term $\frac{1}{e}$, which would lead to second order effects, is not derived. This induces a small imprecision in the tangent matrix but does not introduce any errors in the results of the finite element calculations.

The component of the matrix *K* that couples the additional node to a node *J* is given by equation (A.55):

$$\left[K_{\alpha u}\right]_J^{(2)}=\sigma_z\begin{bmatrix} 0 & 0 \\ N_J & 0 \\ 0 & N_J \end{bmatrix}\left|J\right|w \quad \text{(A.55)}$$

They are no terms $\left[K_{\alpha\alpha}\right]^{(2)}$.

Computation of the third term

The third term of equation (A.42) is given by:

$$\left\{dF_\alpha\right\}^{(3)}=\left[B_\alpha\right]^T\left\{\sigma\right\}d\left(\left|J\right|\right)e\,w \quad \text{(A.56)}$$

The product $\left[B_\alpha\right]^T\left\{\sigma\right\}$ is calculated using equations (A.13) and (A.25):

$$\left[B_\alpha\right]^T\left\{\sigma\right\}=\frac{1}{e}\begin{Bmatrix}\sigma_z \\ x\sigma_z \\ y\sigma_z\end{Bmatrix} \quad \text{(A.57)}$$

The variation of the Jacobian determinant is calculated using equations (A.6) and (A.35):

$$
\begin{aligned}
d|J| &= d\left(\frac{\partial x}{\partial \xi}\frac{\partial y}{\partial \eta}-\frac{\partial x}{\partial \eta}\frac{\partial y}{\partial \xi}\right) \\
&= \left(\frac{\partial dx}{\partial \xi}\frac{\partial y}{\partial \eta}+\frac{\partial x}{\partial \xi}\frac{\partial dy}{\partial \eta}-\frac{\partial dx}{\partial \eta}\frac{\partial y}{\partial \xi}-\frac{\partial x}{\partial \eta}\frac{\partial dy}{\partial \xi}\right) \\
&= \left(\frac{\partial N_J}{\partial \xi}\frac{\partial y}{\partial \eta}-\frac{\partial N_J}{\partial \eta}\frac{\partial y}{\partial \xi}\right)dx_J+\left(\frac{\partial x}{\partial \xi}\frac{\partial N_J}{\partial \eta}-\frac{\partial x}{\partial \eta}\frac{\partial N_J}{\partial \xi}\right)dy_J \\
&= \underbrace{\left(\frac{\partial N_J}{\partial \xi}\frac{\partial N_I}{\partial \eta}-\frac{\partial N_J}{\partial \eta}\frac{\partial N_I}{\partial \xi}\right)}_{S_{JI}}dx_J\ y_I+\underbrace{\left(\frac{\partial N_I}{\partial \xi}\frac{\partial N_J}{\partial \eta}-\frac{\partial N_I}{\partial \eta}\frac{\partial N_J}{\partial \xi}\right)}_{S_{IJ}=-S_{JI}}dy_J\ x_I
\end{aligned}
\tag{A.58}
$$

Finally, the component of the matrix *K* that couples the additional node to a node *J* is calculated using equations (A.56), (A.57) and (A.58):

$$
\left[K_{\alpha u}\right]_J^{(3)}=\sigma_z\begin{bmatrix} S_{JI}y_I & -S_{JI}x_I \\ \left(S_{JI}y_I\right)x & \left(-S_{JI}x_I\right)x \\ \left(S_{JI}y_I\right)y & \left(-S_{JI}x_I\right)y \end{bmatrix}w \tag{A.59}
$$

The matrix (A.59) is the equivalent of the stress matrix (A.33) but for the degrees of freedom α.

There are no terms $\left[K_{\alpha\alpha}\right]^{(3)}$.

Computation of the fourth term

The fourth term of equation (A.42) is given by:

$$
\left\{dF_\alpha\right\}^{(4)}=\left[B_\alpha\right]^T\left\{\sigma\right\}|J|de\,w \tag{A.60}
$$

Using equations (A.36) and (A.57), (A.60) can be written as follows:

$$
\left\{dF_\alpha\right\}^{(4)}=\sum_J\left[K_{\alpha u}\right]_J^{(4)}\left\{du\right\}_J+\left[K_{\alpha\alpha}\right]^{(4)}\left\{d\alpha\right\} \tag{A.61}
$$

where the components of the matrix *K* are given by:

$$
\left[K_{\alpha u}\right]_J^{(4)}=\frac{1}{e}\sigma_z N_J\begin{bmatrix} \alpha_2 & \alpha_3 \\ \alpha_2 x & \alpha_3 x \\ \alpha_2 y & \alpha_3 y \end{bmatrix}|J|\,w \tag{A.62}
$$

$$
\left[K_{\alpha\alpha}\right]^{(4)}=\frac{1}{e}\sigma_z\begin{bmatrix} 1 & x & y \\ x & x^2 & xy \\ y & xy & y^2 \end{bmatrix}|J|\,w \tag{A.63}
$$

A.2.1.3 Summary

The nodal forces are calculated using equations (A.15) and (A.41) for the degrees of freedom u_I and α_I respectively.

The components of the stiffness matrix are given by the sum of the matrices (A.24), (A.33) and (A.39) for K_{uu}; by the sum of the matrices (A.26) and (A.40) for $K_{u\alpha}$; by the sum of the matrices (A.48), (A.55), (A.59) and (A.62) for $K_{\alpha u}$; and finally by the sum of the matrices (A.49) and (A.63) for $K_{\alpha\alpha}$.

A.3 IMPLEMENTATION IN THE LAGAMINE CODE

A.3.1 ADAPTATION OF THE MIXED 4-NODE ELEMENT

The advantage of the mixed 4-node element is that it is an element that has been developed to be used in case of reduced integration, i.e. with one integration point only. As it would make no sense to use this particular element with more than one integration point in the context of this study, it has been decided to implement the new developments, which permit calculations in generalized plane state, for this case only.

It is then automatically assumed in the code that the generalized plane state is associated with a mixed 4-node element with one single integration point and no modifications have been done to the part of the code that concerns mixed 4-node elements with several integration points.

Similarly, no modifications have been introduced with regard to the *anti-hourglass* stresses. For the mixed 4-node element, the *hourglass* modes are modes that appear in the plane of the element; therefore, it is not necessary to introduce the third dimension linked to the generalized plane state for the calculation of these stresses and of the components of the tangent matrix and nodal forces that are associated to them.

In the routine initially implemented by Zhu, the stress matrix has been replaced by the constitutive matrix (A.64):

$$\left[C^*\right]=\begin{bmatrix} C_{11} & C_{12}-\sigma_{xy} & C_{13} & C_{14}+\sigma_x & C_{15}+\sigma_x \\ C_{21}+\sigma_{xy} & C_{22} & C_{23}-\sigma_x & C_{24} & C_{25}+\sigma_{xy} \\ C_{31} & C_{32}-\sigma_y & C_{33} & C_{34}+\sigma_{yx} & C_{35}+\sigma_{yx} \\ C_{41}+\sigma_y & C_{42} & C_{43}-\sigma_{yx} & C_{44} & C_{45}+\sigma_y \\ C_{51}+\sigma_z & C_{52} & C_{53} & C_{54}+\sigma_z & C_{55} \end{bmatrix} \quad \text{(A.64)}$$

Using matrix $[C^*]$ instead of matrix $[C]$ in equation (A.24) is equivalent to doing the sum equation (A.24) calculated using matrix $[C]$ and equation (A.33). Similarly, equation (A.48) calculated using matrix $[C^*]$ is equivalent to equation (A.48) calculated using matrix $[C]$ to which equation (A.59) is added; and equation (A.26) calculated using matrix $[C^*]$ is equivalent to equation (A.26) calculated using matrix $[C]$ to which equation (A.40) is added.

To implement the modifications relative to the generalized plane state for an existing element, attention must be paid to the following points:

- introduction of an additional parameter that indicates the actual number of nodes of the element, i.e. number of traditional nodes plus one;
- identification of the degrees of freedom α_I of the additional node;
- calculation of the thickness of the slice, which appears in the calculation of the tangent matrix;
- calculation of the velocity for the variation of thickness of the slice and for the coordinates *x* and *y* of the integration point of the element as well as the velocities at the integration point;
- calculation of the nodal forces associated to the additional node;
- introduction of the matrices not included in the traditional element; i.e. for the mixed 4-node element, knowing that $[C]$ is replaced by $[C^*]$: for K_{uu} matrix (A.39), which introduce α_2 and α_3, is added; for $K_{u\alpha}$ matrix (A.26) is added; for $K_{\alpha u}$ matrices (A.48), (A.55) and (A.62) are added; and finally for $K_{\alpha\alpha}$ matrices (A.49) and (A.63) are added.

A.3.2 INFLUENCES ON OTHER PARTS OF THE CODE

The pre-processor routines that read the elements data have to be modified to account for the additional node in case of generalized plane state. As this additional node is common to all the elements, the pre-processor reads this node, which in the LAGAMINE program is always, by convention, the last node appearing in the nodes list, and attaches it to each element used in the discretization of the problem, i.e. to every solid or contact element.

The material laws have also to be adapted for the generalized plane state to be taken into account in the finite element calculations. This work has already been done for the majority of the laws in the LAGAMINE code and in particular, for the modified Norton-Hoff law used in this thesis.

Appendix B

Metallographic analysis of the austenitic grain structure

B.1 DESCRIPTION OF THE CHEMICAL ETCHING

The modified Bechet-Beaujard chemical etching is applied to the ferritic steel specimen in order to reveal the grain boundaries of the initial austenitic phase before analysing the sample under the optical microscope. The operation mode for this operation is detailed in Figure B.1.

B.2 MACROGRAPHS

The position of the surfaces to be observed as well as the division of the sample for the metallographic analysis have been defined in section 4.3.1.2: Determination of the austenite grain size and microscopic structure.

Figures B.2 to B.45 result from the microscopic observations of the two surfaces of interest after the Bechet-Beaujard etching. These micrographs have been used for the determination of the grain size (see Tables 4.2 and 4.3) and for the definition of the grains pattern. They are oriented and labelled as defined by Figure 4.6 and Figure 4.7.

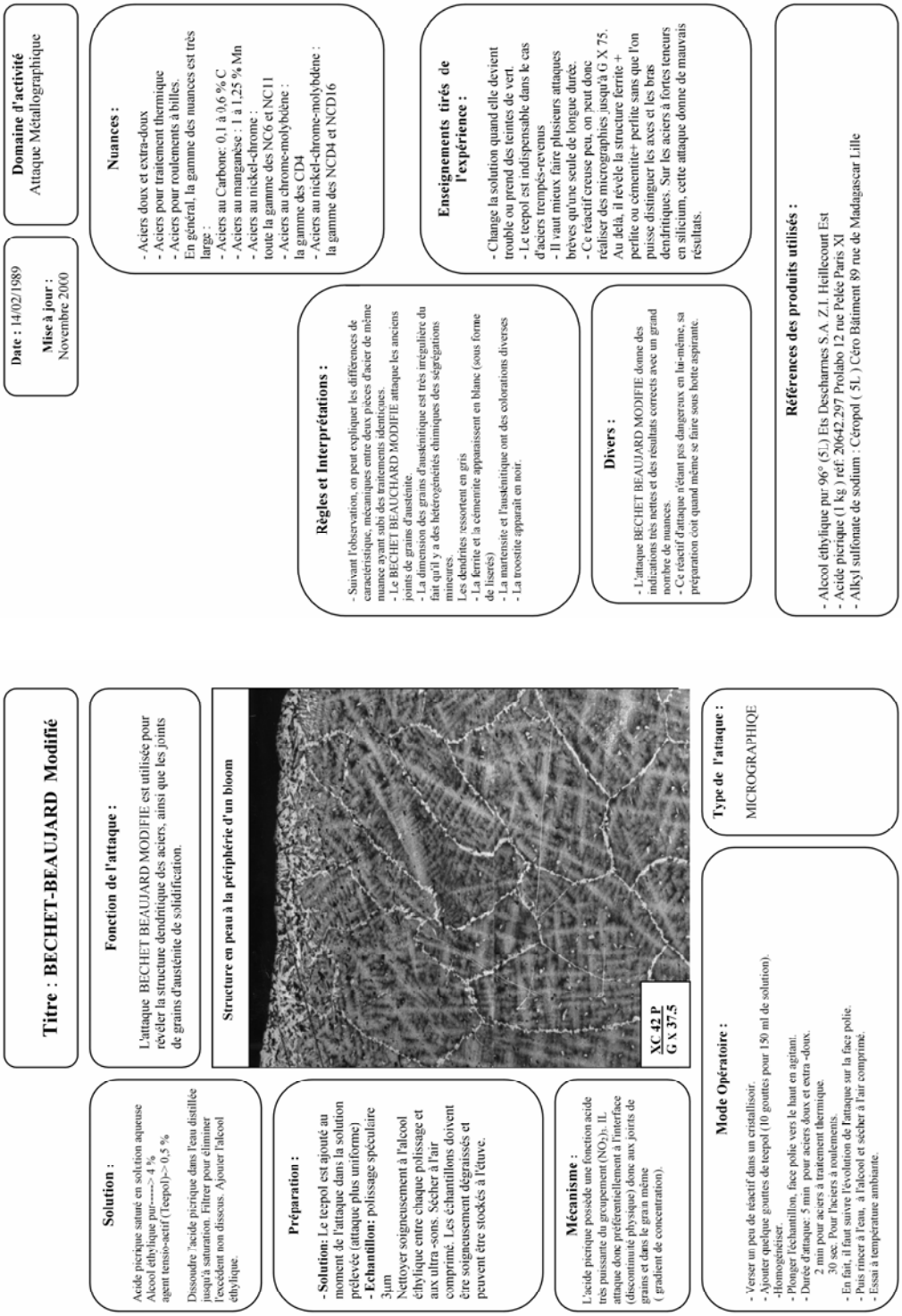

Figure B.1. Operation mode for the modified Bechet-Beaujard chemical etching (source Arcelor – IORC (formerly IRSID)).

Figure B.2. Image Bh1 (used to define mesh).

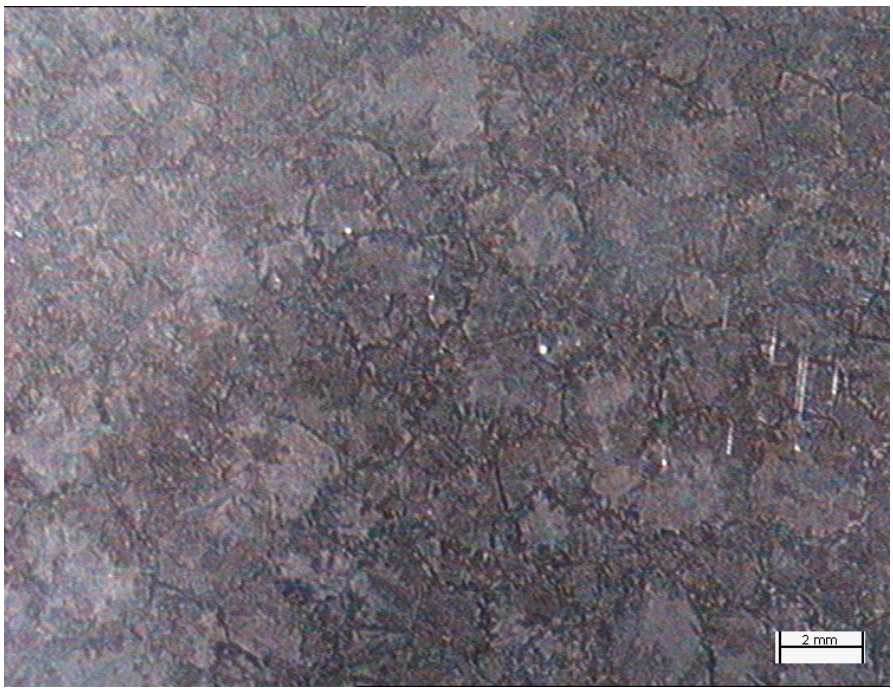

Figure B.3. Image Bh2.

Figure B.4. Image Bh3.

Figure B.5. Image Bh4.

Figure B.6. Image Bh5.

Figure B.7. Image Bh6.

Figure B.8. Image Bh7.

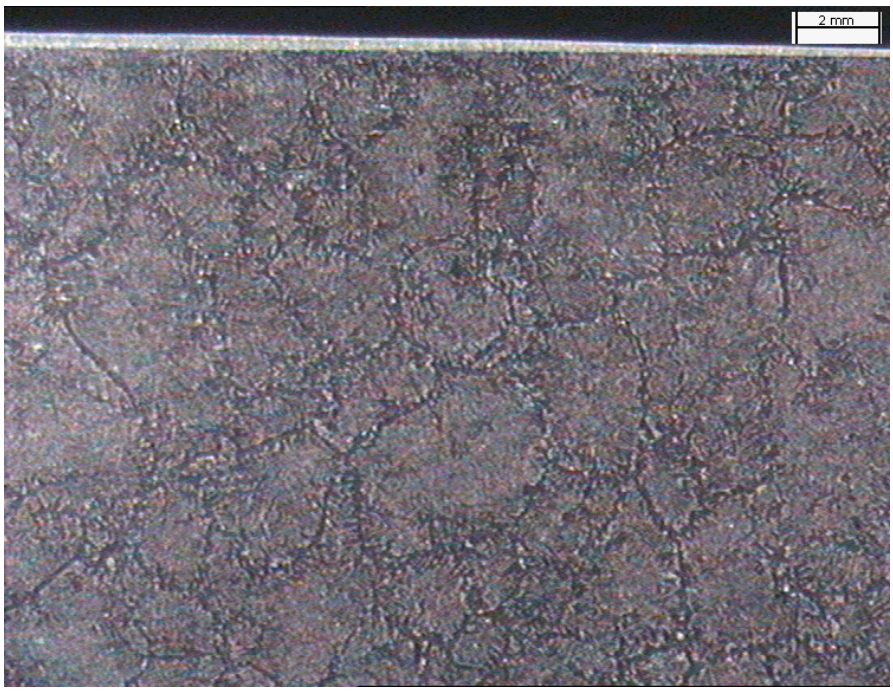

Figure B.9. Image Bh8.

Figure B.10. Image Bh9.

Figure B.11. Image Bh10.

Figure B.12. Image Bh11.

Figure B.13. Image Bh12.

Figure B.14. Image Bh13.

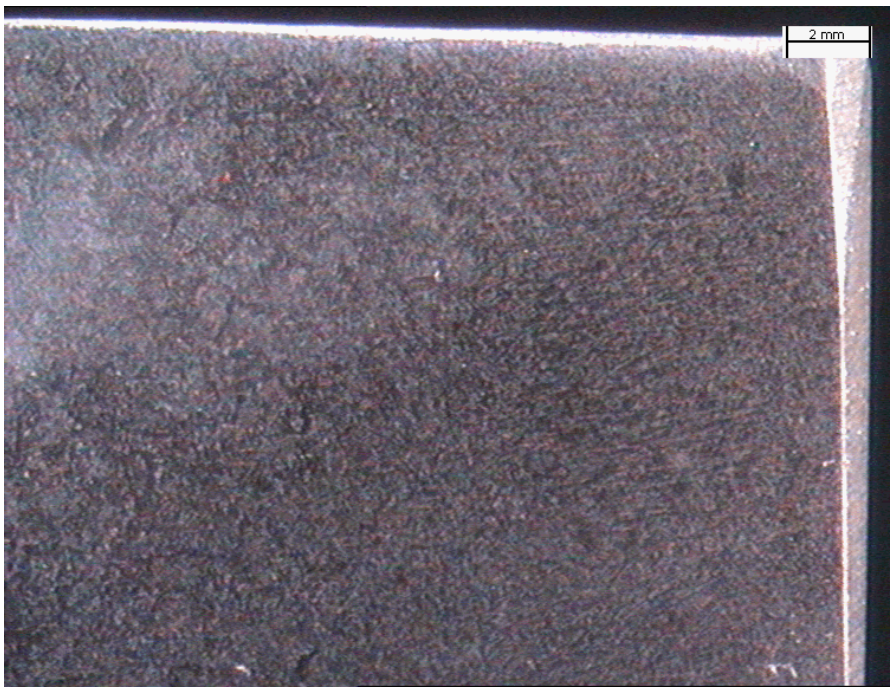

Figure B.15. Image Bh14.

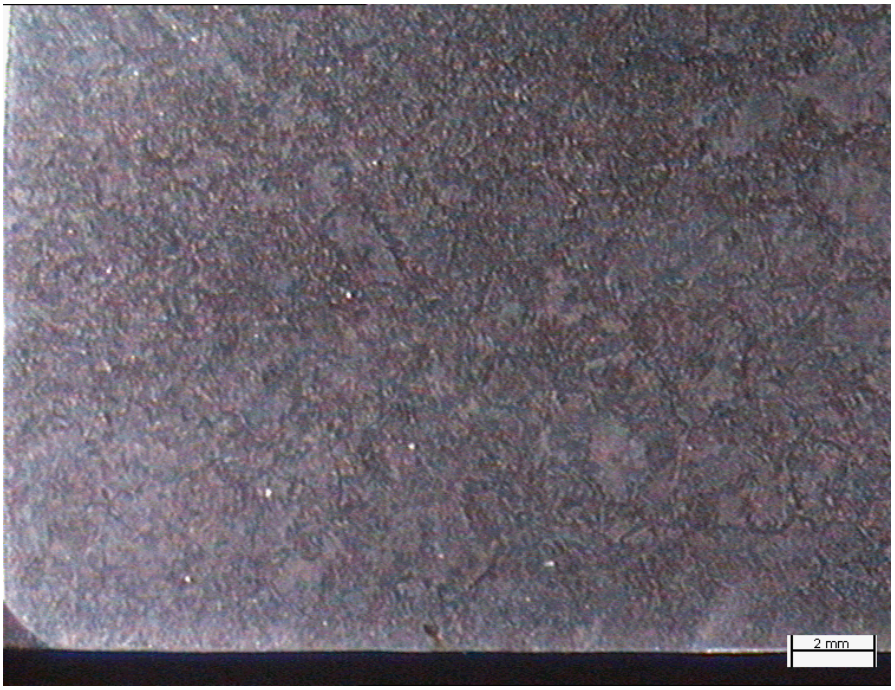

Figure B.16. Image Bb1.

Figure B.17. Image Bb2.

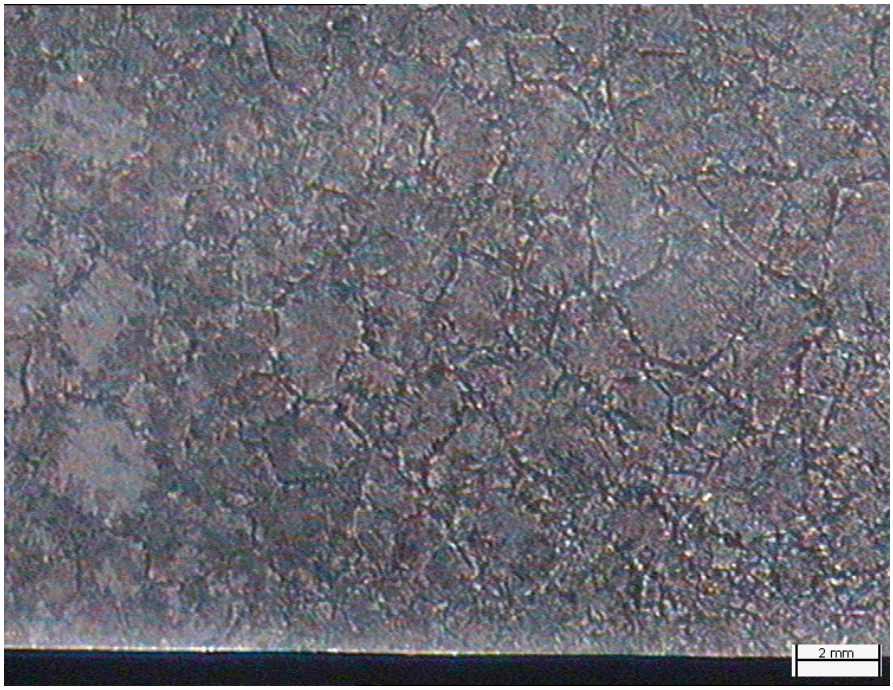

Figure B.18. Image Bb3.

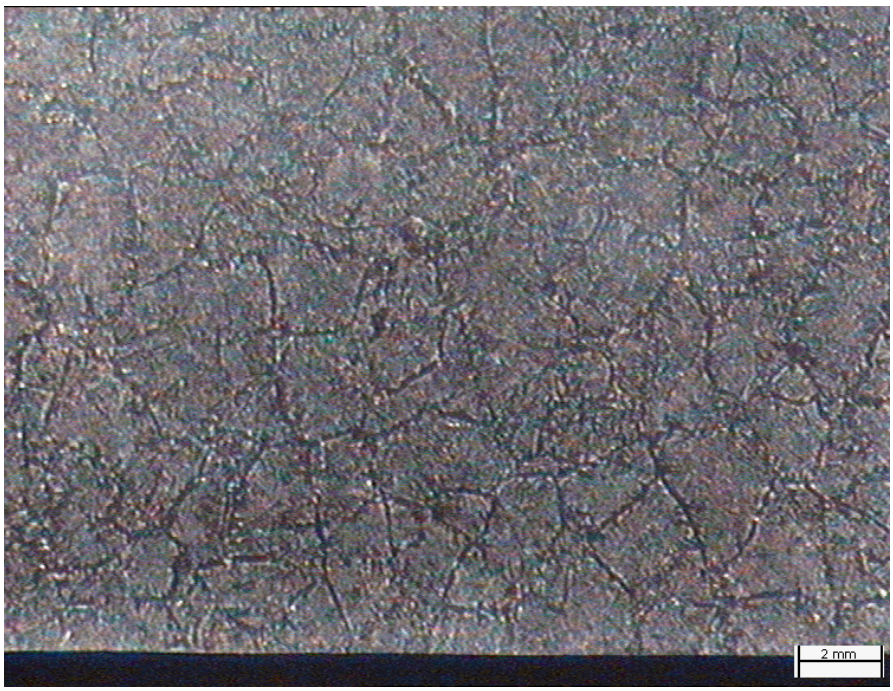

Figure B.19. Image Bb4.

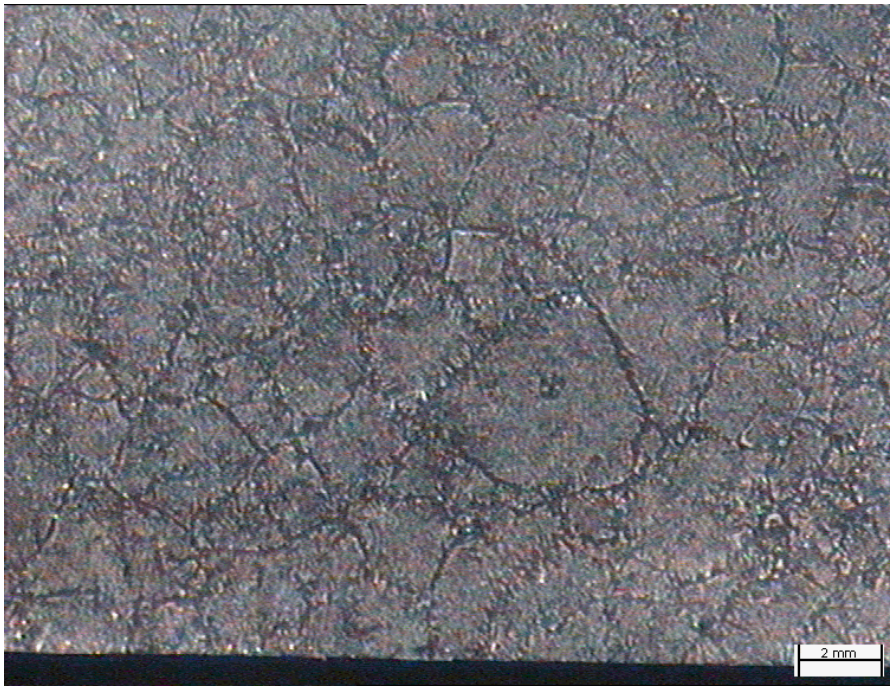

Figure B.20. Image Bb5.

Figure B.21. Image Bb6.

Figure B.22. Image Bb7.

Figure B.23. Image Bb8.

Figure B.24. Image Bb9.

Figure B.25. Image Bb10.

Figure B.26. Image Bb11.

Figure B.27. Image Bb12.

Figure B.28. Image Bb13.

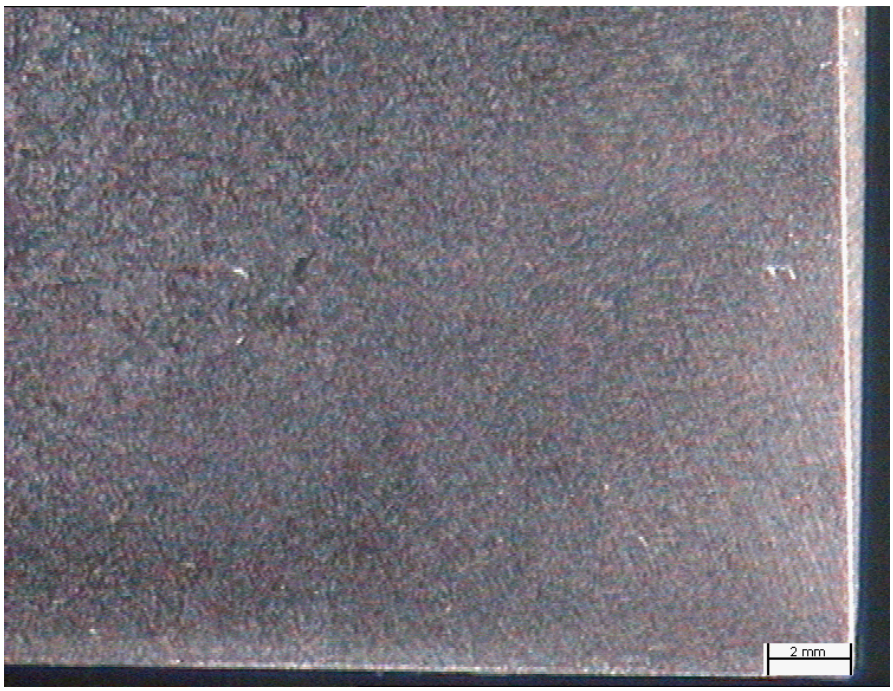

Figure B.29. Image Bb14.

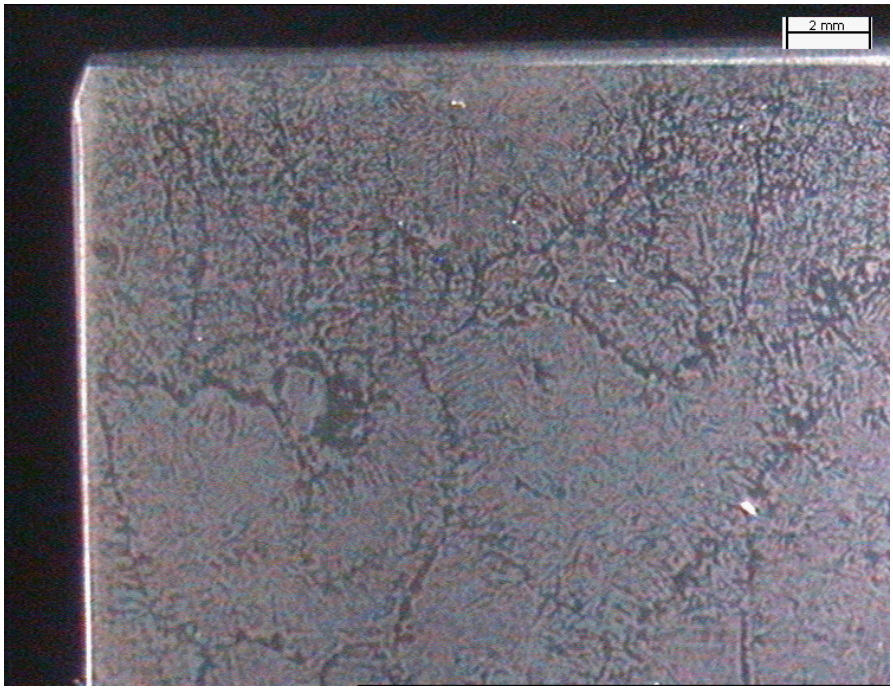

Figure B.30. Image Dh1.

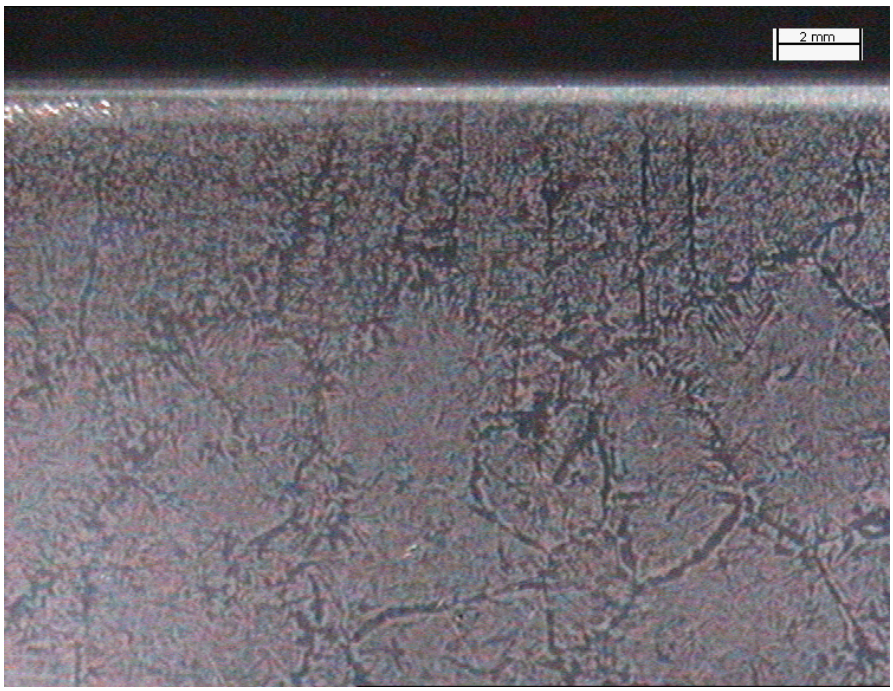

Figure B.31. Image Dh2.

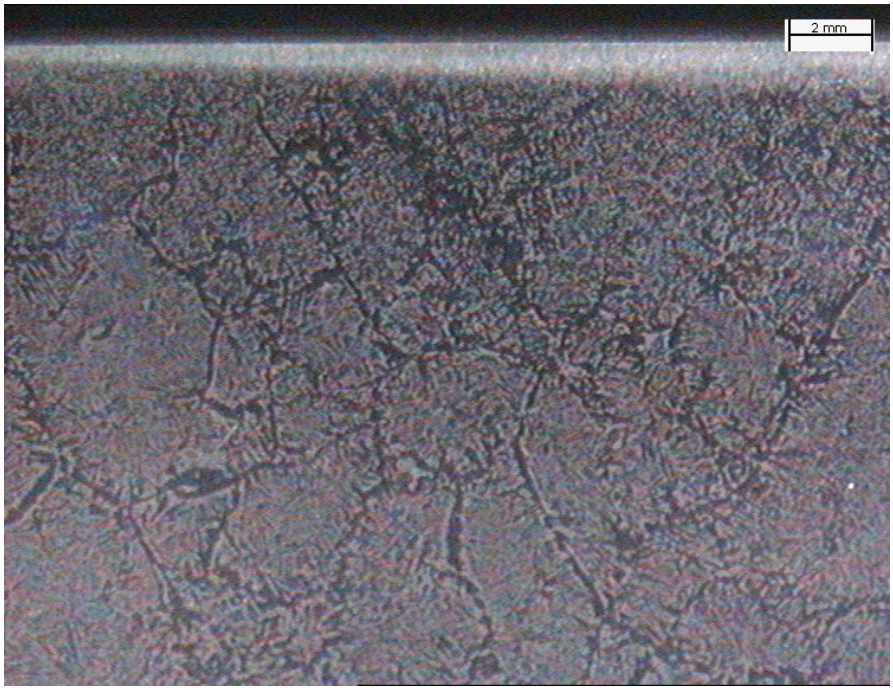

Figure B.32. Image Dh3.

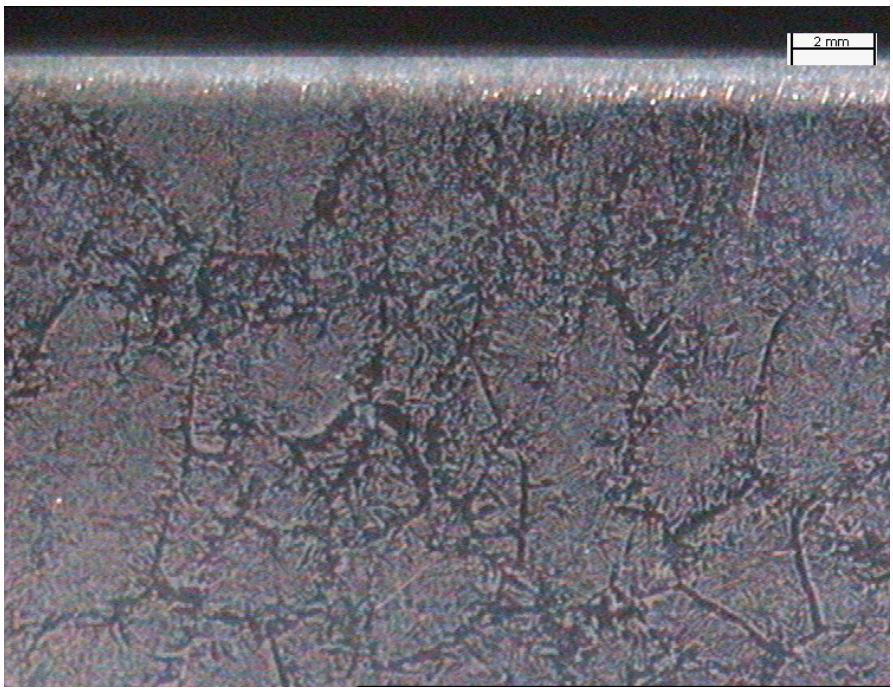

Figure B.33. Image Dh4.

Figure B.34. Image Dh5.

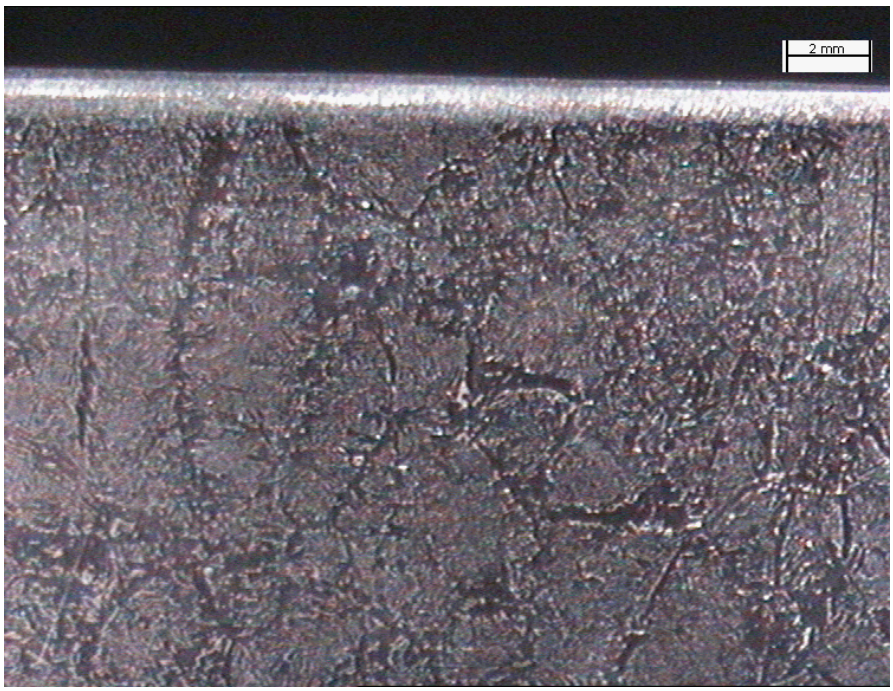

Figure B.35. Image Dh6.

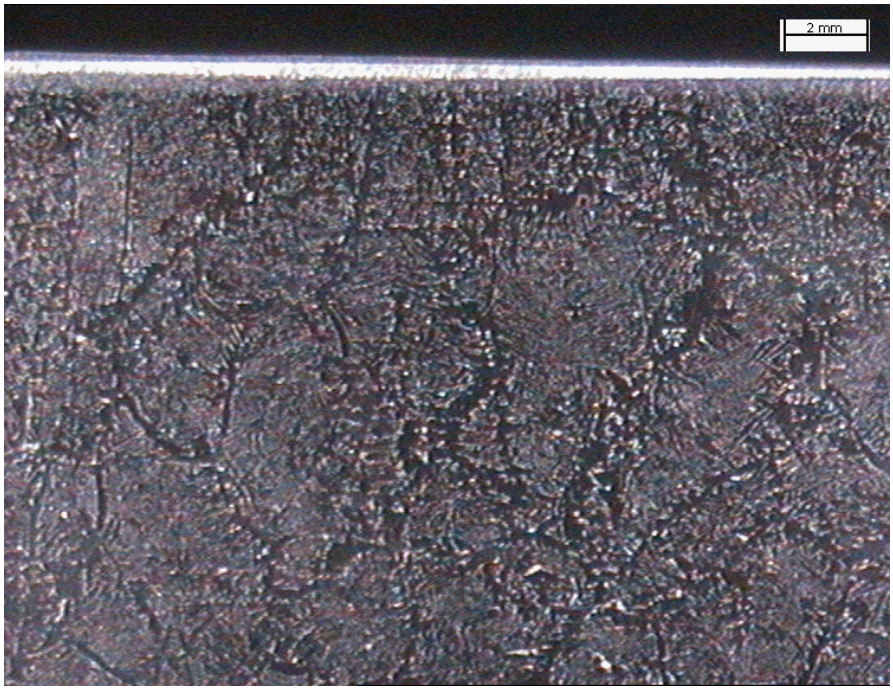

Figure B.36. Image Dh7.

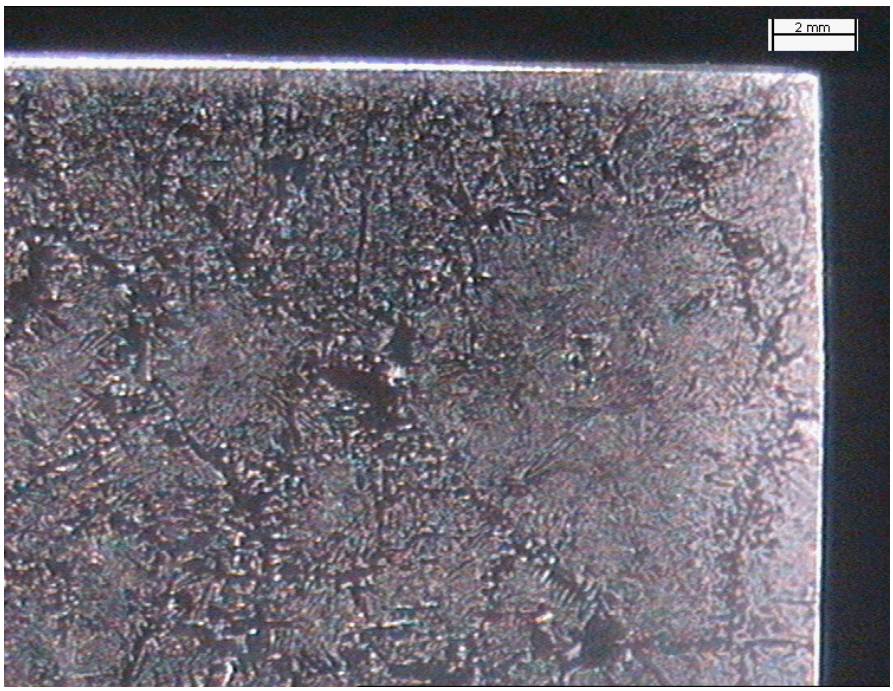

Figure B.37. Image Dh8.

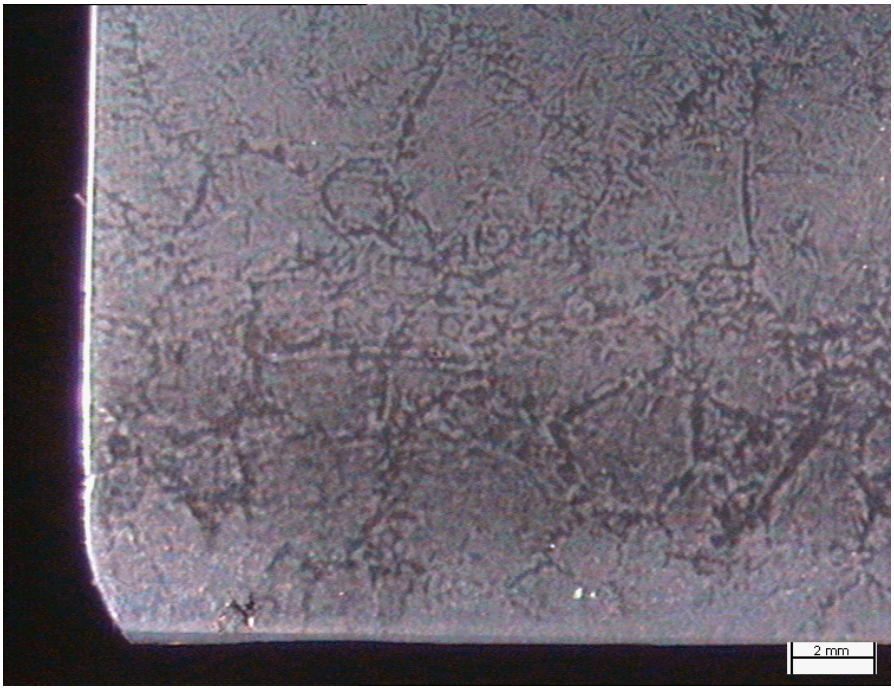

Figure B.38. Image Db1.

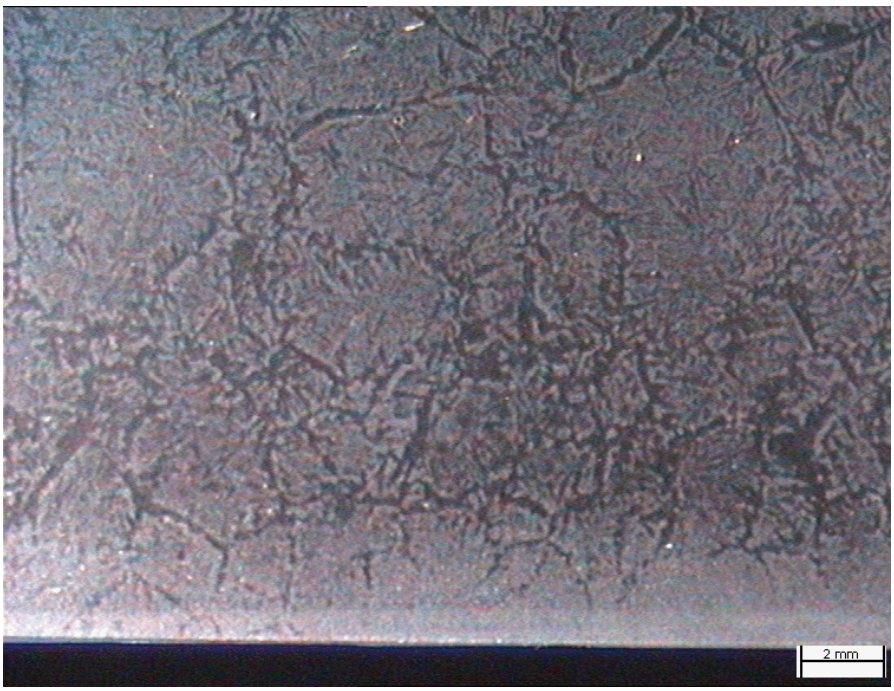

Figure B.39. Image Db2.

Figure B.40. Image Db3.

Figure B.41. Image Db4.

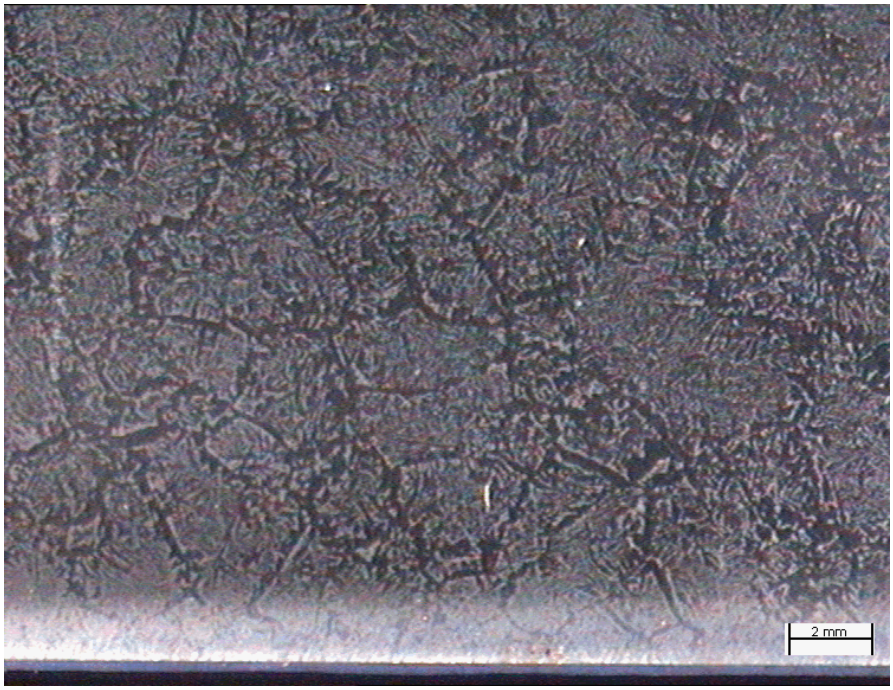

Figure B.42. Image Db5.

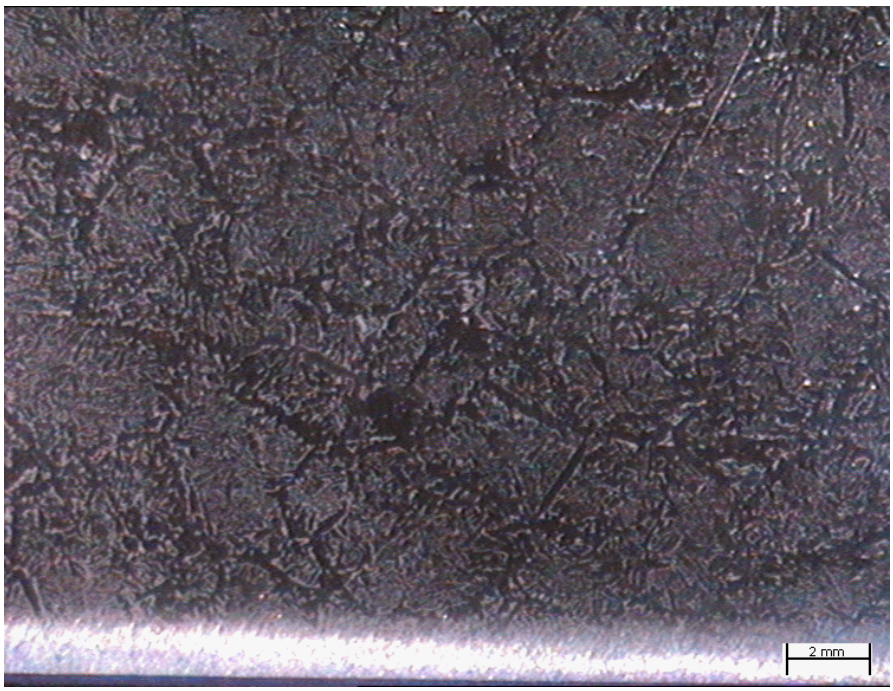

Figure B.43. Image Db6.

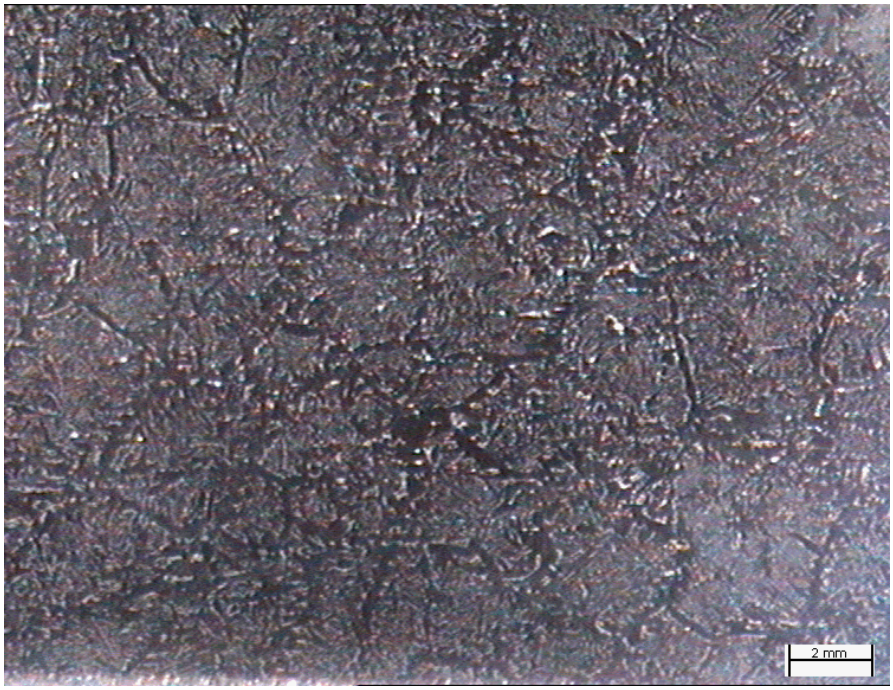

Figure B.44. Image Db7.

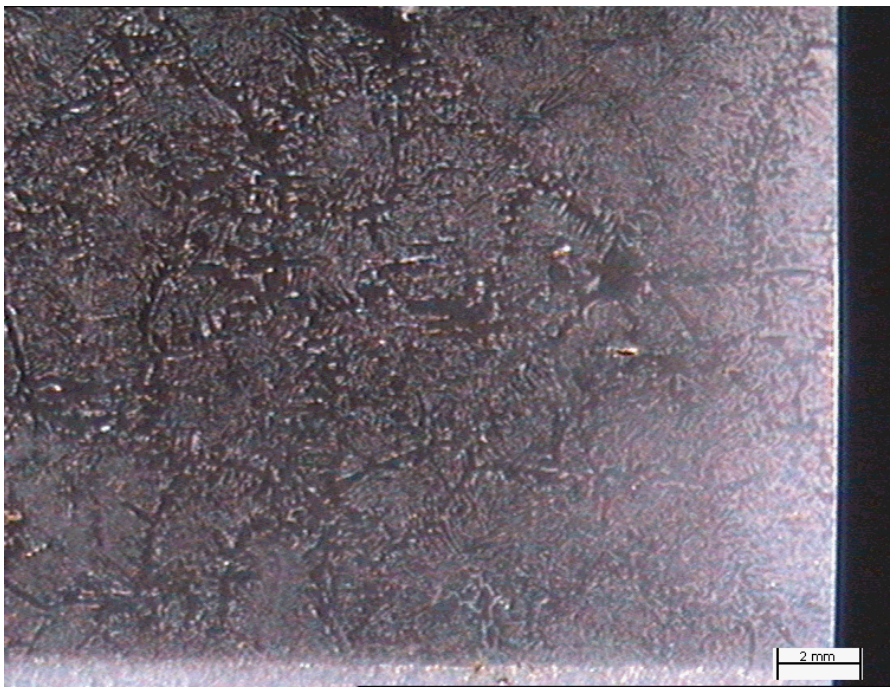

Figure B.45. Image Db8.